

PUBLISHER :



Address of Publisher
& Editor's Office :

GDAŃSK UNIVERSITY
OF TECHNOLOGY
Faculty
of Ocean Engineering
& Ship Technology

ul. Narutowicza 11/12
80-952 Gdańsk, POLAND
tel.: +48 58 347 13 66
fax : +48 58 341 13 66
e-mail : office.pmr@pg.gda.pl

Account number :
BANK ZACHODNI WBK S.A.
I Oddział w Gdańsku
41 1090 1098 0000 0000 0901 5569

Editorial Staff :

Tadeusz Borzęcki Editor in Chief
e-mail : tadbtor@pg.gda.pl

Przemysław Wierzchowski Scientific Editor
e-mail : e.wierzchowski@chello.pl

Jan Michalski Editor for review matters
e-mail : janmi@pg.gda.pl

Aleksander Kniat Editor for international relations
e-mail : olek@pg.gda.pl

Kazimierz Kempa Technical Editor
e-mail : kkempa@pg.gda.pl

Piotr Bzura Managing Editor
e-mail : pbzura@pg.gda.pl

Cezary Spigarski Computer Design
e-mail : biuro@oficynamorska.pl

Domestic price :
single issue : 25 zł

Prices for abroad :
single issue :
- in Europe EURO 15
- overseas US\$ 20

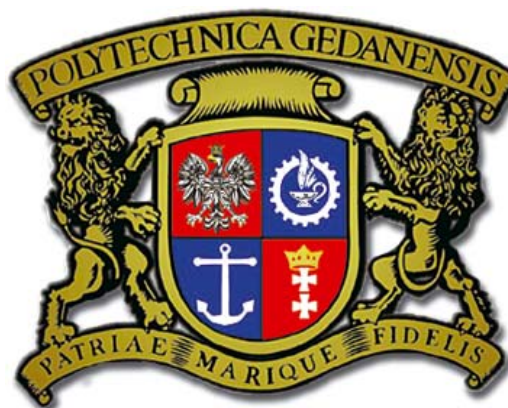
ISSN 1233-2585



**POLISH
MARITIME
RESEARCH**

in internet

www.bg.pg.gda.pl/pmr/pmr.php



POLISH MARITIME RESEARCH

No 2 (78) 2013 Vol 20

CONTENTS

- 3** **TADEUSZ KORONOWICZ, JAN A. SZANTYR**
Comparative analysis of the theoretical models of ideal propulsor, ideal fluid brake, ideal screw propeller and ideal axial wind turbine
- 13** **HASSAN GHASSEMI, MOHSEN TAHERINASAB**
Numerical calculations of the hydrodynamic performance of the contra-rotating propeller (CRP) for high speed vehicle
- 21** **MOHAMMAD HOSEIN KARIMI, MOHAMMAD SAEED SEIF, MADJID ABBASPOOR**
An experimental study of interceptor's effectiveness on hydrodynamic performance of high-speed planing crafts
- 30** **JERZY ŚWIRYDCZUK**
Wake-blade interaction in steam turbine stages
- 41** **MARIUSZ ŻÓŁTOWSKI, BOGDAN ŻÓŁTOWSKI, LEONEL CASTANEDA**
Study of the state a Francis turbine
- 48** **MARIAN PIWOWARSKI**
Design analysis of ORC micro-turbines making use of thermal energy of oceans
- 61** **LAMAS, M. I., RODRÍGUEZ, C. G.**
Numerical model to study the combustion process and emissions in the Wärtsilä 6L 46 four-stroke marine engine
- 67** **DARIUSZ FYDRYCH, JERZY ŁABANOWSKI, GRZEGORZ ROGALSKI**
Weldability of high strength steels in wet welding conditions
- 74** **HUGGO S. BATISTA, TADEUSZ GRACZYK**
An analysis of the welding-induced deformation of ship panels using a statistical tool
- 82** **ANDRZEJ ZAK**
Controlling a team of unmanned underwater vehicles performing water region search tasks
- 90** **MARZENNA POPEK**
The influence of organic polymer on properties of mineral concentrates. Part II

Editorial

POLISH MARITIME RESEARCH is a scientific journal of worldwide circulation. The journal appears as a quarterly four times a year. The first issue of it was published in September 1994. Its main aim is to present original, innovative scientific ideas and Research & Development achievements in the field of :

Engineering, Computing & Technology, Mechanical Engineering,

which could find applications in the broad domain of maritime economy. Hence there are published papers which concern methods of the designing, manufacturing and operating processes of such technical objects and devices as : ships, port equipment, ocean engineering units, underwater vehicles and equipment as well as harbour facilities, with accounting for marine environment protection.

The Editors of POLISH MARITIME RESEARCH make also efforts to present problems dealing with education of engineers and scientific and teaching personnel. As a rule, the basic papers are supplemented by information on conferences , important scientific events as well as cooperation in carrying out international scientific research projects.

Scientific Board

Chairman : Prof. **JERZY GIRTLE**R - Gdańsk University of Technology, Poland

Vice-chairman : Prof. **ANTONI JANKOWSKI** - Institute of Aeronautics, Poland

Vice-chairman : Prof. **MIROSLAW L. WYSZYŃSKI** - University of Birmingham, United Kingdom

Dr **POUL ANDERSEN**
Technical University
of Denmark
Denmark

Prof. **WOLFGANG FRICKE**
Technical University
Hamburg-Harburg
Germany

Prof. **YASUHIKO OHTA**
Nagoya Institute of Technology
Japan

Dr **MEHMET ATLAR**
University of Newcastle
United Kingdom

Prof. **STANISŁAW GUCMA**
Maritime University of Szczecin
Poland

Dr **YOSHIO SATO**
National Traffic Safety
and Environment Laboratory
Japan

Prof. **GÖRAN BARK**
Chalmers University
of Technology
Sweden

Prof. **ANTONI ISKRA**
Poznań University
of Technology
Poland

Prof. **KLAUS SCHIER**
University of Applied Sciences
Germany

Prof. **SERGEY BARSUKOV**
Army Institute of Odessa
Ukraine

Prof. **JAN KICIŃSKI**
Institute of Fluid-Flow Machinery
of PASci
Poland

Prof. **FREDERICK STERN**
University of Iowa,
IA, USA

Prof. **MUSTAFA BAYHAN**
Süleyman Demirel University
Turkey

Prof. **ZYGMUNT KITOWSKI**
Naval University
Poland

Prof. **JÓZEF SZALA**
Bydgoszcz University
of Technology and Agriculture
Poland

Prof. **VINCENZO CRUPI**
University of Messina,
Italy

Prof. **JAN KULCZYK**
Wrocław University of Technology
Poland

Prof. **TADEUSZ SZELANGIEWICZ**
Technical University
of Szczecin
Poland

Prof. **MAREK DZIDA**
Gdańsk University
of Technology
Poland

Prof. **NICOS LADOMMATOS**
University College London
United Kingdom

Prof. **WITALIJ SZCZAGIN**
State Technical University
of Kaliningrad
Russia

Prof. **ODD M. FALTINSEN**
Norwegian University
of Science and Technology
Norway

Prof. **JÓZEF LISOWSKI**
Gdynia Maritime University
Poland

Prof. **BORIS TIKHOMIROV**
State Marine University
of St. Petersburg
Russia

Prof. **PATRICK V. FARRELL**
University of Wisconsin
Madison, WI
USA

Prof. **JERZY MATUSIAK**
Helsinki University
of Technology
Finland

Prof. **DRACOS VASSALOS**
University of Glasgow
and Strathclyde
United Kingdom

Prof. **EUGEN NEGRUS**
University of Bucharest
Romania

Comparative analysis of the theoretical models of ideal propulsor, ideal fluid brake, ideal screw propeller and ideal axial wind turbine

Tadeusz Koronowicz, Prof.

The Szewalski Institute of Fluid Flow Machinery, Gdansk, Poland

Jan A. Szantyr, Prof.

Gdansk University of Technology, Poland

ABSTRACT

The article presents a detailed discussion of the theoretical models of four different fluid dynamic devices: an ideal propulsor, an ideal fluid brake, an ideal screw propeller and an ideal turbine. The four models are presented with all relevant mathematical formulae regarding the forces, the power and the efficiency. It is demonstrated that the application of the model of an ideal optimum fluid brake according to the Betz theorem for determination of the maximum effectiveness coefficient of an axial wind turbine is not correct. In the case of a turbine the inclusion of important rotational flow losses may increase the maximum value of the turbine effectiveness coefficient above the level defined by Betz. Therefore the model of an ideal turbine should be an inversion of the model of an ideal screw propeller. This conclusion is supported by numerical calculations. It may influence the design procedures of wind turbines and may lead to increase in their efficiency.

Key words: ideal propeller, ideal wind turbine, Betz theorem, maximum efficiency

INTRODUCTION

A review of literature concerning the theory and design of wind turbines shows serious deficiencies in proper understanding and correct interpretation of the results of calculations based on modeling the flow of ideal fluid in an unbounded domain by means of principles of conservation of momentum, moment of momentum and energy. An example of this may be the maximum value of the efficiency of an ideal wind turbine, determined by Betz [1] and quoted as an absolute upper limit even in the most recent publications.

Starting from the 1960s the models of an ideal propulsor and an ideal propeller were used at Institute of Fluid Flow Machinery, e.g. for determination of the tunnel wall influence on the hydrodynamic characteristics of propellers [3] and for determination of the hydrodynamic characteristics of propellers by means of the vortex theory. The experience acquired over many years enables a thorough analysis of the applicability of the above mentioned ideal models to problems of operation of real fluid flow machines.

The principles of conservation of momentum, moment of momentum and energy in connection with the appropriate vortex models enable the determination of maximum achievable performance of certain fluid flow machines, such as:

- an ideal propulsor,
- an ideal screw propeller,
- an ideal fluid brake,
- an ideal axial wind turbine.

In the cases of an ideal propulsor and ideal fluid brake the required results may be obtained without resorting to vortex models. However, if the information about flow details in the close vicinity of the disc is required, the application of the vortex model (or the equivalent accelerating or decelerating actuator disc) is necessary. In the cases of an ideal screw propeller or an ideal turbine the application of vortex models is necessary at every stage of calculations. The detailed presentation and discussion of the computational models for all four above mentioned machines is given below.

AN IDEAL PROPULSOR

An ideal propulsor is the simplest form of the fluid propulsor, in which a surface perpendicular to the flow (not necessarily of a circular shape) covered with pressure dipoles accelerates the flow both in front and behind the propulsor (cf. Fig. 1). At the propulsor surface itself a jump in fluid pressure is created. Consequently, a propulsor stream is generated, in which at a certain distance (typically about 3 diameters of the propulsor disc) the velocity achieves constant values at the cross-sections of the stream both behind (section 3 in Fig. 1), in front of the propulsor (section 1) and on the cylindrical side surface of the stream. The sections 1 and 3 are referred to as “far in front” and “far behind” the propulsor. In reality the closest to the ideal propulsor is the magneto-hydrodynamic propulsor, used as the “silent” propulsor on some submarines. In these propulsors a strong electromagnetic field generates

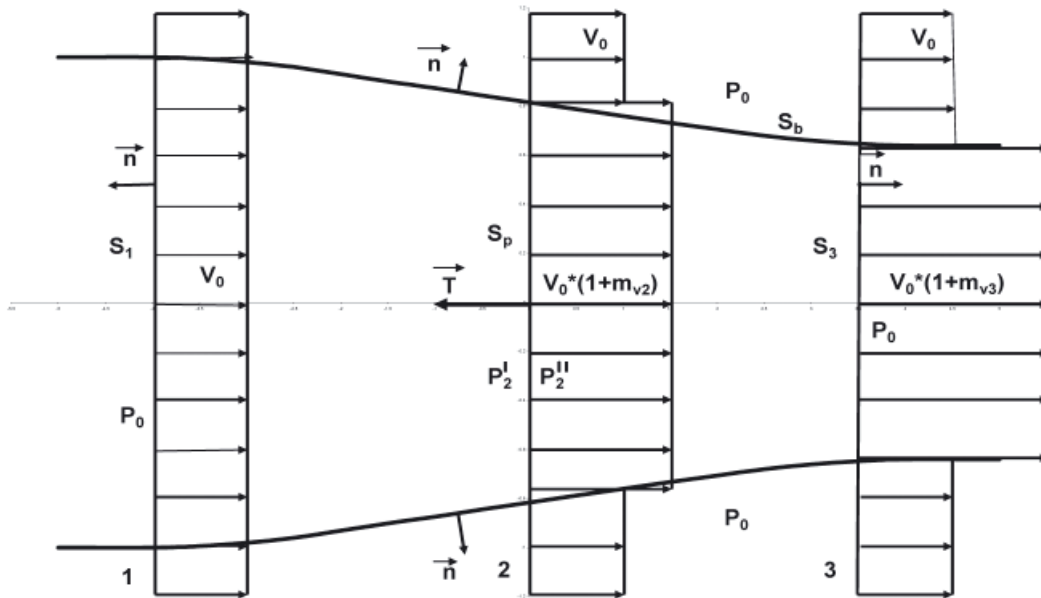


Fig. 1. The stream of an ideal propulsor

motion of particles of salt water. Strictly ideal case of such a propulsor would require elimination of the boundary layer on the propulsor channel walls. Within the model of an ideal propulsor two cases may be distinguished:

- an optimum ideal propulsor,
- a non-optimum ideal propulsor.

The above cases depend strictly upon the uniformity of the velocity field inside the propulsor stream. Namely, every deviation from the uniform velocity field leads to the reduction of efficiency. Further discussion is limited to the optimum case only.

In an optimum ideal propeller the axial force acting on the fluid is equal to the multiple of pressure jump and the area of the propulsor surface:

$$T = \pi R_2^2 (p_2^I - p_2^{II}) \quad (1)$$

In the case of the optimum ideal propulsor the distribution of the pressure dipoles over the propulsor surface is uniform and the pressure jump Δp may be univocally determined from the Bernoulli equation for any streamline in front and behind the propulsor (Fig. 1):

$$\frac{1}{2} \rho V_0^2 + p_0 = \frac{1}{2} \rho (V_0 + V_{x2})^2 + p_2^I \quad (2a)$$

$$\frac{1}{2} \rho (V_0 + V_{x3})^2 + p_0 = \frac{1}{2} \rho (V_0 + V_{x2})^2 + p_2^{II} \quad (2b)$$

After subtracting (2b) from (2a) the pressure jump at the propulsor surface Δp is obtained:

$$\Delta p = p_2^I - p_2^{II} = \rho V_0^2 m_{v3} \left(1 + \frac{1}{2} m_{v3}\right) \quad (3)$$

Substitution to formula (1) yields the thrust of the propulsor:

$$T = \rho V^2 \pi R^2 m_{v3} \left(1 + \frac{1}{2} m_{v3}\right) \quad (4)$$

where:

$$m_{v3} = V_{x3}/V_0$$

The ideal thrust loading coefficient of the propulsor is equal to:

$$C_{T2i} = \frac{T}{\left(\frac{1}{2} \rho V_0^2 \pi R^2\right)} = 2 m_{v3} \left(1 + \frac{1}{2} m_{v3}\right) \quad (5)$$

The thrust of the propulsor may be also obtained from the momentum conservation principle applied to the control surface S consisting of the side surface of the stream S_b , inlet cross-section of the stream S_1 , outlet cross-section of the stream S_3 and the surface containing the external forces acting on the fluid S_p (Fig. 1):

$$\int_S \rho \vec{V} (\vec{V} \cdot \vec{n}) dS = - \int_S p \vec{n} dS \quad (6)$$

If the surface S_p , encompassing the external forces, is excluded from the surface S , then the axial force (thrust) T is equal to the rate of change of fluid momentum on the entire control surface and the force induced by the pressure field on the remaining part of S :

$$T = - \int_{S_p} p \vec{n} dS = \int_S \rho \vec{V} (\vec{V} \cdot \vec{n}) dS + \int_{S-S_p} p \vec{n} dS \quad (7)$$

On the surface S_1 there is $\vec{V} \cdot \vec{n} = -V_0$ and on the surface S_3 there is $\vec{V} \cdot \vec{n} = V_0 + V_{x3}$. Consequently, the following relation between S_1 and S_3 may be established, making use of the continuity equation:

$$\pi R_1^2 V_0 = \pi R_3^2 (V_0 + V_{x3}) \quad (8)$$

In the case of an unbounded fluid domain the same pressure p_0 acts on the entire surface S including surfaces S_1 , S_b and S_3 , hence the second term in equation (7) is zero. In case of a bounded fluid domain (e.g. inside a tunnel) this condition does not hold.

Taking into account that the side surface of the propulsor stream is in fact the stream surface, the scalar multiple $\vec{V} \cdot \vec{n} = 0$. Finally, another formula for the axial force (or thrust) induced by an ideal propulsor is obtained:

$$T = \rho V_0^2 \pi R_3^2 m_{v3} (1 + m_{v3}) \quad (9)$$

Comparing formulae (9) and (4), the relation between the velocities induced at the propulsor and "far behind" the propulsor is obtained:

$$\frac{\pi R_2^2}{\pi R_3^2} = \frac{1 + \frac{1}{2} m_{v3}}{1 + m_{v3}} \quad (10)$$

It may be concluded from this relation that the induced velocity at the propulsor is equal half of the value of the

induced velocity “far behind”. Often this relation is accepted “a priori”, which is not always correct, because it depends on the above assumptions, regarding an unbounded fluid domain and uniformity of velocity distribution over the propulsor surface.

The thrust loading coefficient of the propulsor, related to the area of the propulsor stream cross-section “far behind” the propulsor is equal to:

$$C_{T3i} = \frac{T}{\frac{1}{2}\rho V_0^2 \pi R_3^2} = 2m_{v3}(1 + m_{v3}) \quad (11)$$

The following relation stems from the principle of energy conservation (disregarding heat exchange):

$$P_D = \int_S p \vec{V} \cdot \vec{n} dS + \frac{1}{2}\rho \int_S V^2 (\vec{V} \cdot \vec{n}) dS \quad (12)$$

The scalar multiple on the side surface of the propulsor stream $\vec{V} \cdot \vec{n} = 0$. The sum of integrals on the surfaces S_1 and S_3 is also equal zero according to the continuity equation:

$$\int_{S1} p_0 V_1 dS - \int_{S3} p_0 V_3 dS = p_0 (V_1 S_1 - V_3 S_3) = 0$$

Hence the power (energy per second) lost in the stream is equal to:

$$\begin{aligned} P_{Di} &= \frac{1}{2}\rho \int_S V^2 (\hat{V} \cdot \vec{n}) dS = \rho V_0^3 \pi R_3^2 \left(\frac{V_{x3}}{V_0} - \frac{S_1}{S_3} \right) = \\ &= \rho V_0 \pi R_3^2 m_{v3} \left(1 + \frac{1}{2} m_{v3} \right) \end{aligned} \quad (13)$$

The power loading coefficient of the propulsor, related to the area of the propulsor stream cross-section “far behind” the propulsor is equal to:

$$C_{p3i} = \frac{P_{Di}}{\frac{1}{2}\rho V_0^3 \pi R_3^2} = 2m_{v3} \left(1 + \frac{1}{2} m_{v3} \right) \quad (14)$$

The same coefficient related to the propulsor surface area is equal to:

$$C_{p2i} = \frac{P_{Di}}{\frac{1}{2}\rho V_0^3 \pi R_2^2} = 2m_{v3} \left(1 + \frac{1}{2} m_{v3} \right)^2 \quad (15)$$

The efficiency of the propulsor is defined as the ratio of the power of thrust to the power lost at the cross-section “far behind” the propulsor (cf. Fig. 2):

$$\eta_i = \frac{T_i V_0}{P_{Di}} = \frac{C_{T3i}}{C_{P3i}} = \frac{1}{1 + \frac{1}{2} m_{v3}} \quad (16)$$

The efficiency of an ideal propulsor is often presented as a function of the thrust loading coefficients C_{T3i} or C_{T2i} .

Using the formula (11) a quadratic equation may be solved, leading to the following relation:

$$m_{v3} = \frac{1}{2} (\sqrt{1 + 2C_{T3i}} - 1) \quad (17)$$

which in turn may be used to develop the following formula for propulsor efficiency, depending on the thrust loading coefficient “far behind”:

$$\eta_i = \frac{4}{3 + \sqrt{1 + C_{T3i}}} \quad (18)$$

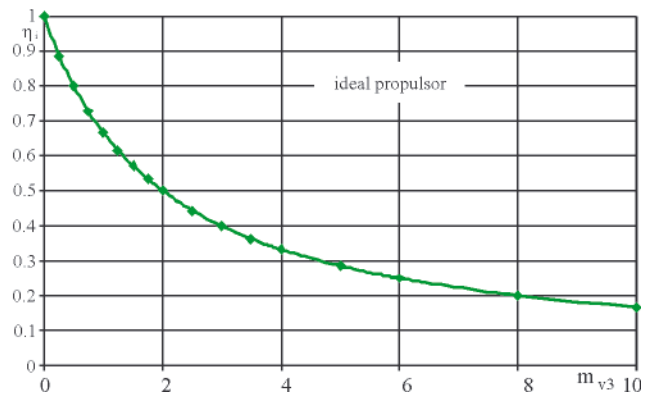


Fig. 2. The dependence of the ideal propulsor efficiency on the relative induced velocity “far behind” the propulsor

In the case when the thrust loading coefficient at the propulsor surface is available, this relation takes a different form:

$$\eta_i = \frac{2}{1 + \sqrt{1 + C_{T2i}}} \quad (19)$$

Fig. 3 shows the dependence of the ideal propulsor efficiency on the thrust loading coefficients determined at the propulsor and “far behind”.

The above formulae refer to the optimum ideal propulsor, i.e. a propulsor operating in an unbounded fluid domain and having uniform distribution of thrust loading at its surface. When these assumptions are not fulfilled (this was the case of determination of the tunnel walls influence on the propulsor characteristics, as described in [3]), the induced velocity at the propulsor is no longer equal to half of the value of this velocity “far behind”. The deviation from this depends on the degree on non-uniformity of the thrust loading and on the ratio of the propulsor surface to the cross-section of the bounded fluid domain [3]. The vortex model of an ideal propulsor is composed of circular vortices distributed on the side surface of the propulsor stream behind the propulsor surface.

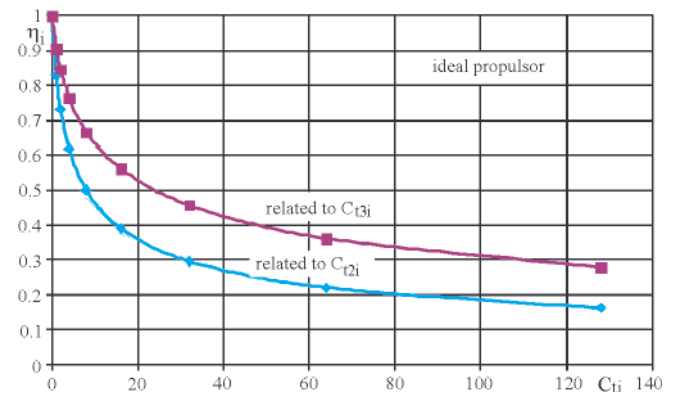


Fig. 3. The ideal propulsor efficiency as the function of thrust loading coefficients

AN IDEAL FLUID BRAKE

Physically an ideal fluid brake operates in the manner similar to an ideal propulsor, but now the pressure dipoles are directed in an opposite direction, i.e. against the direction of flow. Hence instead of an accelerating surface, there is now a decelerating surface and the axial force is generated in an opposite direction. The flow velocity is being reduced both in front and behind the brake surface (cf. Fig. 4). Similarly as before, the principles of momentum and energy conservation may be used for determination of the axial force and power. The

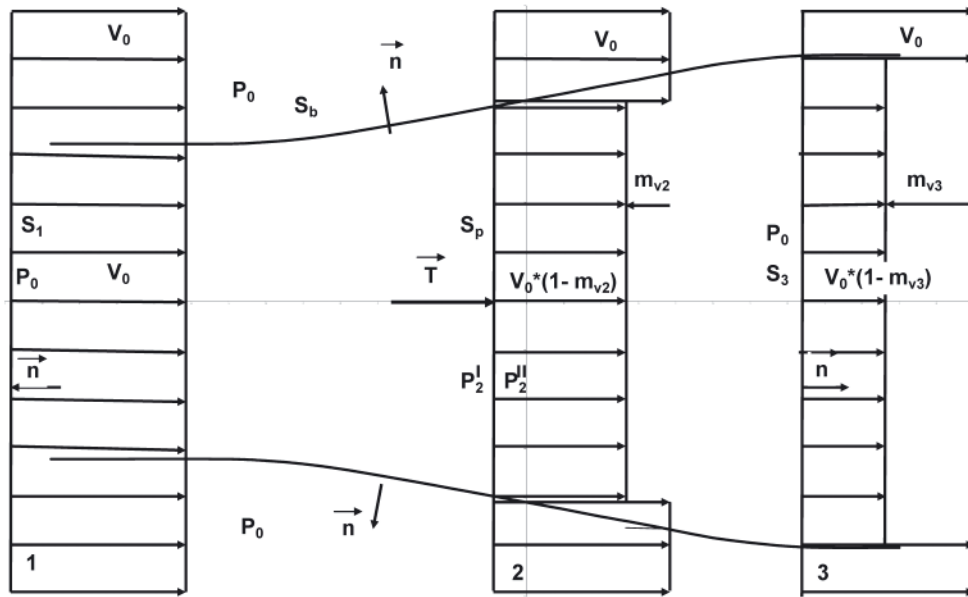


Fig. 4. The stream of an ideal fluid brake

formulae are similar to those describing the propulsor, only the signs of induced velocity are changed and certain limitations in the values of these velocities are introduced.

The axial force (now named the braking force instead of thrust) coefficient related to the stream cross-section “far behind” is now equal to:

$$C_{T3i} = -2m_{v3}(1 - m_{v3}) \quad (20)$$

and the coefficient of power loss in the stream, also related to the cross-section “far behind” is equal to:

$$C_{P3i} = -2m_{v3}(1 - m_{v3}) \left(1 - \frac{1}{2}m_{v3}\right) \quad (21)$$

Similarly as in the case of a propulsor, for the brake operating in an unbounded fluid domain and having uniform loading distribution over its surface, the velocity induced at the decelerating surface is equal to half the velocity induced at the cross-section “far behind” the brake. Hence the ratio between the areas of the brake surface and the stream cross-section “far behind” may be obtained from the continuity principle:

$$\frac{\pi R_3^2}{\pi R_2^2} = \frac{1 - \frac{1}{2}m_{v3}}{1 - m_{v3}}$$

Consequently, the coefficients of axial force and power loading, related to the brake area, have now the following form:

$$C_{T2i} = -2m_{v3} \left(1 - \frac{1}{2}m_{v3}\right) \quad (22)$$

$$C_{P2i} = -2m_{v3} \left(1 - \frac{1}{2}m_{v3}\right)^2 \quad (23)$$

The functions showing the dependence of the above coefficients on the induced velocity are plotted in Figs 5 and 6. The range of variation of the relative induced velocity “far behind” was limited to 1.0, because larger values would lead to physically unrealistic reversed flows.

In case of a fluid brake it is inconvenient to discuss its “efficiency”. The more appropriate parameter is its effectiveness. For example the ratio of the braking force power to the power loss in the brake stream may be proposed as the measure of the brake effectiveness:

$$\zeta = \frac{T \cdot V_0}{P_{D2i}} = \frac{C_{T2i}}{C_{P2i}} = \frac{1}{1 - \frac{1}{2}m_{v3}} \quad (24)$$

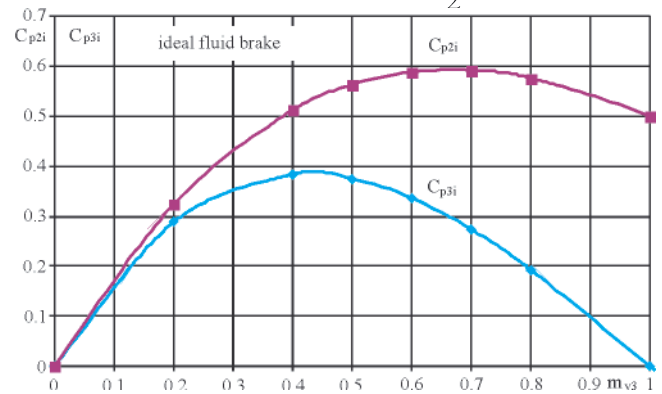


Fig. 5. Coefficients of kinetic energy loss in the brake stream depending on the relative induced velocity “far behind” m_{v3}

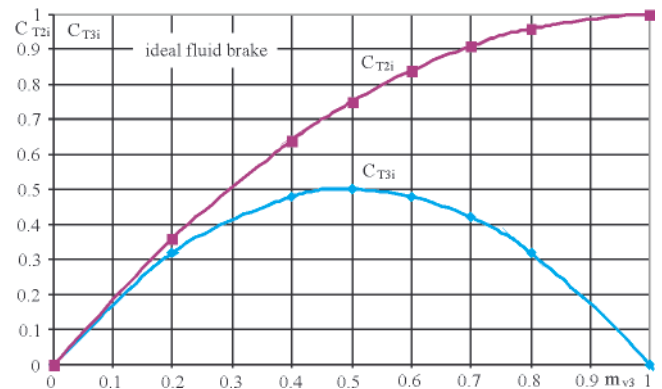


Fig. 6. Coefficients of the braking force depending on the relative induced velocity “far behind” m_{v3}

The value of the above parameter varies from 1.0 for $m_{v3} = 0.0$ to 0.5 for $m_{v3} = 1.0$. The above presented formulae contain all relations between kinematic and dynamic parameters of an ideal brake.

It must be stressed here, that it is not correct to identify the value of C_{P2i} determined by the formula (23) with the ideal efficiency coefficient for the axial wind or water turbines. This was suggested by Betz [1], who has used formula (23) for determination of the maximum ideal efficiency

of a wind turbine (cf. Fig. 5). According to his result, quoted in almost all publications concerning wind turbines, this maximum value is equal to $C_{pmax} = 16/27 = 0.5926$, which is obtained for: $m_{v3} = 2/3 = 0.6667$.

Contrary to the above, in experiments with real turbines having finite number of blades and operating in a real, viscous fluid (e.g air or water) significantly higher values of C_{p2} are obtained. This results from the fact that **the operation of an ideal axial turbine should be determined not on the basis of the ideal fluid brake, but in the way similar to that presented below for an ideal screw propeller.** The power of a turbine depends on the torque on its shaft and consequently, the **circumferential induced velocity** must be taken into account. In this case the principle of conservation of moment of momentum is more appropriate for determination of torque on the turbine shaft and the performance of the turbine should be made dependent on a parameter characterizing the moment of momentum.

The energy conservation principle, taking into account all components of the induced velocities may also be used, but this way of solving the problem is much more difficult and less clear. Both ways lead to the same final result.

AN IDEAL SCREW PROPELLER

An ideal screw propeller model takes into account the rotational motion, therefore it must have a form of a circular disc. In order to determine the relations between the induced velocities and the forces on an ideal screw propeller, a more complicated vortex model should be used (cf. Fig. 7).

This model is constructed of:

- straight line vortices distributed radially on the propeller disc,
- helicoidal tip vortex lines distributed over the cylindrical side surface of the propeller stream behind the propeller,
- straight line vortex located along the propeller axis behind the propeller, having the total intensity Γ ,

The velocity field induced by such a vortex system at a certain distance behind the propeller (practically about one propeller diameter is enough) may be univocally determined by the parameters of the vortex system "far behind" the propeller. These parameters are:

- radius of the cylinder on which the helicoidal vortices are distributed "far behind" R_3 ,

- total intensity of the vortices Γ ,
- velocity of the undisturbed flow V_0 ,
- pitch of the helicoidal vortex lines $\tan\beta_3$

The volumetric mean value of the axial velocity induced inside the stream ($r < R_3$) by the system of infinite helicoidal vortices has a constant value across the stream [4], equal to:

$$V_{xi3} = \Gamma / (2 \pi R_3 \tan\beta_3) \quad (25)$$

This value applies to a single helicoidal vortex line as well as to a system of Z (including $Z = \infty$) helicoidal lines having the same pitch equal to $\tan\beta_3$, as long as the total intensity of all vortex lines is equal to Γ . At the same time the volumetric mean velocity induced outside the stream ($r > R_3$) is equal zero [4].

The volumetric mean circumferential velocity induced inside the propeller stream ($r < R_3$) by the infinite straight line vortex located at the propeller axis is equal to:

$$V_{\phi i3} = \Gamma / (2 \pi r) \quad (26)$$

The volumetric mean of the circumferential velocity induced by the system of tip vortices inside the stream ($r < R_3$) is equal zero, while this value outside the stream ($r > R_3$) is determined by the formula (25) with inverted sign due to inverted direction of the tip vortices. Consequently, outside the stream the volumetric mean of the circumferential velocity induced by the entire vortex system of the propeller (axial vortex together with tip vortices) is equal zero. The volumetric mean of the radial component of the induced velocity "far behind" the propeller is equal zero both inside and outside the propeller stream.

When the non-dimensional value of the intensity of vortices forming the propeller vortex system is introduced as:

$$b_{v3} = \Gamma / (4 \pi R_3 V_0) \quad (27)$$

the relative values (divided by the undisturbed flow velocity V_0) of the induced velocity components may be expressed by the following formulae:

$$V_{xi3} / V_0 = m_{v3} = 2 b_{v3} / \tan\beta_3 \quad (28)$$

$$V_{\phi i3} / V_0 = 2 b_{v3} / r = m_{v3} \tan\beta_3 / r \quad (29)$$

When the velocity field "far behind" the propeller is defined in the above way, the relations between this field and propeller thrust T , torque Q and power loss may be developed

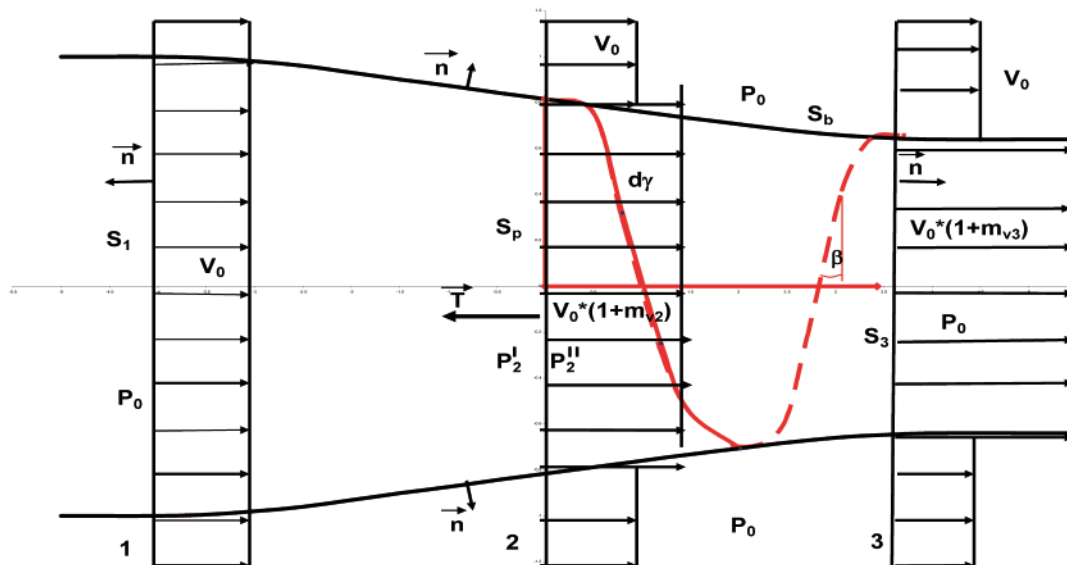


Fig. 7. The stream of an ideal screw propeller with vortex lines

similarly as for an ideal propulsor, making use of the principles of conservation of momentum, moment of momentum and energy.

It may seem that due to the constant value of the axial induced velocity across the stream, the value of propeller thrust may be determined analogically as in the case of an ideal propulsor. Unfortunately, the presence of the axial hub vortex significantly changes the pressure field inside the stream. Therefore, the thrust must be determined on the basis of the momentum conservation principle applied to the control surface S, which includes the side surface of the stream S_b , inlet and outlet surfaces S_1 and S_3 together with the surface encompassing the external forces acting on the fluid Sp (cf. Fig. 7).

$$\int_S \rho \vec{V} (\vec{V} \cdot \vec{n}) dS = - \int_S p \vec{n} dS \quad (30)$$

If the surface S_p (representing the blades of the propeller) is excluded from the control surface S, then the thrust is equal to the rate of change of fluid momentum on the entire control surface and the force generated by the pressure field on the remaining part of S:

$$T = - \int_{S_p} p \vec{n} dS = \int_S \rho \vec{V} (\vec{V} \cdot \vec{n}) dS + \int_{S-S_p} p \vec{n} dS \quad (31)$$

As there is $\vec{V} \cdot \vec{n} = -V_0$ in cross-section 1 and there is $\vec{V} \cdot \vec{n} = V_0 + V_{x3}$ in cross-section 3, the relation between areas of cross-sections 1 and 3 may be determined using the principle of continuity of flow. However, it should be taken into account that on the axis of cross-section 3 there exists a vortex line, which should be treated as a vortex singularity (e.g. a Rankine vortex model), having cross-section area S_w and radius R_{w0} .

$$(S_3 - S_w) (V_0 + V_{x3}) = S_1 V_0 \quad (32)$$

In the case of an ideal propulsor discussed above the same pressure p_0 acts on the entire control surface S (assuming unbounded fluid domain). In the case of ideal screw propeller the pressure in cross-section S_3 is different than p_0 and it is a function of radius, therefore an additional pressure term must appear in the corresponding equation. The side surface of the propeller stream is still a stream surface, where $\vec{V} \cdot \vec{n} = 0$. Taking into account the above, the relation (31) now takes the following form:

$$T = \rho \pi R_3^2 V_{x3} (V_0 + V_{x3}) (S_3 - S_w) + \int_{S_3} (p - p_0) dS \quad (33)$$

Substituting the relative induced velocity, this may be transformed into:

$$T = \rho V_0^2 \pi R_3^2 m_{v3} (1 + m_{v3}) (1 - (R_w / R_3)^2) + \int_{S_3} (p - p_0) dS \quad (34)$$

The first term of (34) is similar to the corresponding term in the formula (9) for an ideal propulsor. Calculation of the second term requires additional assumptions:

- the entire vorticity in the flow is concentrated in the limited space around the tip and axial vortices; outside this limited space the flow is irrotational i.e. potential,
- according to Joukovsky hypothesis the flow is steady in the system of co-ordinates rotating with the propeller.

In such a situation the following relation exists between the velocity field and the pressure field:

$$1/2 V^2 - \vec{V} \cdot \vec{V}_e + p/\rho = \text{const} \quad (35)$$

where:

$\vec{V}_e = \vec{\omega} \times \vec{R}$ – the convective velocity ($\vec{\omega}$ is the angular propeller velocity), hence:

$$p - p_0 = 1/2 \rho (V_{xi}^2 + V_{\phi i}^2) + \rho (V_{xi} V_0 - \vec{\omega} \cdot \vec{r} \cdot V_{\phi i}) \quad (36)$$

Taking into account the equations (28) and (29) and reformulating the equation (36), the following equation for the thrust correction resulting from the pressure field in the screw propeller stream may be obtained:

$$\begin{aligned} \int_{S_3} (p - p_0) dS &= \\ &= 1/2 \rho V_0^2 m_{v3}^2 2\pi R_3^2 \int_{rw}^1 (1 + \tan^2 \beta_3^2 / r_z^2) r_z dr_z + \\ &+ \rho V_0^2 m_{v3} 2\pi R_3^2 \int_{rw}^1 (1 - r_z \tan \beta_3 / \lambda_3) r_z dr_z \end{aligned} \quad (37)$$

where:

$r_z = r/R_3$

$\lambda_3 = V_0 / \vec{\omega} R_3$

$r_w = R_w / R_3$ is the normalized radius of the axial vortex

The above integrals may be solved analytically and ultimately they lead to the formula for the thrust of an ideal screw propeller:

$$\begin{aligned} T &= \rho V_0^2 \pi R_3^2 m_{v3} ((1 + m_{v3})(1 - r_w^2) + \\ &+ 1/2 m_{v3} \tan^2 \beta_3 (2 \ln(r_w) + 1 - r_w^2)) \end{aligned} \quad (38)$$

Now the thrust loading coefficient related to the propeller stream cross-section “far behind” is equal to:

$$\begin{aligned} C_{T3i} &= \frac{T}{\frac{1}{2} \rho V_0^2 \pi R_3^2} = 2 m_{v3} ((1 + m_{v3})(1 - r_w^2) + \\ &+ \frac{1}{2} m_{v3} \tan^2 \beta_3 (2 \ln(r_w) + 1 - r_w^2)) \end{aligned} \quad (39)$$

The power loading coefficient, related to the screw propeller stream cross-section “far behind”, may be determined from the principle of conservation of moment of momentum. In this case only the circumferential component of the induced velocity is important. This leads to the formula:

$$Q_{xi} = \int_{S-S_p} \rho (\vec{P}\vec{O} \times \vec{V})_x (\vec{V} \cdot \vec{n}) dS + \int_{S-S_p} p (\vec{P}\vec{O} \times \vec{n})_x dS \quad (40)$$

where:

$\vec{P}\vec{O}$ – radius-vector from propeller axis

\vec{n} – unit normal vector at the control surface S-Sp

An appropriate selection of the control surfaces enables elimination of some of the integrals. On the entire surface S-Sp the vector multiple $(\vec{P}\vec{O} \times \vec{n})_x$ is zero, eliminating the pressure term. On the stream surfaces the scalar multiple $\vec{V} \cdot \vec{n}$ is zero. On the cross-section S1 the following relations hold:

$$\vec{V} \cdot \vec{n} = -V_0$$

$$(\vec{P}\vec{O} \times \vec{n})_x = [\vec{P}\vec{O} \times (-\vec{n} \cdot V_0)] = 0$$

$$(\vec{n})_x = -1$$

and on the cross-section S_3 the following relations hold:

$$\begin{aligned}\vec{V} \cdot \vec{n} &= V_0 + V_{x3} \\ (\vec{P}\vec{O} \times \vec{n})_x &= \vec{P}\vec{O} \cdot V_{\varphi 3} \\ (\vec{n})_x &= 1\end{aligned}$$

Taking the above into account, together with the continuity equation, the following is obtained:

$$Q_{xi} = \rho \int_{S_3 - S_w} r_z V_{\varphi 3} (1 + V_{x3}) dS \quad (41)$$

After substituting the expressions (28) and (29) for the components of the induced velocity, the following equation is obtained for the power of an ideal screw propeller:

$$\begin{aligned}P_i &= Q_{xi} \cdot \omega_0 = \\ &= \rho V_0^3 \pi R_3^2 \tan \beta_3 / \lambda_3 m_{V3} (1 + m_{V3}) (1 - r_w^2)\end{aligned} \quad (42)$$

where:

$$\lambda = V_0 / (\omega_0 R_3)$$

The power loading coefficient, related to the area of the propeller stream cross-section "far behind", may be now determined as:

$$C_{Pi} = P_i / \frac{1}{2} \rho V_0^3 \pi R_3^2 = \quad (43)$$

$$= 2 \tan \beta_3 / \lambda_3 m_{V3} (1 + m_{V3}) (1 - r_w^2)$$

The efficiency of an ideal propeller is defined as the ratio of the power of thrust to the power loss in the propeller stream "far behind" the propeller:

$$\eta_i = \frac{T_i V_0}{P_{Di}} = \quad (44)$$

$$= (1 + 1/2 m_{V3} \tan \beta_3^2 (2 \ln(r_w) + 1 - r_w^2)) \lambda_3 / \tan \beta_3$$

The formula (44) does not resemble the formula (16) for the efficiency on an ideal propulsor. However, it is similar to the formula used in the vortex theory of propellers for determination of the so called induced pitch for the propeller blades having optimum radial distribution of circulation:

$$\operatorname{tg} \beta = \lambda / \eta \quad (45)$$

where:

$$\lambda = V_0 / \omega R$$

The formula (44) may take the form similar to formula (16) if the following definition of $\tan \beta_3$ is used:

$$\tan \beta_3 = \frac{V_0 + V_{xw}}{\omega R_3 - V_{\varphi w}} = \frac{1 + 1/2 m_{V3}}{1 / \lambda_3 - 1/2 m_{V3} \tan \beta_3} \quad (46)$$

where:

V_{xw} and $V_{\varphi w}$ – the components of the own velocity of the tip vortex. For an ideal propeller they are equal half of these components induced inside the propeller stream [4]. After some reformulations the following equation is obtained:

$$\lambda_3 / \tan \beta_3 = \frac{1}{1 + 1/2 m_{V3} (1 + \tan \beta_3^2)} \quad (47)$$

After substitution of (47) into (45) the formula similar to that for the efficiency of an ideal propulsor is obtained:

$$\eta_i = \frac{T_i V_0}{P_{Di}} = \frac{1 + 1/2 m_{V3} \tan \beta_3^2 (2 \ln(r_w) + 1 - r_w^2)}{1 + 1/2 m_{V3} (1 + \tan \beta_3^2)} \quad (48)$$

The formula (48) differs from the formula (16) in two aspects:

- the numerator is smaller than 1
- the denominator includes an additional factor

Both these differences cause reduction of the ideal propeller efficiency in comparison with an ideal propulsor. Therefore, the efficiency of an ideal screw propeller is always smaller than that of a corresponding ideal propulsor. Moreover, the ideal screw propeller efficiency depends additionally on the pitch of the helical vortex lines and on the diameter of the axial vortex singularity. Both formulae coincide when $\tan \beta_3 = 0$. In this case the helical vortices of an ideal propeller are reduced to the ring vortices of an ideal propulsor.

The radius of the axial vortex singularity requires further explanation. In case of an ideal screw propeller operating in water the cavitating vortex kernel may determine this radius. In case of an ideal screw propeller operating in gas (e.g. in air), there exists an exact relation between the pressure and volume (or density) based on a perfect gas model. In this case the axial vortex may be treated as a perfect whirlwind having a kernel of zero vorticity. The radius of such a kernel may be substituted into all above formulae in the place of r_w .

AN IDEAL AXIAL WIND TURBINE

Similarly as in the case of an ideal propulsor and ideal brake, there exists a close analogy between an ideal screw propeller and an ideal axial wind turbine. Namely, they both may be described by the formulae characterizing the vortex system "far behind":

- radius of the cylindrical propeller stream "far behind" R_3 ,
- total intensity of the vortices Γ ,
- undisturbed flow velocity V_0 ,
- pitch of the helical vortex lines $\tan \beta_3$.

The vortex system of an ideal axial turbine, shown in Fig. 8, is composed of the same elements as the corresponding system for an ideal propeller:

- straight line vortices distributed radially on the propeller disc,
- helicoidal tip vortex lines distributed over the cylindrical side surface of the turbine stream behind the turbine,
- straight line vortex located along the turbine axis behind the turbine, having the total intensity Γ .

Of course it must be remembered that the vorticity vectors for the propeller and for the turbine have opposite direction.

In this case the velocity field is related to the parameters of the vortex system in the same way as in the ideal screw propeller. The relations (25)–(29) have the same form, but the parameters m_v have opposite sign. The relations for the axial force T (38) and for the power P_i (42) have the same form, but the sign of m_{v3} is changed:

$$\begin{aligned}T &= -\rho V_0^2 \pi R_3^2 m_{V3} ((1 - m_{V3})(1 - r_w^2) + \\ &- 1/2 m_{V3} \tan \beta_3^2 (2 \ln(r_w) + 1 - r_w^2))\end{aligned} \quad (49)$$

$$P_{3i} = Q_{xi} \cdot \omega_0 = \quad (50)$$

$$= -\rho V_0^3 \pi R_3^2 \tan \beta_3 / \lambda_3 m_{V3} (1 - m_{V3}) (1 - r_w^2)$$

The definitions of all parameters are the same as for an ideal screw propeller. Consequently, the formulae for the coefficients

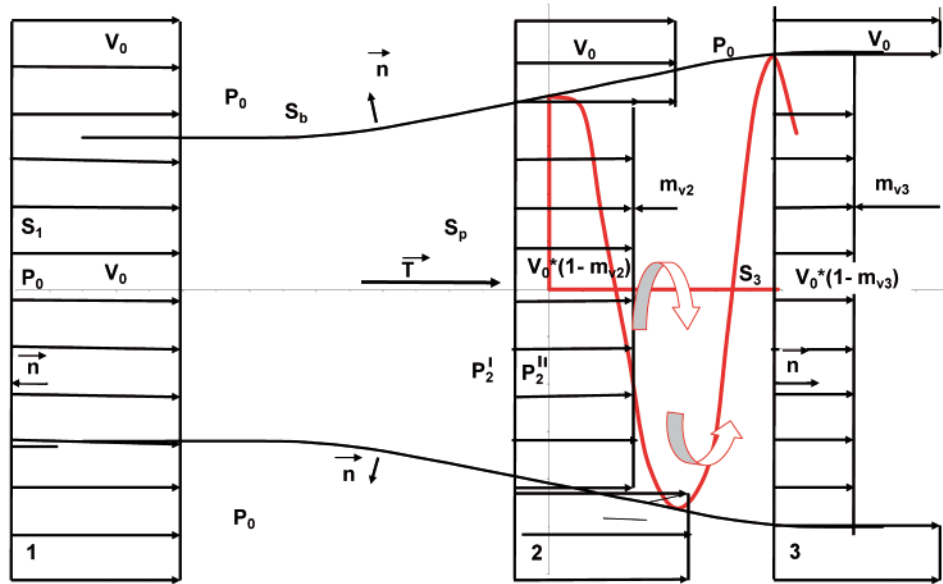


Fig. 8. The stream of an ideal axial turbine with vortex lines

of axial force loading C_{T3} and power loading C_{P3} are similar to those for an ideal propeller:

$$C_{T3i} = \frac{T}{\frac{1}{2} \rho V_0^2 \pi R_3^2} = -2m_{v3}((1 - m_{v3})(1 - r_w^2) + -1/2 m_{v3} \tan^2 \beta_3 (2 \ln(r_w) + 1 - r_w^2)) \quad (51)$$

$$C_{P3i} = P_i / \frac{1}{2} \rho V_0^3 \pi R_3^2 = -2 \tan \beta_3 / \lambda_3 m_{v3} (1 - m_{v3})(1 - r) \quad (52)$$

But now the formula for the pitch of the helical lines $\tan \beta_3$ does change into:

$$\tan \beta_3 = \frac{V_0 + V_{xw}}{\omega R_3 - V_{\phi w}} = \frac{1 - 1/2 m_{v3}}{1/\lambda_3 + 1/2 m_{v3} \tan \beta_3} \quad (53)$$

from which the following relation may be developed:

$$\tan \beta_3 / \lambda_3 = 1 - 1/2 m_{v3} (1 + \tan^2 \beta_3) \quad (54)$$

Taking into account the formula (54) the relation (52) may be transformed into the form similar to (21):

$$C_{P3i} = -2 m_{v3} (1 - m_{v3})(1 - 1/2 m_{v3}(1 + \tan^2 \beta_3))(1 - r_w^2) \quad (55)$$

In this way it may be proved that in the system dependent on the axial component of the induced velocity m_{v3} , the limiting maximum values of the power coefficient C_{P3i} are even smaller than for the ideal fluid brake (assuming that $\tan \beta_3 = 0$ corresponds to the brake model and leads to the formula (21)).

Taking into account that the axial velocity component is only weakly related to the moment of momentum (i.e. to the turbine torque) and that the model experiments indicate values of C_p higher than those obtained from the ideal fluid brake, the analysis of the turbine operation should be performed in another system of co-ordinates. For example, the coefficient b_v more closely characterizes the moment of momentum in the flow.

Considering the definition formula for m_{v3} , the formula for C_{P3i} takes the form:

$$C_{P3i} = P_i / \frac{1}{2} \rho V_0^3 \pi R_3^2 = -4 b_{v3} / \lambda_3 (1 - 2b_{v3} / \tan \beta_3)(1 - r_w^2) \quad (56)$$

As in the case of a turbine the efficiency is not defined in the same way as in the case of propeller, the above formulae complete the relations between the dynamic and kinematic parameters. The radius of the vortex singularity may be determined in the above described way. Taking into consideration the continuity equation in the stream behind the turbine, the power loading coefficient at the turbine may be easily determined:

$$C_{P2i} = P_i / 0.5 \rho V_0^3 \pi R_2^2 = -4 b_{v2} / \lambda_2 (1 - 2b_{v2} / \tan \beta_2)(1 - r_w^2) \quad (57)$$

This power loading coefficient is in fact the effectiveness of utilization of the energy of the oncoming flow by the turbine. The formula (56) enables further analysis of the influence of different parameters on the turbine efficiency described by C_{P3i} :

- the parameter $(1 - r_w)$, characterizing the vortex singularity, has little influence on the turbine efficiency,
- the parameter $b_{v2} = \Gamma / 4\pi V_0 R_2$ characterizes the circulation of the axial vortex and the moment of momentum in the stream. This is a very important parameter, which determines the torque and power of the turbine,
- the parameter $\tan \beta_2$ characterizes the pitch of the tip vortex lines at the turbine, which is difficult to be determined precisely,
- the parameter λ_2 characterizes the location of the turbine operating point on the co-ordinate of the advance coefficient J .

It is difficult to determine the maximum attainable value of C_{P2i} using the formula (57) and the above parameters. Clearly, it will be not equal to the Betz limiting value of $C_{pmax} = 0.5926$, determined for an ideal fluid brake.

The structure of formula (57) implies that the maximum values of C_p are attained when:

- the parameter λ_2 reaches minimum values,
- the parameter Γ describing circulation of the hub vortex, corresponding to b_v , reaches the highest values,

Quantitative determination of these parameters is difficult. Certain idea of this aspect may be drawn from the analysis of the results of calculations for wind turbines with finite number of blades presented in the next section.

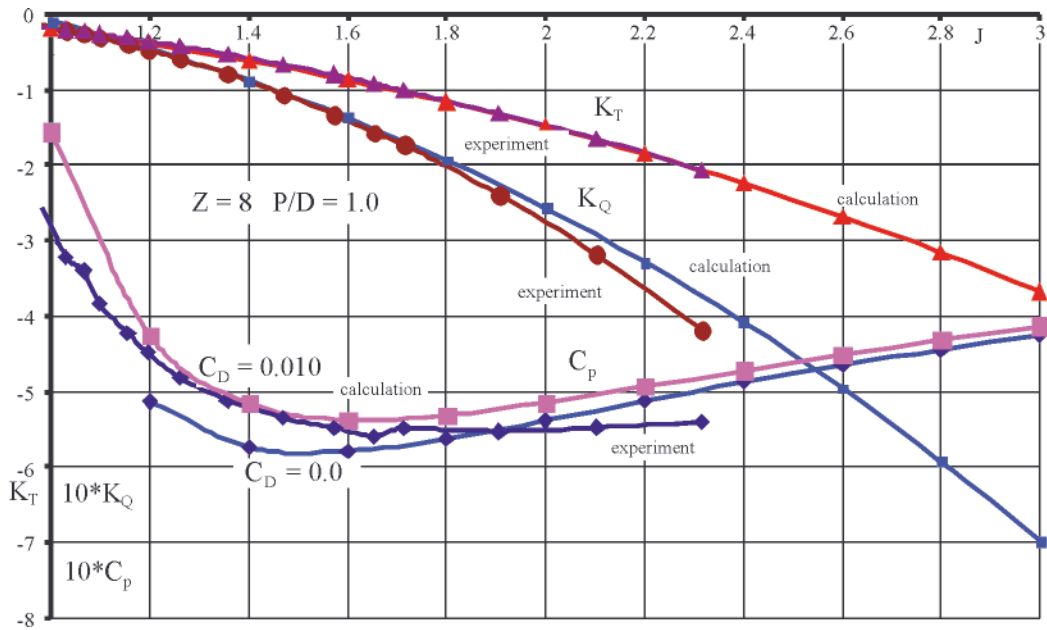


Fig. 9. Experimental verification of the program CHAHYD in application to wind turbines

AN AXIAL WIND TURBINE WITH THE FINITE NUMBER OF BLADES

Results of calculations showing that the effectiveness of a real axial wind turbines C_{pi} may exceed the upper limit defined by Betz have been obtained already in the 1990s, when the computer program for calculation of ship propeller characteristics CHAHYD was adapted for calculations of the axial wind turbines.

The program CHAHYD, based on the vortex lifting surface theory, was very thoroughly verified experimentally in its application to ship propellers. Similar verification with respect to wind turbines was missing until 2010 [2]. Fig. 9 shows an example of such verification. In this figure the coefficients of power loading C_p , axial force K_T , torque K_q obtained experimentally and computed for an 8-bladed turbine, are shown as functions of the advance coefficient J . In this figure the curve C_p calculated for zero drag coefficient is also plotted. In this case the maximum value $C_p = 0.58$ is already close to the limiting value determined by Betz.

The experimentally verified results of calculations are used to formulate the following statement:

The limiting value $C_{pmax} = 16/27 = 0.5926$ as determined by Betz for an ideal brake may take significantly higher values for an ideal axial turbine.

In the following figures the results of calculations of a 8-bladed wind turbine have been shown for four cases:

- model wind turbine having pitch coefficient $P/D = 1.0$ and viscous drag coefficient $C_D = 0.010$ (these results are correlated with model experiments [2]),
- the same model with $P/D = 1.0$ but with zero viscous drag,
- the model with pitch reduced to $P/D = 0.8$ and zero viscous drag ($C_D = 0.0$),
- the model with pitch reduced to $P/D = 0.6$ and zero viscous drag ($C_D = 0.0$).

As may be seen in Fig. 11 for the blade pitch $P/D = 0.8$ the C_{pmax} value already exceeds the Betz maximum of 0.5926. Still higher values of C_{pmax} are obtained for a turbine with $P/D = 0.6$. If such values are obtained for a real wind turbine operating

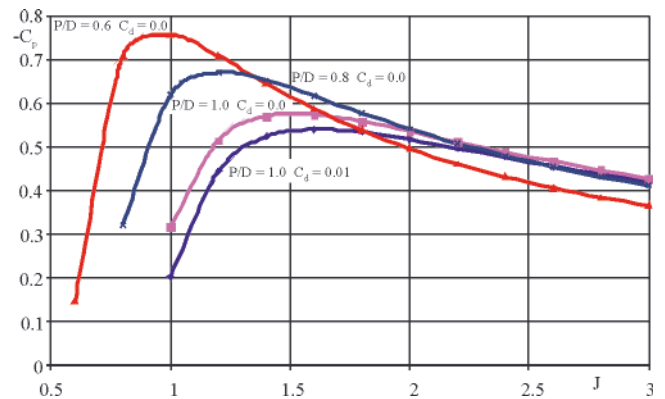


Fig. 10. Results of calculations of the effectiveness C_p for an 8-bladed wind turbine

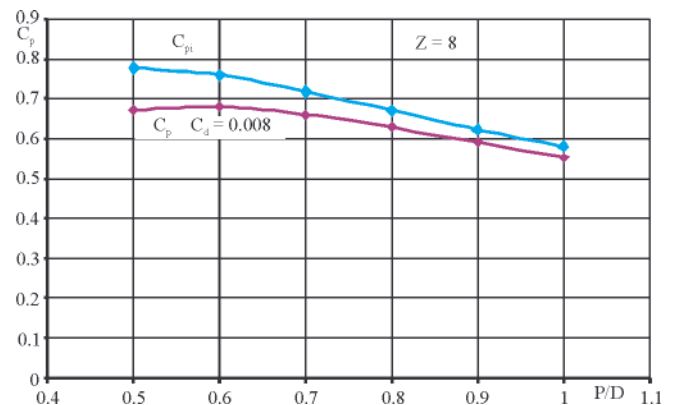


Fig. 11. Calculated maximum values of C_p obtained with viscous drag coefficients $C_d = 0.008$ and $C_d = 0.0$ as functions of the turbine pitch coefficient P/D

in a viscous flow and having finite number of blades, then the corresponding values for an ideal wind turbine must be even higher. In Fig. 12 the results for wind turbines having different numbers of blades are presented.

The quantitative assessment of terms in equation (57) is difficult because the vortex model of a wind turbine with finite number of blades is markedly different from the ideal turbine with infinite number of blades. First of all, the fields of induced velocity are different and the limits of the turbine

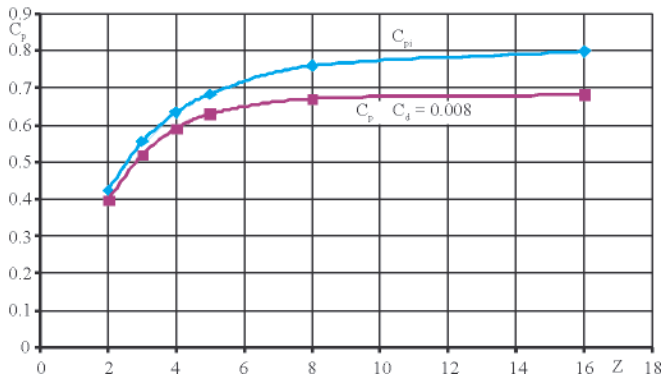


Fig. 12. Calculated maximum values of C_{pi} and C_p ($C_d = 0.008$) as functions of the turbine number of blades

stream are not univocally determined. It is difficult to determine the parameters b_v and m_v for a turbine with finite number of blades. However, the above presented results of numerical calculations lead to the following recommendations for the wind turbine designers:

- the design point of an axial wind turbine should be located at low advance coefficients,
- the optimum pitch of a wind turbine blades lies near the value $P/D = 0.6$,
- the computed effectiveness coefficient C_p of a turbine increases with the number of blades, but for real turbines operating in viscous fluid and suffering from flow deformations near the hub, which grow with increasing number of blades, the number of blades should not be too high.

CONCLUSION

Analyzing the above results it may be concluded that the models of ideal propulsor and ideal screw propeller correlate well with the experimental data. The efficiency of real propellers is always lower than that of the ideal ones and the effectiveness coefficient (defined as the ratio of real propeller efficiency to the efficiency of an ideal one) characterizes correctly the losses connected with fluid viscosity and with the finite number of real propeller blades.

The problem of turbines is significantly different, namely:

- there is no correlation between the experimental results and the results of calculations,

- the analogy between a turbine and an ideal fluid brake, for which the axial induced velocity component m_v is the basic parameter defining the performance, is a misunderstanding,
- the turbine performance is characterized by its torque: the model of an ideal turbine reduces the values of C_p as function of m_v even further than the model of an ideal brake, but as it was mentioned earlier the torque is not well correlated with m_v ,
- when the results of model experiments are accepted as more trustworthy than calculations based on ideal models, the inadequacy of the Betz theorem for the determination of the limiting maximum value of the turbine effectiveness must be also accepted.

BIBLIOGRAPHY

1. Prandtl L., Betz A.: *Schraubenpropeller mit geringstem Energieverlust*, enthalten in "Vier Abhandlungen zur Hydrodynamik und Aerodynamik", Goettingen, Reprint 1927.
2. Chaja P., Góralczyk A., Koronowicz T.: *Experimental and Numerical Investigation of Small Axial Turbines*, TASK Quarterly vol. 14 No 3, 2011.
3. Koronowicz T.: *The Influence of the Cavitation Tunnel Walls on the Propeller Characteristics* (in Polish), Bulletin of IFFM No 356/1965.
4. Koronowicz T.: *The Theoretical Model of the Propeller Slipstream Based on the Concentrated Form of Vorticity with Cavitating Kernels and Hydrodynamic Characteristics of the System of Helicoidal Vortices in Bounded Fluid Domain* (in Polish), Scientific Papers of the IFFM No 58/956/1979.

CONTACT WITH THE AUTHORS

Tadeusz Koronowicz, Prof. (Emeritus),
The Szewalski Institute of Fluid Flow Machinery
Polish Academy of Sciences
Fiszera 14
80-952 Gdansk, POLAND
email: ttk@interecho.com

Jan A. Szantyr, Prof.,
Faculty of Mechanical Engineering
Gdansk University of Technology
Narutowicza 11/12
80-233 Gdansk, POLAND
email: jas@pg.gda.pl

Numerical calculations of the hydrodynamic performance of the contra-rotating propeller (CRP) for high speed vehicle

Hassan Ghassemi, Associate Prof.,
Mohsen Taherinasab, M.Sc.,
Amirkabir University of Technology, Tehran, Iran

ABSTRACT

Several different methods have been used to analyze the marine propellers. In this paper a boundary element method (BEM) for modelling steady hydrodynamic performance of a contra-rotating propeller (CRP) has been developed. The potential flow across the front and rear propellers have been considered. By calculating the induced flow, the interaction between two propellers is studied. This method has been applied to a typical CRP. The results are included in the form of the hydrodynamic performance coefficients, total thrust and torques. Numerical calculations indicate that the predicted hydrodynamic performance shows good conformity with experimental results.

Keywords: boundary element method; contra-rotating propeller; high speed vehicle

INTRODUCTION

Because of increasing demands on higher load - carrying capacity and speed of the marine transport systems the marine research centres have concentrated their study on propeller devices that can meet this demand. However several problems arise when single propellers are used in large displacement ships or submarines to produce the required thrust. Amongst them are: increasing chance of propeller blade cavitation in heavy load conditions and vibrations due to unbalance in torque. The vibrations are transferred from the propeller to the ship body and cause instability of motion. The aforementioned problems must be considered by the designers specially in controlling rolling.

A suitable method to overcome such problems is applying the contra-rotating propellers. Such propellers are composed of two propellers which are installed on two coaxial shafts and rotate in opposite directions. Despite the disadvantages such as complexity of design and heavy weight due to the propeller's motor, the contra-rotating propellers have many advantages over single propellers, including the following:

- a. generally, the rotational energy produced by the single propeller not only has no effect on the thrust but also causes loss of energy. The most important benefit of the contra-rotating propellers is their improved efficiency due to energy recovered by the back propeller. In fact, the back propeller recovers some amount of the rotational energy that is transferred to the water by the front propeller. Therefore using such propellers leads to a lower fuel consumption.
- b. the torque between the two propellers is balanced, that is used to eliminate the reverse torque in devices in case when

- c. maintaining stability of motion is important.
- c. the load on the blades is lower and cavitation is delayed. The lower load also allows to reach a higher power output from CRP propellers of similar diameter compared with single ones.
- d. the produced noise is lower because of the uniformity of the downstream wake field of the contra-rotating propellers.

Unfortunately there is no optimized design procedure for contra-rotating propellers and the full- scale test data are not published widely.

There is no exact record of the history of contra-rotating propellers, but the first mention of them was given by Dollman and Perkins before 1800. Later, Ericsson performed experiments on model and real- scale propellers. Rota was the first who showed that the efficiency of the contra-rotating propellers is higher than the single propellers. He found that the reason for the increase in efficiency is the recovery of rotational energy transferred to water by the first propeller [1]. Several researchers performed numerical and experimental studies on the performance of the propellers and their parameters that affect it and their results were published in different papers some of which are listed by Cox *et al.* in [2]. Using lifting surface theory, Tsakonas *et al.* [3] computed the hydrodynamic forces applied on the contra-rotating propellers in stable and instable conditions. Yang [4, 5] used the lifting surface theory taking into account the interaction of the trailing wakes of the two propellers. Hoshino [6] also used the lifting surface theory to analyze the loads exerted onto the contra-rotating propeller shaft and has compared the results with the experimental

where:

- (x_c, y_c) – camber line coordinates,
- $y_t (=0.5t_{(x_c)})$ – the half thickness of the blade,
- \dot{r} – the slope of the camber line.

For obtaining the coordinates of points on other blades, we use the following mapping in which φ is the phase angle of each blade:

$$\begin{bmatrix} X_p \\ Y_p \\ Z_p \end{bmatrix} = \begin{bmatrix} 1 & 0 & 0 \\ 0 & \cos\varphi & \sin\varphi \\ 0 & \sin\varphi & \cos\varphi \end{bmatrix} \begin{bmatrix} x_p \\ y_p \\ z_p \end{bmatrix} \quad (5)$$

Modelling the trailing vortex wake

We assume that the surface of the wake, S_w , is very small and there is not any discontinuity in pressure and flow on this surface. Discontinuity in potential values is allowable. The wake geometry should be modelled so as to satisfy the Kutta condition. As mentioned earlier, in order to simplify the solution procedure the thickness of the wake is assumed equal to zero. But the edge of each cross-section has some thickness and therefore the average of the coordinates of the top and bottom surface of the blade is used to determine the wake points on the edges of the blade. The total wake propagation in the direction of the blade axis is equal to the propagation of the propeller after two complete revolutions. Experimentally, this amount of propagation is sufficient to satisfy the Kutta condition.

Changes in axial direction when the wake passes over the trailing edge of each section, are assumed negligible. It is also assumed that the propagation of each streamline of the wake is made on a constant-radius cylinder. In real situation, the radius of the trailing vortex wake (TVW) initially increases (transient region) and then decreases.

The potential-based boundary element method (BEM)

According to the made assumptions the disturbance potential satisfies the Laplace equation. Let's consider the closed region V with the boundary S (Fig. 2).

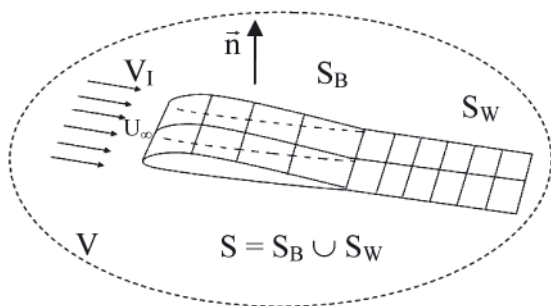


Fig. 2. Body mesh arrangement and its entering flow

The boundary value problem for the potential equation could be expressed as Neumann problem as follows:

$$\begin{cases} \nabla^2\phi = 0 & \text{in } V \\ \frac{\partial\phi}{\partial n} = \phi_n & \text{on } S \end{cases} \quad (6)$$

The kinematic boundary condition which should be satisfied on the boundary S_B , is described by the following equation:

$$\frac{\partial\phi}{\partial n} = -\vec{V}_1 \cdot \vec{n} \quad \text{where: } \vec{V}_1 = \vec{V}_A + \vec{\omega} \times \vec{r} + \vec{v}_{ind} \quad (7)$$

Here, ω is the propeller angular velocity of the propeller, V_A is the advance velocity and \vec{v}_{ind} is the induced velocity of each propeller coming from the other propeller.

To determine the vorticity the Kutta condition on the trailing edge of the blade should be satisfied. The Kutta condition is usually described as a finite velocity on the trailing edge. In other words:

$$|\nabla\phi|_{T.E.} < \infty \quad (8)$$

Considering the surface of the front and rear propellers and using Green theorem for the central point p on the surface of the front and rear propellers, S_B , the potential problem is defined as:

$$\begin{aligned} 2\pi\phi(p) = & \iint_{S_B} \phi(q) \frac{\partial}{\partial n_q} \frac{1}{R(p,q)} dS + \\ & - \iint_{S_B} \phi_n \frac{1}{R(p,q)} dS + \\ & + \iint_{S_w} \Delta\phi(q) \frac{\partial}{\partial n_q} \frac{1}{R(p,q)} dS \end{aligned} \quad (9)$$

S_B is the sum of the surface of the front propeller, S_{Bf} , and that of the back propeller, S_{Bb} . S_w is composed of the surface of the wake of the front propeller, S_{wf} , and that of the wake of the back propeller, S_{wb} . The matrix form of Eq. (9) is [16]:

$$\begin{aligned} [2\pi I - D]_{N \times N} \{\phi\}_{N \times 1} = \\ = [S]_{N \times N} \{\phi_n\}_{N \times 1} + [W]_{N \times N} \{\Delta\phi\}_{N \times 1} \end{aligned} \quad (10)$$

Here, I is unit matrix, D , S and W are full matrices. ϕ_n is determined by Eq. (7). The Kutta condition must be used for determining the unknowns $\Delta\phi$ of the doublet strength for trailing sheet vortex surface. From Eq. (10) the velocity potential ϕ is calculated at each element. After the velocity potential over each element is determined, velocity and pressure distributions can be calculated directly by using Bernoulli's equation:

$$\begin{cases} \vec{v}_t = \nabla\phi \\ P = 0.5\rho(2\vec{V}_1 \cdot \vec{v}_t - \vec{v}_t \cdot \vec{v}_t) \end{cases} \quad (11)$$

The pressure coefficient can be expressed as:

$$C_p = \frac{P}{0.5\rho V_1^2} \quad (12)$$

Thrust and torque of the propellers with two components of pressure and friction are expressed as follows:

$$T = Z \sum_{i=1}^N P_i n_{xi} \Delta S_i - T_{Fric} \quad (13)$$

$$Q = Z \sum_{i=1}^N P_i (n_{yi} \cdot z_i - n_{zi} \cdot y_i) \Delta S_i + Q_{Fric}$$

where T_{Fric} and Q_{Fric} are the frictional component of thrust and torque of the propeller, respectively. They are determined by using empirical formulae proposed by ITTC. The total thrust and total torque produced by the CRP is given by:

$$\begin{aligned} T = |T_f| + |T_a| \\ Q = |Q_f| - |Q_a| \end{aligned} \quad (14)$$

Hydrodynamic coefficients

The hydrodynamic coefficients of each propeller can be obtained. For the front propeller we have:

$$\begin{aligned} K_{Tf} &= \frac{T_f}{\rho n_f^2 D_f^4}, & K_{Qf} &= \frac{Q_f}{\rho n_f^3 D_f^5} \\ \eta_f &= \frac{K_{Tf}}{K_{Qf}} \frac{J}{2\pi}, & J &= \frac{V_A}{n_f D_f} \end{aligned} \quad (15)$$

In which n_f is the rotational velocity, D_f is the diameter, T_f is the thrust and Q_f is the torque produced by the front propeller. For the rear propeller we have:

$$\begin{aligned} K_{Ta} &= \frac{T_a}{\rho n_a^2 D_a^4}, & K_{Qa} &= \frac{Q_a}{\rho n_a^3 D_a^5} \\ \eta_a &= \frac{K_{Ta}}{K_{Qa}} \frac{J}{2\pi} \end{aligned} \quad (16)$$

In which n_a is the rotational velocity, D_a is the diameter, T_a is the thrust and Q_a is the torque produced by the rear propeller.

Finally, as the thrust and torque of the rear and front propellers and performance coefficients of each of them are known the performance coefficients of the CRP can be obtained as follows:

$$\begin{aligned} K_T &= K_{Tf} + K_{Ta} \\ K_Q &= K_{Qf} + K_{Qa} \\ \eta &= \frac{K_T}{K_Q} \frac{J}{2\pi} \end{aligned} \quad (17)$$

Induced velocities

From Green's theorem, as applied to the potential field in Eq. (9), we can alternatively construct the velocity field by taking the gradient of the perturbation velocity:

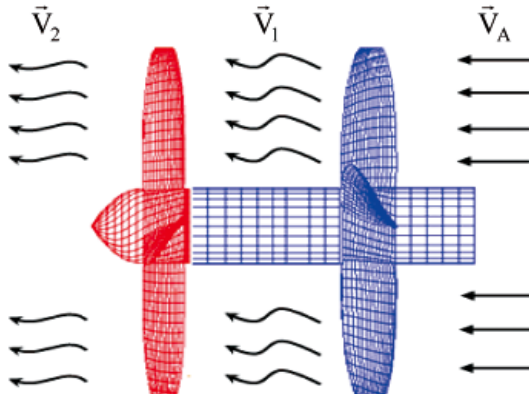


Fig. 3. Inflow velocities of CRP

$$\begin{aligned} 4\pi\vec{v}_{ind} &= \iint_{S_B} \phi(q) \nabla \left(\frac{\partial}{\partial n_q} \frac{1}{R(p,q)} \right) dS + \\ &- \iint_{S_B} \phi_n \nabla \left(\frac{1}{R(p,q)} \right) dS + \\ &+ \iint_{S_w} \Delta\phi(q) \nabla \left(\frac{\partial}{\partial n_q} \frac{1}{R(p,q)} \right) dS \end{aligned} \quad (18)$$

The induced velocities due to the front propeller, directed to the aft one, is defined by $\vec{v}_{ind(FA)}$ and vice-versa - by $\vec{v}_{ind(AF)}$. Therefore, the inflow velocity to the aft propeller is obtained as follows (Fig. 3):

$$\begin{cases} \vec{V}_1 = \vec{V}_A + \vec{\omega}_f \times \vec{r} + \vec{v}_{ind(FA)} + \vec{v}_{ind(AF)} \\ \vec{V}_2 = \vec{V}_A + \vec{\omega}_a \times \vec{r} + \vec{v}_{ind(AF)} + \vec{v}_{ind(FA)} \end{cases} \quad (19)$$

The action of the rear propeller onto the front one is very low compared with the action of the front propeller onto rear one, hence it can be neglected in some cases.

NUMERICAL RESULTS

Hydrodynamic performance

In this section, the results of analysis of a typical CRP are presented. The analyzed propeller is of a 3686F-3687A type. The front propeller (3686F) is a CCW propeller and the rear propeller (3687A) is a CW one. The geometrical parameters of the propellers are given in [13]. Main parameters of both the propellers are presented in Tab. 1. An image of the whole CRP is shown in Fig. 4. The trailing vortex wake (TVW) is shown in Fig. 5.

Tab. 1. Main dimensions of the CRP

Parameters	3686F	3687A
Blade number	4	4
Diameter [m]	0.3052	0.2991
P/D at 0.7R	1.0	1.33
EAR	0.303	0.324
Rotation	Anticlockwise	Clockwise
Blade section	NACA66 a = 0.8	NACA66 a = 0.8

Run of the hydrodynamic coefficients of the front propeller (3686F) is shown in Fig. 6. and for the rear propeller - in Fig. 7. The coefficients for both the propellers (i.e. whole CRP), compared with experimental results, are shown in Fig. 8. The numerical results show good agreement with the experimental data.

In 2003, Gu and Kinnas [6] analyzed this type of propeller (3686F-3687A) using coupling vortex lattice and finite volume methods. In Fig. 9 is presented a comparison made between results of the present study, Gu and Kinnas research and experimental one. It can be observed that the results of the present study are within a small error range, hence rather acceptable.

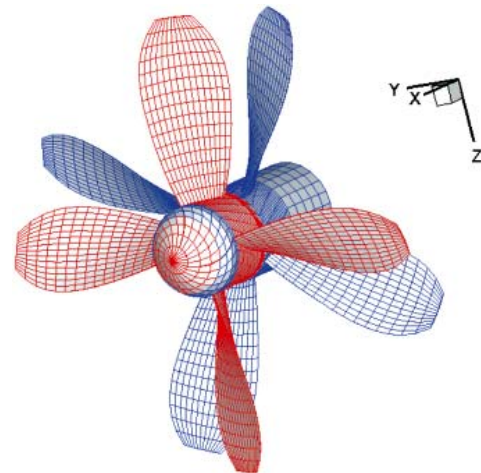


Fig. 4. 3686F-3687A CRP model

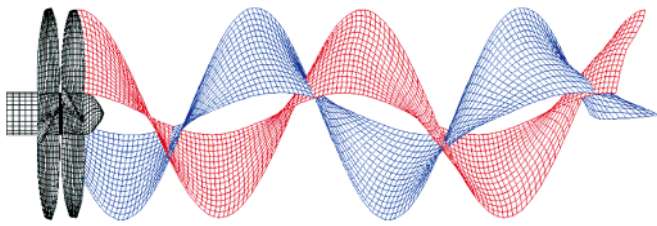


Fig. 5. TVW of the 3686F-3687A CRP model

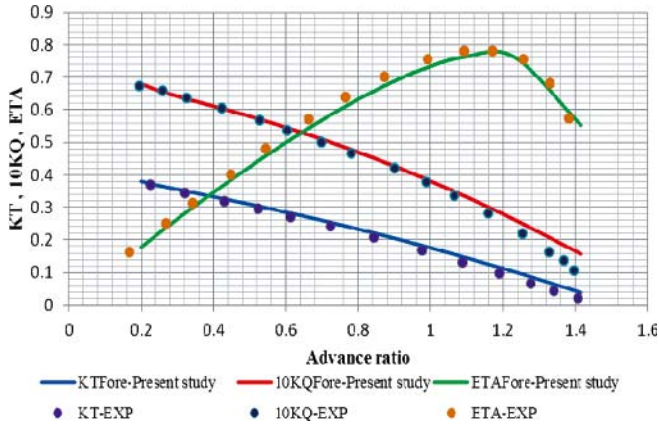


Fig. 6. Hydrodynamic coefficients of the front propeller

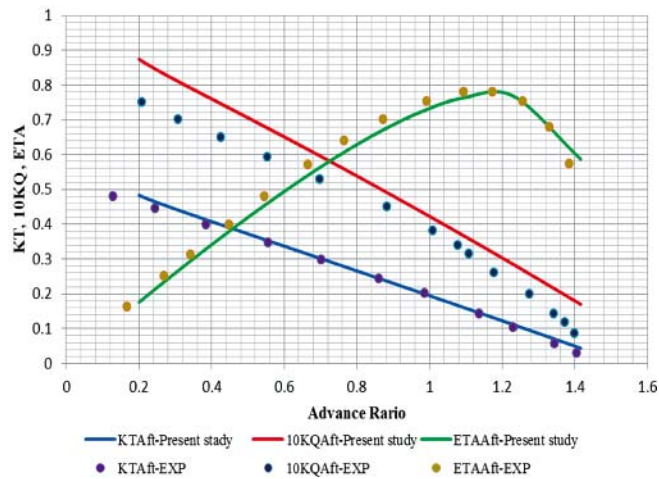


Fig. 7. Hydrodynamic coefficients of the rear propeller

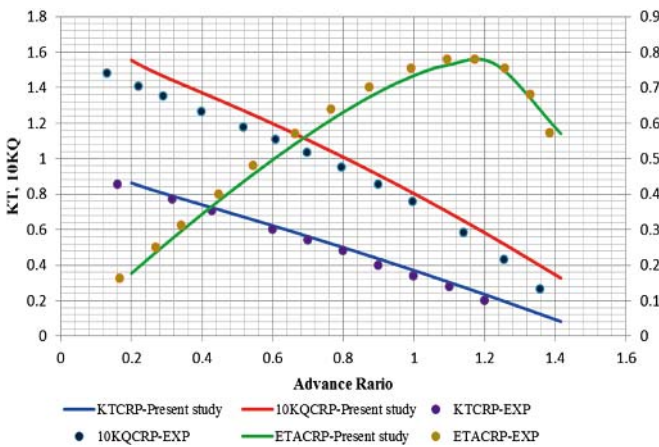


Fig. 8. Hydrodynamic coefficients of the 3686F-3687A CRP model

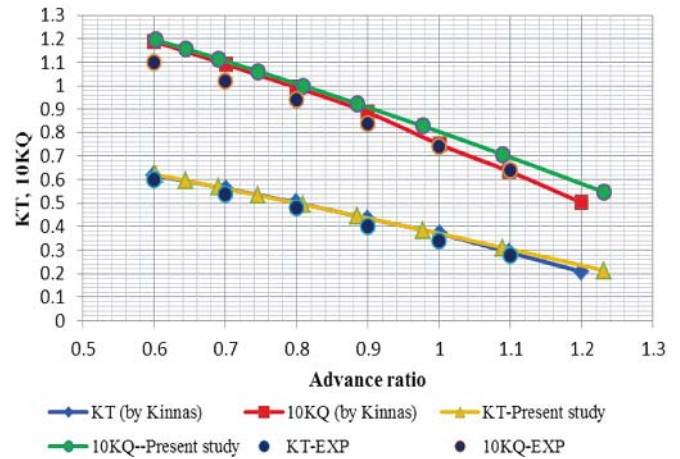


Fig. 9. Comparison of the numerical results (of the present study and Kinmas [6]) and experimental data for the considered CRP

Calculations of the thrust and torque

Values of the ratio of the thrust produced by the front propeller and the rear one related to the total thrust at the relative radius $r/R = 0.7$ are obtained, respectively, as follows:

$$T.R_{Fore} = \frac{\text{Thrust}_{Fore}}{\text{Thrust}_{total}} = 47.27\%$$

$$T.R_{Aft} = \frac{\text{Thrust}_{Aft}}{\text{Thrust}_{total}} = 52.73\%$$

It can be seen that the thrust produced by the rear propeller is higher. This may be due to the effect of the front – propeller - induced wake on the rear propeller.

Fig. 10 and 11 illustrate the thrust-RPM, torque-RPM, total thrust-RPM and total torque-RPM relations, respectively. Vectors of the torque produced by the front and rear propellers are directed against each other and thus the total torque are much lower than the individual torque of each propeller.

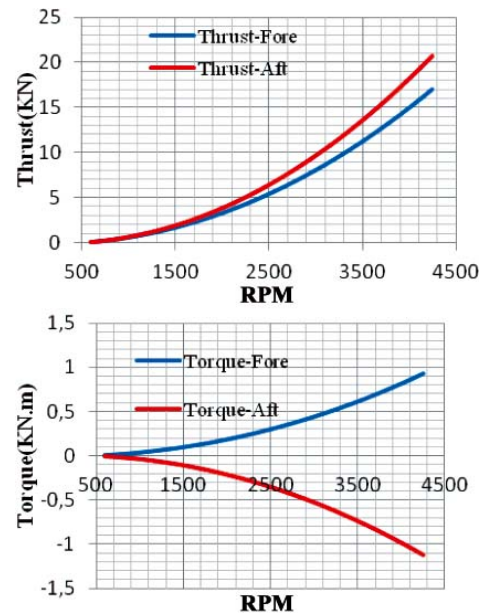


Fig. 10. Individual thrust and torque of each propeller versus propeller rotational speed (RPM)

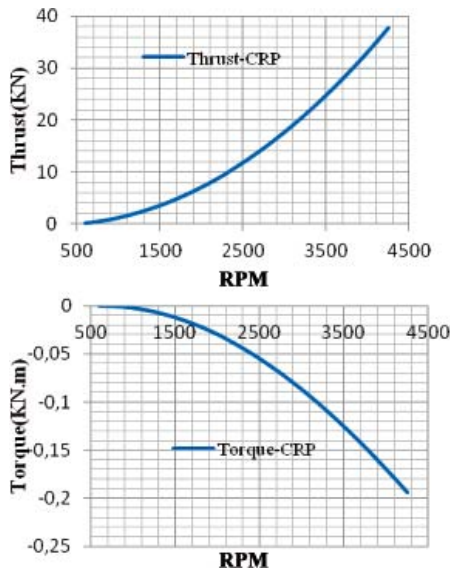


Fig. 11. Total thrust and torque of the whole CRP versus propeller rotational speed (RPM)

Pressure distributions on blades and induced velocities

The coefficient of contour pressure distribution on the propeller blade surfaces at $J = 1.19$ are shown in Fig. 12 and 13. Red colour shows the high pressure face side and blue one indicates the low pressure back side. The induced velocities are very important because the interactions between two propellers are caused by them. The axial induced wake velocity between two propellers and that behind the rear propeller is shown in Fig. 14 and 15, respectively.

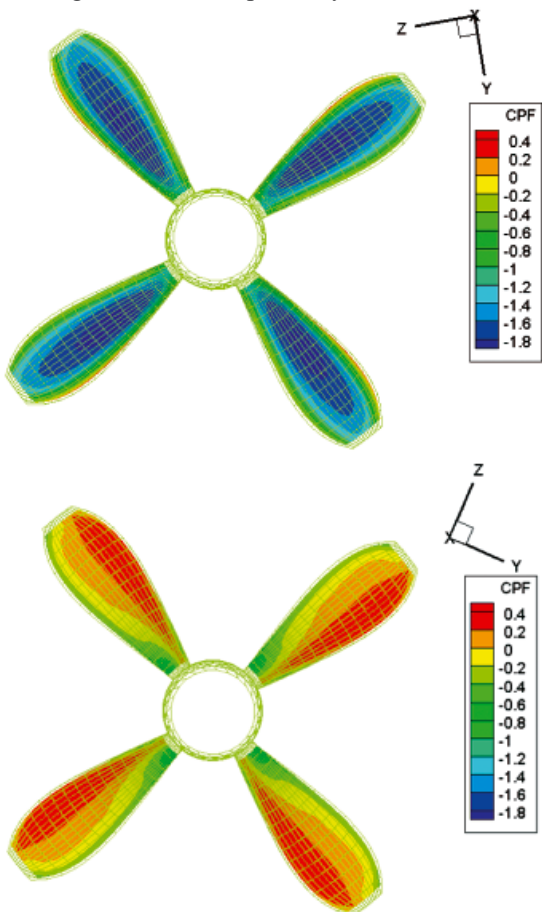


Fig. 12. Pressure distributions on the back (upper or left?) and face (lower or right?) surface of the front propeller

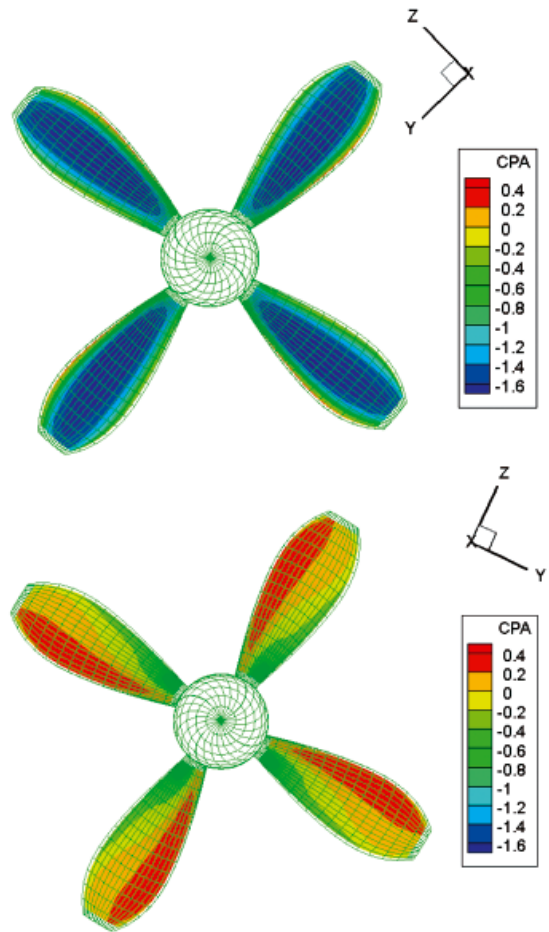


Fig. 13. Pressure distributions on the back (upper or left?) and face (lower or right?) surface of the rear propeller

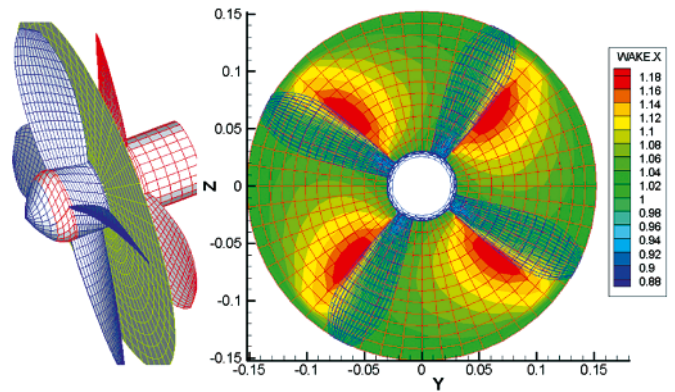


Fig. 14. Axial induced wake velocity between two propellers ($X/R=0.22$)

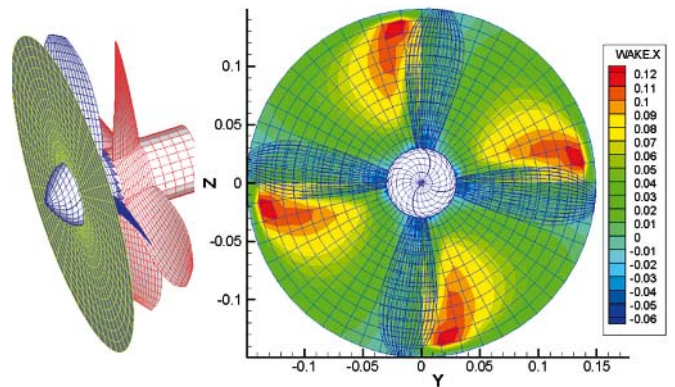


Fig. 15. Axial induced wake velocity behind the rear propeller ($X/R = 0.34$)

CONCLUSIONS

With regard to the numerical results of the 3686F-3687A CRP calculations the following conclusions can be offered:

- As for the hydrodynamic characteristics of the front and rear propellers, it could be mentioned that the thrust and torque hydrodynamic coefficients for the rear propeller are higher than those for the front one. This is due to the effect of the front propeller wake.
- The hydrodynamic performance parameters of the CRP were obtained by superposition of the parameters of individual propellers. This is consistent with the experimental results.
- The CRP minimizes the torque produced by the propeller; hence it is recommended to apply it to devices for which elimination of roll movement is important (e.g. torpedoes). Also eliminating the torque causes less vibration to be transmitted to the ship body and thus increases the stability of motion of the ship.
- As for the pressure distribution on the rear and front propellers, it could be concluded that in a CRP the load is divided between front and rear propellers. Each propeller has its own contribution in producing the total thrust. Therefore using this system results in smaller loads on each propeller and consequently more uniform pressure distribution on the blades. Therefore in contra- rotating propellers chance of cavitation appears lower.

NOMENCLATURE

D	– propeller diameter
D_f	– fore propeller diameter
D_a	– aft propeller diameter
EAR	– expanded area ratio
Z	– number of blades
J	– advance velocity ratio
P/D	– propeller pitch
K_{Tf}	– thrust coefficient of the fore propeller
K_{Ta}	– thrust coefficient of the aft propeller
K_T	– thrust coefficient of the propeller
K_{Qf}	– torque coefficient of the propeller
K_{Qa}	– torque coefficient of the propeller
K_Q	– torque coefficient of the propeller
P	– pressure
C_p	– pressure coefficient
S_w	– trailing wake surface
S_B	– blade surface
T	– total thrust
T_f	– fore propeller thrust
T_a	– aft propeller thrust
T_{Frict}	– frictional component of thrust
Q	– total torque
Q_f	– fore propeller torque
Q_a	– aft propeller torque
Q_{Frict}	– frictional component of torque
V_A	– advance velocity
\vec{V}_1, \vec{V}_2	– downstream velocities of the propellers
\vec{V}_I	– inflow velocity to the propeller
\vec{V}_t	– tangential induced velocity
\vec{V}_{ind}	– induced velocity
$\vec{V}_{ind(FA)}$	– induced velocity by fore propeller to aft propeller
$\vec{V}_{ind(AF)}$	– induced velocity by aft propeller to fore propeller
D, S, W	– potential matrix coefficients
n_f	– fore propeller rotating
n_a	– aft propeller rotating

\vec{n}	– normal vector of the surface
$y_{u,L}$	– distance from upper and lower surfaces to the chord line
(x_c, y_c)	– camber line coordinates
$t_{(x_c)}$	– half thickness of the blade
ω_f	– angular velocity of fore propeller
ω_a	– angular velocity of aft propeller
β_G	– geometric pitch angle
θ	– rotating angle of blade
θ_R	– rake angle
θ_S	– skew angle
φ	– phase angle of each blade
ψ	– camber line slope
ϕ	– velocity potential
ϕ_n	– normal derivative of potential
$\Delta\phi$	– difference potential at trailing edge
ϕ_{in}	– inflow velocity potential
ΔS_i	– surface area of each element
η	– propeller efficiency
η_f	– fore propeller efficiency
η_a	– aft propeller efficiency

BIBLIOGRAPHY

1. Rota, G.,: *The Propulsion of Ships by Means of Contrary-Turning Screws on a Common Axis*. Transactions of the Institute of Naval Architects, Vol. 51, (1909).
2. Cox, B. D. and Reed, A. M.,: *Contra-rotating propellers – design theory and application*. In Propellers/Shafting '88 Symposium, Virginia Beach, VA. (1988).
3. Tsakonas, S., Jacobs, W.R., Liao, P.: *Prediction of steady and unsteady loads and hydrodynamics forces on contra-rotating propellers*, Journal of Ship Research. 27(3), pp.179÷214, (1983).
4. Yang C. J., Tamashima M., Wang G. Q., Yamazaki R.,: *Prediction of the steady performance of contra-rotating propellers by lifting surface theory*, Transactions of the West-Japan Society of Naval Architects No. 82, (1991).
5. Yang C. J., Tamashima M., Wang G. Q., Yamazaki R., Koizuka H.,: *Prediction of the unsteady performance of contra-rotating propellers by lifting surface theory*, Transactions of the West-Japan Society of Naval Architects No. 83, (1992).
6. Hoshino, T.,: *Experimental and Theoretical analysis of propeller shaft forces of contra-rotating propellers and correction with full scale data*, Propeller/Shafting'94 Symposium, Society of Naval Architects and Marine Engineers, Virginia Beach, (1994).
7. Gu, H., Kinnas, S.A.,: *Modelling of contra-rotating and ducted propellers via coupling of a vortex-lattice with a finite volume method*. Propellers/Shafting 2003 Symposium, Society of Naval Architects and Marine Engineers, Virginia Beach (2003).
8. Ghassemi, H.: *Hydrodynamic performance of coaxial contra-rotating propeller (CCRP) for large ships*, Polish Maritime Research (59), Vol., 16, pp.22÷28, (2009).
9. Ghassemi, H., Mardan, A., Ardeshtir, A.: *Numerical analysis of hub effect on hydrodynamic performance of propellers with inclusion of PBCF to equalize the induced velocity*. Polish Maritime Research, 2 (73), Vol. 19; pp. 17÷24, (2012).
10. Koronowicz, T., Krzemianowski, Z., Tuskowska T., Szantyr J.A.,: *A complete design of ship propellers using the new computer system*, Polish Maritime Research (59), Vol. 16, pp.29÷34, (2009).
11. Hecker, R., and McDonald N. A.,: *The effect of axial spacing and diameter on the powering performance of contra-rotating propellers*. David Taylor Model Basin, Report 1342, Feb. (1960).
12. Van Manen J. D. and Oosterveld M. W. C.,: *Model Tests on Contra Rotating Propellers*. 7th Symposium on Naval Hydrodynamics, Rome, Italy (1968).
13. Miller, M. L.,: *Experimental determination of unsteady forces on contra-rotating propellers for application to torpedoes*. David Naval Ship Research and Development Centre Report, SPD-659-02, (1981).

14. Brizzolara, S., Tincassi, E.P.A., Grassi, D.: *Design of contra-rotating propellers for high speed stern thrusters*. Ship and Offshore Structures, Publication no. 2:2, pp.169÷182, (2007).
15. Carlton J. S.: *Marine Propellers and Propulsion*. Second edition, published by Elsevier Ltd, (2007).
16. Ghassemi, H., Ghadimi, P.: Hydrodynamic efficiency improvement of the high skew propeller for the underwater vehicle under surface and submerged conditions. J. Ocean Univ. of China (JOUC), Vol. 10, pp.314÷324 (2011).

CONTACT WITH THE AUTHORS

Hassan Ghassemi, Associate Prof.,
Mohsen Taherinasab, M.Sc.,
Department of Ocean Engineering,
Amirkabir University of Technology, Tehran, IRAN
e-mail: gasemi@aut.ac.ir,
tel.: +98-21-64543112, fax: +98-21-66412495.

An experimental study of interceptor's effectiveness on hydrodynamic performance of high-speed planing crafts

Mohammad Hosein Karimi, Ph.D. Student,
Mohammad Saeed Seif, Prof.,
Madjid Abbaspoor, Prof.,
Sharif University of Technology, Iran

ABSTRACT

Trim control mechanisms such as interceptors and trim flaps have been widely used in recent years in high-speed crafts for ride and trim control. In spite of their extensive application, a few studies investigating the impact of interceptors on planing craft performance, have been published. In the present study, the impact of interceptors on planing crafts hydrodynamic quality is investigated through application of an experimental method. Two scaled-down models of high-speed planing mono-hull and catamaran are tested with and without interceptors in calm water at different heights of the interceptors to investigate the effect of interceptors on drag reduction of the models. The first one is a scaled-down model of 11 m planing mono-hull boat and the test was conducted at the towing tank of Sharif University of Technology, Iran. The second one is a scaled-down model of 18 m planing catamaran boat and the test was conducted at the towing tank of Krylov Shipbuilding Research Institute (KSRI), Russia. The experimental results show a remarkable drag reduction of up to 15% for mono-hull model and up to 12% for catamaran model over the wide speed range of the models.

Keywords: interceptors; drag reduction; hydrodynamic quality; planing catamaran; mono-hull

INTRODUCTION

Interceptors have been used for trim and ride control of planing and semi-planing boats since the 1970s and the application of these devices has steadily increased over the years. Interceptors are nowadays also used for steering and motion control of high speed crafts. An interceptor is a thin plate or blade, protruded from the hull normal to the flow direction causing a stagnating flow region near the blade. The resultant pressure acts on the hull bottom creating the effects such as the trim moment, which adds lift and finally controls the attitude of the craft. The interceptors are normally installed at the boat transom and/or amidships or at a distance ahead of transom depending on the boat loading, position of the centre of gravity and initial trim. Hydraulic or electric actuators adjust the height of the interceptors and the blades can be retracted completely when they are not needed. The most common application of interceptors is to serve as a trim control device that can help to reduce the overall resistance of planing vessel. There is also another way to decrease the resistance of a planing vessel by means of interceptors, i.e. through installing the interceptor amidships. This results in the reduction of the wetted area, both by increasing the dynamic lift and creating an air cavity behind the interceptors. The magnitude of the lift created by the interceptors normally depends on their height and flow velocity. However, there are other parameters possible to have an

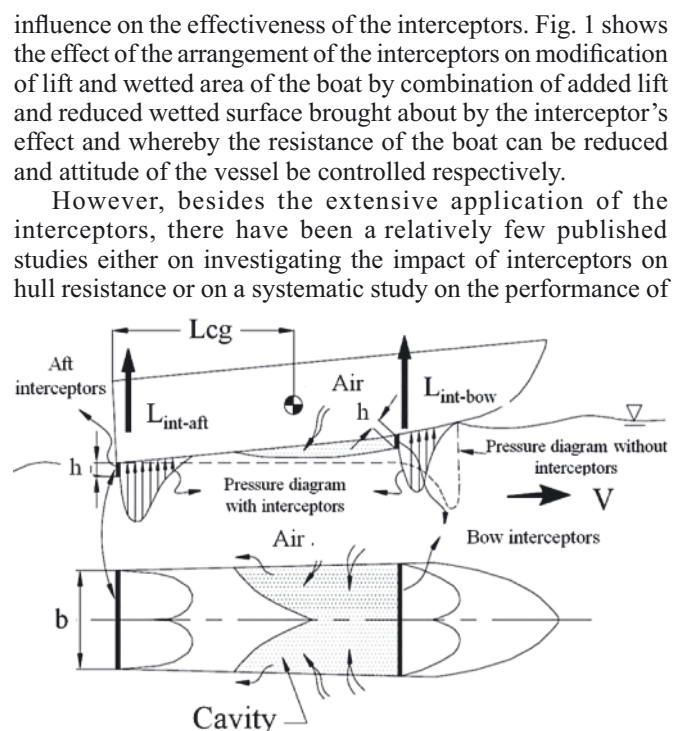


Fig. 1. Illustration of physical phenomena associated with interceptors

these devices. Thus, the present study aims at improving the understanding of the impact of interceptors on hull resistance by reviewing the published literature sources, examining the impact of the interceptors on hydrodynamic quality of planing mono-hull and catamaran through an experimental study, and to develop further insight into the procedures by which interceptors can cause reduction of resistance.

LITERATURE REVIEW

The effect of stern wedge on ship powering performance of planing and semi-planing vessels has been studied by several researchers [1]. Bannikov, Bannikova et al. experimentally investigated the transom interceptor influence on the hydrodynamic characteristics of planing surfaces with 0.3 m beam, dead rise angle of 0, 15 and 30 deg at 4-9 m/s speed, at different heights of the interceptor, and derived an empirical formula for the added lift and drag of planing surfaces [2, 3]. By using several planing surfaces and flat plates' experimental results, Savitsky devised a computational procedure to evaluate the performance of a planing hull. The foregoing procedure is used in calculating the running trim and resistance at a given running speed as well as the load and location of the centre of gravity [4].

Like interceptors, the trim flap has also been widely used on semi-planing and planing vessels and there is a large amount of published data on its performance. A thorough investigation was conducted by Brown as "an experimental and theoretical study of planing surfaces with trim flaps" [5]. Furthermore, the effect of the trim flaps was implemented to the planing boat model by Savitsky and Brown [6].

Tsai et al. carried out a model test on a 1/20 scale model of 20 m patrol boat at designed speed of 40 knots and a 1/10 scale model of a 29.5 m patrol boat at designed speed of 32 knots, including interceptors and with and without stern flaps. The application of even small interceptors (h/L of the order of 0.1%) changed the trim and as a result reduced the resistance considerably (up to 17% at interceptor height of 0.5, 1, 1.5 mm in model scale) [7, 8].

The Krylov Shipbuilding Research Institute also performed several tank tests on catamaran and mono-hull models to explore the effectiveness of interceptors on resistance reduction and motion control of high speed crafts [9, 10].

A new formulation has been developed by Dawson and Blount as the basis to predict the equivalent lift of interceptors [11].

Brizzolara carried out one of the most detailed studies on interceptor's hydrodynamics. He used a CFD method to study the local flow around a 2D interceptor fitted to a flat boundary, which represented the hydrodynamic flow around the bottom of a ship and was the most idealized model of interceptors ever used. This model allowed for viscous effects and through limited series of CFD-based simulations provided the relationships between the hydrodynamic forces and the interceptor's main parameters [13]. Successively, Molini and Brizzolara introduced a simple potential flow model for the predicting of pressure and lift forces in front of the interceptors [14]. D.Villa and Brizzolara put forward a new study, which changes context and approach considerably in comparison with the previous ones. In fact, CFD-based hydrodynamic models consider the complete description of planing hull form with stern appendages. Of course, not only interceptors but also stern flaps have been considered with the scope to compare relative performance; the CFD solution with RANES solver were used to simulate the flow around planing hulls and stern appendages more precisely [15].

In a series of M.Sc.-theses elaborated in the Department of Marine Technology at Norwegian University of Science and Technology (NTNU), Norway, their authors tried to establish a database for performance data on lift and drag of interceptors installed at the transom of prismatic planing hulls. Sverre Steen summarized the experimental results suggesting various approaches to empirical formulas for the coefficients of added lift and drag due to interceptors [16].

Alterskjar performed the tank test of the model of 26 m catamaran with stern and mid-interceptors in calm water and waves to investigate whether the application of stern and mid-interceptors could help reducing the calm water resistance and if the good results observed in calm water are also present in seaway [17]. Based on his finding, Allema has reported a successful attempt in reducing the required power for a cruise ship [18].

Fridman has presented the most thorough research material available on interceptors used as a means to ventilate ship's hull bottom. He also reported the research results on a system consisting of both under-bottom-mounted and stern-mounted interceptors on cutter-class vessels. Fridman also suggested theoretical models to predict lift and drag due to the interceptors [19].

Alexander H. Day et al. carried out a comprehensive experimental tank test program on a scaled model of a yacht hull to examine the impact of interceptors. The results indicate a significant reduction in calm water resistance over a wide speed range with gains of 10 ÷ 18 % in the speed range between 8 and 20 knots, accompanied by a reduced trim and sinkage. The performance of the interceptors was also compared with Gurney flap, and in addition the effect of interceptors on trim change was compared with the longitudinally moving ballast, and as observed, the benefits appear to be largely sustained in small waves [21].

The literature review of the available results on interceptor and its application indicates that in spite of the popularity of interceptors, there have been a relatively low number of published studies comprehensively exploring the effect of interceptors on hull resistance, and apparently, the foregoing surveys were not specifically aimed at high speed planing mono-hull and catamaran resistance. Therefore, the aim of the present study is to provide a method to evaluate the effect of interceptors on high speed planing mono-hull and catamaran and fill the knowledge gap that currently exists, by carrying out the tank test of the scaled-down planing mono-hull and catamaran models with interceptors at full planing speed.

SELECTING INTERCEPTOR SIZE AND DIMENSIONS

Interceptor height

Several researchers have studied the optimal height of interceptors to maximize the interceptor effectiveness in terms of improving hydrodynamic quality of planing vessels. Most of them agree that the selection of interceptor height depends mostly upon the boundary layer thickness at interceptor location. The idea widely adopted is that the interceptors should be contained entirely within the boundary layer, so that the interceptor height is partly a fraction of the boundary layer thickness. Thus, as the initial approximation, the boundary layer near the transom (for aft interceptor location) can be considered in the same way as that over the flat plate having the same length as the hull. The thickness for the boundary layer in the turbulent flow can be calculated from Eq. (1), [22]:

$$\delta(x) = 0.37 \times \text{Re}_x^{-1/5} \quad (1)$$

Several manufacturers producing interceptor systems have put forward various suggestions for the interceptor height. Humphree suggested the interceptor height of up to 50 mm for power boats between 18 and 45 m, [25], while other manufacturers recommended a height extended to 75 mm for heavier vessels between 18 and 60 m in length.

Brizzolaro used an interceptor at the maximum height of 200 mm on the steering interceptor of STENA HSS-1500 vessel of 127 m overall length and 40 kn speed [13]. Alexander H.Day et al. surveyed the literature and plotted the found interceptor height values against the Reynolds number. The mentioned author compared then the results with the boundary layer thickness values obtained from Eq.(1), [22]. The relevant figure is re-plotted in Fig. 2 with the additional data, showing non-dimensional interceptor height in relation to the boat length. Since tank tests usually cover a wide range of speeds, only several values are plotted for each study, which represent different interceptor heights and different speeds in order to put the scatter in context. Because of the fact that in the case of planing vessels the wetted length can vary substantially with speed, the static wetted length is used.

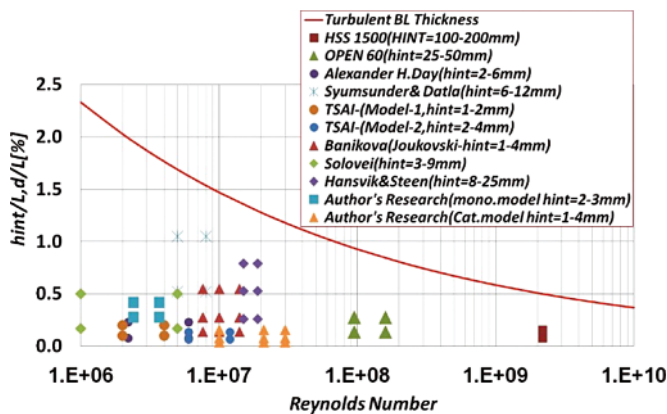


Fig. 2. Experimental data on non-dimensional height of interceptors

As depicted in Fig. 2, the selected interceptor's heights become much smaller proportionally to the boundary layer thickness. Based on the above-mentioned suggestion and as shown in Fig. 2, in the present experimental study the interceptor was tested at model-scale height of 2 to 3 mm for mono-hull model and 1 to 4 mm for catamaran model. Therefore, the non-dimensional interceptor height varies from 0.4 % to 0.6 % of the model waterline length for mono-hull model, and from 0.03 % to 0.13 % of the model waterline length for catamaran model. As Fig. 2 shows, at corresponding Reynolds numbers, the selected interceptor heights are located well within the range of the boundary layer thickness (from 13.6 % to 23.7 % of the boundary layer thickness for mono-hull model and from 2.8 % to 13.5 % of the boundary layer thickness for catamaran model, respectively).

Interceptor spans and positions

In addition to selection of interceptor height, the other important parameters for the case of the location of both stern and mid-interceptors are: span and longitudinal position of interceptors. As for the span, the full beam of the mono-hull and the half beam of each twin-hull (130 mm) of the catamaran model are used as interceptor's span. For both the models transom is considered as the location of the stern interceptor and the longitudinal position of the mid-interceptor for the catamaran model is the distance of about $3 \div 5$ % of waterline length ahead of the model's centre of gravity, [12].

CATAMARAN MODEL EXPERIMENTAL PROCEDURE

Model and model tests

The 18 m planing catamaran selected for the tank-test investigation, has V-shaped cross sections and hard chine twin-hulls. In the current study, all tank tests were performed in the KSRI high-speed towing tank of the dimensions: 650 m (L) \times 14 m (W) \times 6 m (D). Its carriage is able to travel at the speed of up to 16m/s (from 0.01 m/s up to 16m/s with 0.01 m/s step) with the speed measurement accuracy of ± 0.001 m/s. During the tests, the model was fixed against sway and yaw, while free to heave, trim and roll. The 1/6 scale model was built of wood and a special lightweight foam and formed with the use of CNC milling machine followed by special paint spraying procedures to give perfect finishing to the hull surface. The model had special windows in the bottom of each of twin-hulls for monitoring wetted surface boundary behind the mid-interceptor. The experimental procedure in general conformed to the ITTC standard procedures for model making and resistance testing [23, 24]. During the towing tests the following parameters were measured: speed of the model, total resistance of the model, dynamic trim and dynamic sinkage at the point of towing strut attachment. In addition, the boundary of hull-wetted area was also recorded at each test speed. The model's principal dimensions are given in Tab.1.

Tab.1. Model's principal dimensions

Model	Boat	Main particulars
3 m	18 m	Length overall
0.70 m	4.2 m	Beam (total)
65 Kg	14.4 t	Displacement
11.55 m/s	55 knots	Design speed
$(0.32 \div 0.38) \times L$ measured from transom	$(0.32 \div 0.38) \times L$ measured from transom	Lcg (centre-of-gravity location)
20 deg	20 deg	Dead-rise at Lcg
0.26 m	1.56 m	Twin-hull beam
0.180 m	1.08 m	Tunnel beam

Test matrix

As Fig. 1 shows, in the case of considering location of both stern and mid-interceptors, the relative position of interceptors and the boat centre of gravity will define the state of dynamic stability of the vessel, and before implementation of any control mechanism the vessel itself should be dynamically stable in terms of porpoise motion etc. Then in the present study, the optimum position of the model's centre of gravity was selected on the basis of the bare hull performance, and next the tank test was performed for the selected position of the centre of gravity and various interceptors' height values.

Performance of bare hull at different centre-of-gravity positions

The model of 65 kg in weight was tested in bare hull condition for three relative positions of centre of gravity corresponding respectively to 0.32L, 0.35L and 0.38L measured from transom ahead, over the speed range corresponding to full-scale speeds up to 60 knots. Fig. 3 and 4 show the variation of relative resistance and trim angle along with the displacement Froude number (F Δ), respectively. Based on the results

a number of observations can be made: the variation of the Lcg of the model has remarkable effects on the relative resistance and trim angle over the wide range of Froude number values corresponding to the planing speeds.

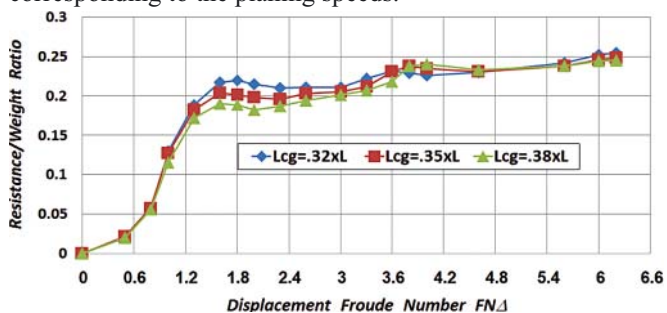


Fig. 3. Variation of relative resistance with Froude number

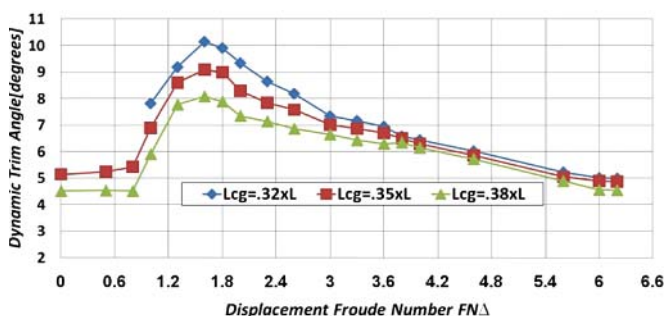


Fig. 4. Variation of running trim angle with Froude number

Tab. 2 shows the variation of the relative resistance and trim angle along with $FN\Delta$. As Tab. 2 shows, at the Froude number corresponding to the first hump ($FN\Delta = 1.5 \sim 1.8$), the shift of the Lcg up to 6 %L to the bow will give the resistance reduction up to 11 ÷ 14%.

As Fig. 3 shows the second hump is observed at $FN\Delta = 4$. At this $FN\Delta$ value which corresponds to 38 kn speed in the full scale (lower than cruising speed), the maximum resistance is observed at the $Lcg = 0.38L$ measured from transom. From $FN\Delta = 4$ up to $FN\Delta = 5.82$ (corresponding to the full scale design speed), the resistance will be decreased by shifting the Lcg to the bow. From the dynamic stability point of view, as observed during the tank test, at the relative position of the centre of gravity, corresponding to $0.32L$, the model suffered porpoising instability at $FN\Delta > 6 \div 6.2$. Based on the above given results, the relative longitudinal position of the centre of gravity corresponding to $0.38L$ measured from transom was then selected for execution of tank test of models with interceptors.

Tab. 2. Variation of resistance and trim with $FN\Delta$

$FN\Delta$	Relative resistance reduction ratio			Relative dynamic trim reduction		
	0.32L	0.35L	0.38L	0.32L	0.35L	0.38L
$FN\Delta = 1.0$	1	0.97 (3%)	0.88 (11.5%)	1	0.88 (12%)	0.76 (24%)
First Hump $FN\Delta = 1.5 \div 1.8$	1	0.92 (8%)	0.86 (14%)	1	0.90 (10%)	0.79 (21%)
$FN\Delta = 3.0$	1	0.97 (3%)	0.95 (5%)	1	0.96 (4%)	0.90 (10%)

Test-setup for interceptor and actuator system

Resistance test in calm water is carried out not only with the fixed-height interceptors but also the selected relative position of centre of gravity ($Lcg = 0.38L$) at the model displacement of 65 kg.

The stern interceptors of the height $h_{int} = 1$ mm, $h_{int} = 2$ mm and $h_{int} = 4$ mm and the mid-interceptors of the height $h_{int} = 1$ mm and $h_{int} = 2$ mm, were tested. The stern interceptors were mounted on the transom board. The distance between the stern interceptors and the mid-interceptors was 1.3 m.

The interceptor pull-rod was inserted through an opening in the model hull and connected to a lever, with hinge axle. Another lever mounted to the same axle was connected to a lanyard attached to a foundation on the model's deck. By turning the lanyard the lever axle is caused to rotate and finally the interceptors is brought about to slide vertically along the hull side. a pointer mounted to the axle indicates the extended height of the interceptors.

Prior to each test run, the interceptor's height settings were calibrated within 0 and 6 mm. This calibration established the relation between the position of the axle-mounted pointer and the interceptor's extended heights measured vertically.

The interceptors were made of 4 mm thick Al-alloy plates. Lower edges of the plates followed the relevant portion of the hull lines. In order to reduce the friction of the movement of the interceptors, the bottom step surfaces in the way of interceptor's attachments were flush-covered with the vinyl plates. Each interceptor was secured to the respective step by two bolts. The interceptor's shapes and the attachment details are shown in Fig. 5 and Fig. 6 depicts the model hull lines.

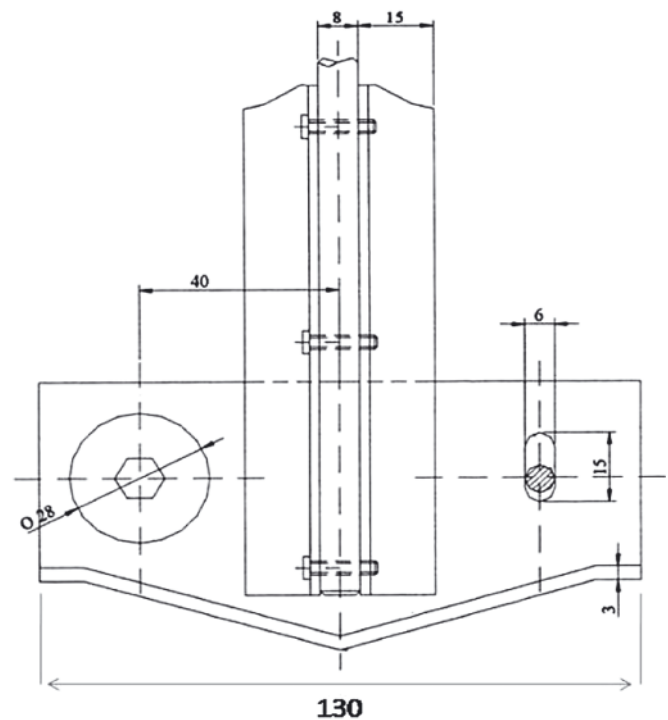


Fig. 5. Interceptor's shape and the installation details

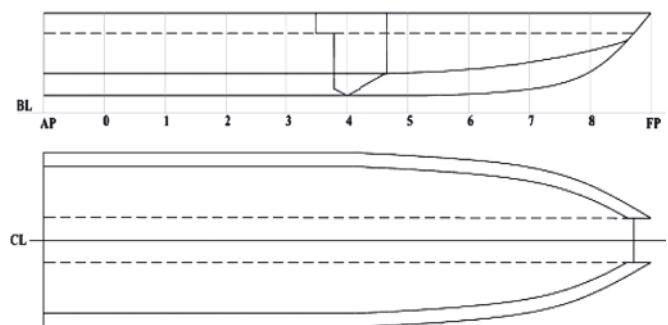


Fig. 6. Catamaran model hull lines drawing

Results of calm-water tests with fixed-height interceptors

During the calm-water tests of the model having the displacement $\Delta = 65$ kg and centre-of-gravity location $L_{cg} = 0.38L$, the interceptors were located individually either at the middle or transom section, with various interceptor height settings simultaneously at the both sections. Testing a series of the fixed-height settings was sufficient for finding the optimum interceptor height. The test was performed for the complete speed range corresponding to the range of $FN\Delta$ up to 6.0. Measurements made during the tests were as follows: model speed, hydrodynamic resistance, and trim at towing strut attachment point. Besides, observers visually marked the foremost boundary of the portside twin-hulls wetted keel and at the chine. The information were necessary to predict the wetted area for subsequent full-scale extrapolations by using the Froude method.

Plots in Fig. 7 through 12 demonstrate the interceptor height and their configuration effects in relation to the relative resistance (R/Δ), the trim and the rise of the centre of gravity, at $FN\Delta = 1.8$ and $FN\Delta = 5.6$, corresponding to the hump and design speed of the full-scale vessel, respectively.

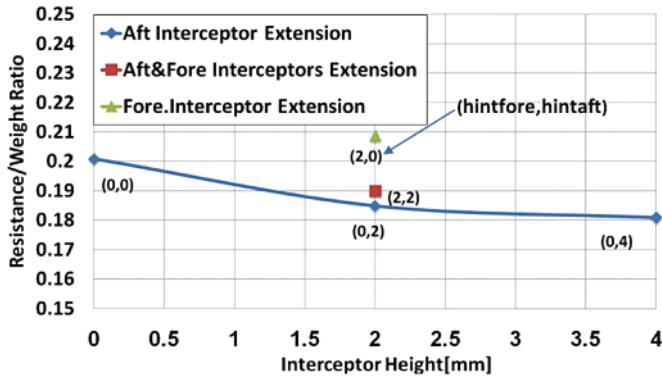


Fig. 7. Variation of the relative resistance with the interceptor height at hump speed

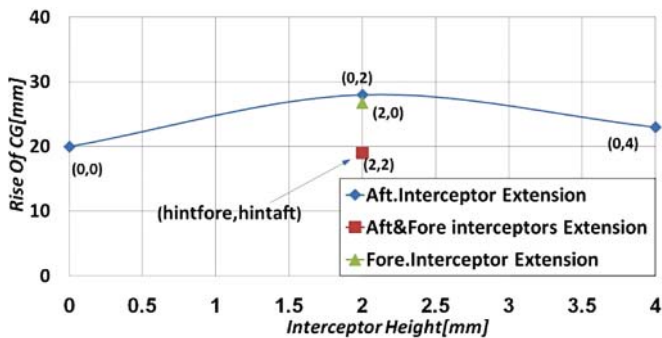


Fig. 8. Variation of the rise of the centre of gravity with the interceptor height at hump speed

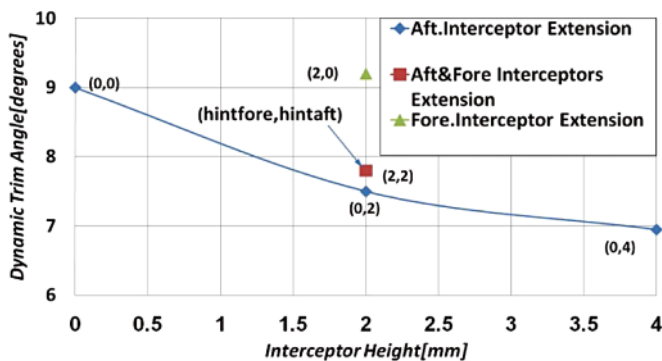


Fig. 9. Variation of the running trim with the interceptor height at hump speed

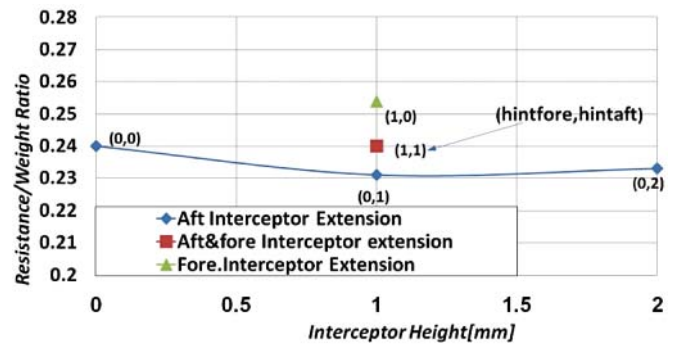


Fig. 10. Variation of the relative resistance with the interceptor height at the design speed

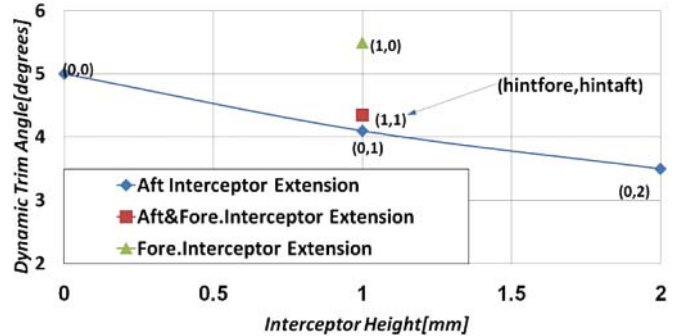


Fig. 11. Variation of the dynamic trim angle with the interceptor height at the design speed

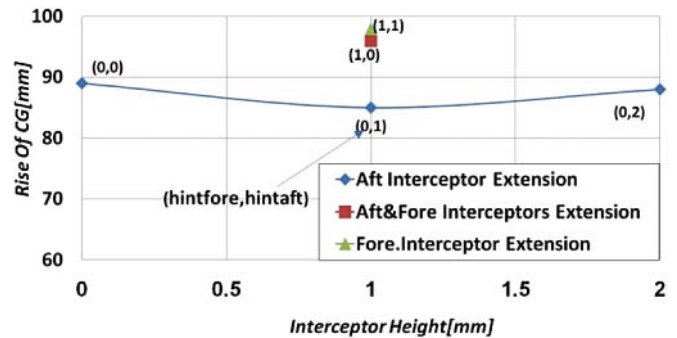


Fig. 12. Variation of the rise of the centre of gravity with the interceptor height at the design speed

A number of observations can be made based on the obtained results:

When the model runs with the hump speed ($FN\Delta = 1.8$), extending only the mid-interceptors by 2 mm (2, 0), $h/L = 0.06\%$, causes a sizeable resistance growth and the model was unable to ride faster than with $FN\Delta = 3.6$ because of the onset of intensive oscillations.

Simultaneous 2 mm extension, ($h/L = 0.06\%$), of both the mid- and stern- interceptors (2, 2) brings a certain decrease in the resistance only at $FN\Delta = 1.8$, whereas at higher speeds the resistance abruptly starts to grow.

Extending only the stern-interceptors by 2 mm (0, 2), $h/L = 0.06\%$, reduces the resistance significantly compared to riding without interceptors at low speeds. Further increasing the interceptor height to 4 mm (0, 4), $h/L = 0.13\%$, had virtually no effect on the resistance at the hump speed. In accordance with this interceptor height setting (0, 4), by increasing the speed the model trim angle and rise of centre of gravity decreased drastically.

During higher-speed tests ($FN\Delta = 4.5 \div 6.0$), interceptor height settings were varied within the range of 1 ÷ 2 mm.

Extending the interceptor height to 1 mm ($h/L = 0.03\%$) for the mid-interceptor only (1, 0), similar to the extending of

interceptors at the both sections to the same height (1, 1), results in increasing resistance at higher speeds.

Extending the interceptor height to 1mm ($h/L = 0.03\%$) at the transom only (0, 1), reduces the resistance at the moderate Froude number values, $FN_{\Delta} = 4.5 \div 5.6$.

Based on the analysis of the obtained results, the most efficient measure in terms of reducing the resistance at the hump and higher speeds was to extend the stern interceptors to 2 mm ($h/L = 0.06\%$). In some cases, the resistance reductions were as much as by $10 \div 12\%$, accompanied by noticeable reduction of trim angle. For the higher speed values ($FN_{\Delta} > 6$), extending the interceptors resulted in a sizeable resistance growth and the model became unstable (started performing intensive oscillating motions), therefore it is not advisable to use the fixed interceptors when the model rides with such high speeds.

MONO-HULL MODEL EXPERIMENTAL PROCEDURE

The 11 m planing mono-hull designed by the authors and selected for the tank-test investigations, has V-shaped cross sections and hard chine. In the present study, all tank tests were performed in the marine laboratory towing tank, Sharif University of Technology, with the dimensions of: 25 m (L) \times 2.5 m (W) \times 1.25 m (D). Its carriage is able to travel at speeds up to 6 m/s (from 0.01 m/s up to 6 m/s with 0.5 m/s step) with the speed measurement accuracy of ± 0.001 m/s. During the tests, the model was fixed against sway and yaw, and free to heave, trim and roll. The 1/15 scale model was made of wood and a special lightweight foam and formed by means of CNC milling machine, followed by special paint spraying procedures to ensure perfect finishing to the hull surfaces. The experimental procedure in general conformed to the ITTC standards, procedures for model making and resistance testing [23, 24]. During the towing tests, the following parameters were measured: speed of the model, total resistance of the model, dynamic trim and dynamic sinkage at the point of towing strut attachment. In addition, the boundary of hull-wetted area was also recorded at each test speed. Principal dimensions of the model are given in Tab. 3.

Tab. 3. Model principal dimensions

Model	Boat	Main particulars
0.73 m	11.0m	Length overall
0.16 m	2.40 m	Beam
2.02 kg	6.83 t	Displacement
5.31 m/s	40 knots	Max speed
0.35 \times Lk measured from transom	0.35 \times Lk measured from transom	Longitudinal position of centre of gravity
15 deg at transom, 18 deg at centre of gravity	15 deg at transom, 18 deg at centre of gravity	Dead-rise angle
Model initial trim = 1.25 deg Model keel wetted length (Lk) = 0.6 m Model chine wetted length (Lc) = 0.4 m Model draught at transom = 0.05 m		

Fig. 13 shows the model hull lines and Fig. 14 presents the model and related instruments in the towing tank.

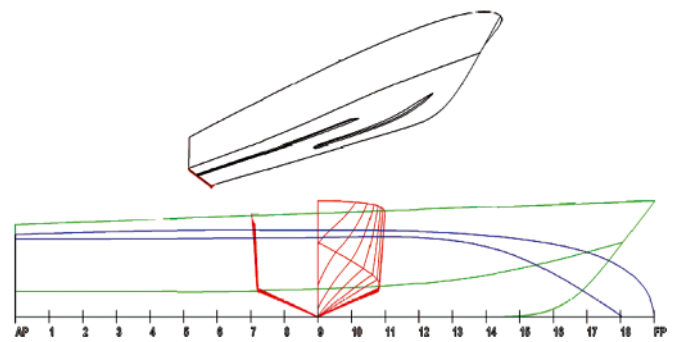


Fig. 13. Monohull model hull lines drawing

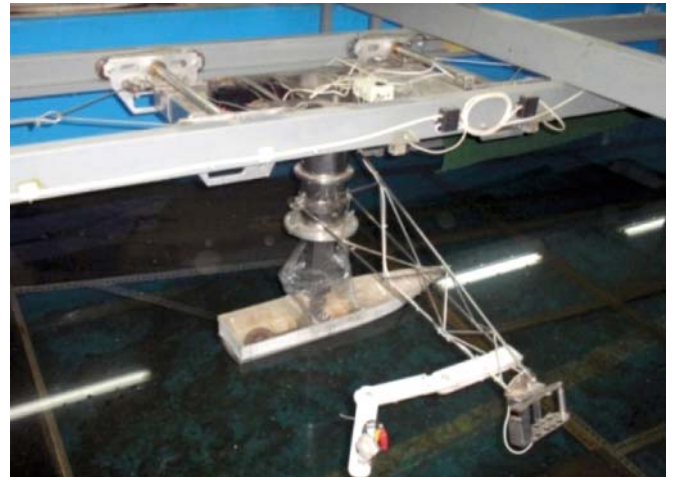


Fig. 14. Model and related instruments in towing tank

Test matrix

The model having 2 kg weight and one relative position of centre of gravity corresponding to $0.35L$ measured from transom, was tested in bare hull condition over a speed range corresponding to full-scale speeds of up to 45 knots. Fig. 15 and 16 show the variation of relative resistance and trim angle along with displacement Froude number, respectively. The stern interceptors of the height $h_{int} = 2$ mm and $h_{int} = 3$ mm were tested. The stern interceptors were mounted to the transom board. The interceptors were made of 4 mm thick special plastic plates attached to transom by means of a special paste.

Details of shape of the interceptor are shown in Fig. 17. Resistance test in calm water was carried out not only with fixed-height interceptors but also with the selected relative position of centre of gravity ($Lcg = 0.35L$), and the model displacement of 2 kg.

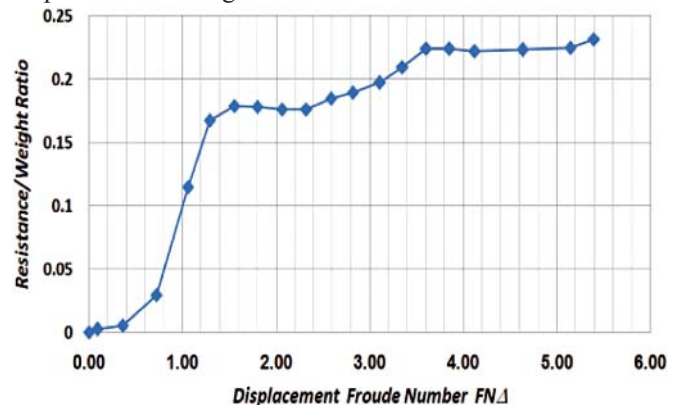


Fig. 15. Variation of the relative resistance with Froude number

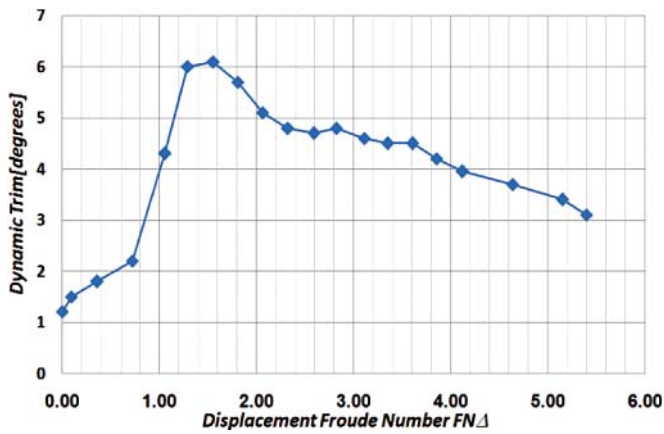


Fig. 16. Variation of dynamic trim angle with Froude number

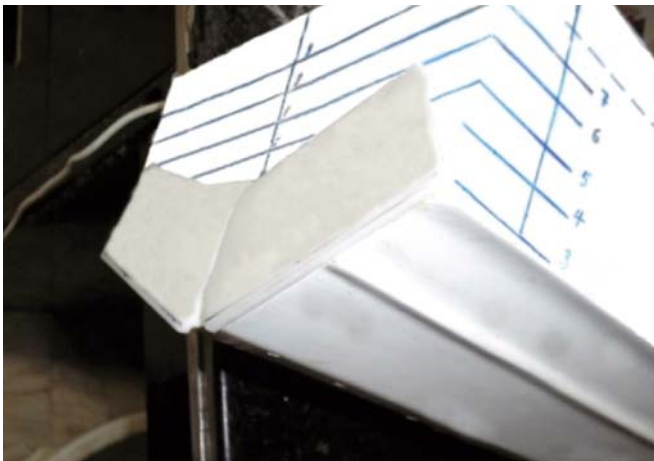


Fig. 17. Details of shape of the interceptor

Results of calm water tests with fixed-height interceptors

During the calm-water tests of the model of the displacement $\Delta = 2$ kg and the centre-of-gravity position $L_{cg} = 0.35L$, the interceptors were located at the transom section, with various height settings. The test was performed for the complete speed range corresponding to the FN_{Δ} values of up to 5.3. Measurements made during the tests were as follows: model speed, hydrodynamic resistance and trim at towing strut attachment point. Besides, observers visually marked the foremost boundary of the portside hull wetted keel and at the chine. The information was necessary to estimate the wetted area for subsequent full-scale extrapolations by using the Froude method. Plots in Fig. 18 through 21 demonstrate the interceptor height and its configuration effects in relation to the relative resistance (R/Δ) and trim at different Froude number values.

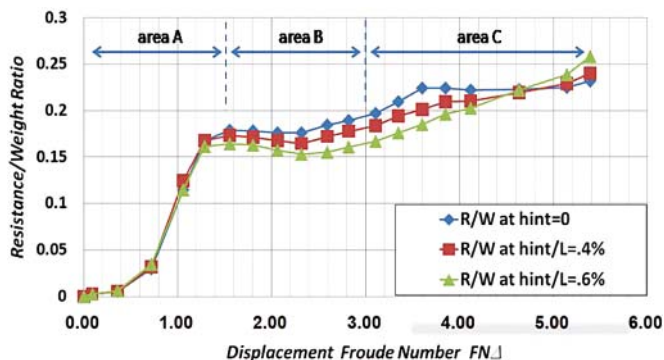


Fig. 18. Resistance test results for two interceptor's height

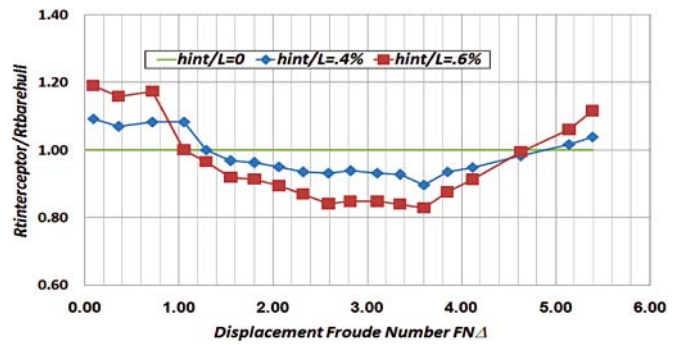


Fig. 19. Drag reduction effect due to 2 and 3mm interceptor

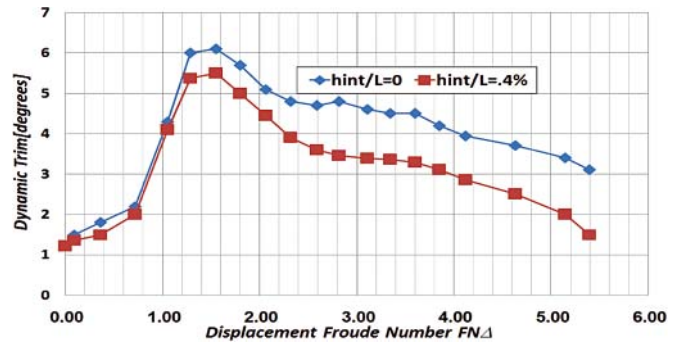


Fig. 20. Dynamic trim test results for one interceptor height

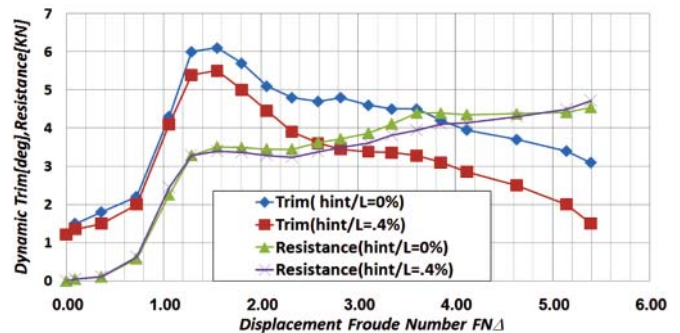


Fig. 21. Variation of the relative resistance and trim with Froude number

A number of observations can be made based on the obtained results:

Based on Fig. 15 it is found that the first resistance hump occurs at $FN_{\Delta} = 1.56$ which corresponds to the maximum running trim angle of 6 deg (Fig. 16), as Fig. 16 shows the running trim at the design speed of 40 kn ($FN_{\Delta} = 4.8$) is equal to 3.7 deg.

Fig. 18 depicts the relative resistance of the model with two different interceptor height values. Fig. 19 illustrates the drag reduction effect compared to the bare hull test results. Fig. 20 shows the effect of the interceptor on running trim. As Fig. 18 shows, the effect of the interceptor on relative resistance of the model is different in terms of Froude number. As shown in Fig. 18 three different areas correspond to various Froude number ranges; each of them can be considered in evaluating the interceptor effectiveness. When the model runs at hump speed (area A, $FN_{\Delta} = 0 \div 1.5$), extending the interceptors by 2 mm, $h/L = 0.4\%$, and 3 mm, $h/L = 0.6\%$ causes a small resistance growth resulted from low lift/drag ratio of the interceptor at such low speed values. When the model runs under transition to planing speed (area B, $1.5 < FN_{\Delta} < 3$), extending the interceptors significantly reduces the resistance compared to riding without the interceptors. Extending the interceptor by 2 mm, $h/L = 0.4\%$, reduces the resistance up to 5.2 %, and extending it by 3 mm, $h/L = 0.6\%$, lowers the resistance by 10.5 % at $FN_{\Delta} = 1.56$. When the model runs

at fully planing speed (area C, $3 < FN\Delta$), extending the interceptors still reduces the resistance of the model, but the sign of the resistance reduction in relation to the interceptor height, is changed at some Froude number depending on the interceptor height. Except that Froude number, extending the interceptor causes a sizeable resistance growth. Tab. 4 shows the percentage of resistance reduction for different interceptor height values.

Tab. 4. Resistance reduction at different interceptor height extension values

Resistance reduction percentage at $h/L = 0.6\%$	Resistance reduction percentage at $h/L = 0.4\%$	Range of $FN\Delta$
8 ÷ 11%	3.3 ÷ 5.5%	1 ÷ 2
15 ÷ 17%	7 ÷ 11%	2.5 ÷ 3.6
17 ÷ 19%	11%	3.6

Extending the interceptor at higher speeds causes a sizeable reduction in running trim, and results in a noticeable resistance growth. As Fig. 19 shows, the increase in resistance occurs at $FN\Delta = 4.7$ for interceptor extension of 3 mm, ($h/L = 6\%$) and $FN\Delta = 5.2$ for interceptor extension of 2 mm, ($h/L = 4\%$), respectively. Then at higher speeds the rate of resistance growth is increased by a rise in the interceptor height. At the design speed of 40 knots, the resistance reduction was as much as 12 % for 2 mm interceptor extension, whereas 3 mm interceptor extension results in increasing resistance. Fig. 20 shows that extending the interceptor by 2 mm, ($h/L = 4\%$) leads to a remarkable reduction in running trim. In fact, the trim reduction is about 10 % when the model rides at the hump speed and about 30 % when the model rides at the design speed.

CONCLUSIONS

The following conclusions can be obtained from the model-test results:

1. Based on the present analysis and achieved results, it is proved that the interceptors can be applied as a highly effective device to reduce the resistance of high-speed planing crafts, and in addition their performance can be improved by appropriate varying, in an integrated manner, Leg and size of the interceptors.
2. Use of the stern- and mid- interceptors can give the remarkable reduction in the resistance and running trim.
3. It is clear from the present study that for higher speeds extending the interceptors involves a sizable resistance growth.
4. As for the catamaran model, the extension of the stern interceptor by 2 mm results in some cases in the resistance reduction of up to 10 ÷ 12 %.
5. As for the mono-hull model, the extension of the stern interceptor by 2 mm results in the resistance reduction of up to 7 ÷ 11 % in some cases, and for its extension by 3 mm the resultant reduction in resistance was up to 15 ÷ 19 %.
6. Performing the experimental studies and developing the mathematical models for evaluating effectiveness of automatically controlled interceptor in calm water and in waves could be valuable future research tasks aimed at making the application of interceptors more effective in whole range of speed and loading conditions.

NOMENCLATURE

- $\delta(x)$ – Turbulent boundary layer thickness [mm]
 R_{ex} – Reynolds number at relative length position

- $h_{int}/L, h/L$ – non-dimensional interceptor height/length ratio
 d/L – non-dimensional turbulent boundary layer thickness
 R/W – resistance/weight ratio

- $FN\Delta$ – displacement Froude number $(\frac{V}{\sqrt{g\nabla}})^{1/3}$

- V – ship speed [m/s]
 ∇ – volume of displacement [m³]
 g – acceleration of gravity in [m/s²]
 Δ – boat or model displacement
 Leg – longitudinal position of centre of gravity as a fraction of boat length, measured from transom.
 h_{ints}, h – interceptor height.
 L – ship or model length.

BIBLIOGRAPHY

1. Wang C.T.: *Wedge Effect On Planing Hulls*, Journal of Hydronautics, Vol. 14, No.4, (1980).
2. Bannikov Yu.M., and Luckashevsky V.A.: *Experimental Investigation Of Lift And Drag Of Planing Plates*, TSAGI Report, Vol. 7, No.1, Moscow, Russia, (1976).
3. Bannikova T.A., Bannikov Yu.M., Luckashevsky V.A., and Zeitlin M.Yu.: *The Investigation Of The Hydrodynamic Characteristics Of The Planing Surface With a Spoiler On The Trailing Edge*, TSAGI Report No. 1908, pp.1÷22, Moscow, Russia, (1978).
4. Savitsky D.: *Hydrodynamic Design Of Planing Hulls*, Journal of Marine Technology, Vol. 1, pp.71÷95, (1964).
5. Brown P.W.: *An Experimental And Theoretical Study Of Planing Surfaces With Trim Flaps*, Stevens Institute of Technology, Davidson Laboratory Report No. 1463, (1971).
6. Savitsky D., and Brown P.W.: *Procedures For Hydrodynamic Evaluation Of Planing Hulls In Smooth and Rough Water*, Journal of Marine Technology, Vol.13, No.4, pp. 381÷400, (1976).
7. Tsai J., and Huang J.K.: *Study On The Effect Of Interceptor On High Speed Craft*, Journal of The Society of Naval Architects and Marine Engineering, Vol.22, No. 2, pp. 95÷ 101, (2003).
8. Tsai J., Hwang J., and Chou S.: *Study On The Compound Effects Of Interceptor With Stern Flap For Two Fast Monohulls With Transom Stern*, Proceedings of the 7th International Conference on Fast Sea Transportation, Fast 2003, Ischia, Italy, pp.23÷28, (2003).
9. Krylov Shipbuilding Research Institute (KSRI): *a Radically New System For High Speed Ship Motion Stabilization And Speed Increase Based on Automatically Controlled Interceptors*, KSRI Report, St.Petersburg, Russia, (2002).
10. Krylov Shipbuilding Research Institute (KSRI): *Evaluation of Effectiveness of Automatically Controlled Interceptors for Decrease of Oscillations of High Speed Catamaran*, KSRI Report, St.Petersburg, Russia, (2004).
11. Dawson D., and Blount D.: *Trim Control*, Professional Boat builder, No. 75, (2002).
12. Karimi M.H.: *Hydrodynamic Quality Improvement Techniques For High Speed Planing Crafts*, Proceeding of 7th Conference on Marine Industries, Tehran, Iran, (2006).
13. Brizzolara S.: *Hydrodynamic Analysis Of Interceptors With CFD Methods*, Proceedings of The 7th International Conference on Fast Sea Transportation, Fast 2003, Ischia, Italy, pp.49÷56, (2003).
14. Molini A., Brizzolara S.: *Hydrodynamics Of Interceptors: a Fundamental Study*, Proceeding of the International Conference on Marine Research and Transportation, ICMRT 2005, Vol.1, Ischia, Italy, (2005).
15. D. Villa., Brizzolara S.: *a Systematic CFD Analysis Of Flaps/ Interceptors Hydrodynamic Performance*, Proceeding of 10th International Conference on Fast Sea Transportation, Fast 2009, Athens, Greece, pp.1032÷1038, (2009).
16. Hansvic T., and Steen S.: *Use Of Interceptors And Stepped Hull To Improve Performance Of High Speed Planing Catamaran*,

- Proceeding of International Conference on High-Speed Craft-ACV's, WIG's and Hydrofoils, London, UK, (2006).
17. Steen S.: *Experimental Investigation Of Interceptor Performance*, Proceeding of 9th International Conference on Fast Sea Transportation, Fast 2007, Shanghai, China, pp. 237÷244, (2007).
 18. Allema J.: *Intercepting The Interceptors*, MARIN Report No. 86, pp.6÷7, (2005).
 19. Fridman G. M., Rozhdestvensky K.V., and Shlyakhtenko A.: *Theory And Practice Of Application Of The Interceptors On High Speed Ships*, Proceeding of 9th International Conference on Fast Sea Transportation, Fast 2007, Shanghai, China, pp. 214÷236, (2007).
 20. Syamsundar S., and Datla R.: *Performance Prediction Of High Speed Planing Craft With Interceptors Using a Variation Of The Savitsky Method*, Proceedings of the first Chesapeake Power Boat Symposium, Annapolis, Maryland, USA, (2008).
 21. Day A.H., and Cooper C.: *An Experimental Study Of Interceptors For Drag Reduction On High Performance Sailing Yachts*, Ocean Engineering, Vol. 38, pp.983÷994, (2011).
 22. Schlichting H.: *Boundary Layer Theory*, seventh Ed. McGraw-Hill Inc- New York, (1979).
 23. ITTC 2002.: *Model Manufacturing Ship Models*, 23rd International Towing Tank Conference, (7.5-01-01-01), pp.1÷6, Revision-01, (2002).
 24. ITTC 2002.: *Testing and Extrapolation Methods for High Speed Marine Vehicles Resistance Test*, 23rd International Towing Tank Conference, (7.5-02-05-01), pp.1÷18, Revision-01, (2002).
 25. *Interceptor Guide*, retrieved from <http://www.humphree.com/>, March 15, 2011.

CONTACT WITH THE AUTHORS

Mohammad Hosein Karimi, Ph.D. Student,
 Mohammad Saeed Seif, Prof.,
 Madjid Abbaspoor, Prof.,
 Center of Excellence in Hydrodynamics
 and Dynamics of Marine Vehicles,
 Department of Mechanical Engineering,
 Sharif University of Technology, IRAN
 e-mail: seif@sharif.edu

Wake-blade interaction in steam turbine stages

Jerzy Świryczuk, Prof.
Institute of Fluid-Flow Machinery, Gdansk, Poland

ABSTRACT



The article discusses the phenomenon of stator *Wake/Rotor* cascade (*W/R*) interaction in a steam turbine stage, and the ability to capture it in turbine stage design calculations making use of standard numerical codes. Firstly, the *W/R* interaction is analysed by comparing its real, experimentally recorded course with the numerical results obtained using vortex theory models and methods. This part of the analysis ends with formulating a conclusion about stochastic nature of the *W/R* interaction and indicating its reason, which is the vortex structure of the stator wake. Next, a question is discussed whether and how this stochastic nature of the examined phenomenon can be taken into account in calculations of Reynolds Averaged Navier-Stokes (*RANS*) equations. Differences are indicated between the uniform pattern of the stator wake obtained using a *RANS* code and the vortex structure of the real wake. It is concluded, however, that despite these differences the *RANS* results correctly reflect the time-averaged course of the real *W/R* interaction, and the process of averaging the flow parameters on the sliding plane between stator and rotor calculation areas can be treated as sort of “numerical averaging” of different realisations of the *W/R* interaction.

Key words: turbine passage; secondary vortices; stochastic behaviour; CFD calculations

SECONDARY VORTEX STRUCTURES IN A TURBINE ROW

Steam turbines are widely used in shipbuilding industry as the main engines on ships which need huge driving power (large super-tankers, for instance), or the nature of their operation is characteristic for long-distance sailing without calling at a harbour (ice-breakers or marine submarines with nuclear propulsion systems). Permanent competition between turbine producers forces them to offer high-quality and high-efficiency products, the working characteristics of which are to be presented to the buyer at an earliest possible stage of negotiations. These characteristics are to be calculated very precisely, as delivering the product which does not meet parameters named in the contract would result in fines paid by the producer. On the other hand, when the sold turbine reveals the real power output or efficiency much higher than that declared in the offer, it means an extra bonus for the buyer, or, looking from the other side, loss for the seller who could have sold it for a higher price. That is why steam turbine designers attempt to calculate basic turbine parameters very accurately, taking into account as many factors as possible. One of these factors which were given special attention in recent years is the effect of interaction of the secondary vortices forming in turbine blade stator and rotor passages on the level of the generated stage loss.

The flow through a steam turbine stage is extremely complex, Fig. 1 [1]. Even in high pressure stages of relatively simple radial geometry in which the flowing superheated steam has physical properties close to those of the perfect gas, a number of secondary vortices, both forming in stator or rotor cascades and approaching from upstream rows, can be observed. Looking from the cascade front, two pairs of horseshoe vortices 1 and 2 are formed at the leading edge of each blade, one pair near the hub endwall and one near the tip endwall. Then, inside the rotor passage these vortices mix, partially or entirely, with the passage

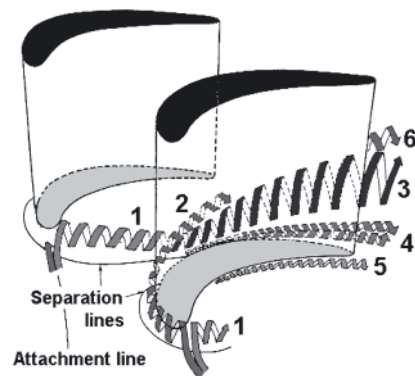


Fig. 1. Secondary flow structure in turbine stage: 1, 2) pressure and suction side horseshoe vortices, 3) passage vortex, 4, 5) suction and pressure side corner vortices, 6) trailing shed vortex

vortices 3 generated by the passage cross flows. In the corners between the blade hubs, or tips, and the passage endwalls, the action of the passage vortices leads to the formation of corner vortices 4 and 5. The rear parts of the stator and rotor blades are the sources of wakes which shed from their trailing edges and move downstream into next turbine parts. The interaction of the passage vortex with the blade trailing edge is believed to be a source of a so-called trailing shed vortex 6, having the rotation opposite to that represented by the passage vortex [2]. Flow separations, occasionally observed at rotor blade surfaces, can lead to the creation of large-scale vortices of various orientations. And last but not least, leakage flows over the blade tips in the rotor cascades usually generate characteristic vortex structures the intensity of which depends on the adopted type of sealing systems.

The scale and direction in which the interaction of all above vortices affects turbine performance parameters is not clear. Generally it is assumed that neglecting this phenomenon leads to underestimation of stage losses [3], but opinions can also be found that in some cases the presence of vortex structures improves the stage performance by periodical sweeping out the stagnation areas.

Although extremely complex, the abovementioned vortex interaction in a steam turbine stage can be successfully analysed using Computational Fluid Dynamics (CFD) codes which solve the Reynolds Averaged Navier-Stokes (RANS) equations in computational domains of arbitrary geometry. It should be stressed, however, that these CFD calculations require extremely fine grids to take into account the widest possible range of small-scale vortices. A commonly accepted approach here is to perform the calculations in the geometry consisting of one stator and one rotor passage in combination with special procedures taking into account the relative rotor/stator motion when passing the flow field parameters between these two computational domains. The assumption which is believed to justify this approach is that all unsteady phenomena take the identical course in each stator and each rotor passage.

However, there is one exception to this assumption, which is the interaction of the wakes shedding from the stator blade trailing edges with the downstream rotor blade cascades, the W/R interaction. A detailed analysis of this phenomenon and its effect on the turbine stage design process is the basic subject of this article, which synthesises the experience gained by the author in this area over the recent decade. Due to the lack of reliable experimental data on W/R interaction coming from marine steam turbines, in order to keep the geometrical and physical conditions of the analysis within realistic regimes the geometry of the cascade used in the analysis was assumed identical with the midspan cross-section of a real HP impulse turbine rotor in

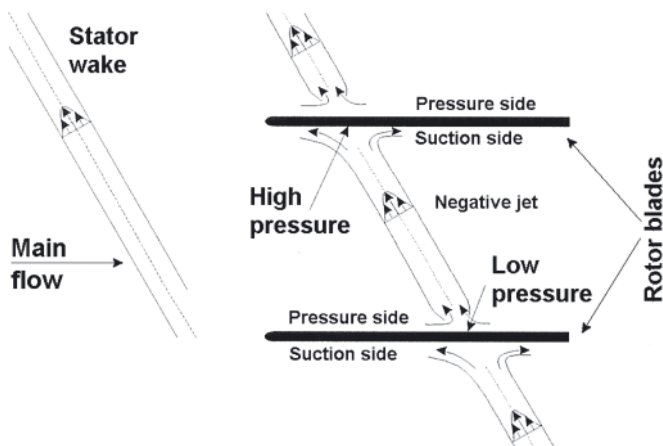


Fig. 2. Negative jet concept of wake model

operation in one of inland power plants in Poland. The selected parameters of the flow through the rotor cascade were also taken from the measurements performed in this turbine. The conclusions resulting from the presented analysis are valid for both inland and marine applications of steam turbines.

WAKE MODELLING

In the past, the wakes shedding from turbine blades were modelled in various ways depending on a current state of knowledge on the phenomenon. In one of the first models proposed by Meyer in 1958 [4] the wake was represented by a regular band of velocity deficit, a so-called “negative jet”, immersed in the otherwise uniform flow, Fig. 2. The stator wakes were transported with the main flow and chopped into linear segments by the rotor blades. Within the rotor passage the wake segments, keeping their linear shapes, generated secondary velocity fields responsible for fluid transport from the pressure side to the suction side of the passage.

Due to a very simplified geometry assumed for both the stator wake and the rotor blades, the Meyer’s model could not take into account any possible deformation of the stator wake on its way through the rotor. However, as was noticed by Smith [5], the velocity difference between the rotor blade pressure and suction sides in a real turbine row makes the opposite ends of the wake segment move with different velocities, which leads to stretching and shearing of the entire segment. Consequently, when the wake leaves the rotor, its structure resembles a saw rather than the initial linear and continuous shape.

Taking into account the wake deformation was only possible after the development of computer technology and the appearance of CFD codes which solve the fluid flow equations in two and three dimensions. Initial attempts to capture the wake deformation based on the potential flow model with a continuous vortex layer of changing intensity shed from the blade trailing edge, which was an adaptation of the classical Prandtl’s concept of unsteady flow over an airfoil [6] to the cascade geometry [7, 8]. Once shed to the flow, successive wake segments moved with local flow velocities through the rotor cascade, thus making a further contribution to unsteady flow effects in this area, Fig. 3. Instantaneous intensities of the vortices, being the response to changing flow conditions in the vicinity of blade trailing edges, were calculated from a set of integral equations.

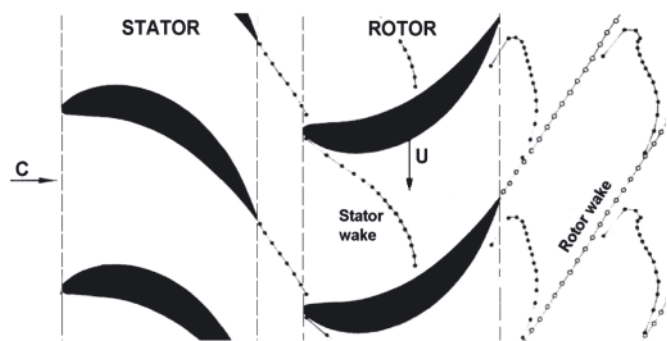


Fig. 3. Vortex wake model

It is noteworthy that despite a discrete representation, the wakes in these models were still interpreted classically as continuous bands of fluid in otherwise inviscid and incompressible flow, with the velocity deficit changing uniformly along the wake axis.

More advanced studies of the stator wake behaviour in the rotor cascade were possible using specialised 3D codes developed to solve RANS equations for turbulent, compressible, and viscous flows through fluid-flow machines.

In the calculations performed with the aid of those codes the stator wakes were obtained as part of the solution and their characteristics did not have to be assumed *a priori*. The RANS codes enabled studying numerous aspects of W/R interaction, including wake deformation [9], profile losses [10], unsteady heat transfer [11], boundary layer transition [12], pressure fields and blade load fluctuations [13], etc. Experimental verification of the obtained results was, generally, good – at the level determined by the accuracy and resolution of the measuring devices used in those times.

The initial calculations performed with the aid of 3D RANS codes made use of grids of relatively moderate resolution. As a result, the generated wakes had the forms of regular layers of increased entropy and decreased flow velocity, without visible traces of inner structure, Fig. 4. However, the experiments oriented on taking more detailed insight into the stator wakes revealed clear frequencies in the signals recorded in the wake area, which testified to the presence of regular fine vortex structures in there [14, 15]. More recent numerical computations performed for isolated stators using sufficiently fine grids and time steps also produced wake patterns in which two rows of well developed vortices having the structure similar to that of the von Karman vortex street was observed [16 ÷ 19]. In this context, a question should be raised about the consequences brought by the presence of active vortices in the wake to conventional CFD analyses making use, as a rule, of RANS codes as basic tools.

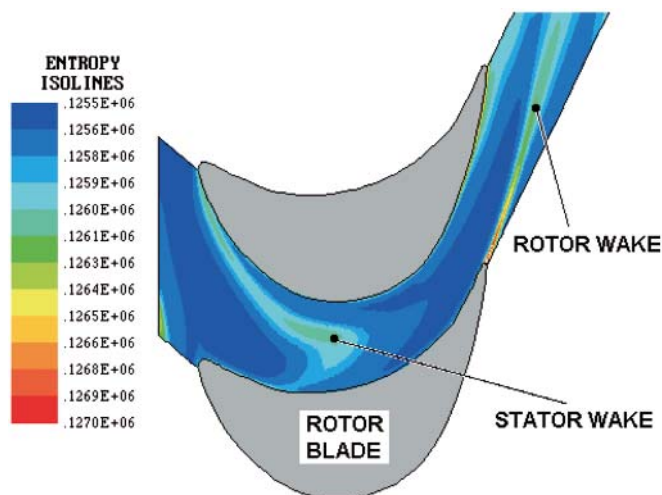


Fig. 4. Stator wake deformed inside the rotor passage – NS calculations

VORTEX STRUCTURE OF THE WAKE AND ITS CONSEQUENCES

Analysing numerically the development and interaction of the vortex stator wake with the rotor cascade is much more difficult than in case of all other secondary structures described in section 1. Particular wake segments chopped off by the rotor blades do not have, in general, the same characteristics, i.e. do not consist of vortices of identical strengths and positions at the time of chopping. And any differences in the initial structure of the chopped-off wake segment result in inevitable differences in its further motion through the rotor passage. Unlike the passive band-like wakes observed in conventional CFD calculations, the sample of which is shown in Fig. 4, active vortices interact both with each other and with the boundaries, which makes their trajectories differ from those estimated on the basis of pure main flow convection.

The initial arrangement of the vortices in the wake segment at the time of chopping-off by the rotor blade may be described

using a so-called phase shift, φ , which defines the range of displacement of the von Karman vortex structure along the wake axis. The definition of the phase shift is shown in Fig. 5 where it is interpreted as the ratio of the distance s between corresponding vortices in two different von Karman wake vortex segments a and b to the distance l between two adjacent vortices of the same rotation in one segment.

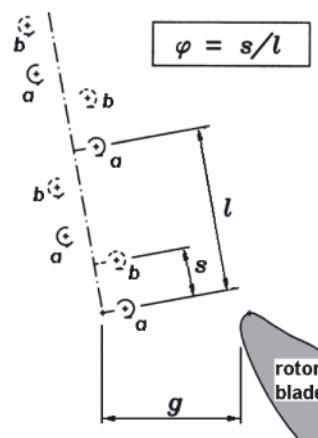


Fig. 5. Phase shift in the stator wake vortex arrangement

The above aspect of the W/R interaction cannot be effectively analysed using a NS code. Due to possible differences in phase shifts of the particular chopped-off wake segments we cannot assume any longer that their behaviour inside each rotor passage is the same. Consequently, to capture the complete W/R interaction and its effects we should generate a computational grid covering all stator and rotor blade passages. And what is even more challenging, this grid should be fine enough to detect and study the behaviour of such small structures as the wake vortices. Keeping in mind that the number of passages in the stator or rotor row can exceed a hundred in a real turbine, the creation of a sufficiently fine grid in those circumstances is beyond capabilities of even most powerful computing centres.

That is why studying vortex related aspects of the W/R interaction needs a flow model which would take into account the differences between vortex arrangements in individual wake segments. The model applied in the present study makes use of the Vortex Dynamics Theory (VDT) which defines principles of motion of vortices in multiply connected regions [20]. Along with the ability to model arbitrary phase shifts of the wake vortex configurations, VDT provides several invariants of vortex motion which can be used as additional tools to increase the accuracy of flow calculations. The here applied VDT model bases on the 2D potential flow through an infinite cascade of blades, with the wake represented by vortex singularities. Unlike the earlier works making use of the vortex model [7, 8], in the present study each singularity represents an individual coherent vortex.

FLOW MODEL

A procedure which is frequently applied in studying unsteady vortex phenomena bases on generating, step by step, a series of instantaneous vortex configurations to illustrate the course of the phenomenon. In this procedure each previous configuration is used as the input data for calculating the next one. Therefore of crucial significance for the accuracy of the final result is the accuracy with which transient configurations are calculated.

In most typical vortex model applications in blade flow analyses the shape of the blade is modelled using a sequence

of discrete vortices representing the bound vorticity distributed along the blade contour - see, for instance, Basu and Hancock for a single profile [21], or Lienhart [7], and Kramer [8] for a cascade. The above blade description can be a source of relatively large inaccuracy in evaluating instantaneous velocities of free vortices, especially those moving close to the blade contour. To reduce this inaccuracy, the present study makes use of conformal mapping [22] and the circle theorem based inversion technique [23] which move all singularities used for defining the blade shape off the boundaries, thus creating a continuous and regular velocity field in the entire flow area. A detailed procedure of constructing the stream function for a system of blades in various configurations can be found in Refs. [24 ÷ 28]. The accuracy of the solutions obtained using the conformal mapping is believed to converge asymptotically to the accuracy of the analytical solutions.

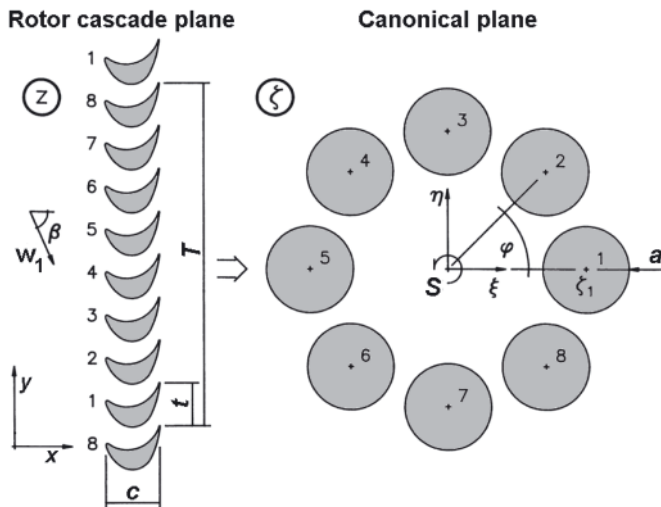


Fig. 6. Infinite blade cascade mapped into a circular cascade of circles

The mapping function used in the present analysis maps a K -element segment of an infinite linear cascade of blades into a circular cascade of K circles, Fig. 6. A general formula for this function has the form of an infinite fraction series [22]:

$$z = \frac{T}{2\pi} \ln \left[\zeta + \sum_{k=1}^K \sum_{n=1}^{\infty} C_n e^{i(n+1)(k-1)\phi} \left(\frac{a}{\zeta - \zeta_1 e^{i(k-1)\phi}} \right)^n \right] \quad (1)$$

The number K of the blades composing the transformed cascade segment can be chosen arbitrarily. The resultant length of the cascade segment is $T = tK$, where t is the cascade pitch. In numerical applications the infinite sum of mapping coefficients is reduced to a limited number, N , the choice of which compromises between the required accuracy and the available computation time. Unknown parameters in Eq. (1) are the centre of the first circle ζ_1 , the circle radius a , equal for all circles, and a series of complex coefficients C_n . For the analysis performed in the rotor reference frame these parameters are to be calculated once in the entire flow calculation process.

In the canonical plane, ζ , the parallel flow transformed from the rotor cascade plane, z , is represented by the source Q_r and the vortex Γ_r located at the origin S . The strengths of these two singularities are related with the assumed inlet flow velocity, w_1 , and inlet flow angle, β , in the physical plane and are calculated as:

$$\Gamma_r = \frac{w_1 T}{2\pi} \cos \beta \quad (2)$$

for the vortex and:

$$Q_r = \frac{w_1 T}{2\pi} \sin \beta \quad (3)$$

for the source.

A general formula for the complex flow velocity in the canonical plane ζ is also given in the form of a fraction series [22]:

$$\bar{v}(\zeta) = \frac{Q_r - i\Gamma_r}{\zeta} - \sum_{l=1}^L \sum_{s=1}^S \left[\frac{i\Gamma_0}{\zeta - \zeta_{s,l}^+} - \frac{i\Gamma_0}{\zeta - \zeta_{s,l}^-} \right] + \sum_{k=1}^K \sum_{w=1}^W \frac{i\Gamma_{w,k}}{\zeta - \zeta_{w,k}} + \sum_{k=1}^K \sum_{n=1}^N D_{k,n} \left(\frac{a}{\zeta - \zeta_k} \right)^n \quad (4)$$

Here $D_{k,n}$ are unknown complex coefficients calculated from the system of equations expressing the condition of zero normal velocity along the entire contour of each blade, and zero tangent velocity at circle points corresponding to the blade trailing edges. These coefficients represent the reaction of the circles to both steady and unsteady flow components. S is the number of pairs of vortices in a single stator wake, and Γ_0 is the strength of the positive vortex in the stator wake, a significant parameter in the present study. $\zeta_{s,l}^+$ and $\zeta_{s,l}^-$ are instantaneous locations of the positive and negative vortex, respectively, in the l -th stator wake. W is the number of vortices in one rotor wake and $\zeta_{w,k}$ is an instantaneous location of the rotor wake vortex generated in the w -th step downstream of the k -th blade. All those parameters are to be calculated at each step of computation.

The flow velocities calculated in the canonical plane are transformed to the physical plane using the formula [22]:

$$v(z) = \frac{v(\zeta)}{\frac{dz}{d\zeta}} \quad (5)$$

where $dz/d\zeta$ is calculated from Eq. (1).

The velocity v_i of the i -th vortex situated at point ζ_i in the canonical plane (here i stands for all indices of both stator and rotor vortices) can be calculated from Eq.(4) using the Helmholtz and Kirchhoff's principle that the vortex does not act upon itself [23]:

$$\bar{v}_i(\zeta_i) = \bar{v}(\zeta_i) - \lim_{\zeta \rightarrow \zeta_i} \frac{i\Gamma_i}{\zeta - \zeta_i} \quad (6)$$

The vortex velocities are transformed from the canonical plane to the physical plane using the formula [23]:

$$\bar{v}_i(z_i) = \bar{v}_i(\zeta_i) / \frac{dz}{d\zeta} \Big|_{\zeta_i} - \frac{i\Gamma_i}{2} \frac{d^2z/d\zeta^2}{[dz/d\zeta]^2} \Big|_{\zeta_i} \quad (7)$$

The derivatives in Eq. (7) are calculated from Eq. (1).

In the VD Theory, the strengths and initial positions of the wake vortices are to be assumed a priori based on the available information on the examined flow, including in particular the scale of the velocity deficit generated by the wake and the width of the wake. Unfortunately, the literature on the subject gives little and rather incomplete data on the inner structure and strength of the vortex wakes in any turbine stages. In this situation, in order to obtain the wake characteristics which could be considered reliable and representative for the examined turbine flow, in the reported study the initial wake

parameters were reconstructed from preliminary 3D RANS calculations done using a specialised code FlowER for the stage being the prototype for the rotor geometry examined in the present study.

STEADY FLOW TESTS

Before the basic part of the analysis, the applicability of the VDT flow model to the examined phenomenon of vortex interaction inside the turbine rotor passage was checked on a series of comparison tests performed using the results of the FlowER calculation as the reference.

The first test consisted in comparing the velocity distributions inside the rotor passage obtained using the potential flow model, without vortices, and FlowER. The input data for the potential flow calculations were the rotor inlet velocity w_1 , and angle β , computed by FlowER and averaged at the rotor inlet mid-span. The results of the test are shown in Fig. 7 as velocity modulus and angle distributions in selected passage sections located at: $x/c = -14.85\%$, 25.73% , 66.52% and 101.68% from the rotor blade leading edge. Bars in the diagrams represent the FlowER data, while the points located close to their tops stand for the results obtained using the potential flow model. The presented data well match each other, except for the rotor blade boundary layer near the blade suction side and the rotor wake where the viscous effect are dominating.

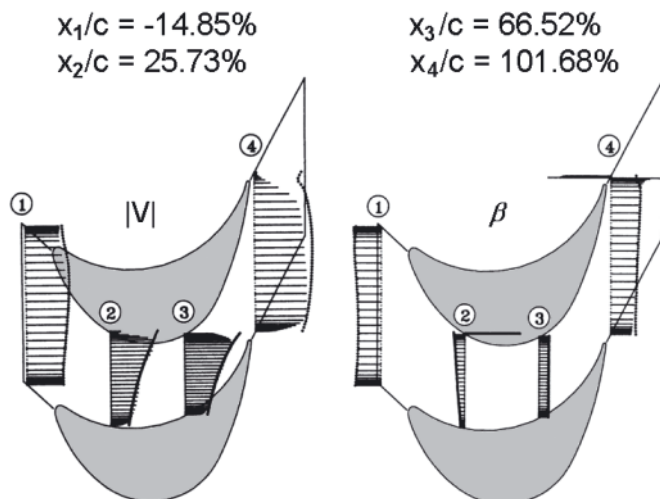


Fig. 7. Distributions of steady flow velocity modulus (left) and angle (right) in rotor passage

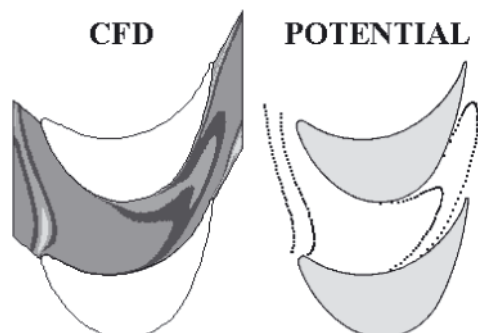


Fig. 8. Stator wake deformation in the rotor passage: 3D CFD midspan solution (left) and potential flow model (right)

The second test was oriented on comparing instantaneous images of wakes computed by FlowER with those obtained using the potential model. A sample FlowER wake is shown in Fig. 8 (left). The corresponding potential model of the passive wake, $\Gamma_0 = 0$, was generated by placing two parallel lines of fluid particles upstream of the rotor and then allowing them

to move with the flow through the rotor. Two instantaneous locations of these pairs of lines, selected so as to correspond to the wake locations generated by FlowER, are shown in Fig. 8 (right). The agreement between the both curves is surprisingly good, bearing in mind complex structure of the flow in a turbine stage. These two tests testify to good credibility of the potential model to determine accurately the velocity fields inside the rotor passage, and thus to create a realistic pattern of the wake motion through it.

THE W/R INTERACTION

Following the standard procedure mentioned in the section entitled Flow model the course of the stator wake/rotor cascade interaction was studied by calculating a sequence of instantaneous flow patterns showing current distributions of stator wake vortices inside the rotor passage. The input parameters for these calculations were: the inlet flow velocity w_1 , the inlet flow angle β , and the strengths of the stator vortices Γ_0 . The main variable parameter of the study was the phase shift factor, φ , defined in Fig. 5 (the basic distribution of the wake vortices, corresponding to $\varphi = 0.0$, is labelled "a" in this figure).

Figure 9 shows a selection of these flow patterns covering one period of wake passing. The flow is from left to right. Stator wake vortices are represented in the diagrams by small circles, green and red for the positive – counter-clockwise and negative – clockwise rotation, respectively. Black circles downstream of the rotor blades mark initial segments of the rotor wake. The diagrams also include two sequences of small black dots representing hypothetical positions of the stator wake vortices in case they moved passively with the potential flow velocity, like the fluid particles in Fig. 8, right.

In the initial diagram, step N, the wake has just approached the cascade and is being cut apart by the blade. So far the only noticeable effect of activity of the vortices is the reduced velocity of their motion, compared to the potential flow velocity (compare the positions of the active vortices and the corresponding passive dots). The reduced velocity of motion of the von Karman vortex street in the flow, resulting from an additional velocity component induced by the street on itself, was first proved, both theoretically and experimentally, by von Karman [32], and its presence here testifies to the correctness of wake motion modelling. The next diagrams, steps $N + 0.2T$ and $N + 0.4T$, show early stages of wake deformation. Negative vortices composing the central part of the wake segment are accelerated, while those situated close to its end are decelerated. An opposite tendency is observed in the motion of the positive vortices. As a result, the outer vortices of the two rows come closer to each other while the central ones become more distant. All this leads to noticeable segregation of vortices representing different rotation signs, with their further motion in two nearly isolated groups, visible in the final diagrams, steps $N + 0.6T$ and $N + 0.8T$. Of these two groups, only the second group of vortices moves approximately with the velocity predicted by FlowER for the entire wake, while the first group moves faster, contributing to the growing rate of deformation of the inner structure of the wake.

Beside the basic variant, $\varphi = 0$, the study included three more variants of wake vortex distribution, which were denoted by phase shifts, φ , equal to 0.25, 0.5, and 0.75. The above described segregation of a one-sign vortices and their further motion in nearly isolated groups were recorded in all cases. The most spectacular differences were observed in the motion of the vortices located close to the cut-off area. These vortices took visibly different trajectories, which in extreme cases led to the separation of isolated vortices from the wake.

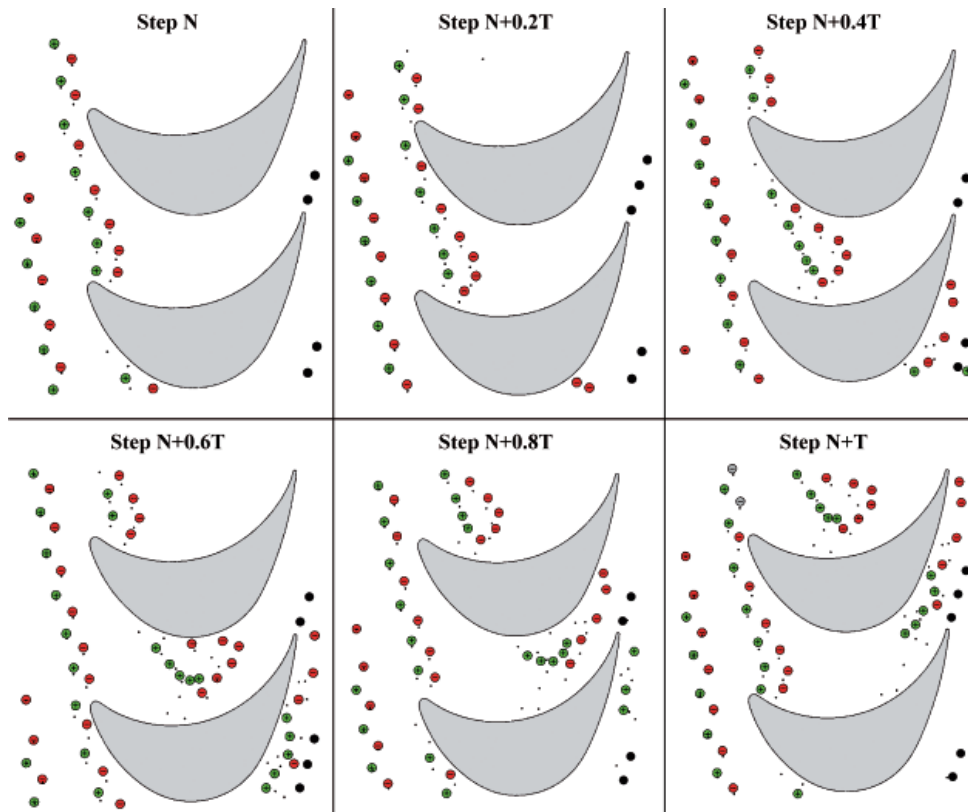


Fig. 9. Stator wake deformation in the rotor passage: $\Gamma^* = 0.005$; $\varphi = 0.0$

Characteristic wake configurations with isolated vortices are shown in Fig. 10.

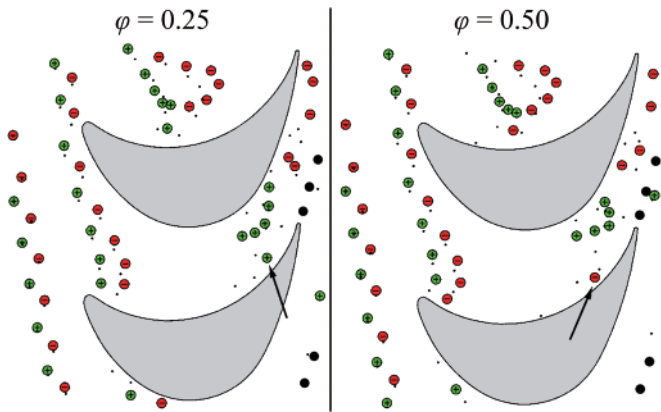


Fig. 10. Extreme cases of wake deformation. Step $N+T$: separation of isolated positive vortex (left) and negative vortex (right)

The above result prove and clearly illustrate the existence of mechanisms in the flow which make the same stator wake behave in a different way in the rotor passage only because of a different phase shift in the initial vortex distribution. In real wakes this distribution may be generally assumed a stochastic parameter, as for the time being, there is no evidence which would link the timing of the generation of stator wake vortices with the relative stator-rotor location. That means that consecutive segments of the same wake shed from a stator blade may behave in a different way in corresponding rotor passages. Or, in other words, **consecutive segments of identical wakes shed from consecutive identical stator blades may behave in a different way in one and the same rotor passage.**

NUMERICAL AND EXPERIMENTAL VALIDATION

The best way to validate the correctness of the above presented VDT results would be to compare them with the experiment, preferably performed in the same geometrical and flow conditions. Unfortunately, this way of validation is not possible in the present case, as the examined stage was

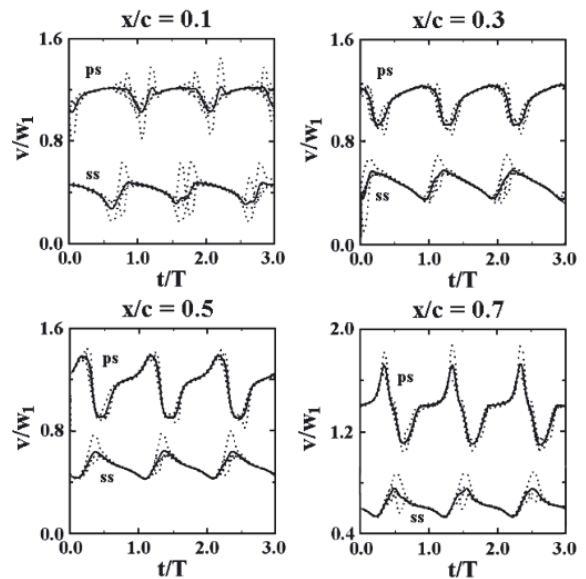


Fig. 11. Velocity fluctuations calculated for the passing vortex wake at selected points inside the rotor passage: *dashed lines* – individual realisations, *continuous line* – averaged realisation; *ps, ss* – rotor blade pressure and suction side, respectively

part of a real turbine in operation in a Polish power plant. Instead, an indirect method was applied which made use of the data recorded in other, but qualitatively similar conditions. It is noteworthy that despite a relatively large number of both numerical and experimental studies on W/R interaction which were recently published, finding appropriate data in which the wake development analysis goes as deep as to the vortex structure of the wake was extremely difficult. The most comprehensive and most valuable analysis from the point of view of the present validation was published by Kost et al [33]. Its authors presented the results obtained in a single-stage model turbine in the form of time-histories of velocity fluctuations recorded at points located inside the rotor passage

at selected dimensionless distances x/c from the rotor blade leading edge and at a distance equal to $1/16$ of the rotor pitch from the blade surface, slightly off the rotor blade boundary layer. The experimental time-histories of velocity fluctuations presented by Koch et al. were averaged over 20 realisations. To provide better conditions for comparison, the VDT curves were also averaged, this time over 4 available realisations of the phase shift, $\varphi = 0.00, 0.25, 0.50$ and 0.75 , as shown in Fig. 11 in which the dashed lines represent individual realisations while the continuous lines show the result of averaging.

Figure 12 compares the averaged VDT curves from Fig. 11 with the time-histories presented by Kost et al. Due to different steady-flow velocity levels, the curves shown in the diagrams

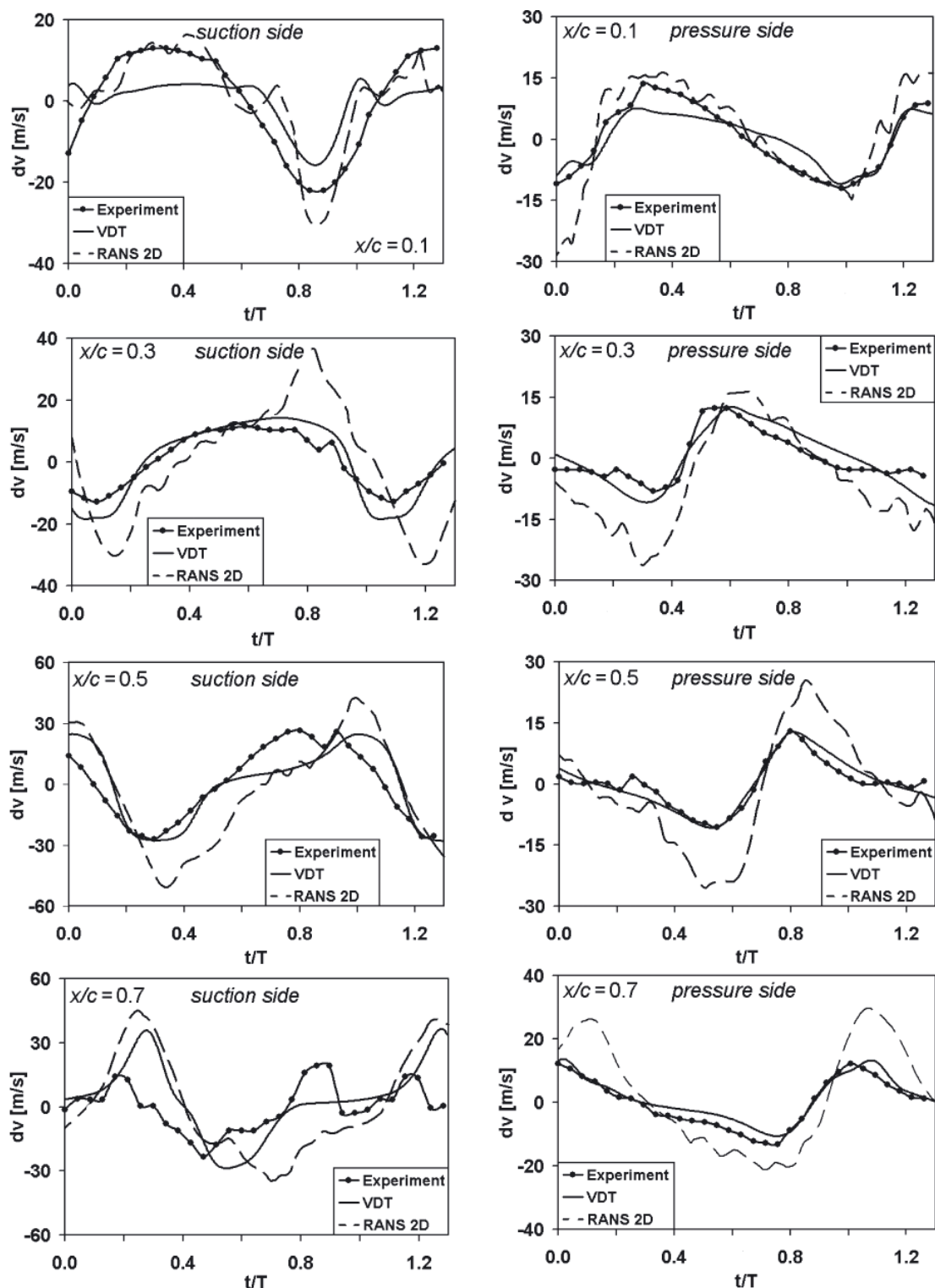


Fig. 12. Velocity fluctuations inside the rotor passage: numerical results vs. experiment

represent velocity increments, dv , from an average level and not the absolute values. In each diagram the continuous line shows the averaged VDT time-history, while the two remaining curves represent the results presented by Kost et. al. The curve with thickened dots shows the experimental result and the dashed line - RANS calculations performed on 2D grid (only one realisation, without averaging).

When comparing the experimental and VDT curves in successive diagrams we can notice high similarity of their patterns, especially at points located close to the pressure side of the rotor blade. Larger differences are observed at points situated close to the suction side, especially in diagrams for $x/c = 0.1$ and 0.7 . Relatively high differences in the intensity of velocity fluctuations observed at point $x/c = 0.1$ may result from insufficient accuracy with which the vorticity distributed in the linear wake is modelled by a sequence of point vortices. When the wake deforms, these differences decrease significantly and only at point $x/c = 0.7$ remarkable differences can be observed again. This time they are of both quantitative scale referring to the amplitude of fluctuations, and qualitative nature observed in different shapes of the curves being the object of comparison. It is difficult to indicate clearly possible reasons of those differences, which would originate, for instance, from different exit flow conditions, which especially concerns flow angles calculated and recorded in the experiment. This suggestion is made more reliable by the fact that the results of the 2D RANS calculations reveal similar differences to those observed in the VDT time-histories.

EFFECTS OF WAKE DEFORMATION IN VDT AND RANS FORMULATION

The analysis described in the previous sections delivers a relatively clear and consistent pattern of the W/R interaction as an unsteady process controlled by the initial distribution of stator wake vortices at the time when the wake is cut apart by the rotor blades. Different distributions of these vortices provoke differences in their further behaviour and different effects of their interaction with each other and rotor blades.

When confronting this interaction pattern with the RANS procedure of calculations, a basic question can be formulated **whether and to which extent the RANS calculations, generally having the form of a single realisation, can be considered as representative for the general W/R interaction process.** This question becomes even more important when we keep in mind that the RANS calculations, even performed in unsteady mode, provide rather limited opportunities for re-constructing the vortex structure of the stator wake inside the rotor cascade. Except special cases of integer stator/rotor blade number ratios, this reconstruction would require using the calculation region which covers all passages in stator and rotor rows. When we take into account the grid resolution required for proper capturing of the vortex interaction phenomena, meeting this conditions goes well beyond the calculating potential of even biggest computers in the world. In unsteady RANS calculations the above problem is usually solved using a special periodicity condition, bearing the name of phase lag, which allows the entire calculation region to be reduced to one stator and one rotor passage. Between the stator and rotor cascade a sliding plane is placed, on which the phase lag condition is met. When the wake is treated in a classical way, as a uniform structure shown in Fig. 4, the phase lag condition allows instantaneous wake parameters to be effectively passed between the stator and rotor calculation domains. Unfortunately, the vortex structure of the wake is lost in this process due to a conflict, in general, between the phase shift of the wake

vortices and the phase lag defining the instantaneous position of the rotor with respect to the stator blades. As a consequence, the wake approaching the rotor calculation area is an averaged effect of various realisations representing different vortex phase shifts. In this situation the above formulated question can be rephrased to **whether the wake “numerically averaged” at the inlet to the rotor calculation domain will behave in the same way, i.e. generate the same time-averaged effects as the real wake in multiple realisations.**

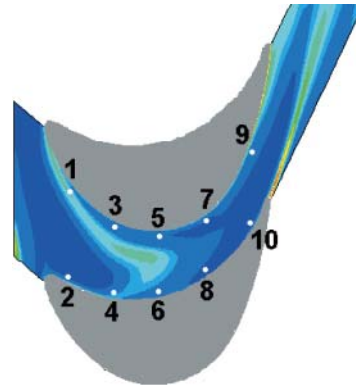


Fig. 13. Locations of recording points inside the rotor passage

In order to find an answer to this question, comparison was made between velocity fluctuations generated by RANS and VDT codes at ten points situated close to the rotor blade trailing edge, Fig. 13. The dimensionless distances x/c of these points from the rotor blade leading edge were equal to 0.1; 0.3; 0.5; 0.7 and 0.9, while the distance from the blade surface was equal to $1/16$ of the rotor pitch. The RANS calculations were performed in two variants differing by grid resolution. The first variant used the grid with 337 792 nodes (6032 nodes in the circumferential plane $y0z$). This grid resolution can be considered similar to those used in turbine stage flow calculations performed for design purposes. The parameters of the second grid equalled to 698 880 nodes in the rotor passage (13 440 in the circumferential plane $y0z$) and were selected according to recommendation given by Arnone et al [18].

The results of the comparison are shown in Fig. 14. Dashed curves represent coarse-grid RANS calculations (variant 1) while those with large dots were obtained from the fine-grid calculations (variant 2). The third curve represents the VDT calculations used as the reference.

As was shown in Fig. 9, the stator wake inside the rotor passage tends to take a trajectory close to the suction side of the rotor blade. That is why the velocity fluctuations recorded at the pressure side, points 2, 4, 6, 8 and 10, i.e. at a distance from the wake trajectories, are more regular and very similar to each other. What is also noticeable, the RANS results obtained for the fine grid are closer to the VDT curves than those obtained for the coarse grid. The observed differences between RANS and VDT curves seem to be accidental and do not reveal any regular tendency. Average velocities at the same points are slightly higher in RANS than in VDT calculations.

In the vicinity of the suction side of the rotor blade, points 1, 3, 5, 7 and 9, the differences in the shapes of the RANS and VDT curves are more pronounced. Paradoxically, the largest differences can be observed in the leading section located close to the rotor passage inlet. Downstream, the shapes of the corresponding curves become closer to each other. Like for the pressure side, the RANS results obtained on the fine grid are closer to the VDT results than those obtained on the coarse grid.

Special attention should be paid to the results recorded at point 9. This point is located near the rotor passage exit, close to the

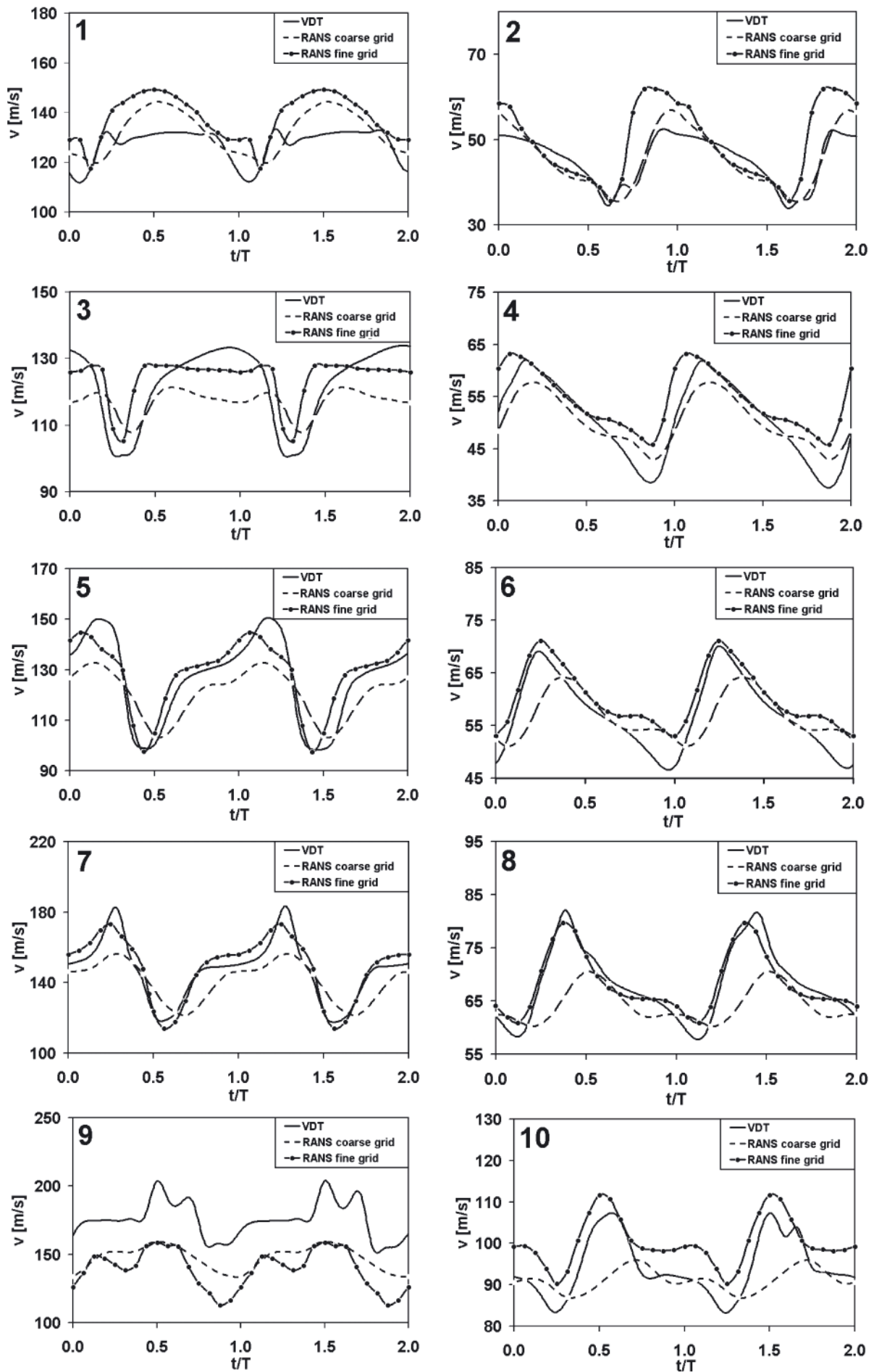


Fig. 14. Velocity fluctuations inside the rotor passage: the effect of grid resolution

rotor blade suction side, and close to the hypothetical trajectories of vortices composing the stator wake. In these circumstances, all physical differences between the RANS and VDT approaches to modelling the W/R interaction, and all numerical errors that cumulate during the step-by-step calculations are expected to be the most remarkable at this point. However, the RANS curve obtained on the fine grid reveals a visibly similar pattern to that shown in the VDT calculations. Moreover, comparable locations and intensities of local extremes are also observed.

The most remarkable difference between RANS and VDT results at point 9 is the average velocity level, visibly lower in the RANS calculations. The reason for this difference results from the fact that the boundary layer is thicker in this passage area and the recording point, unlike all other points, is situated inside it.

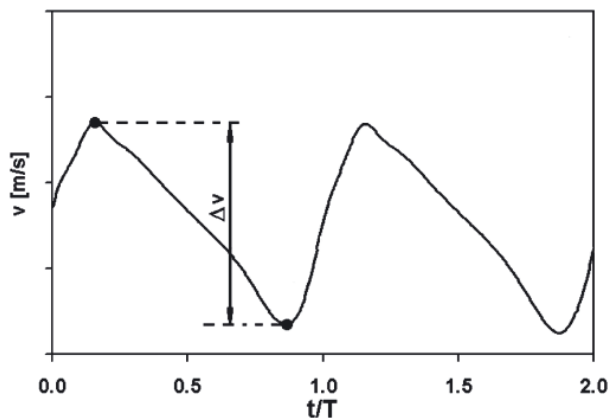


Fig. 15. Definition of velocity fluctuation amplitude

The velocity fluctuation curves observed for coarse-grid RANS calculations suggest that in this case any quantitative assessment of the global effects of the W/R interaction on stage performance (forces, losses, efficiency) can be burdened with rather substantial error.

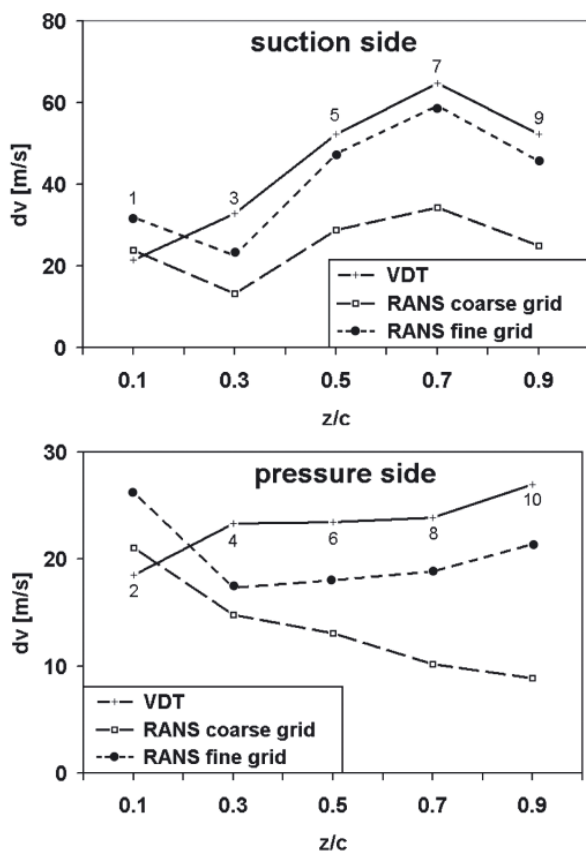


Fig. 16. Velocity fluctuation amplitudes recorded along the rotor passage

To assess the correctness of modelling the rate of stator wake dissipation in the 3D RANS model, velocity fluctuation amplitudes were calculated at the rotor passage points from Fig. 13 in the way illustrated in Fig. 15. The results of these calculations, shown in Fig. 16, reveal that increasing the grid resolution in RANS calculations leads to considerable reduction of wake dissipation. This tendency is illustrated by higher consistency of the amplitude change pattern obtained from RANS calculations with that representing the VDT solution, in which the wake dissipation is not directly taken into account.

Good agreement between the VDT and RANS (fine grid) results shown in Figs. 14 and 16 is highly valued as a definitely positive answer to the question asked at the beginning of this chapter. **The RANS calculations, performed on a sufficiently fine grid and making use of a “numerically averaged” stator wake, correctly predict time averaged effects of the real course of W/R interaction.**

CONCLUSIONS

The article discusses the interaction between the stator wakes and the rotor cascade (the W/R interaction) in a turbine stage. Taking into account most recent result of both experimental and numerical studies of the inner structure of the wake, the stator wakes were modelled as segments of von Karman vortex streets. To achieve sufficiently high accuracy of unsteady calculations presenting consecutive stages of the W/R interaction, the rotor cascade was represented by an infinite row of blade profiles, the flow through which was calculated using the potential flow with vortex singularities and the conformal mapping method. Geometrical parameters of the stator wake and inlet conditions for the rotor flow were reconstructed from the preliminary 3D RANS calculations done for a stage, the geometry and flow conditions of which were taken from a real high pressure turbine in operation in a Polish power plant. The study has demonstrated that the deformation of the stator wake on its way through the rotor cascade leads to the segregation of two groups of one-sign vortices which then move down the passage along trajectories situated, as a rule, close to the rotor blade suction side. Different phase shifts in the initial distribution of vortices in the stator wake result in noticeable differences in the wake deformation course.

The course of deformation predicted by the VDT analysis was compared to that observed experimentally and analysed numerically by other researchers in a turbine stage. The comparison revealed good qualitative agreement both with respect to particular stages of the wake deformation and its effects, having the form of velocity fluctuations recorded at selected points near the pressure and suction sides of the rotor blade.

The last section of the article analyses the potential of RANS codes for determining quantitative effects of real W/R interaction in a turbine stage. The assumed criterion of applicability was the level of agreement of the RANS results with the time-averaged VDT data. It was stated that despite certain differences in the wake structure model used in each of these two codes and the resultant different nature of wake behaviour in the rotor passage: deterministic in RANS calculations and stochastic in VDT calculations, the RANS results obtained on a grid with a sufficiently fine resolution correctly represent the time-averaged effects of the real W/R interaction. The process of averaging of the vortex structure of the wake on the sliding plane between the stator and rotor calculation areas can be considered sort of “numerical averaging” of different realisations of the real vortex W/T interaction.

REFERENCES

- Goldstein R.J., Spores R.A.: *Turbulent transport on the endwall in the region between adjacent turbine blades*, ASME J. Heat Transfer, vol. 110, pp. 862-869, 1988.
- Doerffer P., Rachwalski J., Magagnato F.: *Numerical Investigation of the Secondary Flow Development in Turbine Cascade*, TASK Quarterly, vol. 5, pp. 165-178, 2001.
- Dawes, W. N.: *Current & Future Developments in Turbomachinery CFD*, Proceedings, 2nd European Conference on Turbomachinery – Fluid Dynamics and Thermodynamics, Antwerpen, March 5-3, 1997.
- Meyer, R. X.: *The Effect of Wakes on the Transient Pressure and Velocity Distributions in Turbomachines*, ASME Journal of Basic Engineering, vol. 80, pp. 1544-1552, 1958.
- Smith, L. H.: *Wake Dispersion in Turbomachines*, ASME Journal of Basic Engineering, vol. 88, September, pp. 688-690, 1966.
- Prandtl L.: *Über die Entstehung von Wirbeln in der idealen Flüssigkeit, mit Anwendung auf die Tragflugeltheorie und andere Aufgaben*, In Gesamt. Abhandl. T. II, Springer-Verlag Berlin Gottingen Heidelberg, 1961, S. 696-513, 1924.
- Lienhart, W.: *Berechnung der instationären Strömung durch gegeneinander bewegte Schaufelgitter und der Schaufelkraftschwankungen*, VDI-Forschungsheft, vol. 562, VDI Verlag, Düsseldorf, 1974.
- Krammer, P.: *Computation of Unsteady Blade Forces in Turbomachines by Means of Potential Flow Theory and by Simulating Viscous Wakes*, ASME Paper 82-GT-198, 1982.
- Korakianitis, T.: *On the Propagation of Viscous Wakes and Potential Flow in Axial-Turbine Cascades*, ASME Journal of Turbomachinery, vol. 115, pp.118-127, 1993.
- Hodson, H. P., and Dawes, W. N.: *On the Interpretation of Measured Profile Losses in Unsteady Wake –Turbine Blade Interaction Studies*, ASME Journal of Turbomachinery, vol. 120, pp. 276-284, 1998.
- Michelassi, V., Martelli, F., Dénos, R., Arts, T., and Sieverding, C. H.: *Unsteady heat Transfer in Stator-Rotor Interaction by Two-Equation Turbulence Model*, ASME Journal of Turbomachinery, vol. 121, pp. 436-447, 1999.
- Solomon, W. J., Walker, G. J., and Hughes, J. D.: *Periodic Transition on Axial Compressor Stator: Incidence and Clocking Effects: Part II - Transition Onset Predictions*, ASME Journal of Turbomachinery, vol. 121, pp. 408-415, 1999.
- Dénos, R., Arts, T., Paniagua, G., Michelassi, V., and Martelli, F.: *Investigation of the Unsteady Rotor Aerodynamics in a Transonic Turbine Stage*, ASME Journal of Turbomachinery, vol. 123, pp. 81-89, 2001.
- Sieverding, C. H., and Heinemann, H.: *The Influence of Boundary Layer State on Vortex Shedding From Flat Plates and Turbine Cascades*, ASME Journal of Turbomachinery, vol. 112, pp. 181-187, 1990.
- Cicatelli, G., and Sieverding, C. H.: *The Effect of Vortex Shedding on the Unsteady Pressure Distribution Around the Trailing Edge of a Turbine Blade*, ASME Journal of Turbomachinery, vol. 119, pp. 810-819, 1997.
- Mensink, C.: *Numerical Prediction of Periodic Vortex Shedding in Subsonic and Transonic Turbine Cascade Flows*, International Journal for Numerical Methods in Fluids, vol. 22, pp. 881-897, 1996.
- Currie, T. C., and Carscallen, W. E.: *Simulation of Trailing Edge Vortex Shedding in a Transonic Turbine Cascade*, ASME Journal of Turbomachinery, vol. 120, pp. 10-19, 1998.
- Arnone, A., Marconcini, M., and Pacciani, R.: *On the Use of Dual Time Stepping in Unsteady Turbomachinery Flow Calculations*, ERCOFTAC Bulletin No. 42, September, pp. 37-42, 1999.
- Magagnato, F.: *Unsteady flow past a turbine blade using non-linear two-equation turbulence models*, Proceedings III European Conference on Turbomachinery: Fluid Dynamics and Thermodynamics, London, March, pp. 221-230, 1999.
- Lin, C. C.: *On the Motion of Vortices in Two Dimensions*, University Toronto Press, Toronto, Canada, 1943.
- Basu, B.C.; Hancock, G.J.: *The unsteady motion of a two-dimensional airfoil in incompressible inviscid flow*, Journal of Fluid Mechanics, vol. 87, pp. 159-178, 1978.
- Prosnak, W. J.: *Computation of Fluid Motions in Multiply Connected Domains*, Wissenschaft + technik series, G. Braun, Karlsruhe, Germany, 1987.
- Milne-Thomson, L.M.: *Theoretical Hydrodynamics*, London, III edition, 1968.
- Swirydczuk, J.: *A numerical analysis of changes in the conditions of the flow over two identical airfoils caused by the passing vortex structure (in Polish)*, Reports of the PAS Institute of Fluid-Flow Machinery, No. 94, pp. 3-17, 1992.
- Swirydczuk, J.: *Modelling the interaction of an isolated free vortex with a finite cascade of airfoils with the aid of conformal mapping*, Reports of the PAS Institute of Fluid-Flow Machinery, No. 94, pp. 95-111, 1992.
- Swirydczuk, J.: *The Flow Through a Blade Cascade With a Local Shape Deformation*, ZAMM, 77, vol. 5, pp. 399-402, 1997.
- Swirydczuk J.: *Vortex Dynamics of the Stator Wake – Rotor Cascade Interaction*, ASME Journal of Fluids Engineering, vol. 124, pp. 400-412, 2002.
- Swirydczuk, J.: *The interaction of vortex structures with the approached profiles*, (in Polish) D.Sc. thesis, Scientific Reports of the Institute of Fluid-Flow Machinery, No. 533/1492, 233 p, 2004.
- Swirydczuk, J.: *CFD modelling of turbine stage stator/rotor interaction*, TASK Quarterly, vol. 10, No. 2, pp. 113-124, 2006.
- Swirydczuk J.: *Analysing Stator/Rotor Interactions in Rotating Machines*, Awiacjonno-Kosmiczeskaja Technika i Technologia, vol. 8/44, pp. 116-120, 2007.
- Sarpkaya, T.: *Computational Methods With Vortices - The 1988 Freeman Scholar Lecture*, ASME Journal of Fluids Engineering, vol. 111, pp. 5-52, 1989.
- Karman, T. von, and Rubach, H.: *Über den Mechanismus des Flüssigkeits- und Luftwiderstandes*, Physikalische Zeitschrift, vol. 13, pp. 49-59, 1912.
- Kost, F., Hummel, F., and Tiedemann, M.: *Investigation of the Unsteady Rotor Flow Field in a Single HP Turbine Stage*, Proceedings, ASME TURBO EXPO 2000, May 8-11, Munich, Germany, 2000.

CONTACT WITH THE AUTHOR

Jerzy Świryczuk, Prof.
 Institute of Fluid-Flow Machinery
 Polish Academy of Sciences
 Fiszerka 14
 80-952 Gdansk, POLAND
 e-mail: jsk@imp.gda.pl

Study of the state a Francis turbine

Mariusz Żółtowski, Ph.D.,
Bogdan Żółtowski, Prof.,
University of Technology and Life Science in Bydgoszcz, Poland
Leonel Castaneda, Ph.D.,
EAFIT University of Colombia

ABSTRACT

*This paper presents a methodology to evaluate the technical state of a Francis turbine by shaft rotor dynamic simulation. There are several rotor dynamic criteria that define the technical state of a **turbo-machine**. To feed the shaft rotor dynamic model this delivers the required information to accomplish the technical assessment. The numerical rotor dynamic model uses as input, the field forces obtained by the fluid-solid interaction analysis undertaken over the blades of the runner.*

*The rotor dynamic numerical simulations allow to determinate the record-in-time of the displacements of any point along the shaft. This information is relevant for diagnosis tasks, because it is possible to decompose it spectrally and to estimate the severity of the vibrations. Comparing the results of the numerical model against those obtained from machines that operates under normal conditions, it is possible to determinate the technical state of the **turbo-machine**. This allows studying the stability of the turbine working on several operation ranges.*

A Francis turbine is a very complex machine that involves many physical phenomena of different nature. In this way, the hydraulic input forces needed by the rotor dynamic model should not be assumed but calculated directly from the fluid interaction over the turbine structure.

Key words: FEM; Francis turbine; diagnosis; fluctuations; hydrodynamic

INTRODUCTION

The technical diagnosis is a set organized of methods and a half that allow the evaluation of the technical condition state (his reason, evolution and consequence) of systems of engineering. In most cases they are systems in operation, designed to fulfill a principal function. These appliances generate and transform information, which is used later to study his technical condition state.

For the definition of the field of application of the technical diagnosis, are studied the processes of destruction of the objects during the whole period of his existence and certain situations, in which it is necessary to consider the actions (shares) of diagnosis. The term "period of existence of the machines" refers to the cycle that initiates in the instant that there are formulated the requirements of design that must fulfill the new object up to his respective liquidation (residues, felling and reutilization) (Żółtowski B., 2002).

The current technology (skill) is a result of the models' analysis, which they describe with certain degree of accuracy. The process, which takes as an aim the construction of the best model of operation (mathematical or empirical), is named a process of identification, and includes shaped, you

try, estimation and check. The methodology of the studies of diagnosis includes the heuristic and mathematical models (Żółtowski B., 1996).

"The identification in the diagnosis is a process of searching complex, in that, based on the knowledge of the structure and the functioning of the object, there are realized the analysis and the synthesis of the model of the object for the obtaining of the information of diagnosis". The idea on the methodical construction of the dynamic model of the mechanical system is supported of the information of the modal experiment and the information of the measurements of the quantities of vibration (acceleration of the vibration, moment rotational, force and etc.) in conditions of exploitation development. The models of analysis of loads are constructed depending on his application in the procedures of dynamic optimization and diagnosis of exploitation development. (Żółtowski B., Cempel C., 2004).

During the electric generation process, the turbines develop hydraulic phenomena that extend along all the components of the machine represented in vibrations, sound and instabilities. Recently, the evaluation of the machine state using modern diagnosis techniques has become important. These diagnosis techniques, expert systems in particular, are based on the knowledge of the technical system and on the

use of artificial intelligence. To enlarge the understanding of machines for failure detection, the study of their dynamical behavior plays a significant role. This methodology is known as maintenance based on models and pretends to achieve the failure identification by establishing relations between the real object and a virtual model (Kicinski, 2006).

The vibration analysis has been an important tool in the technical diagnosis. Instruments for measuring vibrations (accelerometers) are implemented in large machines and the parameters extracted from the acquired signals are used as effective indicators of the technical state. The rotor dynamical study of turbines, in this case, pretends to develop the knowledge to correctly identify the relations between the symptom and its causes.

The objective of the present study is to develop a study method that allows calculating the displacements of any point along the shaft of the turbine using FEM simulations. This information is relevant for diagnosis tasks, because it is possible to decompose it spectrally and to estimate the severity of the vibrations.

CASE OF STUDY

This investigation considers a Francis turbine composed by 20 stay and guide blades and 15 runner blades. It rotates at 900 rpm and generates a maximum output of 10MW. For this case, only the Best Efficiency Point (BEP) is analyzed. The turbine head is 230 m and the discharge at this point is 4.8 m³/s.

The assembly of the turbine / generator can be observed in Fig. 1. The set is assembled on a rigid shaft, to which are attached: the runner, the flywheel, the generator core and poles, and the exciter. The shaft is supported by three hydrodynamic bearings. The first of them (nearest to the runner) has axial and radial effect; the other two have only radial effect.

METHOD OF EXPERIMENTAL MEASURES

A series of measurements using dynamic pressure sensors arranged along the guide vanes and draft tube were carried out. Also, a set of strain gages installed in the turbine shaft were employed with the purpose of measuring deformations to determine the torque and the radial forces.

There were installed sensors along different components of the turbine. Three of them were installed near the zone where the rotor-stator interaction occurs (between the guide vane and the runner). Fig. 2 shows an image of the approximate position of one sensor.

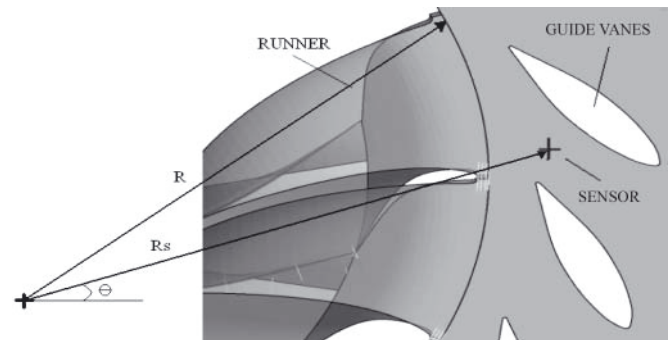


Fig. 2. Position of the sensors

The task of these sensors was to capture pressure fluctuations generated by the rotor-stator interactions. Fig.3 shows an image of the experimental assembly carried out. It can be appreciated the physical conditions of the sensor installation.



Fig. 3. Photo of the experimental location of the sensor

Another six dynamic pressure sensors were installed along the draft tube. The objective of the sensors was to obtain

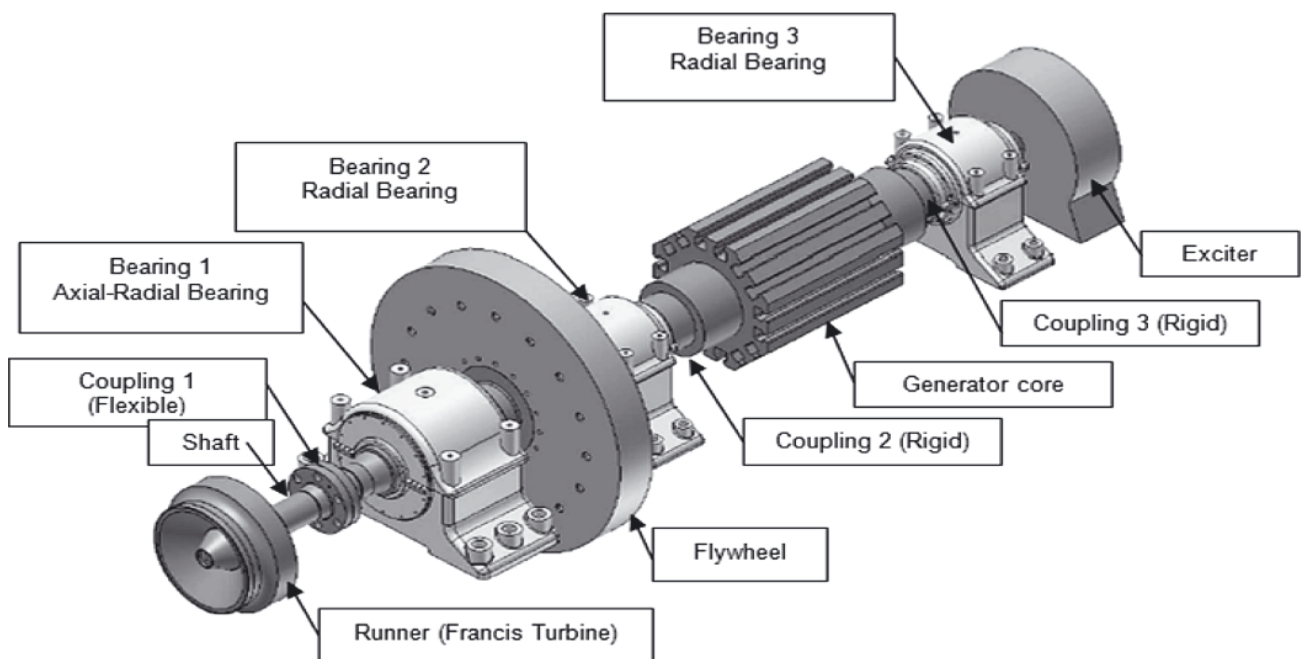


Fig. 1. Turbine shaft with bearings and attached mechanical elements

information on the vortex rope generated at the exit of the runner. The sensors were distributed in two cross sections: i.e. A and B; in each section were installed 3 sensors (Fig. 4).

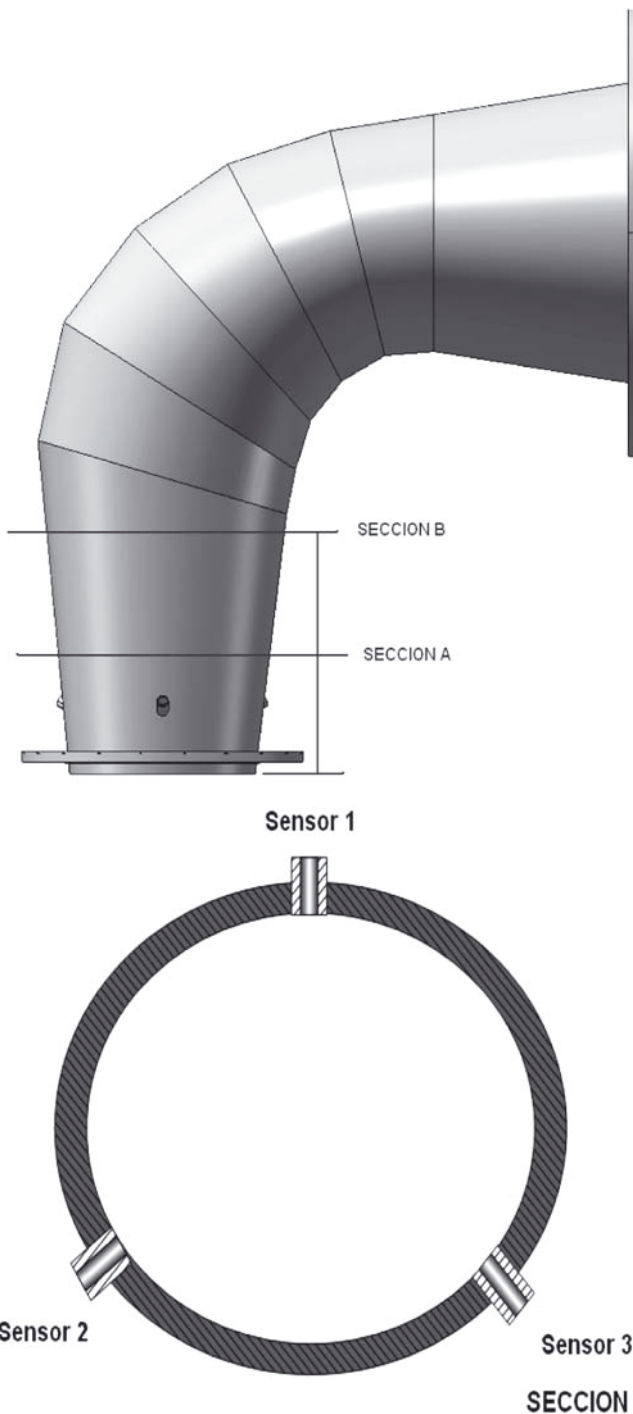


Fig. 4. Distribution of the sensors in the draft tube

The measurements were recorded performing a simultaneous sampling during 3 seconds of every channel at 102 kHz, i.e. more than 40 rotor revolution and more than 6500 samples per channel. It allows to capture all the hydraulic phenomena present at low and high frequencies.

For the measurement of the torque and the radial force a strain gage technique applied to the generation shaft was used. The use of this technique did not affect the turbine operation in any way. The strain gage signals were registered via wireless connection.

Fig. 5 shows the position in the shaft where the strain gages (SG) were installed. For the measurement of the radial

force it was use of four bi axial well doable SG meanwhile the measurement of the torque used one bi axial well doable SG. The strain gages were connected to a transmitter tied to the shaft.

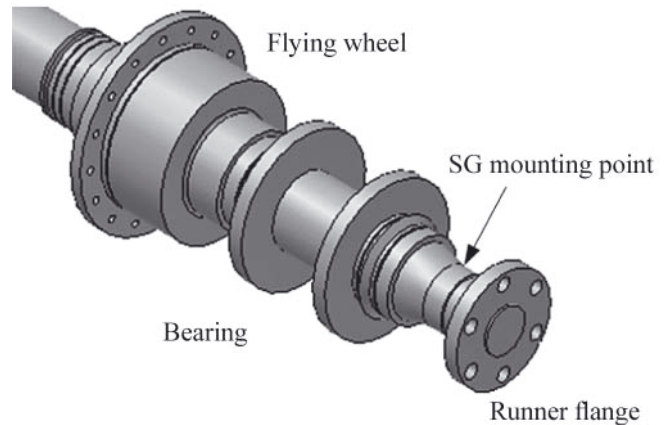


Fig. 5. Strain gages position in the shaft

Fig. 6 shows an image of the experimental installation of the SG. The distribution of the strain gages and its position in the shaft can be observed.



Fig. 6. Photo of the experimental installation of the gages in the shaft

The information give by all this pressure sensors and the strain gages is used to validate the CFD numerical model.

ROTODYNAMIC METHOD

The goal is to develop a model that accurately predicts the dynamic behavior of the shaft of a Francis turbine by means of numerical methods. To achieve this goal, it is necessary to find an approximated solution to the equations of motion of the system. These equations are a set of non linear differential equations:

$$M\ddot{x} + D(x, \dot{x})\dot{x} + K(x, \dot{x})x = P(t) \quad (1)$$

where:

- M – global matrix of inertia
- D – global matrix of damping
- K – global matrix of stiffness
- P(t) – generalized vector of external excitations
- x – generalized vector of position

The model is implemented in the computational environment MESWIR®. This software was developed by the Institute of Fluid Flow Machinery (IFFM) from the Polish Academy of Science. It composed by a set of codes to determine static and dynamic parameters of rotors, including analysis of the hydrodynamic bearings. The software uses the finite element method to analyze the rotor shaft and the finite difference method to determine the characteristic of the hydrodynamic bearings. With the software it is possible to analyze lateral vibrations with linear and non linear models.

The required entries of the model are: the conditions of support, the forces or external excitations, the mechanical and geometrical properties of the shaft. The shaft is supported in three hydrodynamic bearings but for the rotordynamic model they are represented by springs and dampers. The determination of the oil film stiffness and damping coefficients required additional computation of the fluid dynamics involved. The oil film stiffness and damping coefficients depend on the relative position and velocity of the journal in the bearing causing the non linearity in the equations of motion. However the results obtained under the assumption of linear stiffness and damping coefficients are acceptable. For the purpose of this work, the MESWIR® linear models were used.

The bearings are also attached to a foundation. The foundation is replaced in the mechanical model by springs and dampers, whose coefficients were prior determined by experimental measurements and numerical simulations. The shaft is modeled coupled rigid discs with masses and inertias equivalent to those of the real objects.

Geometry and physical properties

The real model is simplified in a mechanical model to make possible its analysis (Fig. 7). The shaft is discretized into 33 cylindrical Timoshenko beam elements with six degrees of freedom to use the finite element method. These elements are provided of mass, stiffness and damping, which are estimated from the physical properties of the material of the shaft, such as: density, Young modulus, Poisson coefficient and damping coefficients. In the Tab. 1 are listed the material properties.

Tab. 1. Physical properties of the material of the shaft.

Density	Young modulus	Poisson coefficient	Damping coefficient A	Damping coefficient β
7800 kg/m ³	200 GPa	0.3	1.96 rad/s	5.09*10 ⁻⁵ s/rad

Support parameters

In the oil film in the hydrodynamic bearings appears a hydrodynamic pressure distribution induced by the rotation and originating the reaction force. This pressure distribution is described by the Reynolds equation:

$$\frac{1}{R^2} \frac{\partial}{\partial \theta} \left(h^3 \frac{\partial p}{\partial \theta} \right) + \frac{\partial}{\partial z} \left(h^3 \frac{\partial p}{\partial z} \right) = 6\eta \left(\frac{1}{R} \frac{\partial (hU)}{\partial \theta} + 2 \frac{\partial h}{\partial t} \right) \quad (2)$$

where:

- p – pressure in the oil film
- h – film thickness
- U – oil velocity in tangential direction
- η – dynamic oil viscosity
- R – radius of journal

Assuming that the flux is laminar and that the viscosity is constant along the oil film the pressure distribution could be found. The magnitude and orientation of the reaction force depend of the position and velocity of the gravity center of the rotor shaft. The stiffness and damping coefficients are computed based on the reaction force. The stiffness coefficients are the derivatives of the reaction force respect to the displacements.

$$\begin{aligned} k_{11} &= \frac{\partial W_x}{\partial x}, & k_{22} &= \frac{\partial W_y}{\partial y} \\ k_{12} &= \frac{\partial W_x}{\partial y}, & k_{22} &= \frac{\partial W_y}{\partial x} \end{aligned} \quad (3)$$

where:

- $k_{11}, k_{22}, k_{12}, k_{22}$ – oil film stiffness coefficients
- W_x, W_y – components of the reaction force

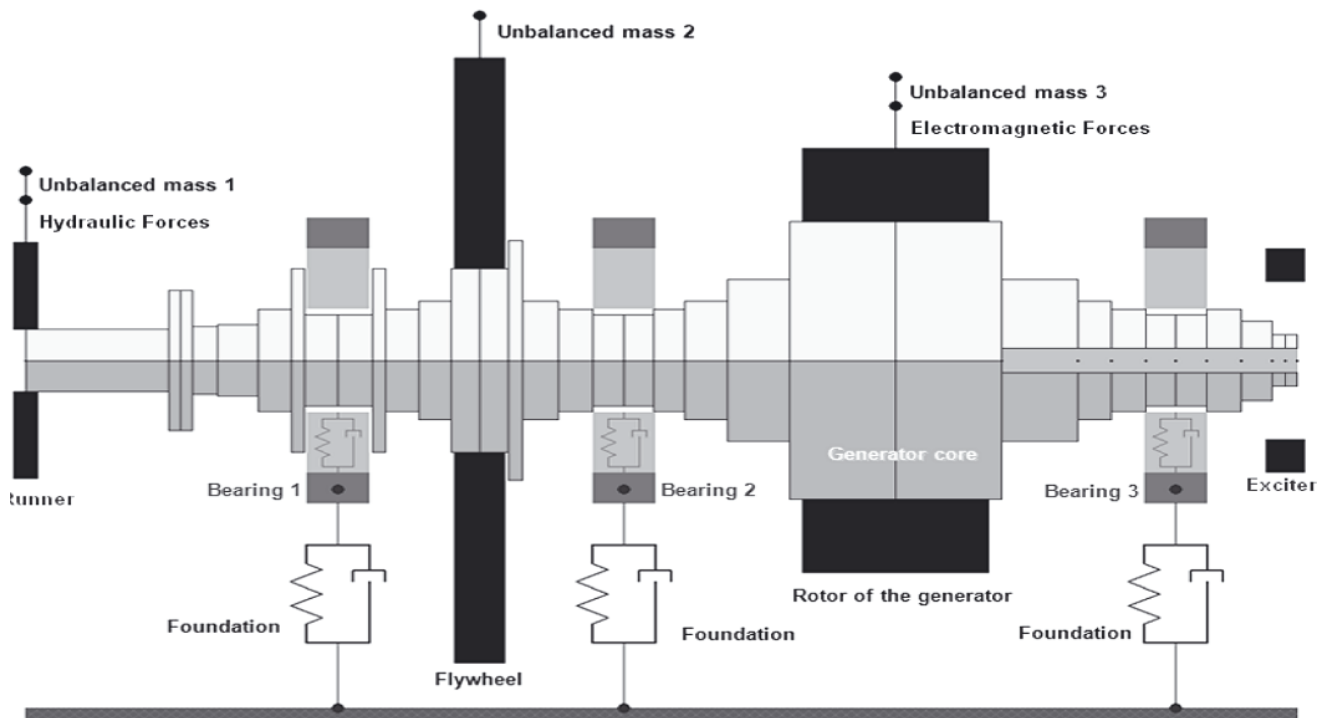


Fig. 7. Numerical model

The damping coefficients are found as the derivatives of the reaction force respect to the velocities.

$$c_{11} = \frac{\partial W_x}{\partial \dot{x}}, \quad c_{22} = \frac{\partial W_y}{\partial \dot{y}} \quad (4)$$

$$c_{12} = \frac{\partial W_x}{\partial \dot{y}}, \quad c_{21} = \frac{\partial W_y}{\partial \dot{x}}$$

where:

c_{11} , c_{22} , c_{12} , c_{21} – oil film damping coefficients

The Fig. 8 presents a representation of the oil film as springs and dampers.

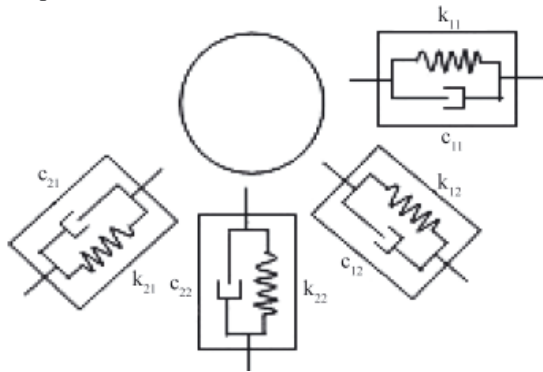


Fig. 8. Stiffness and damping coefficients the oil film

The shaft is affected by static and dynamic loads. The static loads are the masses of the elements attached to the shaft. The dynamic loads are originated by: residual unbalanced masses, the solid-fluid interaction in the runner and electromagnetic phenomena in the generator.

Static and dynamic loads

The static loads are determined by the geometry and physical properties of the discs assembled to the shaft. For the model, it is supposed that these discs are made of steel. The discs add mass and inertia to the system but they do not represent additional stiffness or damping. Other properties of the discs are list in Tab. 2.

Tab. 2. Elements assembled to the shaft

Element	Runner	Flywheel	Generator poles	Exciter
Outer diameter [m]	0.900	2.300	1.614	0.850
Inner diameter [m]	0.240	0.706	1.054	0.600
Thickness [m]	0.146	0.300	1.090	0.225
Mass [kg]	673	8806	9977	500
Inertia [kgm ²]	73	6372	4634	68

As it was mentioned the dynamic loads could be inertial, hydraulic or magnetic. The inertial forces are used to tune the model and the represent an output of the model. The hydraulic forces are estimated by CFD simulations. Regarding to the magnetic forces only unbalanced magnetic pull is considered.

The unbalanced magnetic pull appears when the rotor is eccentrically positioned respect to the stator. This causes

asymmetric distribution of the magnetic flux and then an unbalance force in the direction of the smallest air gap. This force depends in a non linear way of the relative eccentricity, which is defined as:

$$\varepsilon = u_r / \Delta R \quad (5)$$

where:

ε – relative eccentricity

u_r – distance between the rotor center line and the stator center line

ΔR – difference between the stator inner radius (R_s) and the rotor radius (R_r)

The unbalance magnetic pull has a constant and a variable part. The variable force oscillates with a frequency equal to the supply frequency. If the number of poles increases, the variable part decreases. The mean value for the unbalance magnetic pull could be found as (Gustavsson, 2005):

$$F = \frac{\mu_0 S_s^2 R_s^3 h \pi}{2p^2 \Delta R^2} \frac{e}{\sqrt{(1-e^2)^3}} \quad (6)$$

where:

μ_0 – magnetic permeability

S_s – lineal density of current

R_s – stator inner radius

h – rotor length

e – relative eccentricity

p – nNumber of poles

By means of a static analysis the deflection of the shaft in the generator core section is found. With this value and the technical information of the machine the unbalance magnetic pull is computed and is found that it has a value of 4966 N.

RESULTS

The experimental data used in rotor dynamic calculations is obtained from displacement sensors installed in the bearings. In each bearing are two sensors forming a rectangular angle between them and an angle of 45 degrees respect the horizontal plane as is shown in Fig. 9. Then, the vibration is measure in a coordinate system that is 45 degrees rotated respect the general coordinate system and some transformations should be made to compare the results.

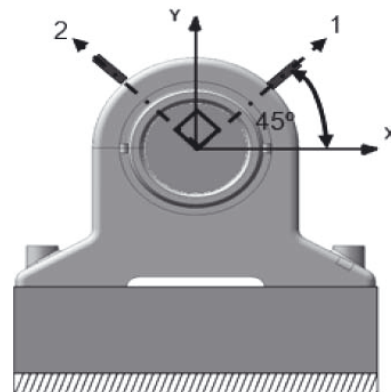


Fig. 9. Place of the sensors on the rotor

The most relevant component in the spectrum is at 15 Hz, which is the rotational frequency of the machine. The other force components are very low and are not considered in this analysis. In the model the force should be introduced as an unbalanced mass at specific unbalance radius. The transformation is made using the definition of centrifugal acceleration.

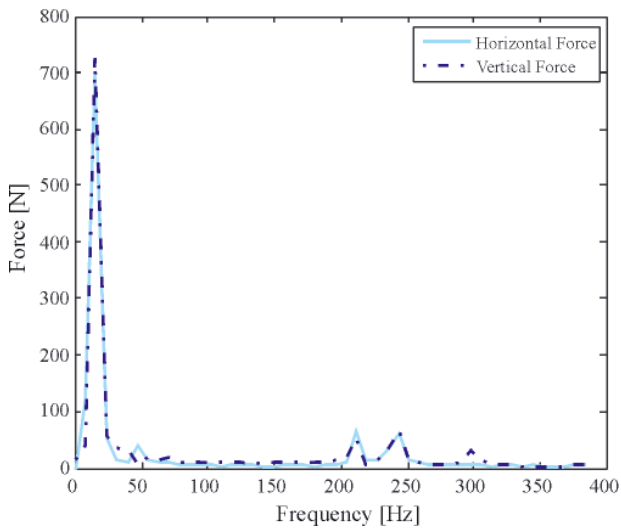


Fig. 10. Spectral analysis of the radial force

Tab. 3. Spectral components of the radial force.

Frequency [Hz]	Horizontal force [N]	Vertical force [N]
15	696.2	723.50
210	65.53	53.52
240	61.58	64.93
300	-	30.60

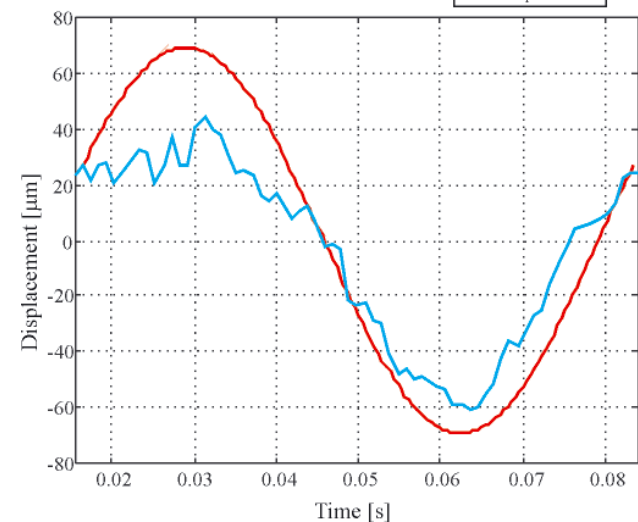
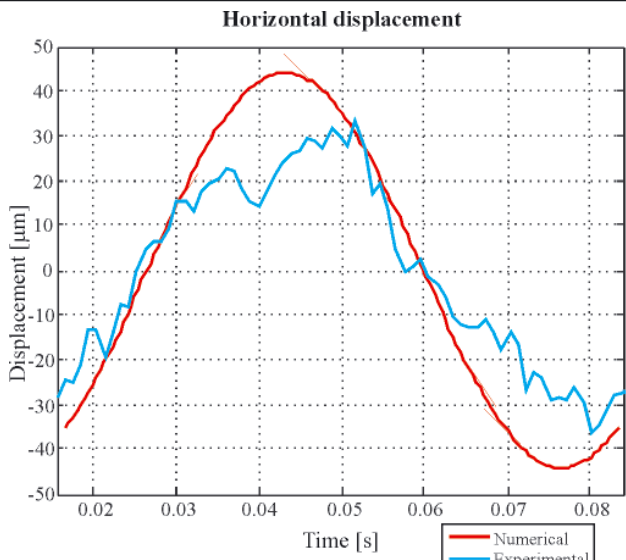


Fig. 11. Numerical and experimental displacement signals for the bearing 1

The analyses are made with the modules of MESWIR® for studying lateral vibrations with linear models. Hence, only excitations at first harmonic are taken into account and the numerical signals are sine functions with the rotational frequency. In Fig. 11, 12 and 13 the experimental and numerical results for the displacement vibration are compared for each bearing.

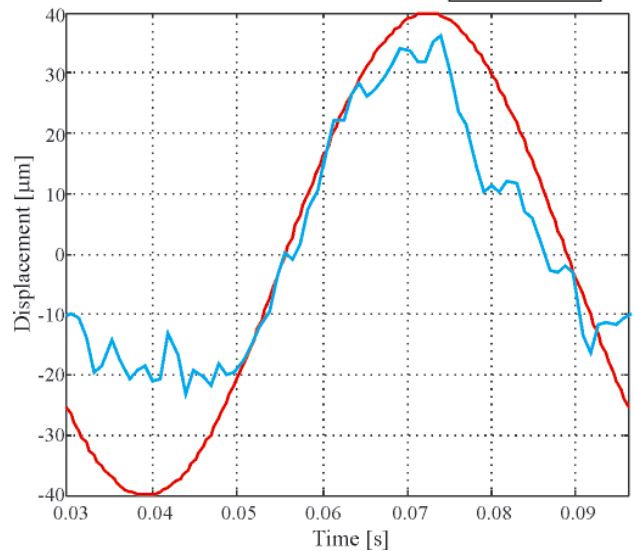
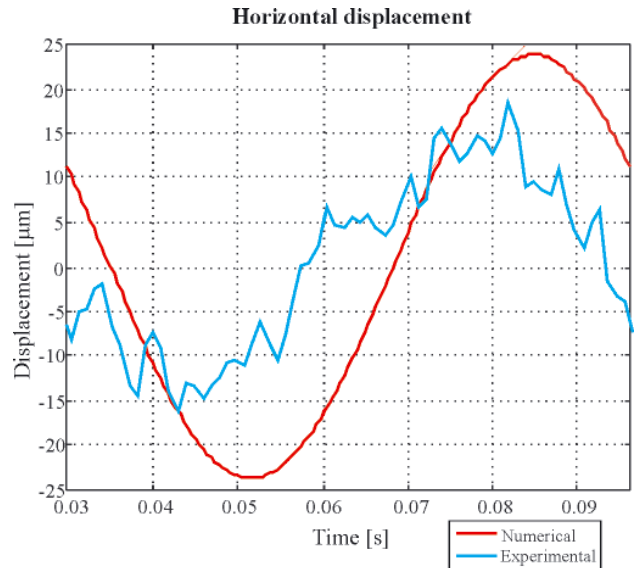


Fig. 12. Numerical and experimental displacement signals for the bearing 2

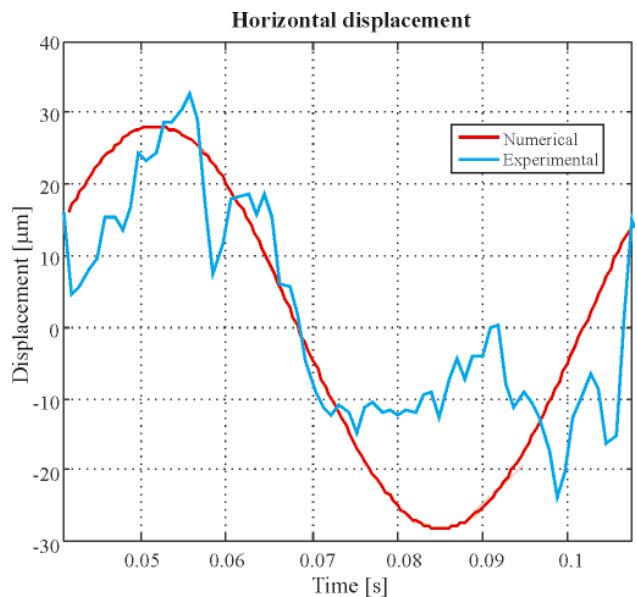


Fig. 13. Numerical and experimental displacement signals for the bearing 3

As it was mentioned the unbalanced forces are tuned until the numerical vibration amplitudes adjust to those measured in the real technical object. The final required values represent a result from the rotor dynamic model.

Tab. 4. Resultant unbalance masses

Position	Unbalance d mass [kg]	Unbalance e radius [m]	Phase [degrees]
Runner	7.000	0.5	0
Flywheel	15.000	0.5	180
Generator poles	12.400	0.5	0
Runner (hydraulic force)	0.157	0.5	0
Runner (hydraulic force)	0.163	0.5	90

FINAL CONSIDERATIONS

The radial forces obtained via numerical methods were used to feed the FEM rotor dynamic software. These forces have a consistent predominant spectrum component at the frequency of rotation which was used in the linear rotor dynamic model. However this resultant radial component has a low magnitude, because for the simulations the runner is completely symmetrical and the unbalance in the pressure distribution is little. If some imperfections of the runner are included in the simulations, the magnitude of force would probably become more significant.

It was possible to develop a rotor dynamic model whose results are in agreement with the experimental data. In this case, the unbalance masses required are relative large. This could be caused because the rotor is very rigid and important amounts of residual unbalanced could be bear with acceptable vibration amplitudes.

The amplitudes of vibration for the displacement obtained by the numerical computations and the experimental measures are acceptable according to the standard ISO 7919-5. This standard establishes a maximum limit of 165µm. From the point of view of vibration the technical state of the machine is acceptable.

BIBLIOGRAPHY

1. Egusquiza E., Nascimento L.P., Valero, C. Jou, E. (1994). *El diagnostico de daños en grupos hidroeléctricos mediante el análisis de vibraciones*. Revista Ing. del agua Vol 1 Num 3.
2. Gagnon J.M., Payette F.A. and Deschenes C. (2007). *Numerical Simulation of a Rotor-Stator Unsteady Interaction in a Propeller Turbine*. CFD Society of Canada, Toronto.
3. Guedes A., Kueny J.L., Ciocan G. and Avellan F. (2002). *Unsteady rotor-stator analysis of a hydraulic pump-turbine – CFD and experimental approach*.
4. *Proceedings of the XXIst IAHR symposium on hydraulic machinery and systems*, Laussane, Switserland.

5. Hoffmann K. (1989). *An introduction to measurements using strain gages*. Hottinger Baldwin Messtechnik GmbH, Darmstadt.
6. Menter F.R. (1994). *Two - equation eddy viscosity turbulence models for engineering applications*. AIAA Journal.
7. Nennemann B. and Farhat M. (2005). *CFD prediction of unsteady wicket gate-impeller interaction in Francis turbines: A new standard hydraulic design procedure*. Waterpower XIV, Austin, USA.
8. Qian Z., Yang J., Huai W. (2007). *Numerical simulation and analysis of pressure fluctuation in Francis hydraulic turbina with air admisión*. Journal of hydrodynamics.
9. Zobeiri A., Kueny J.L., Farhat M. and Avellan F. (2006). *Pump turbine rotor-stator interactions in generating mode: pressure fluctuations in distributor channel*. 23th IAHR symposiums, Yokohama, Japan.
10. Ciocan and others (2007). *Experimental study and numerical simulation of the FLINDT draft tube rotating vortex*. Journal of fluid dynamics. Vol 129.
11. Kicinski J. (2006). *Rotor dynamics*. Institute of Fluid-Flow Machinery Polish Academy of Science, Gdansk.
12. Gustavsson R. (2005). *Modelling and Analysis of Hydropower Generator Rotors*. Lulea University of Technology. The Polhem Laboratory. Division of Computer Aided Design.
13. Zoltowski B., Castaneda Heredia LF. (2009). *Estudio de explotación de vehiculos ferroviarios*. EAFIT University, Colombia, pp.298.
14. Zoltowski B., Castaneda Heredia LF. (2009). *Research rail vehicles*. Transportation. UTP, Bydgoszcz, pp.220.
15. Zoltowski B. (2011). *Fundamentals of diagnostic machines*. UTP Bydgoszcz, pp.200.
16. Zoltowski B., Castaneda Heredia LF. (2010). *Bases del diagnostico tecnico de maquinas*. EAFIT University, Colombia, pp.233.
17. Zoltowski B., Lukasiewicz M. (2012). *Diagnosis of Vibration machines*. ITE-PIB, Radom.
18. Zoltowski B., Landowski, B., Przybyliński B. (2012). *Designing the operation of machinery*. UTP, Bydgoszcz.
19. Zoltowski, B., Lukasiewicz M., Kałaczyński T. (2012). *Information technology in the study of machines*. UTP, Bydgoszcz.
20. Zoltowski B. (2012). *Methods of virtual engineering in clinical status, security threats operated machines and the environment*. UTP, Bydgoszcz.
21. Zoltowski M. (2012) *Operational modal analysis study design building*. UTP, Bydgoszcz.

CONTACT WITH THE AUTHORS

Mariusz Żółtowski, Ph.D.,
Bogdan Żółtowski, Prof.,
University of Technology and Life Science
in Bydgoszcz,
Ks. Kordeckiego 20,
85-225 Bydgoszcz, POLAND
mobile: +48 791 626 848
mazolto@utp.edu.pl
bogzol@utp.edu.pl

Leonel Castaneda, Ph.D.,
EAFIT University of Colombia
Cr 49 N°7 s 50 Medellín, COLOMBIA

Design analysis of ORC micro-turbines making use of thermal energy of oceans

Marian Piwowarski, Ph.D.
Gdansk University of Technology, Poland

ABSTRACT



The article presents the results of the analysis of energy conversion cycles making use of thermal energy of oceans. The objects of analysis were two cases of closed Organic Rankine Cycle (ORC) power plants, which were: the cycle in which the vapour of the working medium was produced by warm oceanic water in the circum-equatorial zone, and the so-called "arctic" cycle in which this vapour was produced by non-frozen water in the circumpolar zone. Between ten and twenty low-boiling media were examined for which operating parameters were optimised to obtain the highest cycle efficiency. A preliminary design of an ORC turbine which was obtained by optimising basic design parameters is included. It has been proved that realisation of the Ocean Thermal Energy Conversion (OTEC) cycle is possible both in the warm and permanently frozen regions. The results of the calculations have also revealed that the efficiency of the OTEC cycle is higher in the circumpolar zone. Selecting a low-boiling medium and designing a highly efficient turbine operating in both abovementioned regimes is technically realisable.

Key words: Ocean Thermal Energy Conversion (OTEC) cycles; Organic Rankine Cycle (ORC); low-boiling media; steam turbines; turbine design

INTRODUCTION

Seas and oceans are the world largest reservoirs in which thermal energy of sunbeams is accumulated. The sunlight falling on the ocean surface is intensively absorbed by the water which collects all its energy in the shallow surface layer. Unlike the solar energy, the intensity and concentration of which is subject to steady cycles and accidental disturbances, the energy of seas and oceans reveals stable intensity, both in 24 hr and annual time scale. This is an important advantage as it leaves aside the problem of energy storage and its costs. In tropical regions of oceans, approximately between 15° north and 15° south latitude, the heat collected from sunbeams heats the water in the shallow surface layer to the practically constant temperature nearing 28 °C. The annual average temperature in the entire region ranges approximately between 27 °C and 29 °C. Below the warm surface layer the water becomes colder, and at the depth between 800 and 1000 m the water temperature drops down to about 4 °C. Depending on the region, temperature changes can take different courses and for instance, at the depth of 200 m the water temperature can be already as low as 7 °C. The temperature difference is kept constant all year round, with small deviations of a few Celsius degrees resulting from seasonal weather and day/night changes. Utilisation of this difference bases on the application of a working medium which evaporates at the surface temperature and condensates when cooled by the water taken from the much deeper level. This type of energy conversion is frequently referred to as

Ocean Thermal Energy Conversion (OTEC). A key issue in case of localisation of a number of OTEC units close to each other is the distance between them. Due to outlet water disposal, this distance should not be excessively small. This aspect is of high importance as the surface waters are cooled each time the outlet water is disposed from an open OTEC installation. In the system of combined units the excessive amount of water disposed by the system can considerably decrease the temperature of the surrounding regions, which in turn can affect the efficiency of all power plants situated nearby. Initial concepts on how to make use of the energy collected in seas were presented by J. d'Arsonval (France) in 1881. The first experimental object of this type was built by his pupil, G. Claude, in Matanzas near Cuba in 1928. The power output of the installation was 22 kW and it worked only for 2 weeks, after which was partially destroyed by typhoons. In late fifties of the last century French researchers began again to study the subject, building an installation in the Ivory Coast region. Further development in this field was initiated in 1960 by Andersens, two Americans, father and son, who established a private company exploring thermal energy from seas using OTEC technology. A few years later a 50 kW semi-technical system was built in the USA, which was followed by a fully technical one of 1 MW power output, built in 1980 and installed on a reconstructed ship. Cold water amounting to 450 tonnes was delivered using polyethylene pipes having the diameter of 1.5 m and length of 700 m. In 1981, on Nauru island in Japan a stationary 100 kW installation was built, to which 1410 t/h

Tab. 1. List of demonstrative OTEC power plants [8]

Item	Year	Location	Producer	Power [kW]	Cycle
1	1930	Cuba	Claude, France	22	Open
2	1979	Hawaii	Mini OTEC, USA	53	Closed
3	1980	Hawaii	OTEC-1, USA	1000	Closed
4	1982	Nauru	Toshiba&TEPC, Japan	120	Closed
5	1984	Saga	Saga University, Japan	75	Open
6	1992	Hawaii	Nelha, USA	210	Closed
7	1992-1998	Hawaii	Nelha, USA	50	Closed
8	1995	Saga	Saga University, Japan	9	Closed
9	2000	Tuticorin	NIOT, Indie	1000	Closed

of cold water having the temperature of 8 °C was delivered from the sea bottom using a 1093 m long pipe. In this area the temperature of surface waters nears 30 °C. About 75 % of the produced energy was used for own purposes of the installation and the remaining part was transmitted to the electric network. Tab. 1 collects demonstrative OTEC power plants which were the objects of examination.

Plans are to build a power plant fed by the Gulf Stream which flows near the USA. The temperature difference between the Gulf Stream and the surrounding waters secures efficient recovery of thermal energy at remarkable cost reduction resulting from a short distance between the lower and upper heat sources, and the disposal of the used water to the Gulf Stream which will transport it away. At the beginning of the 21-th century, numerous countries, mainly Australia, Germany, France, the United Kingdom, the Netherlands, Italy, India, Japan, Canada, and the USA, began to value thermal energy collected from the oceans to produce electric energy and intensified their activities oriented on development of technologies leading to most effective use of this energy [2÷7, 9, 13, 15, 18, 20÷22]. Technical solutions of these installations base on the Open Cycle - Ocean Thermal Energy Conversion (OC - OTEC) cycle and the Closed Cycle - Ocean Thermal Energy Conversion (CC - OTEC) cycle. Open systems make use of the water pumped directly from the ocean. The water evaporates when flowing through the low-pressure chamber in which the pressure is decreased below the condensation point. This way salt is separated from the water. Thermal energy needed for steam

production in the evaporator is released by the surface water which is the upper heat source. After leaving the evaporator, the produced steam expands in the turbine and then flows to the condenser cooled with the water taken from deeper levels of the ocean. Oxygen, carbon dioxide, and nitrogen, which have been dissolved in the oceanic water and are not subject to condensation in the condenser, are released to the environment using the vacuum pump which increases the pressure to the level required for purifying the installation from these gases (Fig. 1). A characteristic feature of open installations is relatively high speed of medium evaporation, which is directly related with the processes of mass and heat transfer. The steam produced in the heat exchanger reveals low, or zero salt concentration, along with relatively low toxicity. Further possible utilisation of the medium used in the system can be an additional attractive feature of the discussed cycle in places where clean water is hardly accessible and highly required.

In case of closed systems, the principle of their operation is the same as in the Rankine cycle (Fig. 2). In this concept the surface water is also used as the upper heat source. The energy from outside is passed to the medium in the heat exchanger to make it evaporate. Due to smaller specific volume of the working medium, the dimensions of the devices are smaller than in open cycle installations. Proposals can be found in the literature to combine OTEC systems with solar collectors, thus creating so called Solar and Ocean Thermal Energy Conversion (SOTEC) systems. Such solutions increase the efficiency of the entire cycle [6], [22].

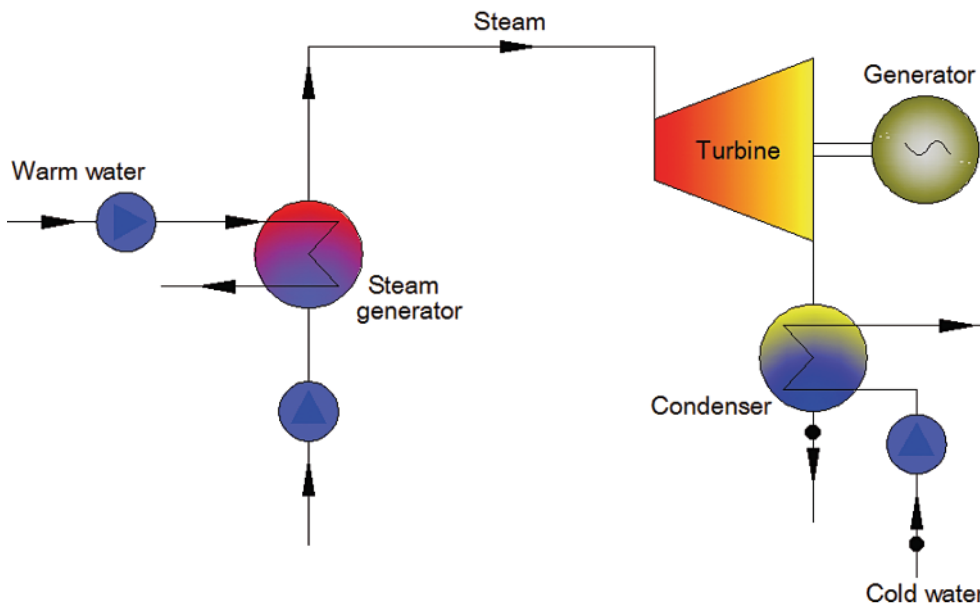


Fig. 1. Scheme of open OTEC cycle

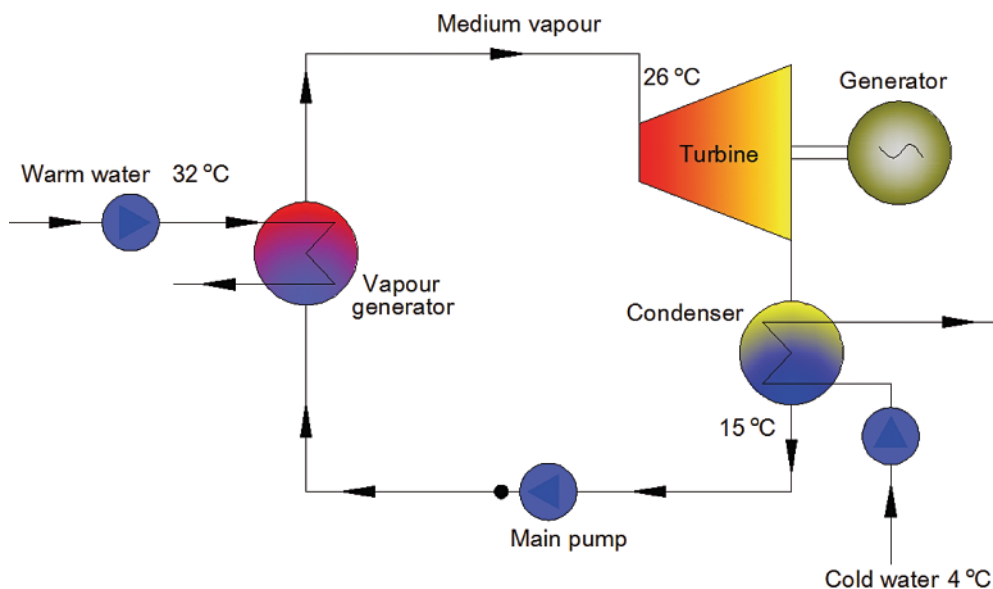


Fig. 2. Scheme of closed OTEC cycle

In each cycle making use of thermal energy of seas and oceans, particular attention is paid to leak tightness of installation components. Due to huge mass flow rates and high requirements for warm and cold water, remarkable part of the produced electric energy is used for covering own needs of the installation, mainly connected with pump feeding. Elimination of leakages to the environment improves the overall efficiency. Both organic and non-organic media can be used in CC – OTEC cycles. Low-boiling media ideally meet conditions for liquids used in those units, and their biggest advantages are low boiling pressure and temperature which is frequently lower than 0°. However, their use is sometimes connected with certain inconveniences, as they reveal, to a smaller or greater extent, flammability and/or toxicity. Their possible direct contact with the environment is highly inadvisable. Advanced protection concerning safety of work, i.e. leakage tightness of the closed cycle, is in this context fully justified.

LOW-BOILING MEDIA

Working media should meet various requirements which are not connected with their thermal characteristics. First of all, they should not be toxic and should be environment friendly. They should be cheap and easily accessible. They cannot react with flow system components. A properly selected low-boiling medium should provide opportunities for system operation at highest possible efficiency, and for maximal possible utilisation of the available heat source. Other very important criteria which are to be met by the working medium and are to be taken into account in its selection include: low freezing temperature, high critical temperature, corrosion passiveness, lack of toxicity, incombustibility, low price, etc. Moreover, it is important for the working medium not to produce any threat for human beings and the environment. The effect of a given medium on the environment is measured using ecological coefficients, mainly ODP (Ozone Depletion Potential) and GWP (Global Warming Potential).

ASSESSMENT OF RESULTS OF CALCULATIONS OF CIRCUM-EQUATORIAL OTEC CYCLE

Within the framework of the present analysis, calculations were performed for the closed OTEC cycle working in conditions characteristic for circum-equatorial regions (see

Fig. 2). The temperatures of the media assumed for the calculations are shown in the figure. The next assumption was the mass flow rate of 100 kg/s used for vapour production in the evaporator. For the closed OTEC cycle power plant several tens of media were analysed, after which more than ten media securing high cycle efficiency and technical realisability were selected [10, 11, 19]. The below presented results refer to the following selected media: Water, Acetone, Methanol, Isobutane, Dimethyl ether, R114, R227ea, R245fa, Trifluoriodomethane, R124, R1234ze, Ammonia. For each medium the pressure at turbine inlet was optimised in such a way that maximum power was reached, and the heat exchanger design was technically realisable.

From the warm water mass flow rate equal to 100 kg/s we can produce, approximately, from 48 to 50 kW of turbine shaft power (see Fig. 3), which corresponds to cycle efficiency not exceeding 2.9 % (see Tab. 2). The power outputs obtained in the analysis were close to each other, therefore medium selection should be based on other parameters which would secure designing a cheap, reliable, and highly efficient installation. The experience gained in Japanese experiments suggests that the costs of the working medium, turbine, pumps and heat exchangers amount to as much as about 20 %. In this situation attempts are to be made for the turbine cycle units to be properly optimised. Main attention was focused here on optimisation of the design parameters of the turbine working with selected low-boiling media [14].

The analysis included optimisation of design parameters for a single-stage axial turbine with respect to the generated power output. The optimised parameters were the following: velocity coefficient, reaction, rotational speed, and supply arc dimension. An attempt was also made to keep the ratio of the effective diameter to the blade length larger than 4. Another parameter which was also assessed and taken into account in the optimisation was the Mach number. Tab. 1 presents a collection of optimal parameters for the single-stage axial turbine. In steam turbines typical values of the velocity coefficient depend on the type of the turbine stage and range from 0.4 to 0.5 for impulse stages, and even as much as from about 0.6 to 0.7 for reaction stages. For the analysed media the selected velocity coefficient not exceeded 0.6 (see Fig. 4), which is a typical range for systems of this type. The stage reaction was selected in such a way that the peripheral efficiency was the highest possible, keeping at the same time the hub reaction not larger than 0.05. Typical reaction used in

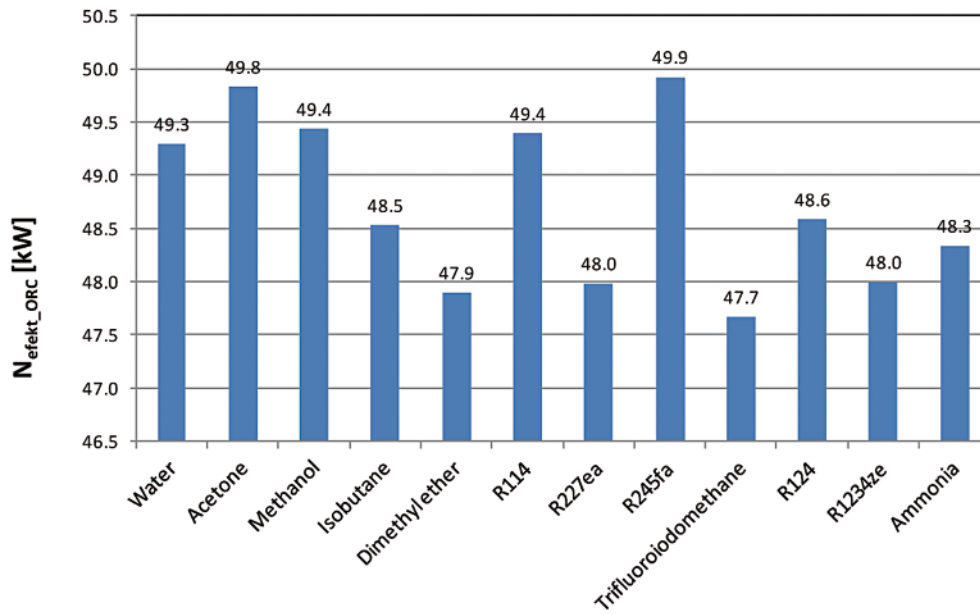


Fig. 3. Turbine shaft power for the examined media

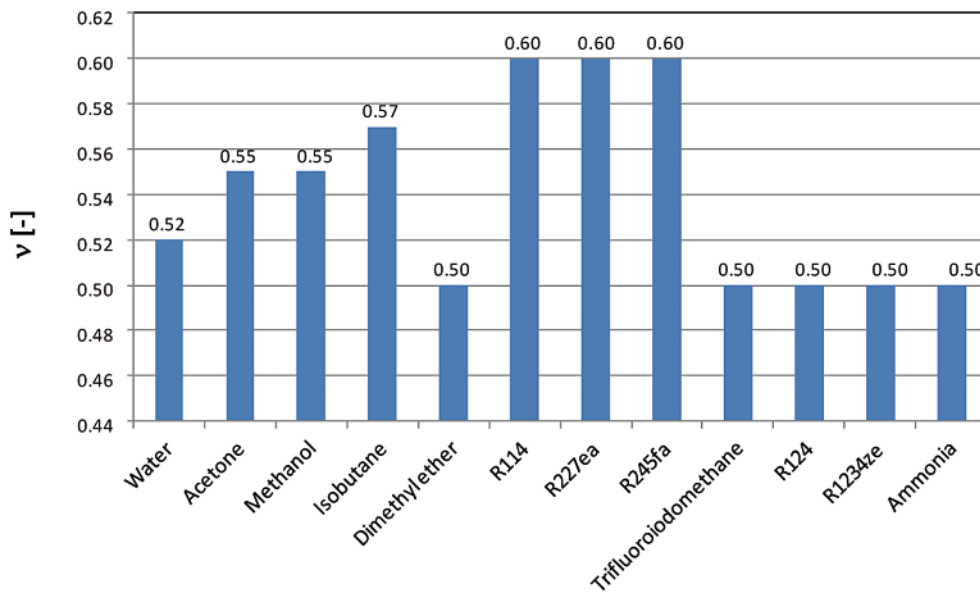


Fig. 4. Single-stage turbine velocity coefficient for the examined media

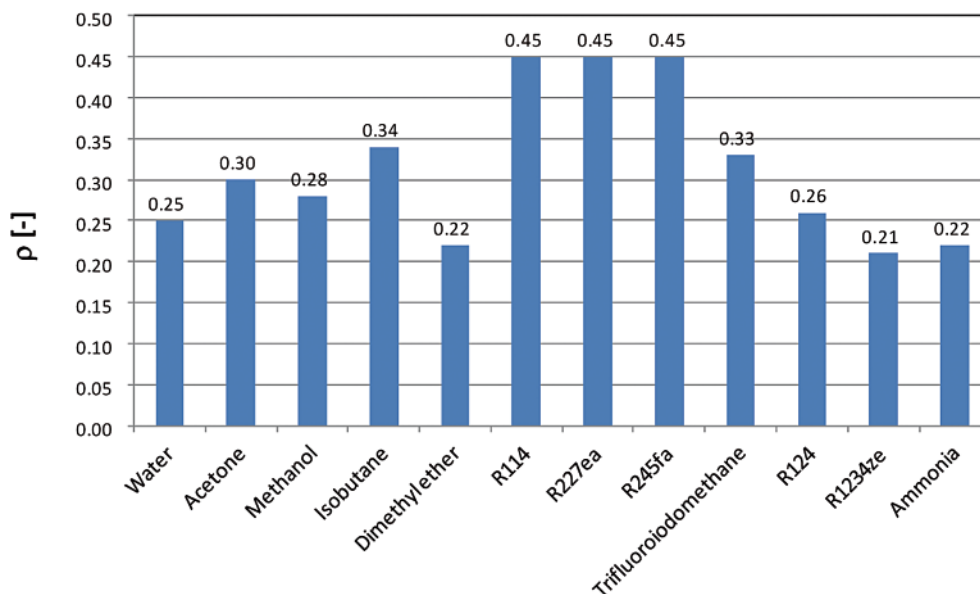


Fig. 5. Single-stage turbine reaction for the examined media

turbine stages does not exceed 0.7. During the present analysis the stage reaction did not exceed 0.5 (see Fig. 5), i.e. it also took typical values [12]. The rotational speed obtained in the analysis depended on the type of medium and was equal to 3000 and 6000 rpm for most media, while for Trifluoroiodomethane and Ammonia it was equal to 15000 and 16000 rpm, respectively (see Fig. 6). All these values are acceptable for technical realisation. In most cases full supply arc was reached, only for Trifluoroiodomethane it did not exceed 5 % (see Table 2). Reduction of the supply arc dimension increases remarkably the ventilation loss and decreases the internal stage work. This result, combined with slightly lower efficiency eliminates the above medium as a working medium.

The turbine was designed in such a way as to obtain the length of the blades not smaller than 10 mm and the D/L ratio not lower than 4 (see Fig. 7 and Fig. 8). This condition was met

for the reported media. The selected design parameters should have secured not exceeding 1 by the Mach number at stator and rotor exits. This condition was also met, and in each case subsonic stages were obtained (see Fig. 9 and Fig. 10). The performed analysis has proved that a highly efficient single-stage axial turbine can be designed for most of the examined media (excluding Trifluoroiodomethane). However, it seems that very low pressure (high negative pressure) eliminates water, acetone and methanol. In this situation, the media which looks most favourable from the technical point of view are R114, R245fa and Ammonia. Here, other criteria are to be taken into account, including toxicity of the medium (safety in case of leakage) and its effect on the environment. A detailed and realistic economic analysis is also to be performed. Final selection of a relevant medium will be a compromise between the advantages and disadvantages of this medium.

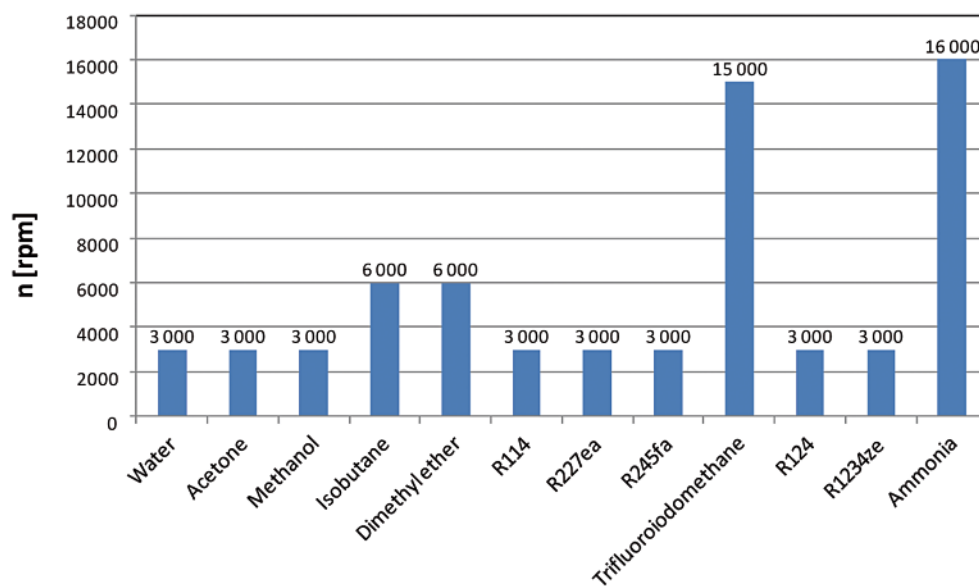


Fig. 6. Single-stage turbine rotational speed for the examined media

Tab. 2. Comparison of calculated results for closed OTEC power plant with turbine design parameters; where: $N_{\text{efekt_ORC}}$ -effective power of the cycle; η_{par} -cycle efficiency; η_{carnot} -Carnot cycle efficiency; p_0 -medium vapour pressure at turbine inlet; $m_{0\text{par}}$ -medium vapour mass flow rate; H_s -isentropic enthalpy drop in the turbine; v -velocity coefficient; ρ -stage reaction; Ma_{e1} -Mach number at stage stator exit; ε -supply arc dimension; n -rotational speed; D_{sr} -mean stage diameter; l_s -stator blade length; D/l -mean diameter-to-blade length ratio; Ma_{w2} -Mach number at stage rotor exit

Parameter	$N_{\text{efekt_ORC}}$	η_{par}	η_{carnot}	p_0	$m_{0\text{par}}$	H_s	v	ρ	Ma_{e1}	ε	n	D_{sr}	l_s	D/l	Ma_{w2}
Medium/Unit	[kW]	[-]	[-]	[MPa]	[kg/s]	[kJ/kg]	[-]	[-]	[-]	[-]	[rpm]	[m]	[m]	[-]	[-]
Water	49.29	0.0289	0.0368	0.0033	0.686	89.81	0.52	0.25	0.24	1	3000	1.403	0.126	11.1	0.17
Acetone	49.83	0.0285	0.0368	0.0319	3.141	19.89	0.55	0.30	0.75	1	3000	0.698	0.081	8.6	0.56
Methanol	49.43	0.0288	0.0368	0.0178	1.436	43.08	0.55	0.28	0.21	1	3000	1.028	0.059	17.4	0.15
Isobutane	48.53	0.0273	0.0368	0.3600	5.105	12.62	0.57	0.34	0.61	1	6000	0.288	0.041	7.0	0.47
Dimethyl ether	47.90	0.0268	0.0368	0.6057	4.198	15.29	0.50	0.22	0.64	1	6000	0.278	0.022	12.7	0.42
R114	49.39	0.0280	0.0368	0.2207	13.108	4.89	0.60	0.45	0.59	1	3000	0.378	0.027	14.2	0.59
R227ea	47.98	0.0267	0.0368	0.4674	15.070	4.37	0.60	0.45	0.59	1	3000	0.357	0.015	23.8	0.59
R245fa	49.92	0.0281	0.0368	0.1533	8.830	7.22	0.60	0.45	0.62	1	3000	0.459	0.023	20.0	0.63
Trifluoroiodomethane	47.67	0.0266	0.0368	0.5046	18.487	3.48	0.50	0.33	0.14	0.045	15000	0.053	0.010	5.4	0.11
R124	48.58	0.0271	0.0368	0.3934	11.472	5.64	0.50	0.26	0.67	1	3000	0.338	0.034	10.1	0.47
R1234ze	47.99	0.0267	0.0368	0.5123	10.086	6.46	0.50	0.21	0.68	1	3000	0.362	0.027	13.3	0.44
Ammonia	48.34	0.0276	0.0368	1.0313	1.443	43.80	0.50	0.22	0.62	1	16000	0.177	0.011	15.8	0.12

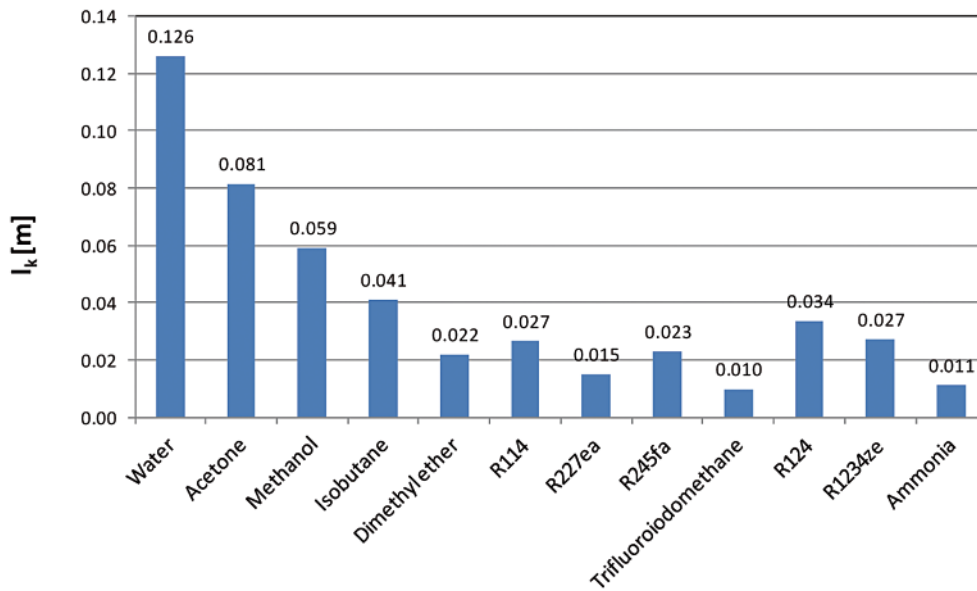


Fig. 7. Single-stage turbine stator blade length for the examined media

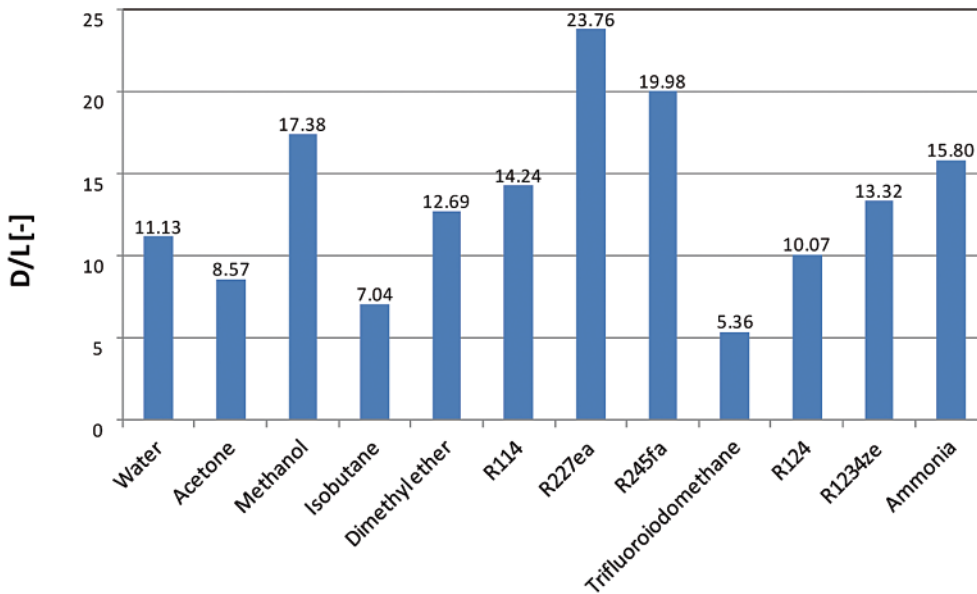


Fig. 8. Single-stage turbine D/L ratio for the examined media

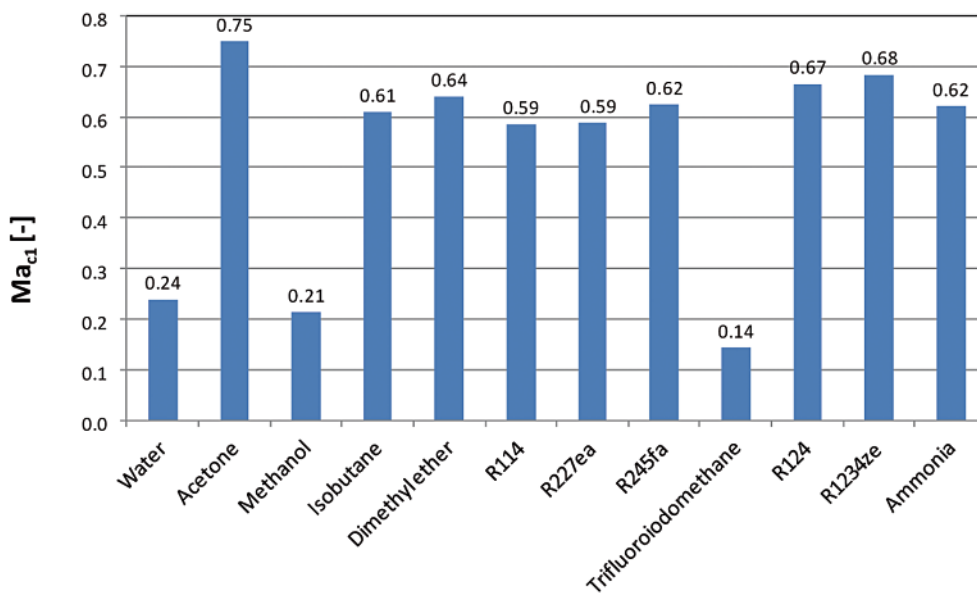


Fig. 9. Absolute Mach number behind single-stage turbine stator for the examined media

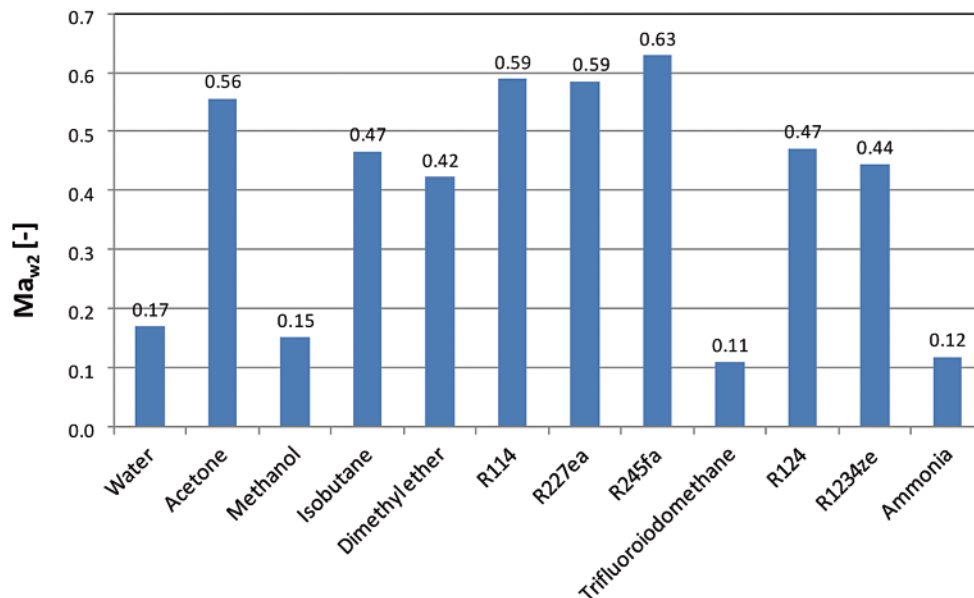


Fig. 10. Relative Mach number behind single-stage turbine rotor

RESULTS OF CALCULATIONS FOR ARCTIC OTEC CYCLE AND THEIR EVALUATION

For this cycle a system was proposed which makes use of temperature difference between the frosty arctic air and the non-frozen oceanic water, which eliminates the use of long pipes for its collection. In the cycle shown in Fig. 11 a condenser cooled with frosty air was applied. Other media revealing low freezing temperature, aqueous solution of calcium chloride for instance, can also be applied [1].

The temperatures of the media assumed in arctic OTEC cycle calculations are shown in Fig. 11. The mass flow rate of the non-frozen water which was used for generating medium vapour in the vapour generator was assumed equal to 100 kg/s. In this case also several tens of media were analysed and, like previously, between ten and twenty media were selected as those which secure high cycle efficiency and technical realisability. Below are presented results of the analysis referring to the selected media, which were: Trifluoroiodomethane, Dimethyl ether, CO_2 , R23, R13, R218, Sulfur hexafluoride, R116, R245fa, R143a, Ethane, R124, R1234ze and Ammonia. Like in previous case, for each medium the turbine inlet pressure

was optimised in such a way that maximum shaft power was obtained for this pressure and the design of the heat exchanger was technically realisable. Approximately, from 30 to 80 kW of the turbine shaft power can be produced from the assumed mass flow rate of the warm water (see Fig. 12). In the examined arctic variant the obtained power levels differed much between each other. The largest power was produced using Trifluoroiodomethane, Dimethyl ether, and Ammonia as working medium. As for the cycle efficiency, the above list of three media was complemented by R218, R245fa, R124 and R1234ze, for which the recorded efficiency exceeded 6 % (see Tab. 3). In the next step, optimisation of the design parameters for a single-stage axial microturbine was carried out. The list of optimised parameters included: velocity coefficient, reaction, rotational speed, and supply arc dimension. An attempt was made to keep the ratio of the effective diameter to the rotor blade length larger than 4. A parameter which was also assessed and taken into account in the optimisation was the Mach number. Table 3 presents a collection of optimal parameters for the single-stage axial turbine.

The velocity coefficient selected for the analysed media ranged up to 0.7 (see Fig. 13). The stage reaction did not exceed 0.5 (see Fig. 14). During the analyses different rotational speeds

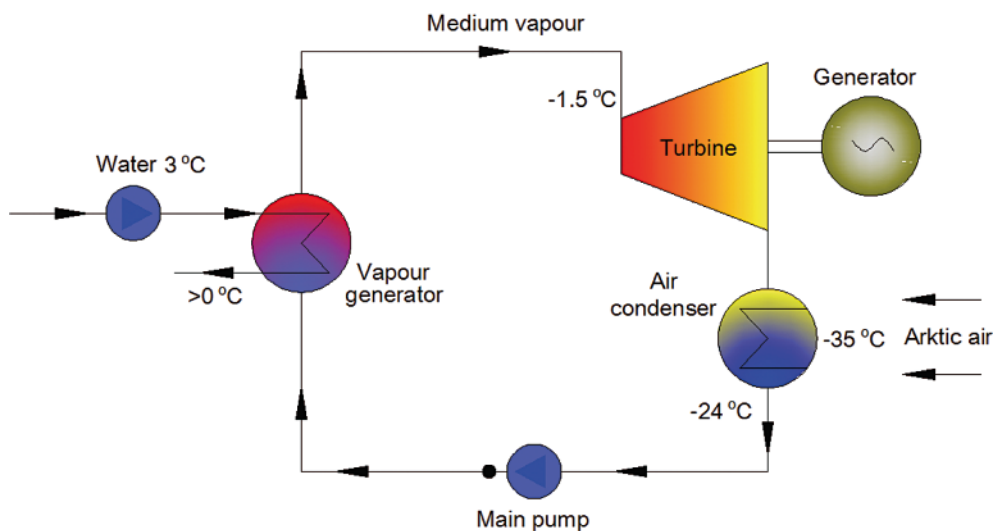


Fig. 11. Scheme of closed OTEC cycle in arctic version

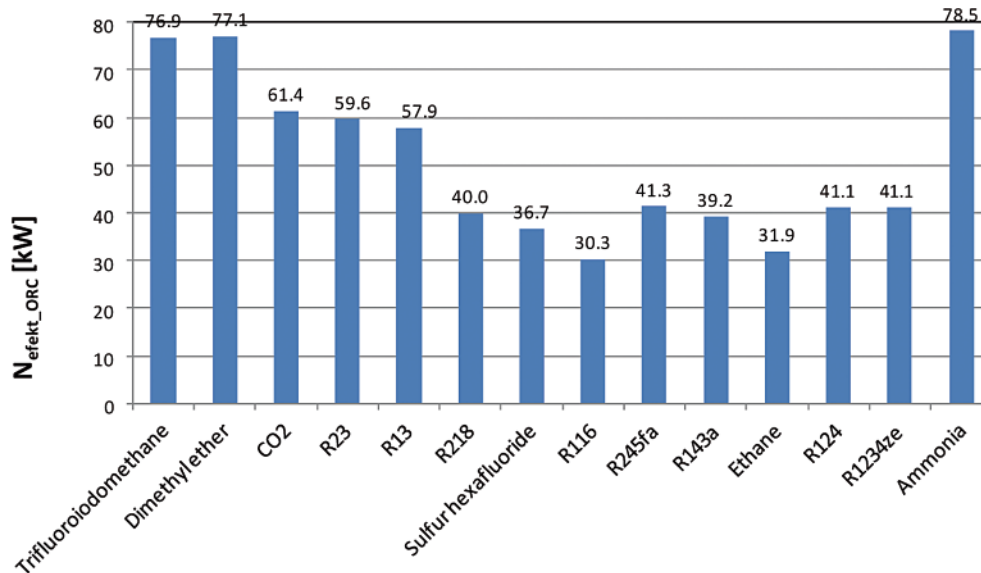


Fig. 12. Turbine shaft power for the examined media

were obtained for different media, they took values from 3000 rpm, to even as much as 37000 rpm for Ammonia (see Fig. 15), which was still technically realisable. In most cases a full supply arc was obtained, excluding Trifluoroiodomethane, Dimethyl ether, Ammonia and Ethane, for which the supply arc dimension did not exceed 20 % (see Table 3). In the latter situation the ventilation loss increases remarkable and the internal stage work decreases. The turbine was designed in such a way as to obtain the blade length not smaller than 10 mm and the D/L ratio not smaller than 4 (see Fig. 16 and Fig. 17). This condition was successfully met for the presented media. The design parameters were selected assuming that the Mach number at turbine stator and rotor exits does not exceed 1. This

condition was also successfully met, and each time a subsonic stage was obtained (see Fig. 18 and Fig. 19). The performed analysis has confirmed that designing a highly efficient single-stage axial turbine is possible for the majority of the analysed media, from which: Trifluoroiodomethane, Dimethyl ether, Ammonia, R218, R245fa, R124 and R1234ze seem to be most favourable from the thermodynamic and technical point of view. If we take into account toxicity of particular media and their effect on the environment (see Tab. 4), the most favourable medium is R245fa which is non-flammable and nontoxic. However, a detailed and realistic economic analysis is to be performed to select finally an optimal medium for the system of this type.

Tab. 3. Comparison of calculation results for arctic OTEC power plant with turbine design parameters; where: $N_{\text{efeakt_ORC}}$ -effective power of the cycle; η_{par} -cycle efficiency; η_{Carnot} -Carnot cycle efficiency; p_0 -medium vapour pressure at turbine inlet; m_{opary} -medium vapour mass flow rate; H_s -isotropic enthalpy drop in the turbine; v -velocity coefficient; ρ -stage reaction; Ma_{el} -Mach number at stage stator exit; ϵ -supply arc dimension; n -rotational speed; D_{sr} -mean stage diameter; l_s -stator blade length; D/l -mean diameter-to-blade length ratio; Ma_{w2} -Mach number at stage rotor exit

Parameter	$N_{\text{efeakt_ORC}}$	η_{par}	η_{Carnot}	p_0	m_{opary}	H_s	v	ρ	Ma_{el}	ϵ	n	D_{sr}	l_s	D/l	Ma_{w2}
Medium/Unit	[kW]	[-]	[-]	[MPa]	[kg/s]	[kJ/kg]	[-]	[-]	[-]	[-]	[rpm]	[m]	[m]	[-]	[-]
Trifluoroiodomethane	76.86	0.0615	0.0828	0.2158	11.31	8.70	0.50	0.30	0.18	0.10	12000	0.105	0.010	10.37	0.13
Dimethyl ether	77.11	0.0617	0.0828	0.252	2.56	38.43	0.49	0.22	0.21	0.20	27000	0.096	0.010	9.70	0.69
CO2	61.37	0.0491	0.0828	3.34	4.42	23.17	0.50	0.23	0.82	1.00	23000	0.089	0.010	8.69	0.56
R23	59.59	0.0479	0.0828	2.3885	7.12	14.18	0.66	0.28	0.30	1.00	3000	0.708	0.108	6.56	0.21
R13	57.90	0.0466	0.0828	1.8885	10.64	9.44	0.70	0.35	0.29	1.00	3000	0.612	0.124	4.93	0.23
R218	39.96	0.0611	0.0828	0.3934	6.24	8.55	0.55	0.45	0.89	1.00	6000	0.229	0.027	8.58	0.82
Sulphur hexafluoride	36.72	0.0533	0.0828	1.1974	6.59	8.31	0.52	0.32	0.91	1.00	9000	0.142	0.016	8.89	0.68
R116	30.31	0.0415	0.0828	1.7673	7.92	7.26	0.50	0.30	0.32	1.00	9000	0.128	0.014	8.96	0.68
R245fa	41.30	0.0627	0.0828	0.0492	2.86	18.17	0.55	0.47	0.99	1.00	4500	0.445	0.061	7.31	0.97
R143a	39.21	0.0584	0.0828	0.5893	3.03	17.30	0.49	0.30	0.24	1.00	11000	0.158	0.018	8.82	0.17
Ethane	31.90	0.0462	0.0828	2.2955	1.82	30.84	0.50	0.22	0.27	0.50	21000	0.113	0.012	9.48	0.55
R124	41.15	0.0621	0.0828	0.1534	3.65	14.35	0.55	0.45	0.92	1.00	6000	0.297	0.036	8.14	0.87
R1234ze	41.11	0.0617	0.0828	0.204	3.17	16.59	0.49	0.40	0.96	1.00	6000	0.284	0.027	10.50	0.85
Ammonia	78.45	0.0630	0.0828	0.4043	0.91	109.32	0.50	0.50	0.19	0.16	37000	0.121	0.010	12.10	0.82

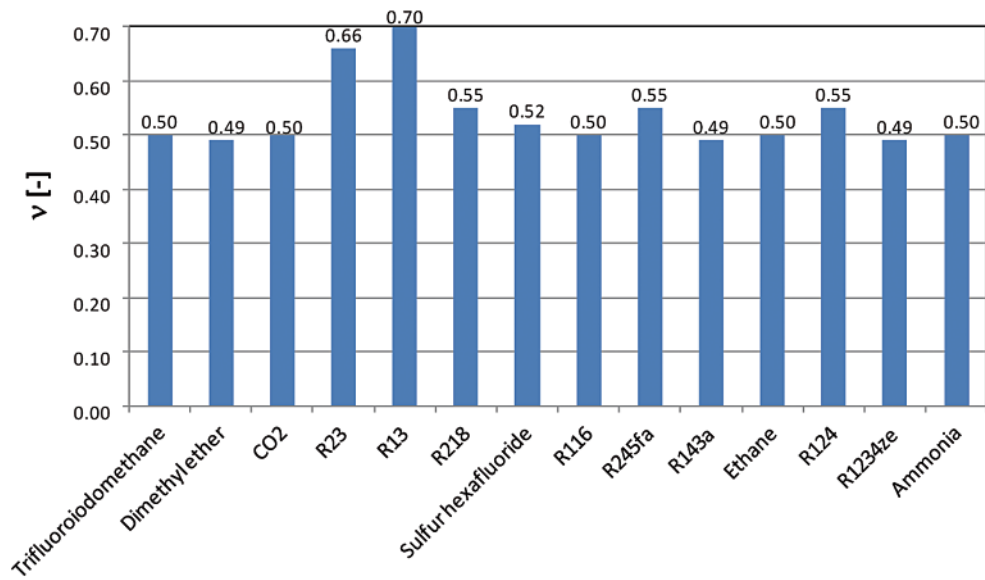


Fig. 13. Single-stage turbine velocity coefficient for the examined media

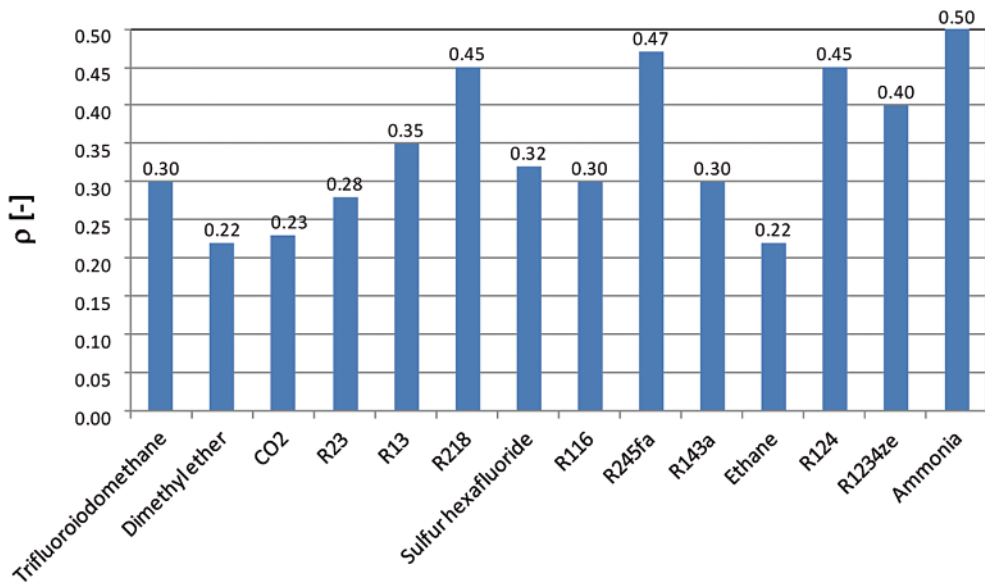


Fig. 14. Single-stage turbine reaction for the examined media

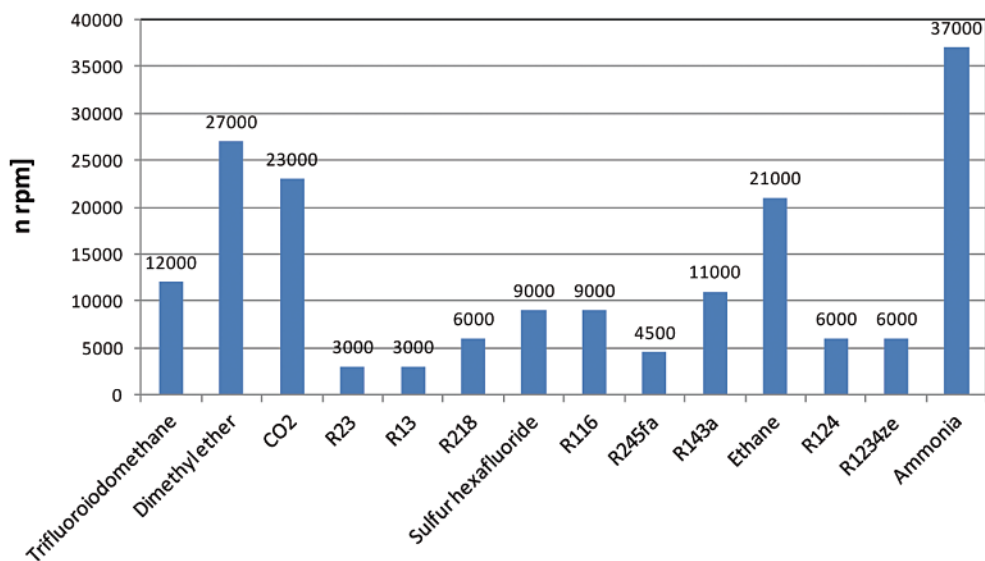


Fig. 15. Single-stage turbine rotational speed for the examined media

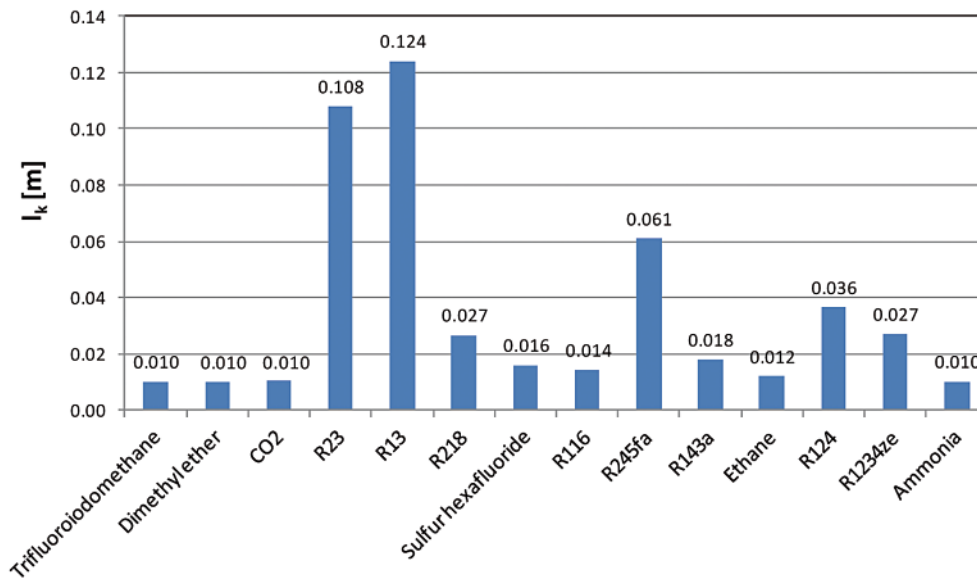


Fig. 16. Single-stage turbine stator blade length for the examined media

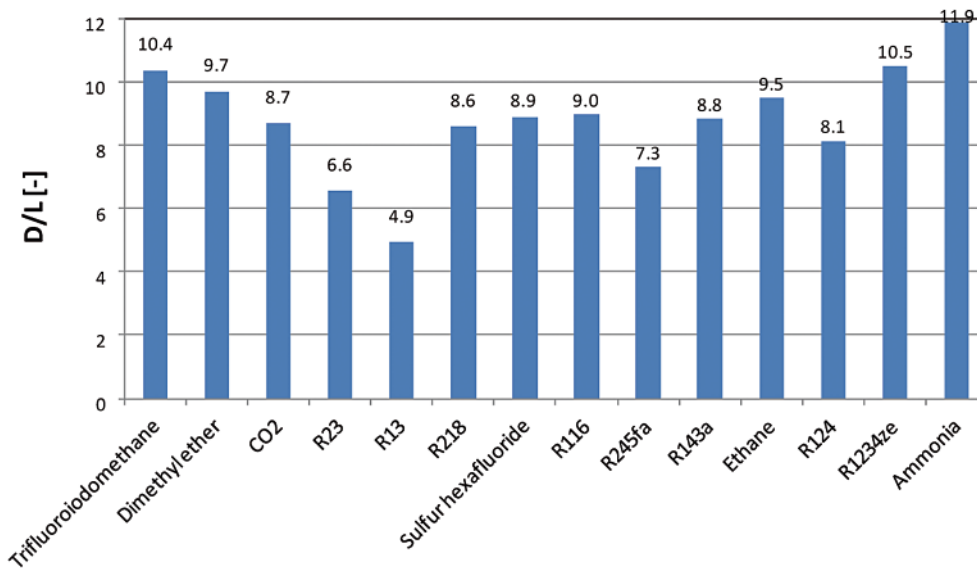


Fig. 17. Single-stage turbine D/L ratio for the examined media

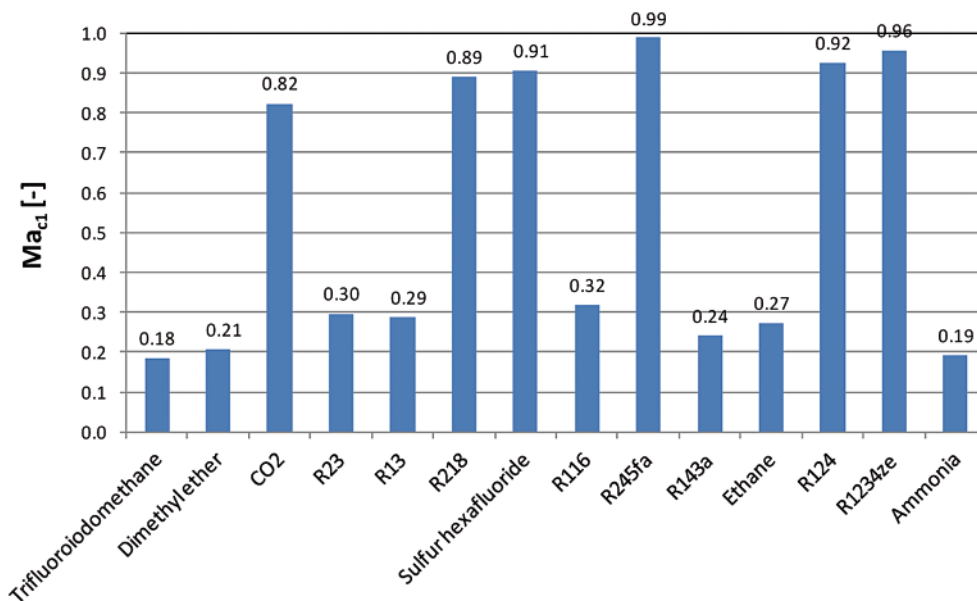


Fig. 18. Absolute Mach number behind single-stage turbine stator for the examined media

Tab. 4. Comparison of features of the recommended media [5, 6, 10, 16, 17, 19]

ASHARE medium number	RE170	R245fa	R717	R114	R1234ze	R218
Type	HC-hydrocarbon	HFC-hydrofluorocarbon	-	CFC-chlorofluorocarbon	HFO-Hydrofluoroolefin	PFC-perfluorocarbon
Medium name	Dimethyl ether	1,1,1,3,3-Pentafluoropropane	Ammonia	1,2-Dichlorotetrafluoroethane	Trans-1,3,3,3-tetrafluoropropene	Octafluoropropane
Chemical formula of the medium	CH ₃ OCH ₃	C ₃ H ₃ F ₅	NH ₃	C ₂ F ₄ Cl ₂	C3F4H2	C ₃ F ₈
Lifetime in the atmosphere [years]	0.015	7.6	0.019	300	0.05	2600
Molar mass [kg/kgmol]	46.07	134.05	17.03	170.92	114.04	188.02
Critical temperature [C]	127.22	154	132.24	145.67	109.36	71.86
Critical pressure [MPa]	5.34	3.65	11.33	3.26	3.64	2.64
Critical specific volume [m ³ /kg]	0.0037	0.0019	0.0012	0.0017	0.0020	0.0016
Thermal conductivity [mW/m-K]	18.45	13.27	25.39	10.47	13.97	12.93
Kinematic viscosity coefficient j [μPa-s]	9.26	10.49	14.53	11.00	12.58	12.70
Ozone depletion potential ODP [-]	0	0	0	1	0	0
Global warming potential GWP [-]	0	1030	0	10000	6	7000
Triple point temperature [C]	-141.51	-102.11	-77.665	-	-104.54	-147.71
Triple point pressure [Pa]	2.21	12.51	6091.22	-	231.28	2.02
Boiling point temperature [C]	-24.79	15.13	-33.34	3.58	-18.97	-36.80
Flammability	Highly flammable	Non-flammable	Flammable	Non-flammable	Flammable	Non-flammable
Effect on human being	Toxic	Not classified as harmful to human being	Heavily toxic	Toxic	Toxic	Toxic

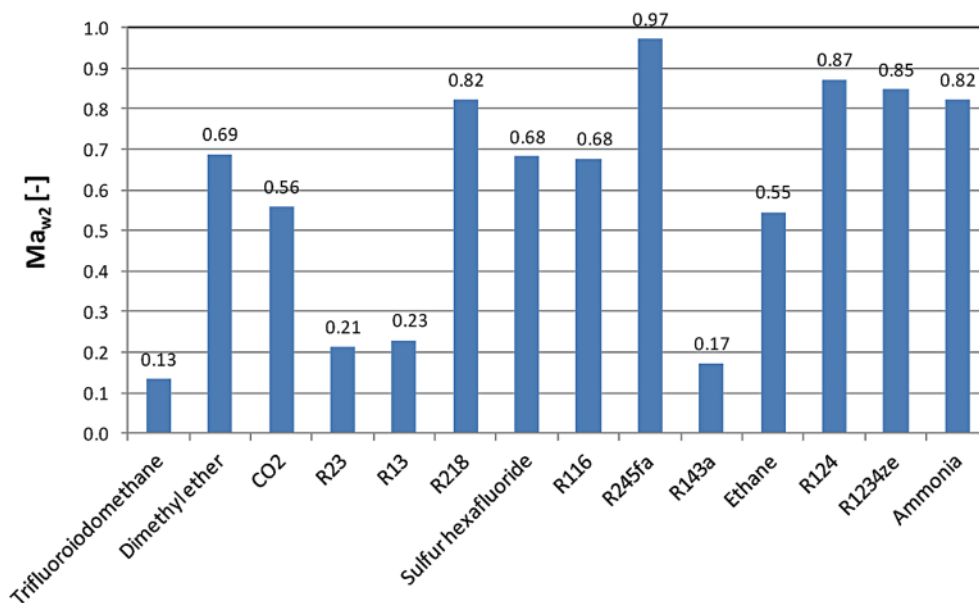


Fig. 19. Relative Mach number behind single-stage turbine rotor for the examined media

CONCLUSIONS

To sum up, OTEC power plants are the source of clean and renewable electric energy. Along with the energy they can produce fresh water, which is of high importance in the areas with its shortages. A properly designed system generates limited, or even zero amount of carbon dioxide. It is optimistically estimated that the resources of thermal energy are so high that they can meet all current power requirements of the human society. Its disadvantage still remains high production cost, which is remarkably higher than in case of energy production from coal. For the operation of this type of power plant to be possible, the temperature difference between the upper and lower heat source should reach about 20 °C, the least. Moreover, vast resources of cold water should be situated close to the land for large power plants to be erected in the vicinity of human agglomerations. Up to the present, certain problems can be observed with collecting financial support for such actions, as only small-scale systems have been tested so far. Another disadvantage is unfavourable effect of on the environment, as localisation of power plants (pipes with warm and cold water) close to the land unfavourably affects the off-shore marine ecosystem and reefs. The here reported analysis has proved that constructing a system which utilises thermal energy stored in oceans is possible. It has also turned out that higher potential is this field can be found in the circumpolar regions. For the assumed mass flow rate of the water used for producing the organic medium vapour, certain media were proposed which secured installation efficiency exceeding 6 %. This result does not seem impressive, but the source of this energy is practically inexhaustible.

For a group of low-boiling media a preliminary design of the axial turbine was presented. The realistic ranges of the selected design parameters have proved that constructing a highly efficient turbine making use of low-boiling medium is possible.

BIBLIOGRAPHY

1. Akulich V., Ilyin A., Tikmenov V.A. *Possibility of Using OTEC Systems in Arctic Regions*, OCEANS '83, Proceedings, Aug. 29 1983-Sept. 1 1983;
2. Bogdanienko J. *Renewable energy sources (in Polish)*, PWN, Warsaw, 1989;
3. Breeze P. *Power Generation Technologies*, ISBN 0 7506 6313 8, Elsevier's Science and Technology Rights Department in Oxford, London, UK, 2005;
4. Chong H-Y., Lam W-H. *Ocean renewable energy in Malaysia The potential of the Straits of Malacca*, Renewable and Sustainable Energy Reviews 23, 2013;
5. Cohen R. *Energy from the ocean*, Phil. Trans. R. Soc. Lond. A 307, 1982;
6. [Electronic document], access mode: <http://www.otec.ws>, [reading: 03-04-2013];
7. [Electronic document], access mode: http://www.buch-der-synergie.de/c_neu_html/c_06_10_wasser_temperaturgradient.htm [reading: 03-04-2013];
8. [Electronic document], access mode: <http://www.seasolarpower.com>, [reading: 03-04-2013];
9. Etemadi A., Emdadi A., Afshar O. A., Emami Y. *Electricity Generation by the Ocean Thermal Energy*, Energy Procedia 12, 2011;
10. Hung T.C., Wang S.K., Kuo C.H., Pei B.S., Tsai K.F. *A study of organic working fluids on system efficiency of an ORC using low-grade energy sources*, Energy 35, 2010;
11. Kim N.J., Ng K.CH., Chun W. *Using the condenser effluent from a nuclear power plant for Ocean Thermal Energy Conversion (OTEC)*, International Communications in Heat and Mass Transfer 36, 2009;
12. Kosowski K. *Selecting favourable values of basic design parameters for thermal turbines. Generalised method of turbine stage design (in Polish)*, Scientific reports of the Gdansk University of Technology, Shipbuilding, no LXII, Gdansk, 1995;
13. Lewandowski W. *Project of renewable energy sources (in Polish)*, WTN, Warszawa, 2001.
14. Mikieliewicz J., Piwowarski M., Kosowski K. *Design analysis of turbines for co-generating micro-power plant working in accordance with organic Rankine's cycle*, Polish Maritime Research, S1, ISSN 1233-2585, 2009;
15. Pelc R., Fujita R. M. *Renewable energy from the ocean*, Marine Policy 26, 2002;
16. computer code *Engineering Equation Solver*, Version 9.218, 2012;
17. Computer code *REFPROP Reference Fluid Thermodynamic and Transport Properties*, Version 8, 2007;
18. Rajagopalan K., Nihous G.C. *Estimates of global Ocean Thermal Energy Conversion (OTEC) resources using an ocean general circulation model*, Renewable Energy 50, 2013;
19. Semmari H., Stitou D., Mauran S. *A novel Carnot-based cycle for ocean thermal energy conversion*, Energy 43, 2012;
20. Vega L.A. *First Generation 50 MW OTEC Plantship for the Production of Electricity and Desalinated*, OTC 20957,

- Offshore Technology Conference, Houston, Texas, USA, 3–6 May 2010;
21. Wu Ch., Avery W. H. *Renewable Energy From the Ocean: A Guide to OTEC*, Oxford University Press, ISBN 0195071999, 1994;
 22. Yamada N., Hoshi A., Ikegami Y. *Thermal Efficiency Enhancement of Ocean Thermal Energy Conversion (OTEC) Using Solar Thermal Energy*, AIAA 2006-4130, 4th International Energy Conversion Engineering Conference and Exhibit (IECEC), San Diego, California, 26 - 29 June 2006.

CONTACT WITH THE AUTHOR

Marian Piwowarski, Ph.D.
Faculty of Ocean Engineering
and Ship Technology
Gdansk University of Technology
Narutowicza 11/12
80-233 Gdansk, POLAND
e-mail: piwom@pg.gda.pl

Numerical model to study the combustion process and emissions in the Wärtsilä 6L 46 four-stroke marine engine

Lamas, M. I., Assoc. Prof.

Rodríguez, C. G., M. Sc.

Escola Universitaria Politécnica. Universidade da Coruña, Spain

ABSTRACT

The aim of the present paper is to develop a computational fluid dynamics (CFD) analysis to study the combustion process in a four-stroke marine diesel engine, the Wärtsilä 6L 46. The motivation comes from the importance of emissions from marine engines in the global emissions, particularly for nitrogen oxides (NO_x) and sulfur oxides (SO_x). The pressure and temperature fields were obtained, as well as the exhaust gas composition. In order to validate this work, the numerical results were satisfactory compared with experimental ones, which indicates that this model is accurate enough to reproduce the fluid pattern inside the cylinder during the combustion process. Accordingly, the aim of future works is to use this numerical procedure to optimize the performance and reduce the emissions of the new marine engine designs.

Key words: Marine engine; emissions; combustion; CFD (Computational Fluid Dynamics)

INTRODUCTION

Nowadays, the world's ships are mainly powered by diesel engines. Marine diesel engines are very efficient, but they emit high levels of carbon dioxide (CO₂), nitrogen oxides (NO_x) and sulfur oxides (SO_x). Studies show that emissions of CO₂, NO_x and SO_x from ships correspond to about 2, 11 and 4% of the global anthropogenic emissions respectively (Skjrlsvik *et al.*, 2000). Carbon dioxide is not toxic, but it contributes to the greenhouse effect (global warming)¹⁾. It is the main greenhouse gas emitted by ships. Nitrogen oxides contribute significantly to the ozone layer depletion²⁾. They also form acids, which fall to earth as rain, fog, snow or dry particles, having harmful impacts on plants, animals and sea. Sulfur oxides, which are formed because of the high sulfur content of marine fuels (in order to reduce costs, ships generally use low quality fuels which tend to have a high sulfur content), are the major source of acid rain. To a lesser extent, other emissions from ships are carbon monoxide (CO), which is toxic to humans and animals; hydrocarbons, which contribute to the greenhouse effect and particulates, which can induce cardiopulmonary diseases and lung cancer. In harbour cities, emissions from ships constitute an important source of pollution. Furthermore, some gases

may be transported in the atmosphere over several hundred of kilometers, contributing to air quality problems on land.

Merchant ships in international traffic are subjected to International Maritime Organization (IMO). In particular, the IMO Marpol Annex VI (Regulations for the Prevention of Air Pollution from Ships) limits SO_x and NO_x emissions from marine engines. As SO_x emissions are a function of the sulfur content of fuel, the IMO has limited the sulfur content in fuels. Concerning the NO_x, the IMO has established a curve which indicates the maximum allowable NO_x emission levels related to the engine speed. Figure 1 shows the maximum NO_x emission levels for marine diesel engines built after 2000 (IMO Tier I), 2011 (IMO Tier II) and 2016 (IMO Tier III, only in designated special areas called emission control areas). Apart from these international limitations, some regions have developed regional and national tougher limits.

Due to this legislation, the reduction of NO_x emissions is very important for the new marine engine designs. Several studies about NO_x emissions and other pollutants from marine engines can be found in the literature. For example, those of Li *et al.* [1], Lü *et al.* [2], Holub *et al.* [3], Jayaram *et al.* [4], Yan *et al.* [5], Uriondo *et al.* [6], Bernecic and Radonja [7], Maiboom and Tauzia [8], Duran *et al.* [9] and Millo *et al.* [10]. These

¹⁾ The greenhouse effect is a process by which thermal radiation from the planetary surface is absorbed by atmospheric greenhouse gases, which re-radiate part of this heat towards the surface again. As a result, the earth's temperature is higher than it would be if direct heating by solar radiation were the only warming mechanism.

²⁾ The ozone layer is a deep layer in the stratosphere. It is composed by molecules of ozone, O₃, which filter out a lot of the sun's UV-B rays. Certain chemical substances can destroy some of the ozone, and the consequences are potentially damage to the life forms on Earth.

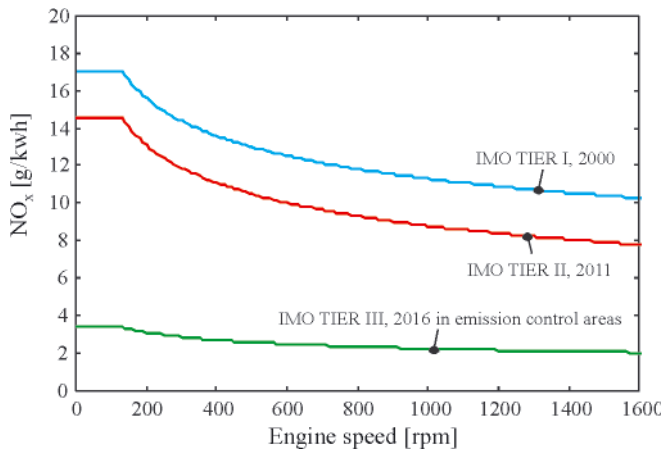


Fig. 1. IMO maximum allowable NO_x emission for marine engines

and other investigations have provided a great progress in the marine emission control technologies. However, the design of an efficient marine engine requires a complete understanding of the combustion process, which has a noticeably influence on the emissions. There are many possible combinations between the operating parameters (compression ratio, injection characteristics, combustion chamber geometry, etc), and the effects on the engine performance and emissions produced by variations of these parameters are non linear and often opposed. In this regard, CFD (Computational Fluid Dynamics) offers an important tool to study the fluid flow in detail. CFD is a branch of fluid mechanics based on the subdivision of the computational domain into small elements overlaying the whole domain. For each subdivision, the governing equations are solved using numerical methods.

This work proposes a CFD model to study the combustion process in the Wärtsilä 6L 46 four-stroke marine engine. The temperatures, pressures, advancing of the flame front and composition of the exhaust gas were obtained. The numerical model was validated with experimental measurements performed on a Wärtsilä 6L 46 installed on a tuna fishing vessel, obtaining a good agreement. This work is a continuation of Lamas *et al.* [11], in which the exhaust, intake and compression strokes of the cylinder operation were simulated.

CASE STUDIED

Technical specifications

The Wärtsilä 6L 46 studied in the present work is shown in Fig. 2. This is a four-stroke marine diesel engine with 6 cylinders in line, 46 cm bore, 58 cm stroke and 96400 cm³ cylinder displacement volume. Each cylinder has two intake valves and two exhaust valves, and the fuel injector is placed at the center of the cylinder head. Figure 3 outlines a cross-section of the engine.

The present work was developed under the conditions studied in Lamas *et al.* [11]. These are 96% load, 499.6 rpm and employing heavy fuel oil (RMG 380 according to ISO 8217). Under these conditions, the power was 5212 kW and the consumption 172 g/kWh (9.96 g of fuel injected per cycle and cylinder). The in-cylinder gauge pressure is shown in Fig. 4, obtained using the engine performance analyzer MALIN 6000 (Malin Instruments, Ltd.).

Performance and combustion process

The performance of this engine was described in Lamas *et al.* [11], where it was explained that combustion takes place



Fig. 2. Engine studied in the present work

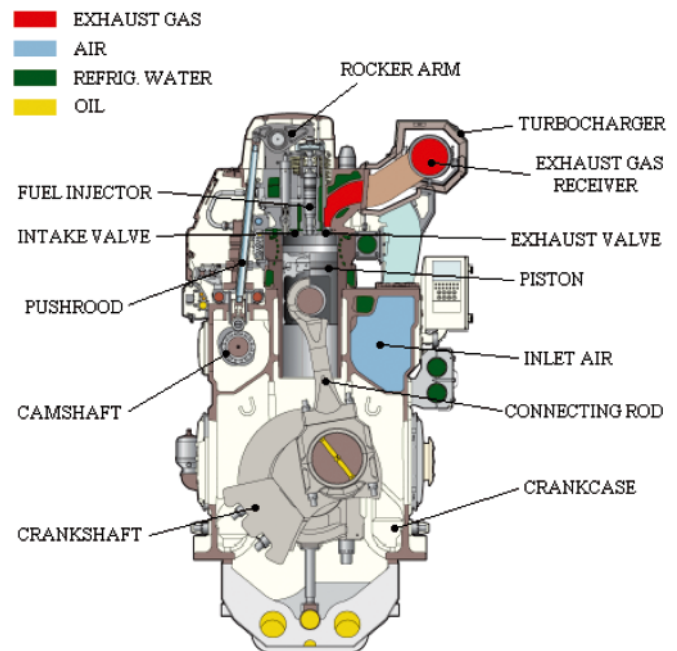


Fig. 3. Cross section. Adapted from Wärtsilä [12]

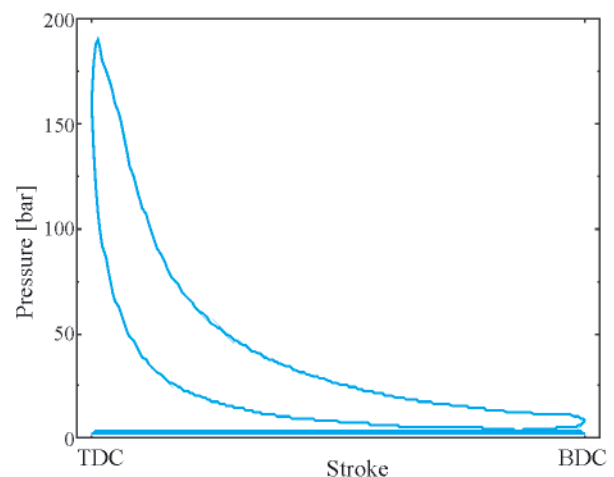


Fig. 4. In-cylinder pressure experimentally measured

towards the end of the compression stroke, with the piston near top dead center (TDC). As this is a direct injection engine, the fuel is injected directly into the combustion chamber. The combustion chamber is a shallow bowl in the piston crown shown in Fig. 5, which illustrates a photograph of three pistons of this engine.



Fig. 5. Pistons of the engine studied in the present work

The injection process is shown schematically in Fig. 6(a). The fuel is introduced by a 10 holes injector, Fig. 6(b), in the form of a spray of liquid droplets. As the air contained in the cylinder is at high pressure and temperature, the fuel vaporizes and mixes with this air. After that, ignition takes place. Atomization, vaporization, fuel-air mixing and combustion continue until all the necessary fuel has passed through each process. In addition, mixing of the air remaining in the cylinder with burning and already burned gas continues throughout the combustion and expansion processes.

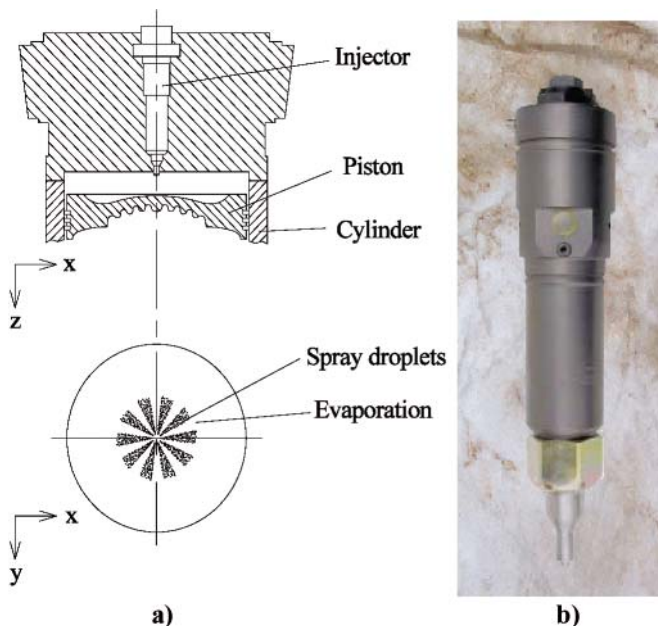
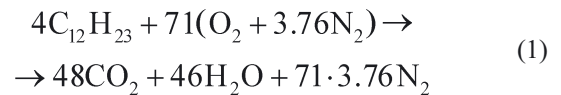


Fig. 6. a) Schematic representation of the spray injection; b) photograph of the injector

COMBUSTION CHEMISTRY AND GOVERNING EQUATIONS

Combustion is a very complex phenomenon which involves different disciplines such as fluid mechanics, chemistry, thermodynamics, heat transfer, etc. It is defined as an oxidation process of a fuel (in this case diesel, $C_{12}H_{23}$) and an oxidant (in this case oxygen, O_2), converting chemical energy into heat energy.

If a fuel is burnt stoichiometrically and ideally, this would be oxidized with air (which has a molecule of oxygen per 3.76 molecules of nitrogen) by means of the following reaction:



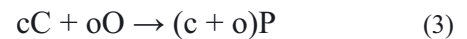
This reaction is very simple because it only involves five chemical species, $C_{12}H_{23}$, O_2 , N_2 , CO_2 and H_2O and four elements, C, H, O and N. Unfortunately, this ideal mechanism never occurs and real combustion processes are governed by hundreds of reactions and tens of chemical species. Currently, there are no computational resources to model all the reactions and species involved in the combustion process. The solution is to simplify the physical phenomenon which governs the chemical reactions, explained in what follows.

Governing equations

In this engine, the cylinder is full of air before the injection of fuel, and combustion takes place as the fuel is being injected. This is known as non-premixed combustion (in contrast to premixed combustion, in which fuel and oxidant are mixed before combustion takes place). In non-premixed combustion, the rate of combustion is controlled by the rate at which fuel and air mix. Under such hypothesis, the equation which characterizes the propagation of the flame front is given by:

$$\frac{\partial}{\partial t}(\rho f) + \frac{\partial}{\partial x_i}(\rho u_i f) = \frac{\partial}{\partial x_i} \left(\frac{\mu_t}{\sigma_\xi} \frac{\partial f}{\partial x_i} \right) \quad (2)$$

where ρ is the density, σ_ξ the turbulent Schmidt number and f the mixture fraction. This is the local mass fraction of burnt and unburnt fuel stream elements (C, H, etc) in all the species (CO_2 , H_2O , O_2 , etc). For the following chemical reaction, in which C represents the fuel, O the oxidant and P the products:



the mixture fraction is given by:

$$f = c/(c + o) \quad (4)$$

In addition to this equation, the equations of conservation of mass, momentum and energy are also necessary, Eqs. (5) to (7) respectively:

$$\frac{\partial \rho}{\partial t} + \frac{\partial}{\partial x_i}(\rho u_i) = 0 \quad (5)$$

$$\begin{aligned} \frac{\partial}{\partial t}(\rho u_i) + \frac{\partial}{\partial x_j}(\rho u_i u_j) = \\ = -\frac{\partial p}{\partial x_i} + \frac{\partial \tau_{ij}}{\partial x_j} + \frac{\partial}{\partial x_j}(-\rho \overline{u_i u_j}) \end{aligned} \quad (6)$$

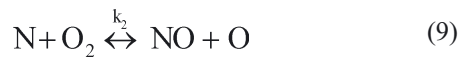
$$\begin{aligned} \frac{\partial}{\partial t}(\rho H) + \frac{\partial}{\partial x_i}(\rho u_i H) = \\ = \frac{\partial}{\partial x_i} \left[\left(\frac{\mu}{\sigma} + \frac{\mu_t}{\sigma_h} \right) \frac{\partial H}{\partial x_i} \right] + S_{rad} \end{aligned} \quad (7)$$

In the equations above, p is the pressure, τ_{ij} the viscous stress tensor, H the enthalpy, μ the, σ the Prandtl number, μ_t the turbulent viscosity, σ_h the turbulent Prandtl number and S_{rad} a source term to include the radiation heat transfer. The term

$-\rho \overline{u_i u_j}$ represents the Reynolds stresses, which were computed by means of the k - ϵ turbulence model.

Concerning the characterization of the chemical species involved, these were computed using the concept of chemical equilibrium (the chemical kinetics is so fast that equilibrium is reached quickly). The following 20 chemical species were considered: $C_{12}H_{23}$ (fuel), O_2 , N_2 , CO_2 , H_2O , CO , C , CH_4 , O , H , H_2 , H_2O_2 , N , OH , HO_2 , HNO , $HONO$, C_2H_6 , HCO and CHO .

NO_x is formed due to the high temperatures reached during the combustion process. Around $1500^\circ C$ and above, enough thermal energy is available to dissociate oxygen and nitrogen, which recombine to form NO_x , Versteeg and Malalasekera [15]. NO_x emissions from ships are relatively high because most marine engines operate at high temperatures and pressures without effective NO_x reduction technologies. The reactions of formation of NO_x are not fast enough to consider chemical equilibrium. For this reason, its treatment was decoupled from the combustion model. Among the NO_x components, NO is the main pollutant (nearly 100% of NO_x is NO). NO is generated by the reactions proposed by Zeldovich [13], reactions (8) and (9), and Lavoie [14], reaction (10).



The rate of formation of NO is given by the following expression:

$$\begin{aligned} d[NO]/dt = & k_1[O][N_2] + k_2[N][O_2] \\ & + k_3[N][OH] - k_{-1}[NO][N] + \\ & - k_{-2}[NO][O] - k_{-3}[NO][H] \end{aligned} \quad (11)$$

where $[NO]$, $[O]$, $[N_2]$, $[N]$, $[O_2]$, $[OH]$ and $[H]$ are the concentrations, mol/m^3 . k_1 , k_2 , k_3 are the rate constants and k_{-1} , k_{-2} , k_{-3} are the corresponding reverse rates. The forward and backward reaction rate constants for these three key reactions are given by:

$$\begin{aligned} k_1 &= 1.8 \times 10^{11} e^{(-38370/T)} \\ k_2 &= 1.8 \times 10^7 Te^{(-4680/T)} \\ k_3 &= 7.1 \times 10^{10} e^{(-450/T)} \\ k_{-1} &= 3.8 \times 10^{10} e^{(-425/T)} \\ k_{-2} &= 3.8 \times 10^6 Te^{(-20820/T)} \\ k_{-3} &= 1.7 \times 10^{11} e^{(-24560/T)} \end{aligned} \quad (12)$$

As can be seen, the reactions above are very dependent on the temperature. The NO formation rate is much slower than the combustion rate and most of the NO is formed after the completion of the combustion, due to the high temperatures present in the combustion zone.

NUMERICAL PROCEDURE

The numerical computations were performed by means of the commercial software ANSYS Fluent. It was carried out a period of time from 30° before TDC to the exhaust valves opening, 127° after TDC. All valves remained closed during the entire simulation. The results of Lamas et al. [11] were continued to 30° before TDC and employed as initial conditions

of the present work. Concerning the boundary conditions, the heat transfer from the cylinder to the cooling water was modeled as a convection type:

$$q = h(T_{gas} - T_{water}) \quad (13)$$

where q is the heat transferred, T_{gas} is the in-cylinder temperature, T_{water} is the cooling water temperature ($78^\circ C$) and h is the heat transfer coefficient, given by the following expression, Taylor [16]:

$$h = 10.4 kb^{-1/4} (u_{piston}/v)^{3/4} \quad (14)$$

where b is the cylinder bore, k the thermal conductivity of the gas, u_{piston} the mean piston speed and v the kinematic viscosity of the gas. Substituting values into the above equation yields $h = 4151 W/m^2K$.

In order to model the movement of the piston, a moving grid was employed. Figure 7 shows the grid at the start of the simulation, 30° before TDC, and at TDC. As can be seen, only the combustion chamber was simulated.

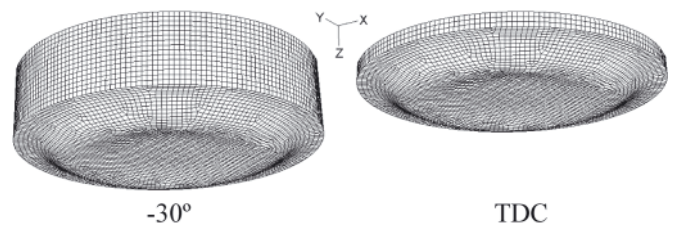


Fig. 7. Computational grid

RESULTS AND DISCUSSION

The spray and mass fraction of fuel are shown in Fig. 8. Under the conditions studied, the injection of fuel takes place from -12° to -1° crankshaft angles. Figure 8 represents -10° , -5° and 0° (PMS). As can be seen, the fuel spray enters the cylinder as liquid drops (which were simulated as $5 \mu m$ diameter). These

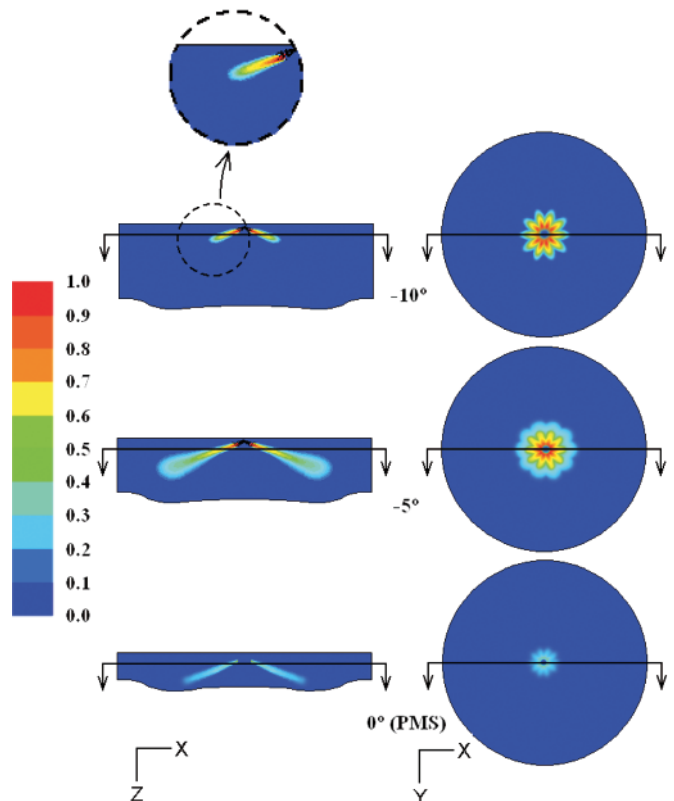


Fig. 8. Spray and mass fraction of fuel

drops are represented as black points in the figure. The structure of each fuel spray is that of a narrow liquid-containing core surrounded by a much larger gaseous-jet region containing fuel vapour. The flame spreads rapidly as the fuel is injected, producing a very fuel rich zone close to the fuel tip (-10° and -5°). After the injection of fuel has finished, the flame is extinguished progressively (0°).

The temperature field is shown in Fig. 9. The fuel is injected at 127°C , creating a cold temperature in the zone closed to the injector. In the rest of the cylinder, the temperature increases as the crankshaft angle is advanced due to the combustion progress and the compression supplied by the piston.

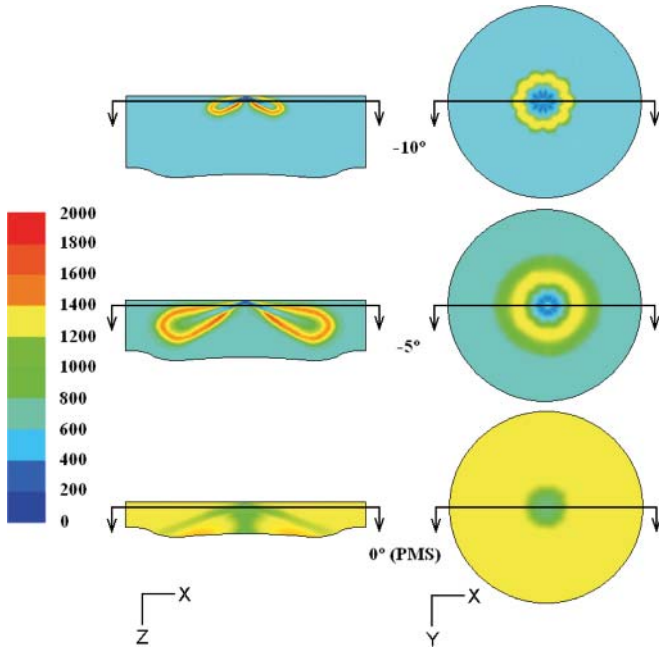


Fig. 9. Temperature field ($^\circ\text{C}$)

Figure 10 illustrates the comparison of simulated and measured in-cylinder pressures. A satisfactory agreement between the experimental and numerical results was obtained.

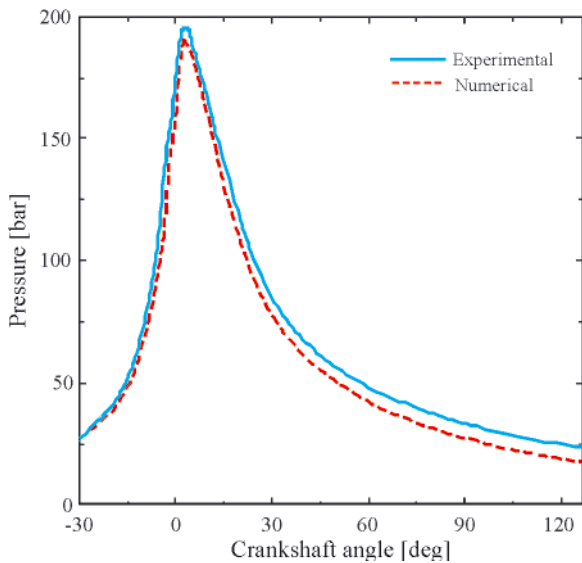


Fig. 10. In-cylinder pressure numerically and experimentally obtained

The emissions of carbon dioxide, carbon monoxide, nitrogen oxides and hydrocarbons are shown in Table 1. The NO_x emissions were measured experimentally using the G4100 analyzer (Green Instruments). According to this apparatus,

the engine emits 1115 ppm of NO_x , which suppose an error of 13.8% with respect to the numerical result given in Table 1. This error is quite acceptable considering the difficulty of simulating the combustion process. As the CFD code provides the quantity of mass inside the cylinder, the NO_x emissions in g/kWh can be easily calculated, obtaining a value of 11.8. This value sticks the IMO TIER I but not IMO TIER II, applicable to engines mounted in vessels built after 1 January 2011. Several solutions to decrease the NO_x levels in this engine were proposed by Millo *et al.* [10].

Tab. 1. Emissions from the engine numerically obtained

Gas	CO_2 (% vol.)	CO (ppm* vol.)	NO_x (ppm vol.)	HC (ppm vol.)
Value	8.3	356	961	569

*ppm: parts per million

It is interesting to study the NO_x emissions against the start of injection (SOI). For the purpose, the SOI was varied between -13° and -10° . The experimental and numerical results are shown in Fig. 11. The peak pressures numerically and experimentally obtained are also shown in the figure. As can be seen, delaying the start of injection reduces the NO_x emissions and the peak pressure, both for the experimental and numerical results. The NO_x emissions are very sensitive to the temperature. The decrease in NO_x emissions with injection retard is related to the decrease in combustion pressure and thus temperature. Unfortunately, the power is lower as the pressure decreases.

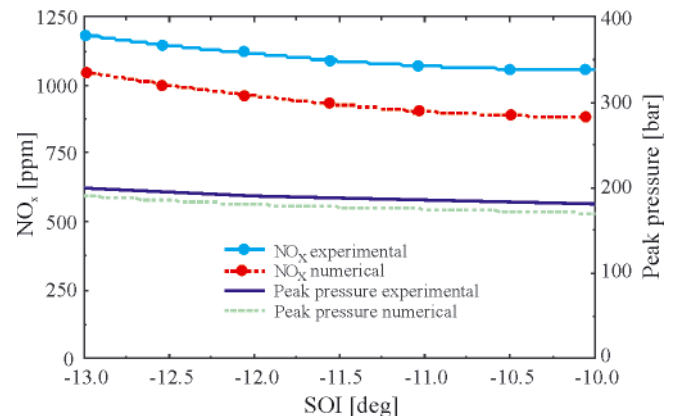


Fig. 11. NO_x emission varying with injection timing

CONCLUSIONS AND FURTHER DEVELOPMENTS

The present paper proposes a CFD model to simulate the combustion process in the Wärtsilä 6L 46 marine engine. The strongest motivation is given by the current legislation, for which the most important gas component that must be reduced in exhaust emissions from marine engines is NO_x .

The pressure and temperature fields were obtained, as well as the composition of the exhaust gas. In order to validate this work, numerical results were satisfactory compared with experimental ones performed on a Wärtsilä 6L 46 installed on a tuna fishing vessel. This work provides a model to study several parameters such as injection pressure, compression ratio, injection timing, etc. In future works, the purpose is to employ this model to design low emission engines, analyzing measures such as water addition, retarded injection, modulated injection, exhaust gas recirculation, etc.

Acknowledgements

The authors would like to express their gratitude to “Talleres Pineiro, S.L.”, marine engines maintenance and repair shop.

NOMENCLATURE

b	–	Cylinder bore
f	–	Mixture fraction
h	–	Heat transfer coefficient
H	–	Enthalpy
k	–	Thermal conductivity
p	–	Pressure
q	–	Heat transfer
t	–	Time
u	–	Velocity

Special characters

μ_t	–	Turbulent viscosity
ν	–	Kinematic viscosity
ρ	–	Density
σ_h	–	Turbulent Prandtl number
σ_ζ	–	Turbulent Schmidt number
τ_{ij}	–	Stress tensor

Subscripts

i	–	Cartesian coordinate (i = 1, 2, 3)
j	–	Cartesian coordinate (j = 1, 2, 3)

REFERENCES

1. Li, K.; Li, B.; Sun, P.: *Influence of fuel injection advance angle on nitrogen oxide emission from marine diesel engine*. Journal of Dalian Maritime University 36(3), pp. 87-89, 2010.
2. Lü, L.; Xu, J.H.; Xu, W.Y.: *Effect of diesel oil quality on particulate and smoke emissions from marine diesel engine*. Chinese Internal Combustion Engine Engineering 31(4), pp. 44-48, 2010.
3. Holub, M.; Kalisiak, S.; Borkowski, T., Myskow, J.; Brandenburg, R.: *The influence of direct non-thermal plasma treatment on particulate matter (PM) and NO_x in the exhaust of marine diesel engines*. Polish Journal of Environmental Studies 19(6), pp. 1199-1211, 2010.
4. Jayaram, V.; Nigam, A.; Welch, W.A.; Millar, J.W.; Cocker, I.I.: *Effectiveness of emission control technologies for auxiliary engines on ocean-going vessels*. Journal of the Air & Waste Management Association 61(1), pp. 14-21, 2011.
5. Yan, P.; Feng, M.Z.; Ping, T.; Fang, W.C.; Wang, X.Q.: *Simulation research on effect of nozzle parameters on combustion and emissions for HPCR marine diesel engine*. Internal Combustion Engine Engineering 32(3), pp. 43-47, 2011.
6. Uriondo, Z.; Durán Grados, C.V.; Clemente, M.; Gutiérrez, J.M.; Martín, L.: *Effects of charged air temperature and pressure on NO_x emissions of marine medium speed engines*. Transportation research Part D: Transport and environment 16(4), pp. 288-295, 2011.
7. Bernećić, D.; Radonja, R.: *The selective catalytic reduction (SCR) application on two stroke slow speed marine diesel engines*. Pomorstvo 25(1), pp. 15-28, 2011.
8. Maiboom, A.; Tazua, X. NO_x and PM emissions reduction on an automotive HSDI Diesel engine with water-in-diesel emulsion and EGR: An experimental study. *Fuel* 90(11), pp. 3179-3192, 2011.
9. Duran, V.; Uriondo, Z.; Moreno-Gutiérrez, J.: *The impact of marine engine operation and maintenance on emissions*. Transportation research Part D: Transport and environment 17(1), pp. 54 -60, 2012.
10. Mollo, F.; Bernandi, M.G.; Delneri, D.: *Computational analysis of internal and external EGR strategies combined with miller cycle concept for a two-stage turbocharged medium speed marine diesel engine*. SAE Paper 2011-01-1141, 2011.
11. Lamas, M.I.; Rodríguez, C.G.; Rebollido, J.M.: *Numerical model to study the valve overlap period in the Wärtsilä 6L46 four-stroke marine engine*. Polish Maritime Research 1(72), pp. 31-37, 2012.
12. Wärtsilä 46: *Project guide for marine applications*. 2001.
13. Zeldovitch, Y.B.; Sadovnikov, D.A.; Kamenetskii, F.: *Oxidation of nitrogen in combustion*. Institute of Chemical Physics, Moscow-Leningrad, 1947.
14. Lavoie, G.A.; Heywood, J.B.; Keck, J.C.: *Experimental and theoretical investigation of nitric oxide formation in internal combustion engines*. Combustion Science Technology 1, pp. 313-326, 1970.
15. Versteeg H.K., Malalasekera W.: *An introduction to computational fluid dynamics: the finite volume method*. 2nd Edition. Harlow: Pearson Education, 2007.
16. Taylor, C.F.: *The internal combustion engine in theory and practice*. 2nd Edition. MIT Press, 1985.

CONTACT WITH THE AUTHORS

Lamas M. I., Assoc. Prof.
Rodríguez C. G., M. Sc.

Escola Universitaria Politécnica. Universidade da Coruña.
Avda. 19 de Febreiro s/n - 15405 Ferrol - A Coruña. SPAIN.
e-mail: isabellamas@udc.es

Weldability of high strength steels in wet welding conditions

Dariusz Fydrych, Ph.D.,
Jerzy Łabanowski, Assoc. Prof.,
Grzegorz Rogalski, Ph.D.,
Gdansk University of Technology, Poland

ABSTRACT

In this paper are characterized problems of high strength steel weldability in underwater wet welding conditions. Water as a welding environment intensifies action of unfavourable factors which influence susceptibility to cold cracking of welded steel joints. The susceptibility to cold cracking of S355J2G3 steel and S500M steel in wet conditions was experimentally estimated (by using Tekken test). It was concluded that the steels in question are characterized by a high susceptibility to formation of cracks in welds. Usefulness of the proposed Temper Bead Welding technique (TBW) was experimentally verified as a method for improving weldability of the steels in the analyzed conditions.

Key words: underwater welding; steel weldability, cold cracking; wet welding; cracks in welds; improving weldability

INTRODUCTION

According to the most general classification, the underwater welding processes can be divided into dry and wet ones [1-5]. The dry methods consist in local isolation of welding area from surrounding water by means of special chambers in which atmospheric pressure (isobaric welding) or an elevated pressure resulting from welding depth (hyperbaric welding) is present. A characteristic feature of the wet welding is direct underwater contact of diver-welder, electrode and base material. An intermediate variant between wet and dry welding is application of a local dry chamber (dry spot welding) [1-3]. Applicability of particular processes in underwater welding conditions is characterized in Tab. 1.

Among wet welding methods, the manual metal arc welding is most often used, hence majority of steel weldability test results accessible in the subject-matter literature concern the above mentioned process [4-6, 11-20].

Transferring the welding process to water environment results first of all in increasing diffusible hydrogen content in deposited metal, as well as in increased cooling rate. Manual metal arc welding in wet conditions generates the diffusible hydrogen content in deposited metal, of the order of a few dozen ml/100g Fe, depending on a type of shielding and welding conditions [14, 15]. The tests [15, 16] performed with the use of rutile-shielded electrodes, the most often applied in such conditions, showed that hydrogen content in deposited metal did not depend on a wetting degree of the shielding, but heat input was the decisive factor (Fig. 1).

Tab. 1. Possibility of application of welding processes in water environment [2-10]

No.	Process	Dry welding	Wet welding	Local chamber method welding
1	MMA (111)	yes	yes	possible
2	SAW (121)	yes	yes	no
3	MIG/MAG (131/135)	yes	possible	yes
4	FCAW (136/138)	yes	yes	yes
5	FCAW-S (114)	possible	yes	possible
6	Plasma arc welding (15)	possible	no	possible
7	Laser welding (521)	possible	no	yes
8	Friction welding (42)	yes	yes	no
9	Explosion welding (441)	no	yes	no
10	Stud arc welding (78)	possible	yes	possible

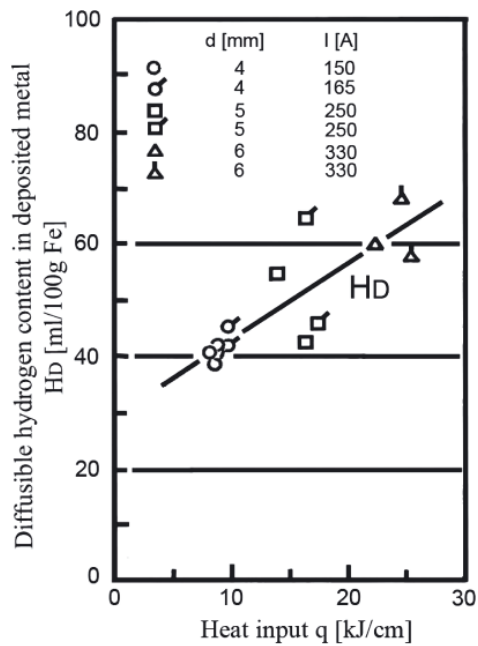


Fig. 1. Effect of heat input of MMA wet welding on diffusible hydrogen content in deposited metal [16]

Cooling rates of joints made underwater are much shorter compared with those for in - air welding conditions. The increase of cooling rate contributes to forming brittle structures in heat affected zone (HAZ) and to increasing values of residual stresses. Such conditions result in that welded structural steel joints made directly in water are characterized by a high susceptibility to forming cold cracks. The cracks appear even in joints made of steel of a low carbon equivalent $C_e \leq 0.3\%$. In the HAZ of such steel joints the increase of hardness up to the level of $350 \div 400$ HV, as well as many hydrogen microcracks were observed [13, 14]. In Fig. 2 are presented the results of Tekken tests performed underwater, which were used for development of an equation for determining the minimum heat input value which protects against cold cracks forming [4].

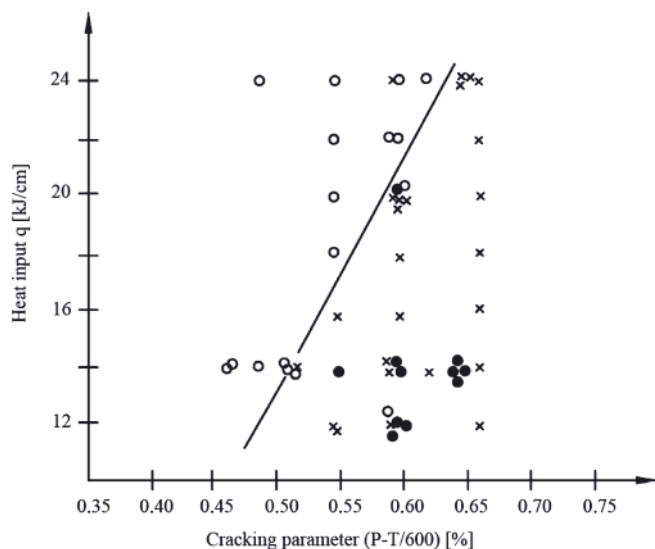


Fig. 2. Results of Tekken tests, underwater wet MMA welding: \circ – no cracks, \times – internal cracks, \bullet – internal and external cracks [4]

The equation is of the following form:

$$q = 200 \times (P - T/600) - 67$$

where:

q – heat input, [kJ/cm],

$P = C_e + H_D/60 + R/200000$,

T – initial temperature, [°C],

C_e – carbon equivalent acc. International Institute of Welding, [%],

H_D – diffusible hydrogen content in deposited metal, [ml/100g Fe],

R – restraint intensity, [MPa].

The tests [17] on Implant specimens, performed in the conditions similar to those for Tekken test, showed that critical stresses were higher than yield point of the tested steel. It goes to show that the steel was crack-resistant, which is not consistent with the results given in [4].

A great number of variable factors which act during underwater welding makes it difficult to formulate safe welding conditions, i.e. those possible to protect joints against cracking. However on the basis of many tests the following approximate criteria for safe wet welding of non-alloy steels, were determined [18]:

- base material carbon equivalent: $C_e < 0.30\%$,
- heat input: greater than 1.5 kJ/mm.

In the case of application of austenitic electrodes value of welded steel carbon equivalent may be even greater – up to 0.40 %. In this case hot cracks should be expected to occur in welds [4, 19]. Increase of toughness of weld metal at wet welding conditions can be also achieved by applying low-alloy electrodes containing nickel. The optimal Ni content in weld is considered as 2% [19].

Another limitation method of susceptibility to forming cold cracks is application of temper bead welding technique (TBW) [20, 21]. In the TBW a reduction of post-welding residual stresses as well as a decrease of hardness in HAZ is achieved. The technique is applied to thick sections, i.e. where it is not possible to perform heat treatment operation after welding. It consists in overlaying successive beads onto weld, that introduces local heat treatment in the area of prior made weld layer. In HAZ of the layer structural transformations may occur in the temperature range higher than A_{C1} temperature. ASME rules require to make six layers, and for three first layers increased value of heat input is often used [21]. In the case of implementation of TBW technique for preventing against cold cracking it is important to determine a time interval between instants of overlaying a tempered bead and tempering one. Depending on a type of applied electrode the time up to crack forming at wet welding may reach from 3 min to 2 hours. Successive parameters important from the point of view of effectiveness of the process are: value of heat input in every bead as well as distance between bead axes (pitch) [21].

EXPERIMENTAL

The tests were aimed at determination of susceptibility to forming cold cracks in joints of high strength steels, made by using covered electrodes in wet welding process. The tests were performed in accordance with the following scheme:

- preparation of welding stands in air and underwater environment
- preparation of Tekken tests
- welding of test joints
- visual testing and penetrant testing
- macroscopic and microscopic metallographic examinations
- Vickers hardness measurements.

Additionally, to assess usefulness of application of TBW technique for improving steel weldability in water environment,

Tab. 2. Chemical composition of S355J2G3 and S500M steel, wt %

S355J2G3	C	Si	Mn	P	S	Cr	Ni	Cu	Al	C _e
	0.17	0.35	1.44	0.014	0.014	0.04	0.077	0.30	0.02	0.44
S500M	C	Si	Mn	P	S	Nb	V	Ti	Al	C _e
	0.067	0.018	1.380	0.009	0.002	0.056	0.054	0.001	0.039	0.30

test padding welds were made and subjected to macroscopic metallographic examinations and hardness measurements.

For the tests 15 mm plates of S355J2G3 and S500M steel were used. Their chemical compositions and mechanical properties are given in Tab. 2 and 3.

Tab. 3. Mechanical properties of S355J2G3 and S500M steel

	Yield point R _e [MPa]	Tensile strength R _m [MPa]	Elongation A ₅ [%]
S355J2G3	464	577	22.1
S500M	525	619	20.5

The test welds were made by using Lincoln Electric OMNIA (E 42 ORC 11) electrodes of 4 mm diameter. They are general application rutile electrodes for welding in all positions, of the chemical composition: C – 0.07%, Mn – 0.5%, Si – 0.5%, and the mechanical properties: R_e – min. 420 MPa, R_m – 500 ÷ 640 MPa, A₅ – min 20%.

The Tekken test joints of S500M steel were made in water and air environment at various heat input values. The Tekken test joints of S355J2G3 steel were made only at underwater conditions. The test joints were prepared in compliance with the standard guidelines [22], on the underwater welding stand at low water depth [3]. In Tab. 4 are presented the conditions for performing Tekken tests on selected joints.

Penetrant testing

The visual and penetrant testing [23-25] of the test joints were performed after 72 h from finishing the welding. Occurrence of cracks in welds of all the specimens made in water environment was observed, but in S355J2G3 steel joints the cracks were placed close to fusion line, whereas in the specimens made of S500M steel – in weld axis. In the Tekken specimens welded in air environment no cracks were revealed.

Macroscopic metallographic examinations

The macroscopic metallographic examinations were performed in accordance with the standard guidelines [26]. Example photos of the cross-sections are presented in Fig. 3÷5. In the specimens made underwater extensive cracks and

a porosity were sometimes found. Tekken specimens of S500M steel welded in air environment were characterized by a much lower susceptibility to cracking, however in one of them some cracks were observed. The results obtained from the Tekken tests are presented in Tab. 5.

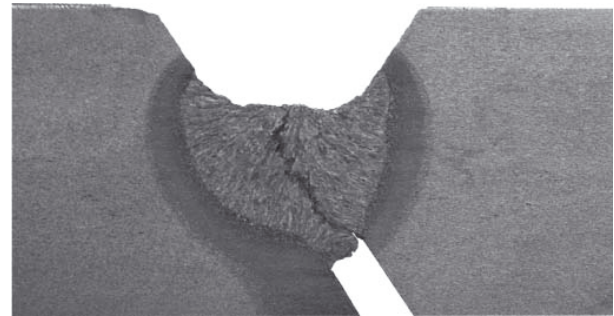


Fig. 3. Cross-section of the W1 (S500M) test joint with the visible crack initiated in weld root

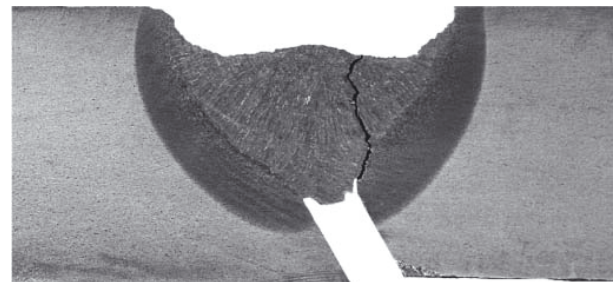


Fig. 4. Cross section of the 1A (S355J2G3) test joint with the visible crack initiated in fusion line



Fig. 5. Cross-section of the P12 (S500M) test joint with the visible crack initiated in weld root

Tab. 4. Conditions of Tekken tests

No. of specimen	Steel	Environ ment	Welding parameters		Welding time t [s]	Heat input value q [kJ/mm]
			U [V]	I [A]		
W1	S500M	water	30.0	228	16.4	1.40
W2	S500M	water	34.3	232	18.5	1.85
W3	S500M	water	32.5	244	16.9	1.68
P6	S500M	air	22.0	168	30.0	1.39
P12	S500M	air	24.3	160	31.0	1.51
1A	S355J2G3	water	30.8	228	33.0	2.90
2A	S355J2G3	water	29.2	232	29.0	2.44

Tab. 5. Results of Tekken tests

No. of specimen	Environment	Penetrant testing	Macroscopic metallographic examinations	Hardness measurements	Percentage of cracks	
				HV _{10 max}	C _f [%]	C _s [%]
W1.1	water	crack	crack	258	40.0	61.0
W1.2		crack	crack	294		79.3
W2.1	water	crack	crack	283	27.5	44.4
W2.2		crack	crack	287		81.4
W3.1	water	crack	crack	262	43.8	73.3
W3.2		crack	crack	298		62.5
P6.1	air	no crack	no crack	248	0.0	0.0
P6.2		no crack	no crack	242		0.0
P12.1	air	crack	crack	251	18.5	30.0
P12.2	air	crack	crack	240		27.0
1A.1	water	crack	crack	417	100.0	83.0
1A.2	water	crack	crack	413		100.0
2A.1	water	crack	crack	430	100.0	78.0
2A.2	water	crack	crack	421		90.0

S500M steel joint

S355J2G3 steel joint

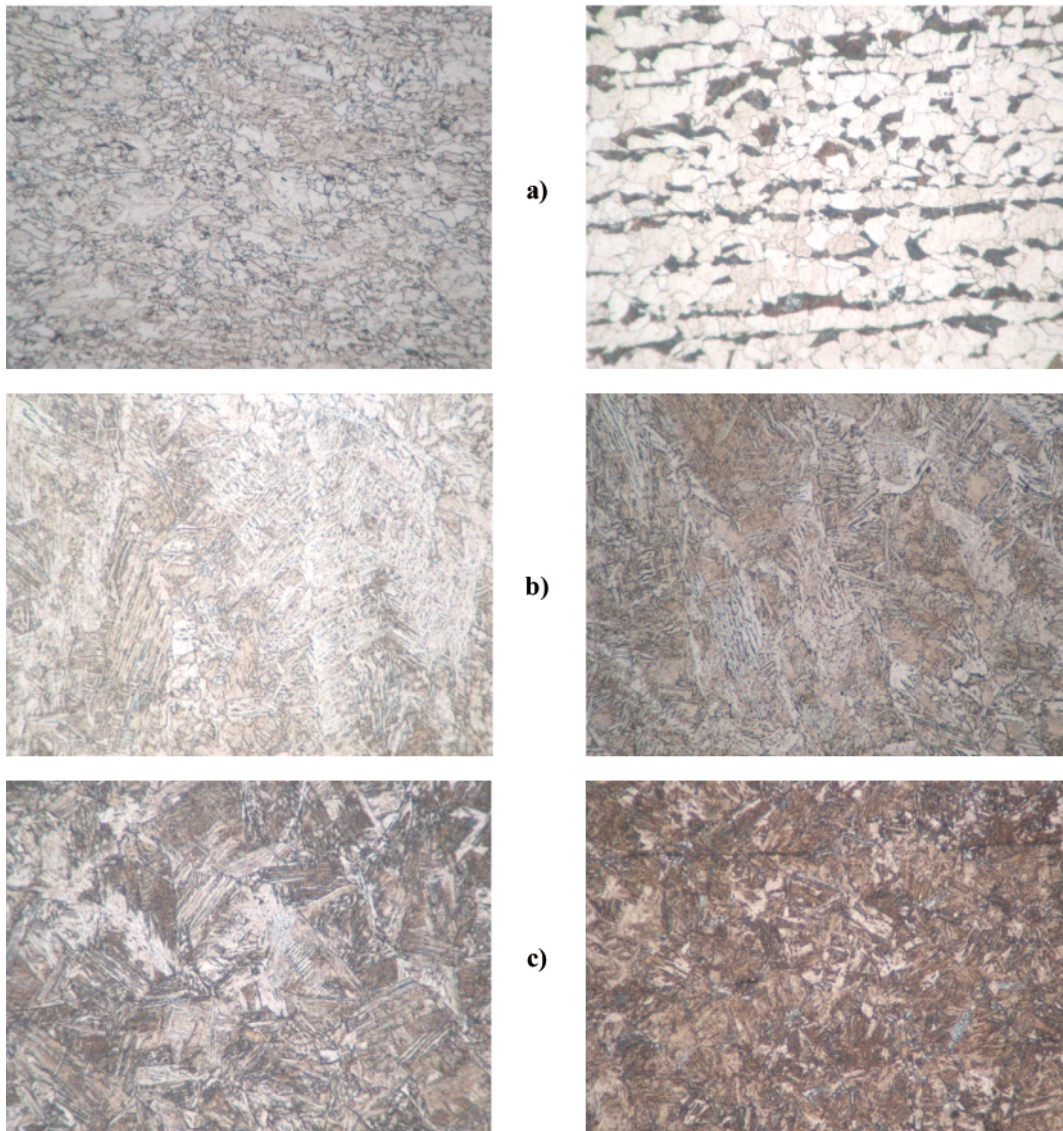


Fig. 6. Microstructure of S500M and S355J2G3 steel joints welded underwater; a) base material, b) weld, c) overheated zone in HAZ. Magnification $\times 200$

Microscopic metallographic examinations

In Fig. 6 are presented typical structures of base material, weld and HAZ at fusion line for the tested joints made underwater. The S500M steel structure consists of ferrite grains of very different sizes with a trace of pearlite content whereas S355J2G3 steel shows a ferritic-pearlitic structure of distinct banding. The weld structure of both the steels is similar and consists of ferrite of column arrangement with an outline of Widmanstätten structure. In the HAZ of S500M steel, quasi-pearlite structures with acicular ferrite bands reaching down the grains, are observed, whereas in the HAZ of S355J2G3 steel acicular quench structures are visible.

Hardness measurements of welded joints

The hardness measurements were performed according to the standard [27] under 98 N load (HV10). Example results are shown in Fig. 7 through 9. In the S500M steel joints made both in the air and underwater, hardness values for weld and base material were close to each other and equal to about 200 HV10. In HAZ only a slight increase in hardness up to 240 HV10 was observed for air environment welding conditions, whereas the transferring of the welding process to water environment resulted in further increase of maximum hardness of HAZ up to about 280 HV10.

However the maximum hardness values in HAZ of the S355J2G3 steel joints were significantly greater. A higher carbon content in this steel in association with an increased cooling rate of the joints resulted in the quenching of HAZ material and increase of its hardness up to over 400 HV10.

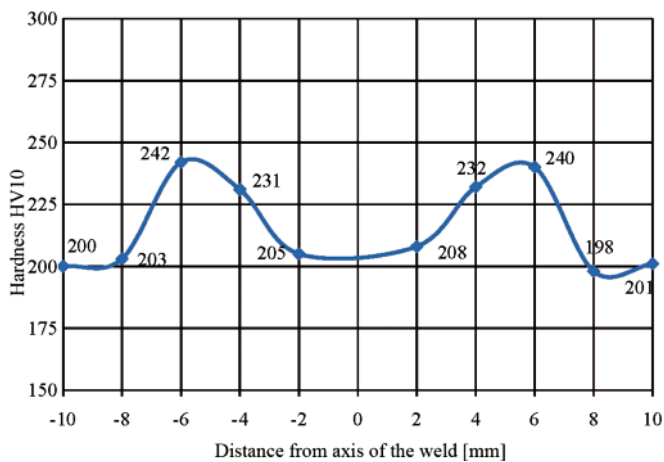


Fig. 7. Hardness distribution across P6.2 test joint of S500M steel welded in the air, $HV_{max} = 242$

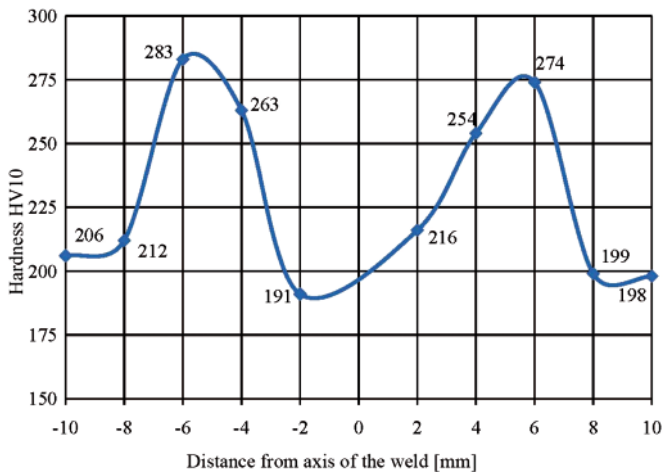


Fig. 8. Hardness distribution across W2.1 test joint of S500M steel welded underwater, $HV_{max} = 283$

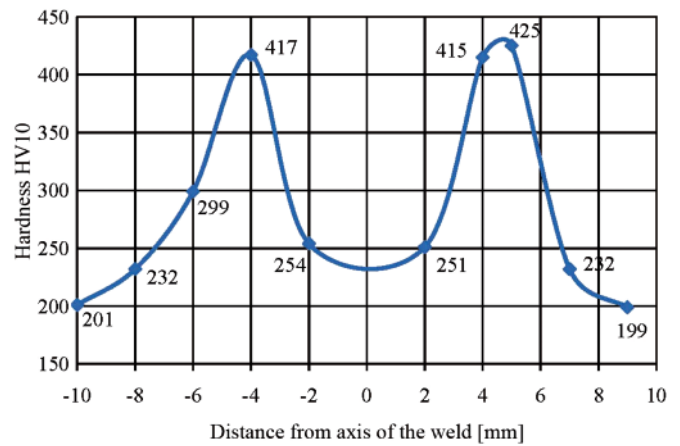


Fig. 9. Hardness distribution across IA.1 test joint of S355J2G3 steel welded underwater, $HV_{max} = 425$

Application of temper bead welding (TBW)

A preliminary assessment of usefulness of application of the tempering bead technique to improve weldability in water environment was performed by using S355J2G3 steel plates. On the testing plate of $12 \times 100 \times 200$ mm dimensions padding welds were made with the use of Omnia electrodes at 10 min interval and 40% pitch. Cross-sections of the padding welds were subjected to the macroscopic metallographic examinations and hardness measurements. Parameters of the padding welding are given in Tab. 6. A photo of polished macroscopic cross-section of test beads with indication of padding weld laying sequence is shown in Fig. 10.

Tab. 6. Welding parameters for S355J2G3 steel

Padding weld	Welding current I [A]	Arc voltage U [V]	Welding speed v [mm/min]	Heat input q [kJ/mm]
1	206	34.5	255	1.67
2	226	41.0	213	2.60

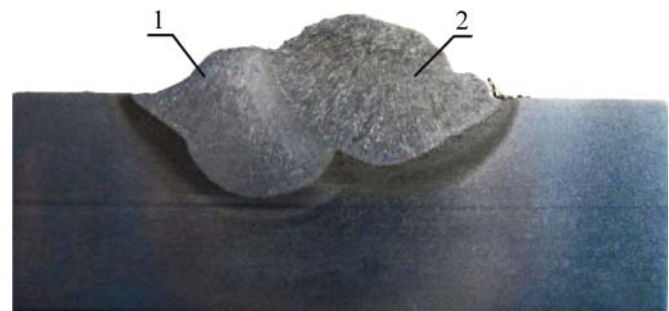


Fig. 10. Cross section of the test weld beads; S355J2G3 steel; 40% pitch

In Fig. 11. is shown location and designation of areas in which hardness measurements were made, and in Tab. 7 and Fig. 12 are presented results of hardness measurements performed at 2 mm distance measured from specimen surface.

The presented results of hardness measurements for padding welds make it possible to conclude that the temper bead welding in underwater welding allows to lower maximum hardness in HAZ to a safe level as regards cold crack forming. In Fig. 12 two characteristic points of increased hardness (swcap and swcbp) can be observed. They appear at fusion line and simultaneously very close to edges of the padded elements. In this place intensive heat sinking occurs, a.o. due to bubble boiling, that leads to forming high hardness structures. In

Tab. 7. Results of hardness measurements of S355J2G3 steel test plates

	mr	swcan	swcap	mna	wswcb	mnb	swcbp	swcbn	mr
HV10	191	256	448	213	198	250	446	245	191

	swca2n	swca2p	wswcan	wswcap
HV10	251	325	223	260

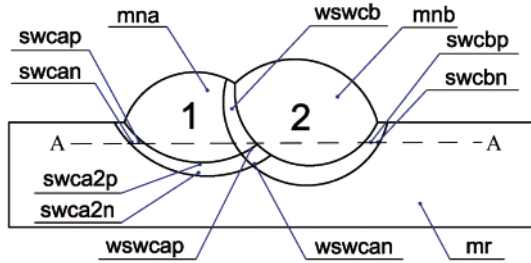


Fig. 11. Location and designation of tested areas on testing plate: *mr* – base material, *mna* – 1st padding weld, *mnb* – 2nd padding weld, *swca* – HAZ of 1st padding weld, *swcb* – HAZ of 2nd padding weld, *wswca* – area of overlapping *swca* and *swcb*, *wswcb* – area of *swcb* overlapping *mna*, *n* – normalization area, *p* – overheated area, *A-A* – hardness measurement line

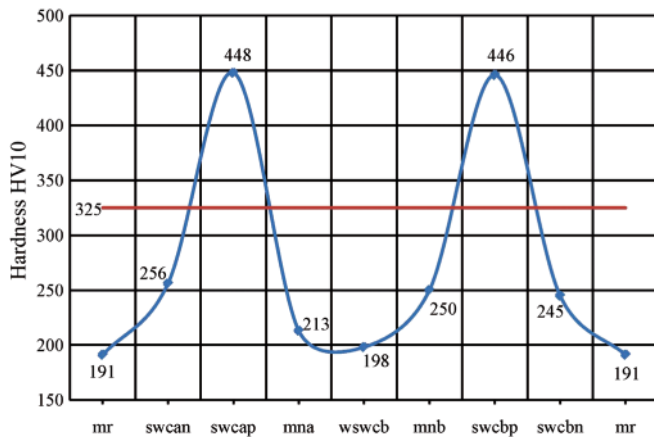


Fig. 12. Hardness distribution along A-A line (see Fig. 11) on S355J2G3 steel test plate. The HVmax of the tempered zone in HAZ of 1st weld bead (*swca2p*) is marked by red horizontal line.

making multilayer joints such phenomenon can be minimized by providing heat again during laying successive tempering beads – in the case in question – it means making the last bead between two padding welds.

DISCUSSION

In all the test joints made underwater, cracks in welds were observed. The phenomenon is in compliance with information contained in the literature sources concerning weldability of the tested steels [28]. Specimens made in the air were characterized by a much lower susceptibility to crack forming. Crack occurrence in the joints made in the air resulted from using rutile electrodes. Application of such electrodes was conditioned in association with real underwater welding conditions with the use of the MMA process as well as convergence with requirements of the PN-EN ISO 15618-1 standard concerning certification of divers-welders for wet welding [29]. In the above mention standard, one of the recommended welding electrodes is that with rutile coating. Welding with rutile electrodes both in the air and underwater is a process of a high hydrogen content. Presence of hydrogen in steel weldments leads to degradation of their structure and mechanical properties [30]. On the basis of the previous tests the diffusible hydrogen

content in deposited material obtained in air environment can be estimated to be about 35 ml/100g Fe, whereas in the case of underwater welding – 50 ml/100 g Fe [15, 31].

In the wet welding conditions for S500M steel the increase of HAZ hardness from 240 ÷ 250 HV10 (characteristic for welding in the air) up to 260 ÷ 300 HV10, took place. Maximum hardness values in HAZ of S500M steel are lower than 350 HV10 value is considered as critical from the point of view of susceptibility to cold cracking. However the test joints of S355J2G3 steel were characterized by the much greater maximum hardness in HAZ of values over 400 HV10. It results from their welding conditions (a. o. greater cooling rates – consequently – shorter cooling times $t_{8/5}$), which, at the carbon equivalent $C_e = 0.44\%$ for S355J2G3 steel, led to forming quenched structures. For Tekken specimens of S355J2G3 steel the initiating of cracks in fusion line is characteristic (Fig. 4), which is confirmed by presence of brittle structures in this area. Hardness distribution over cross-section of Tekken joints made of S500M steel complies with acceptance criteria used for approving welding technologies in the air. Limitation of maximum hardness in HAZ down below 350 HV10 value results from low carbon content in the steel as well as carbon equivalent $C_e = 0.30\%$. The presented results indicate that low-carbon steels after thermo-mechanical processing is applicable for marine and off-shore engineering structures when underwater welding is required.

The application of the TBW technique to S355J2G3 steel allowed to reach satisfactory results, that is manifested by the hardness measurement results in trouble areas of padding welds (Tab. 7). The technique in question is greatly useful in welding elements made of a steel which requires a heat treatment after welding. In wet welding conditions or dry hyperbaric ones such treatment would be very expensive and in most cases impossible to perform. TBW technique makes it possible to obtain, by applying relatively simple technological operations, welded joints which satisfy criteria of subject-matter standards or requirements of classification societies. It may find application e.g. to repair work of underwater piping lines. It should be added that effectiveness of application of tempering beads depends on many factors e.g. welding position, welding parameters (heat input), arc length, torch setting angle, interval between padding weld laying and weld pitch. However further investigations are required to develop TBW technology for wet welded joints. The successive tests should take into account factors, that would make it possible to determine optimum conditions for application of temper bead technique to underwater welding process.

CONCLUSIONS

1. The joints of S355J2G3 and S500M steel, made underwater in the restraint conditions showed high susceptibility to forming cold cracks in welds.
2. In all the Tekken test joints of S500M steel, made with the use of wet welding method cold cracks were revealed, and in the joints made in the air such cracks were found in only one of the two test joints.

3. Maximum hardness in HAZ of the S500M steel joints did not exceed 300 HV, whereas that in HAZ of the S355J2G3 steel joints was over 400 HV10 in value.
4. It was proved that the TBW technique was effective for the joints of high strength steel welded underwater. The application of the TBW resulted in the decreasing of maximum hardness in HAZ of S355J2G3 steel joints down to the value below 350 HV10.

BIBLIOGRAPHY

1. The Standard AWS D3.6M:2010 *Underwater Welding Code*.
2. Łabanowski J.: *Development of underwater welding techniques*. Przegląd Spawalnictwa (Welding Technology Review), 10/2008 (in Polish).
3. Łabanowski J., Fydrych D., Rogalski G.: *Underwater Welding – a review*. Advances in Materials Science, 3/2008.
4. Christensen N.: *The metallurgy of underwater welding*. Proceedings of the International Conference „Underwater Welding”, Trondheim, Norway 1983.
5. Cotton H. C.: *Welding under water and in the splash zone – a review*. Proceedings of the International Conference „Underwater Welding”, Trondheim, Norway 1983.
6. Ibarra S., Grubbs C. E., Liu S.: *State of the art and practice of underwater wet welding of steel*. International workshop on underwater welding of marine structures. New Orleans, USA, 1994.
7. Zhang X., Ashida E., Shono S., Matsuda F.: *Effect of shielding conditions of local dry cavity on weld quality in underwater Nd:YAG laser welding*. Journal of Materials Processing and Technology. Vol. 174, Issues 1-3, May 2006.
8. Fydrych D., Rogalski G.: *Effect of underwater local cavity welding method conditions on diffusible hydrogen content in deposited metal*. Welding International Vol. 27, Issue 3, March 2013, pages 196-202.
9. Ambroziak A., Gul B.: *Underwater friction bonding of overlap joints by means of a plasticized steel pin (FHPP)*. Przegląd Spawalnictwa (Welding Technology Review), 9-10/2006 (in Polish).
10. Ambroziak A., Gul B.: *Investigations of underwater FHPP for welding steel overlap joints*. Archives of Civil and Mechanical Engineering 2/2007.
11. Rodriguez-Sanchez J. E., Rodriguez-Castellanos A., Perez-Guerrero F., Carbajal-Romero M. F., Liu S.: *Offshore fatigue crack repair by grinding and wet welding*. Fatigue and Fracture of Engineering Materials and Structures, 34/2010.
12. Pessoa E., Bracarense A., Zica E., Liu S., Perez-Guerrero F.: *Porosity variation along multi-pass underwater wet welds and its influence on mechanical properties*. Journal of Materials Processing Technology. Vol. 179, Issues 1–3, 20 October 2006, pp. 239–243.
13. Bohme D., Eisenbeis C.: *Investigation into the credibility of the implant test when used to assess the cold cracking sensitivity of underwater wet welds*. Proceedings of the International Conference „Welding Under Extreme Conditions”, Helsinki, Finland 1989.
14. Hoffmeister H., Kuster K.: *Process variables and properties of underwater wet shielded metal arc laboratory welds*. Proceedings of the International Conference „Underwater Welding”, Trondheim, Norway 1983.
15. Fydrych D., Rogalski G.: *Effect of shielded-electrode wet welding conditions on diffusion hydrogen content in deposited metal*. Welding International Vol. 25, Iss. 3, March 2011, p. 166-171.
16. Suga Y.: *Effect of diffusible hydrogen on mechanical properties of underwater welded joints – study on improving the mechanical properties of underwater welded joints (the 1st report)*. Transactions of the Japan Welding Society 10/1985.
17. Brink S. H., Boltje G. W.: *Cold cracking susceptibility of welds obtained by wet underwater welding*. Proceedings of the International Conference „Underwater Welding”, Trondheim, Norway 1983.
18. Fydrych D.: *Cold cracking of steel welded in water environment*. Przegląd Spawalnictwa (Welding Technology Review), 10/2012 (in Polish).
19. Liu S.: *Fundamentos de soldadura humeda*. Seminario de soldadura humeda. Campeche, Mexico 1999.
20. Global Divers & Contractors : *Joint industry underwater welding development program*. Phase I - final report. Colorado School of Mines, 1995.
21. Łomozik M.: *Morphology and toughness of heat affected zone regions of steel welded joints in the aspect of temper beads application*. Uczelniane Wydawnictwa Naukowo-Dydaktyczne AGH (Scientific and Didactic Publishing House, Cracow Mining and Metallurgy Academy), Kraków 2007 (in Polish).
22. The Standard PN-EN ISO 17642-2:2005. *Destructive tests on welds in metallic materials. Cold cracking tests for weldments. Arc welding processes. Part 2: Self-restraint tests*. (in Polish).
23. The Standard PN-EN ISO 17637:2011. *Non-destructive testing of welds. Visual testing of fusion-welded joints* (in Polish).
24. The Standard PN-EN 571-1:1999. *Non-destructive testing. Penetrant testing. Part 1: General principles* (in Polish).
25. The Standard PN-EN ISO 23277:2010. *Non-destructive testing of welds. Penetrant testing of welds. Acceptance levels* (in Polish).
26. The Standard PN-EN 1321:2000. *Destructive test on welds in metallic materials. Macroscopic and microscopic examination of welds* (in Polish).
27. The Standard PN EN ISO 9015-1:2011 *Destructive tests on welds in metallic materials. Hardness testing. Hardness test on arc welded joints* (in Polish).
28. Tasak E.: *Weldability of steel* (in Polish). Wydawnictwo Fotobit (Fotobit Publishers), Cracow 2002.
29. Rogalski G., Łabanowski J.: *Certification of divers-welders for underwater wet welding in hyperbaric conditions*. Biuletyn Instytutu Spawalnictwa (Bulletin of Polish Welding Institute), 1/2011 (in Polish).
30. Ćwiek J.: *Hydrogen assisted cracking of high-strength weldable steels in sea-water*. Journal of Materials Processing Technology, Vol. 164-165 (2005), p. 1007-1013.
31. Fydrych D., Łabanowski J.: *Determining diffusible hydrogen amounts using the mercury method*. Welding International Vol. 26, Iss. 9, September 2012, p. 697-702.

CONTACT WITH THE AUTHORS

Dariusz Fydrych, Ph.D.,
 Jerzy Łabanowski, Assoc. Prof.,
 Grzegorz Rogalski, Ph.D.,
 Faculty of Mechanical Engineering
 Gdansk University of Technology
 Narutowicza 11/12
 80-233 Gdansk, POLAND
 e-mail: jlabanow@pg.gda.pl

An analysis of the welding-induced deformation of ship panels using a statistical tool

Huggo S. Batista, M.Sc.,
Tadeusz Graczyk, Assoc. Prof.,
West Pomeranian University of Technology, Szczecin

ABSTRACT

This paper proposes a practical way to predict the welding-induced deformation of 5-mm-thick steel ship panels prefabricated in a Polish shipyard, developed by means of a number of experiments and a body of data collected on the butt welding line using the submerged arc welding technique. The program of the experiments was so designed as to test different welding energy conditions as well as pressure values generated by the devices used during the welding. Subsequently, different welding trials were carefully carried out and data collected to find the most important parameters which contribute to welding deformation. The data obtained were analysed using the Design-Expert® statistical software, and consideration was given to the data arrangement method that would allow for the most appropriate description of the welding deformation. As a result of the foregoing efforts, an approach to predicting the welding deformation, based on a numerical equation including the main welding parameters, was developed. The accuracy of the equation was partially evaluated and the results turned out to be satisfactory, as the actual and the predicted values were comparable. Another important advantage achieved was the arrangement of data used to compute the welding deformation.

Keywords: ship production technology; welding deformation; design of experiment; statistics

INTRODUCTION

Analysing the contemporary ship production requires some attention on issues related to design of ships, the capacity of shipyards and work stations, as well as production technology due to the fact that business factor is related to them. In consequence these subjects are in permanent development because of their significance for the production costs besides, schedule and quality. Consequently, there is a need in the shipbuilding industry for improvements to shorten delays and avoiding rework due to quality problem or even creating new solutions for the production processes.

The following issues are examples of possible improvements in the ship production technology:

- development of new raw materials that can be used in the shipbuilding industry;
- reduction of rework related to deformations occurring after welding (straightening processes);
- reduction of the time required to prepare cut outs in steel parts;
- development of technologies for fitting parts to be welded (section assembling);
- way to mitigate the welding induced deformation (steel plates).

A computational simulation might aid researchers in planning changes in the shipyard without physical modifications, although other types of experiments will have to be performed so that to verify the actual results, as well. Because of this certain improvements demands practical trials to verify the actual results before the modification implemented.

Looking forward to reduce the process timing, material waste, labour used and, consequently, waste of money, shipyards and design offices involve in wide-scale cooperation. For that reason, over the years researchers have implemented new ideas and carrying out various experiments in shipyards. This work is an example of that, showing a practical way to analyze the deformation in the ship panel after welding in the shipyard. Other examples of this kind of work can be found in [2], where a methodology allowing for the prediction of welding distortions and prevention of rework caused by, for instance, straightening, is presented. This way of thinking is also confirmed in the work [1], where experiments were used to understand the effects of welding on the structure, and in the work [7], which describes investigations of the weld geometry effects on the mechanical properties of undermatched welds.

Generally, steel welding is the source of one of the most fundamental problems in the shipbuilding industry, as it leads to the deformation of steel parts due to residual stresses resulting

from the interaction between welding parameters and the geometry of steel parts. Therefore this work aims at verifying a numerical way to predict the welding induced deformation after submerged arc welding during the normal production in the shipyard.

WELDING PROCESSES IN THE SHIPBUILDING INDUSTRY

According to [4], fusion welding can be described as a joining process which uses the base metal molten by high temperature to join elements..

The welding process has been used in many different types of industries due to:

- the reliability of the structures assembled;
- high speeds in mass production;
- the possibility to use automated robots to perform the welding;
- efficiency in constructing standardized parts through the use of automation;
- high quality.

Welding processes have disadvantages, as well, some of which are listed below:

- complex quality control processes;
- the need for skilled operators;
- expensive and complex infrastructure when automated welding processes are implemented;
- the possibility of substantial hazards and losses in the event a failure of the welded part during its life (the steel structures of civil buildings, vessels, oil rigs or motor vehicles).

In order to avoid these disadvantages the welding technology needs special care about the process control.

In shipbuilding, welding is extensively used because of the significant demand for steel or aluminium alloys to be used in structural elements, such as ship hulls, watertight bulkheads, decks, bottom, being typically all-welded thin plate structures, [3]. Therefore, during fabrication some deformations may occur that are caused by several factors, including the cutting of the plates and pieces, or the welding of the joints between them.

There are several methods for connecting parts. Before commencing joining works, some issues must be considered:

- the type of joint to be made;
- the type of material to be welded;
- the limitations of the production layout;
- the thickness of the plates;
- the purpose of the welding.

Submerged Arc Welding (SAW) is widely used in the shipbuilding industry and, according to [7], it offers high productivity. It is a mechanized welding method that can make use of a single electrode or several ones at the same time. The electric arc burns underneath a layer of protective flux which melts in the vicinity of the arc and produces solid slag on the weld. The non-molten excessive flux is reused.

A Few Characteristics

To arrange the welding procedure and to get reasonable results this is necessary to understand a few characteristics and effects influencing the work pieces which will be welded. Some of them have been commented earlier, such as: the type of the welding process or workpiece geometry. However, other issues are equally important when the welding process is under evaluation.

From this point of view, the following aspects should be treated as equally significant:

Heat input

Heat input can be described as one of the most important factors involved in welding and, according to [8], a significant variable related to the quality of welding, mainly with regard to the warping problem identified in welded products. Heat input affects the dimensions of the welded object, as it brings enough energy to melt the additional material and the workpiece. Such energy may generate local deformation, as indicated in [3]. Heat input is the relation between the welding energy used during the operation and the speed of the welding source along the process. This relation is measured in units of energy (Joules) per units of length (mm or cm). Together they are helpful in determining the amount of heat which will be applied to the metal in order to melt the base material (workpiece) and the fusible wire (additional material).

Residual Stress

The heat that is necessary to melt metal parts in order to join them reaches extremely high temperatures, inevitably causing certain physical phenomena inside the workpiece due to the difference between the molten pool temperature and the room one. As a consequence of this, some characteristics of the particular element may be affected due to the quick heating and cooling cycle that occurs during welding.

Welding deformation

Deformations generated during the welding process are strongly linked to the residual stress, and for many researchers they are an unavoidable problem present in every welding work. In the shipyards, according to [4] and [6], the most representative problem is the one of misalignment between blocks during the hull erection stage. These problems occur due to deformations caused by welding, which in turn cause inaccuracies in entire blocks and structural member misadjustment. These authors also claim that welding deformations do not only interfere with the aesthetical aspect, but also put the structural integrity of the ship at risk when in service.

Hence, all these characteristics must be known during the welding process to minimize the problems once the ship is delivered.

MODELLING

The literature provides a multitude of methods developed over the years using the most diversified tools designed to identify, understand, correct or, at least, mitigate the undesirable effects that the aforementioned problem has on the workflow and other production aspects. Taking advantage of some of them may help eliminate certain inconveniences encountered in the workflow which, in turn, will improve the efficiency of the process.

In order to counter these welding problems, FEM is usually used to simulate and investigate residual stress distribution along the geometry, and subsequently to suggest modifications to improve the process.

For the same reason, statistical tools are used in the process analysis, especially to solve problems or even process management. This approach drives the research toward the understanding of the process, once a number of trials are necessary to be performed. In addition, this can lead to a better insight into the current situation, which may help minimize the unfavourable effects or increase the production capacity.

The purpose of the experiments is to explain the process through its behaviours based on the actual results which are acquired from the process. The trials need to be carefully modelled, contemplating the major of the variables that take part in the analysis to know all effects of those variables in the

process. It means that all of the characteristics of the process should be evaluated in order to make sure that no inaccurate results are obtained.

It is very important to know which factors exist within the process that have a tangible effect on the final output. From the point of view of analysis, these are factors that contribute to the occurrence of the problem. To illustrate this, only a few of the various relevant factors are mentioned below regarding to the welding induced deformation:

- welding energy (current and voltage);
- welding speed;
- welding type;
- the thickness of the plates;
- the boundary conditions during the welding process.

In this case, experiments and evaluations were carried out during the normal production in the shipyard following the design of experiment (DoE) methodology.

Defining the Problem

According to [5], a number of experiments were carried out in Polish shipyard aiming at the prediction and mitigation of the welding-induced deformation which occurs after the butt-welding of 5 mm thick plates using SAW. The trials were developed on the stiffened panels with the following dimensions: width of 12 m and length of 10 or 12 m. These panels were used on the deck or in bottom area. These panels usually consist of 4 or 5 plates (depending on the length of the panel) and consequently 3 or 4 weld seams (12 m long). The plates were laid on the SAW work line to be joined by the weld seam, once their edges were already prepared.

In this case, when the panels lay properly and flat on the welding line, the causes of such deformations were sought. Certain conclusions were drawn from the analyses and the shipyard staff came up with the idea to verify the welding gantry facilities used to perform butt welding on the first side of the panels.

Fig. 1a provides a general view of the magnetic bed and the copper bar used for butt welding the first side of the panels. Fig. 1b is a simple diagram showing the forces (arrows) affecting the plates during welding. A Design of Experiment needed to be carried in order to figure out the effects of the welding parameters adding to the effect of the pressure induced by the copper bar and the magnetic bed. The first plate was positioned on the right side of the magnetic bed and then aligned along the edge and clamped by the magnetic blocks. The second plate was pulled towards the first edge plate until the span between them was around 0 to 5 mm, after this the second plate was also clamped by the magnetic blocks from the left side (Fig. 1b). Once properly positioned, the manual tack welding was performed by the operator, afterwards the operator puts down the tack welding using the pneumatic countersink. From this condition, the copper bar acted on the plate junction (I-profile) and then was possible to perform the first side butt welding using the SAW gantry.

The copper bar has been used on SAW processes to guarantee that the molten material will not leak between the plates during the process, besides it works as ground for the electric procedure and holds the 2 plates at the correct position to perform the weld.

The magnetic bed was used to fix the plates before welding and its working parameters were previously defined together with the experienced shipyard staff. The pressures were set up directly on the pressure board according to the values determined to be used during the trails (DoE – see Tab. 1.)

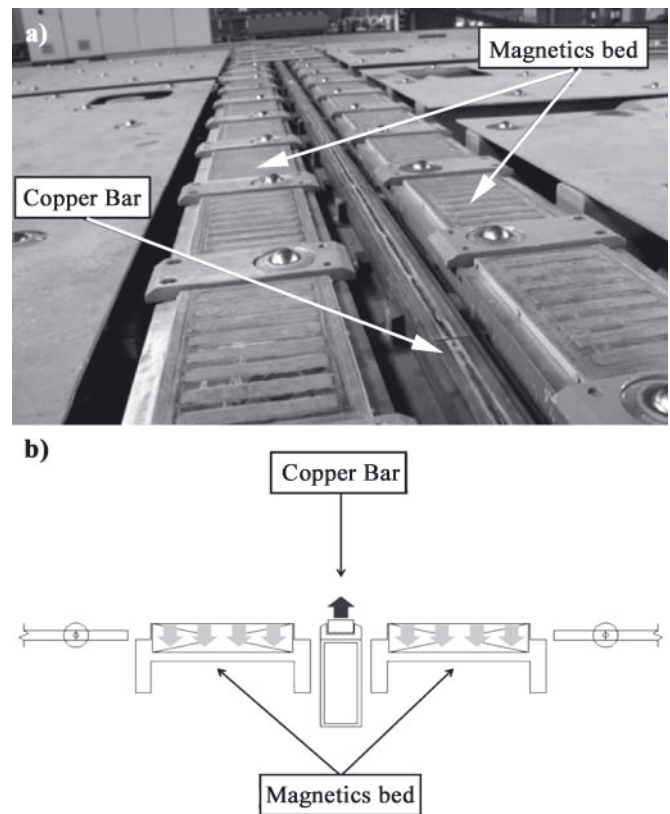


Fig. 1. The welding gantry

Data Processing

The first idea for arranging the data was to evaluate the mean value for related points distributed along the entire panel. However, this plan was discarded due to the fact that each panel had 3 different weld seams connecting its plates. The deformation should be investigated by examining each weld seam with the intention of narrowing down the number of sources of errors caused by external factors, and even excluding initial plate deformation. Thus, concentrating the measurement on areas near the weld seam could help to mitigate negative influence from these factors.

Hence, a number of approaches were examined. On the one hand, we examined the mean value of deformation between points related to the weld seam and, on the other hand, the largest value of deformation on the way from the centre of the plate to the weld seam.

Based on these examinations, two methods for data arrangement were analysed, as explained below:

- **Option 1** – Mean value arrangement

This option is illustrated in Fig. 2 showing the diagram adopted for the purposes of obtaining the value. To facilitate the analysis, this arrangement will hereinafter be referred to simply as “Option 1”.

This diagram consists of the mean value between two points (in the middle of the plate) neighbouring on a point on the weld seam.

$$D_{Op_1,i,j} = \left| \frac{P_{(i+3)+6 \cdot (j-1)} + P_{(i+9)+6 \cdot (j-1)}}{2} - P_{(i+6)+6 \cdot (j-1)} \right| \quad (1)$$

$$D_{Op_1(seam_j)} = \text{Max}(D_{Op_1,i,j}) \quad (2)$$

with i varying from 1 to 3

Where:

- j – characterizes the weld seam. This number varies from 1 to 3;

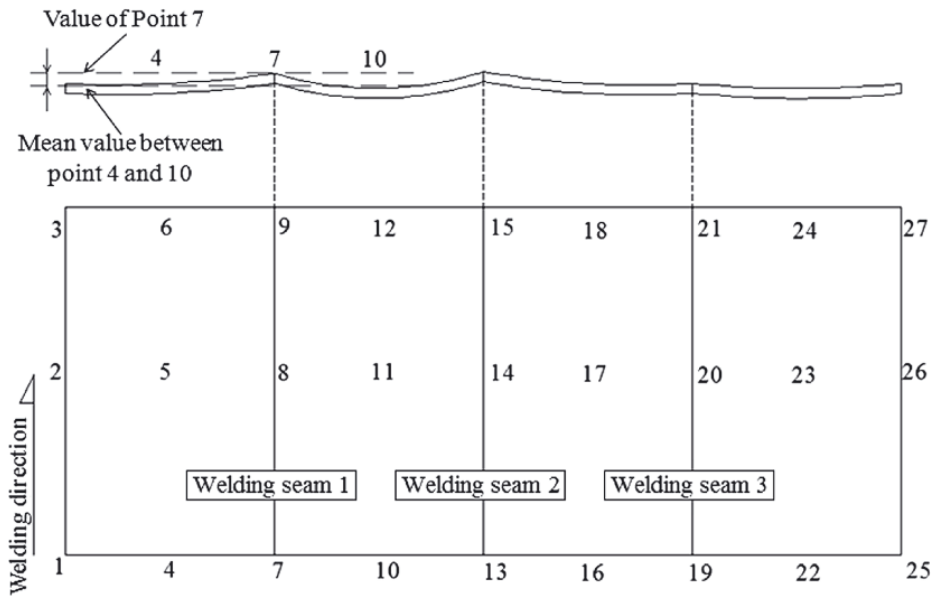


Fig. 2. Mean value arrangement: Option 1

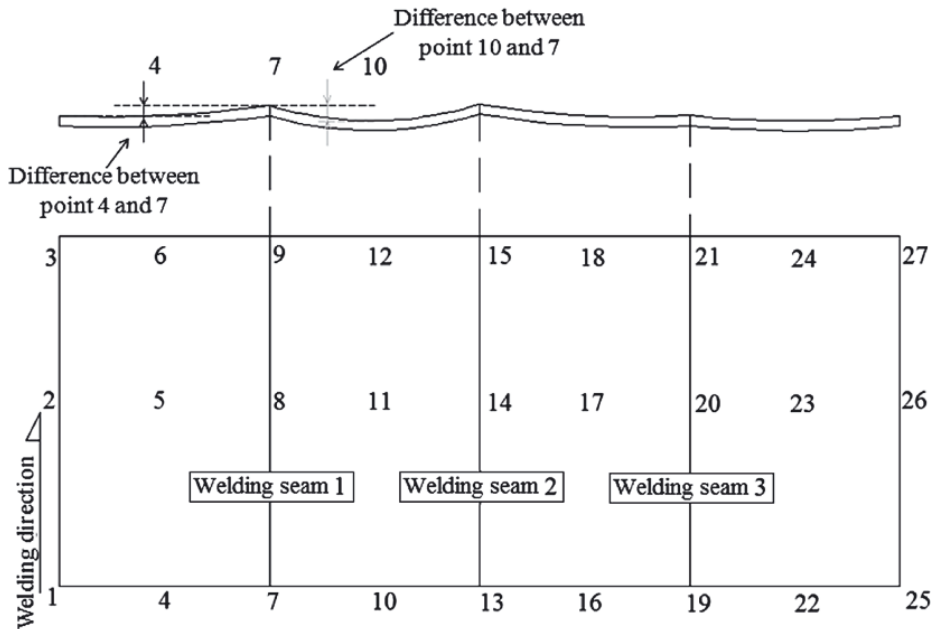


Fig. 3. Largest value arrangement: Option 2

- i – the value which determines the position of the deformation along the weld seam. This number varies from 1 to 3;
- P_x – the value measured in mm at point x;
- x – the index of point P. This number varies from 4 to 24;
- $D_{Op_1,i,j}$ – the deformation calculated at weld seam j at point i;
- $D_{Op_1(seam_j)}$ – the largest value among the three $D_{Op_1,i,j}$ values calculated at weld seam j. In other words, it is 1 out of 3 values of deformation analysed during the data processing;

◦ **Option 2** – the largest value

Fig. 3 illustrates the arrangement that takes into account the largest value of deformation around each weld seam. Similarly to Option 1, this arrangement will hereinafter be referred to as “Option 2”, simply to make the analysis easier.

This diagram makes use of the largest value of the difference between individual points neighbouring on the weld seam.

$$D_{Op_2,i,j} = \text{Max} \left(\left| P_{(i+3)+6 \cdot (j-1)} - P_{(i+6)+6 \cdot (j-1)} \right|, \left| P_{(i+9)+6 \cdot (j-1)} - P_{(i+6)+6 \cdot (j-1)} \right| \right) \quad (3)$$

$$D_{Op_2(seam_j)} = \frac{1}{3} \sum_{i=1}^3 (D_{Op_2,i,j}) \quad (4)$$

Where:

- j – characterizes the weld seam. This number varies from 1 to 3;

- Adopting this point of view, it is possible to realize that:
- each weld seam has three different $D_{Op_1,i,j}$ values (one for each edge and another one for the centre of the plate);
- the largest value among the three values measured is considered as an amplitude on the current weld seam $D_{Op_1(seam_j)}$;
- consequently, each panel yields three values for data processing.

- i – the value which determines the position of the deformation along the weld seam. This number varies from 1 to 3;
- P_x – the value measured in mm at point x ;
- x – the index of point P. This number varies from 4 to 24;
- $D_{Op_2i,j}$ – the deformation calculated at weld seam j at point i ;
- $D_{Op_2(seam_j)}$ – the largest value among the three $D_{Op_2i,j}$ values calculated at weld seam j . In other words, it is 1 out of 3 values of deformation analysed during the data processing;

Adopting this methodology, it is also possible to realize that:

- each weld seam also has three different values (one for each edge and another one for the centre of the plate);
- the average value among the three values measured is considered as an amplitude on the weld seam;
- consequently, each panel yields three values for data processing.

Once the arrangement is defined, the values for plate deformation used during the data processing are showed in Tab. 1.

Tab. 1. Deformation values from two data arrangements

Panel	Heat Input (Q) [kJ/cm]	Copper Bar (CB) [bar]	Magnetics (M) [bar]	Weld Seam	Deformations	
					Option 1 [mm]	Option 2 [mm]
01	10.96	0.35	1.0	1	33.0	19.33
				2	39.0	28.67
				3	39.0	22.67
10	10.44	0.35	1.0	1	34.5	26.33
				2	20.5	17.67
11	10.44	0.35	1.5	2	33.0	30.33
				3	36.0	32.00
12	10.44	0.35	2.0	2	33.0	16.00
				3	34.0	24.00
13	10.44	0.4	1.0	1	34.5	29.00
				2	42.0	31.00
				3	37.5	29.67
14	10.44	0.4	1.5	1	33.5	31.33
				2	31.0	29.67
				3	25.0	22.33
15	10.44	0.4	2.0	1	22.5	14.67
				2	18.0	13.67
16	10.44	0.45	1.0	1	35.0	28.33
				2	31.0	23.67
17	10.44	0.45	1.5	1	32.0	28.00
				2	23.5	18.00
				3	28.0	20.33
18	10.44	0.45	2.0	2	16.0	17.00
				3	27.0	13.33
19	11.88	0.35	1.0	1	31.0	23.00
				2	27.5	20.00
				3	17.0	14.67
20	11.88	0.35	1.5	1	28.5	25.67
				2	20.0	21.33
				3	32.5	18.67
21	11.88	0.35	2.0	2	28.0	27.67
				3	24.0	20.00
22	11.88	0.4	1.0	1	14.0	13.33
				2	34.5	19.67
				3	24.0	21.00
23	11.88	0.4	1.5	1	31.0	22.33
				2	32.0	29.33
				3	22.0	21.00
25	11.88	0.45	1.0	1	39.0	32.00
				2	27.0	25.00
				3	20.5	19.00
27	11.88	0.45	2.0	1	27.0	27.33
				2	30.5	28.33
				3	30.0	27.00

RESULTS AND DISCUSSION

Aided by the statistical software to compile the results obtained from the experiment, the values used generated two numerical equations. These equations make it possible to verify the results and the accuracy of each value provided by the models, by comparing it to the actual value of deformation measured on the steel ship panel in the shipyard. All the variables were considered by the software, including the data arrangement (see Fig. 2 and Fig. 3), to get these 2 final equations and a number of consideration were taken into account to choose the models. These considerations are described below.

For boundary conditions, the values for copper bar pressure, magnetic pressure and heat input (according to Table 1) were considered as well as the data arrangement to build the DoE (according to Figure 2 and Figure 3). The values from the plate edge were not considered and only real data (measured along the plate, according to the Figure 2 and 3) were inputted to get the equation to predict the welding deformation.

The numerical equations are presented below:

- Option 1 – Mean value arrangement

$$D_{Op_1} = 185.70 - 13.49 \cdot Q - 90.69 \cdot M + 7.74 \cdot Q \cdot M \quad (5)$$

- Option 2 – Largest value arrangement

$$D_{Op_2} = 422.45 - 35.87 \cdot Q - 574.08 \cdot CB + -113.80 \cdot M + 52.41 \cdot Q \cdot CB + 10.01 \cdot Q \cdot M \quad (6)$$

The values obtained from Option 1 demonstrate a standard deviation of approx. 6.1 mm, while the values obtained from Option 2 demonstrate a standard deviation of approx. 4.7. This difference exists because the data arrangements are different from each other. Therefore, an obvious consequence of that is that Option 1 presents a larger range of differences in deformation values than the one provided by Option 2 in trials illustrated in Tab. 2:

Tab. 2. A comparison between the results from Option 1 and Option 2

Option	Limits	Values [mm]	Amplitude of the differences in deformation values [mm]
1	Maximum	14.52	26.76
	Minimum	-12.26	
2	Maximum	11.62	20.29
	Minimum	-8.67	

A graphical comparison of these values is better at visualising the difference between the models.

Fig. 4 (a) and (b) show that although the points are not fully distributed on the 45° straight line (which would be the ideal condition for the values predicted), they are concordant to a certain extent with the actual values. It is also obvious that the manner in which the points are laid down in Option 2 is

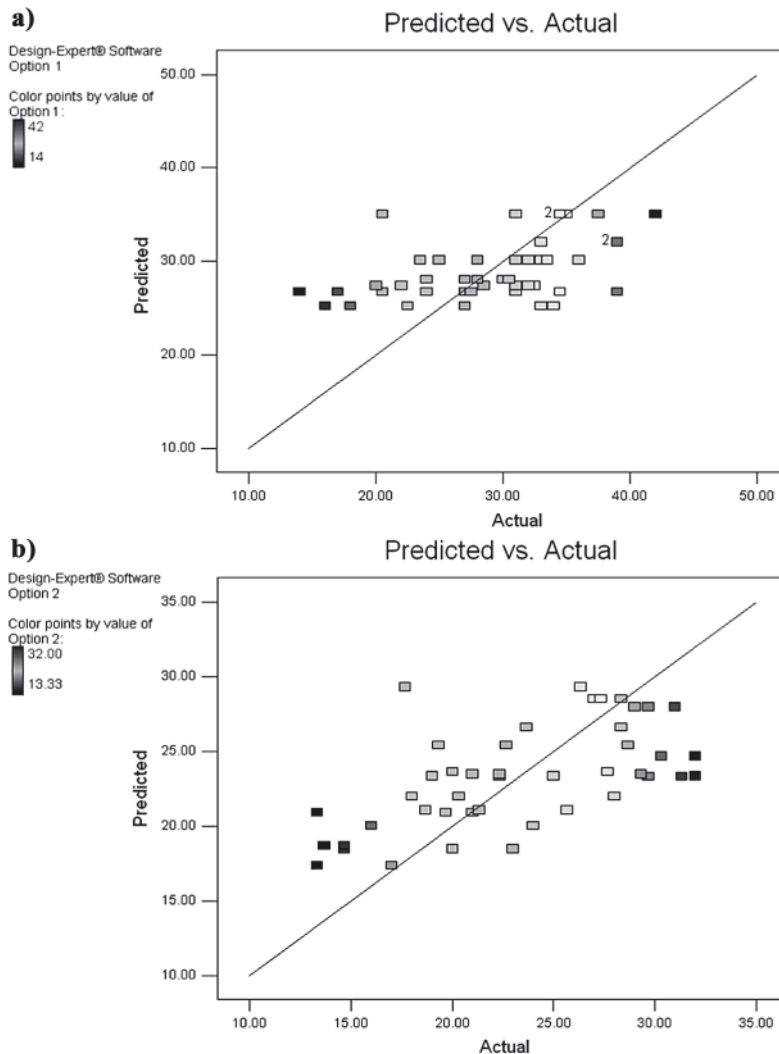


Fig. 4. A comparison between the actual and the predicted deformation values: a) Option 1 and b) Option 2

superior to the shape created in Option 1. This particularly refers to the points located at the extremities of the curve (the larger and smaller values obtained in the arrangement). In Option 2, they are spread along the line, whereas the points in Option 1 are concentrated near the mean values.

Another method for verifying the predicted deformation values for both the cases studied is shown in Fig. 5.

The cube chart makes it possible to verify all the predicted deformation values across the entire spectrum of the variability of the main factors. Highlighted in Fig. 5 (a) and (b) are the maximum (the black rectangle) and minimum (the grey rectangle) results for the deformation predicted for both the models. The best condition for work (i.e. the condition which renders the lowest deformation values according to those models) is with the following values: heat input = 10.44 kJ/cm, copper bar pressure = 0.45 bar, magnetic pressure = 2 bar.

According to these results, Option 2 demonstrates better results than Option 1 due to the smaller amplitude of the residual variation.

After the results of these two options were verified from the statistical and dimensional points of view, it was confirmed that the model described by Option 2 yielded better outcome than the one described by Option 1. There are a number of reasons

that justify these results, one of them being leaving out the copper bar effects of the model.

Moreover, another aspect of the approach adopted in this paper is the fact that the models developed through the DoE account for the average of the input values, i.e. the models operate based on the average deformation between the weld seam values. If we compare the predicted values to the average values of the weld seam the standard deviation becomes smaller, which in turn means that the model is capable of properly reflecting most of the results.

Therefore, for future evaluations using this methodology, it would be reasonable to evaluate the welding deformation of 5 mm thick steel plates.

SUMMARY

After the work done in the shipyard, the numerous trials performed on the panel welding line, the measurements taken and the result analyses carried out, a number of interesting conclusions can be drawn from the investigation, which can be formulated as follows:

1. Unlike the main methodology making use FEM simulation as proposed by several authors, the welding deformation in

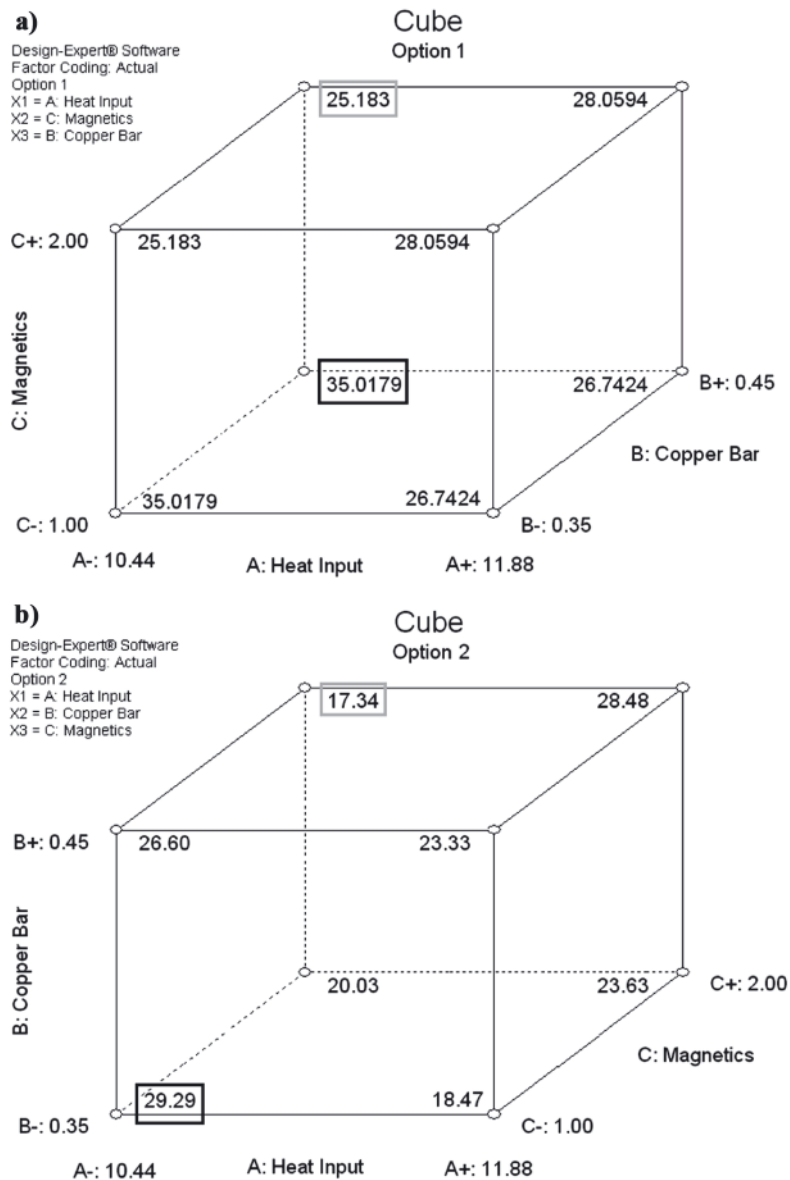


Fig. 5. Predicted deformation values: a) Option 1 and b) Option 2

butt joints on 5 mm thick steel plates can also be predicted by a statistical method, as shown in this paper.

2. An analysis subject to statistical principles may yield different results depending on how the data are inputted, and this characteristic became an important issue encountered in the course of this paper. Because of this, specific data arrangements were chosen and their results verified with the intention to derive a numerical equation capable of predicting, with the highest accuracy possible, the values of deformation similar to the ones measured in the shipyard. Surprisingly, from each data arrangement a different equation could be derived and, sometimes, such an equation did not take into account the influence of the all of the factors present.
3. The numerical equation obtained from the statistical software, through the data arrangement described by Option 2, rendered reasonable results, as compared to the data collected in the shipyard. Therefore, it can be considered a satisfactory method for predicting the welding-induced deformation in 5 mm thick steel panels.

It is also worth noting that all kinds of experiments, especially those performed under strict conditions dependent on time and equipment availability, are subject to the influence of the existing sources of errors. Such sources should be identified and, whenever possible, avoided. For future projects related to analyses through experiments, the following recommendations should be taken into account:

1. Measurements: the same person, the same equipment and the same conditions should be used to perform the measurements.
2. Feedback: throughout the task, there is a need for intensive communication with the workers responsible for the process to make sure they have sufficient understanding of the experiment. These workers will be in charge of the quality control; therefore, if during the trials something goes wrong they will be able to introduce the required corrections and fix the problems as they occur.
3. Feedback: similarly, the key person (tasked with rendering assistance whenever necessary) must be identified before the start of the experiment.
4. Noise in the model: verification of the initial condition (deformation) of the plates before the commencement of the welding process. It can help the researcher to sort the noise out of data processing, improving the overall results.

A few of the aforementioned errors may have some minor influence on the final results presented. However, the methodology used was developed taking as careful measures as possible to ensure its reliability.

A number of extra trials should be performed in order to verify the actual accuracy of the model.

BIBLIOGRAPHY

1. Awang M.: *The effects of process parameters on steel welding response in curved plates*. Thesis of Master of Science in Mechanical Engineering. West Virginia University. 2002.
2. Birk-Sørensen M.: *Simulation of welding distortions in ship section*. Industrial PhD Thesis. Technical University of Denmark. 1999.
3. Deng D., Murakawa H., Ueda Y.: *Theoretical Prediction of Welding Distortion Considering Positioning and the Gap between Parts*. 2002. The Proceedings of the Twelfth International offshore and polar engineering conference. Accessed 17 November 2011.
4. Kou S.: *Welding metallurgy*. 2nd ed. USA: John Wiley & Sons, Inc. 2003.
5. Sena Batista H.: *Analysis and prediction of welding deformations of ship panels in prefabrication process*. Master Thesis for the double degree: "Advanced Master in Naval Architecture" conferred by University of Liege "Master of Sciences in Applied Mechanics, specialization in Hydrodynamics, Energetics and Propulsion" conferred by Ecole Centrale de Nantes, work developed at West Pomeranian University of Technology, Szczecin in the framework of the "EMSHIP" Erasmus Mundus Master Course in "Integrated Advanced Ship Design". Ref. 159652-1-2009-1-BE-ERA MUNDUS-EMMC. 2011.
6. Sukovoy O., Kuo C.: *a risk-based method for minimizing welding distortion in steel ship production*. *Engineering for the Maritime Environment*, 217 (3), 123-131. 2003.
7. Törnblom S.: *Undermatching Butt Welds in High Strength Steel*. Master Thesis. Luleå University of Technology. 2007.
8. Tsai C. L., Park S. C., Cheng W. T.: *Welding Distortion of a Thin-Plate Panel Structure [online]*. American Welding Society. 1999. Accessed 12 December 2011.

CONTACT WITH THE AUTHORS

Huggo S. Batista, M.Sc.,
huggosena@gmail.com
+55 92 8804 9416

Tadeusz Graczyk, Assoc. Prof.,
tadeusz.graczyk@zut.edu.pl
+48 91 449 4696

Faculty of Maritime Technology and Transportation
West Pomeranian University of Technology, Szczecin
70-310 Szczecin, Al. Piastów 17, POLAND

Controlling a team of unmanned underwater vehicles performing water region search tasks

Andrzej Zak, Ph.D.
Polish Naval Academy, Poland

ABSTRACT



The article discusses a problem of performing a mission and controlling a team of unmanned underwater vehicles which perform a task of water region search. The team of underwater vehicles has been modelled as a multi-agent system, which made it possible to use the mechanism of multi-agent systems for controlling the team of cooperating underwater vehicles, with each vehicle being treated as an individual agent. Solutions to cooperation problems in multi-agent systems were proposed, including the presentation of the system structure and the data exchange method. Issues relating to cooperation actions in the team of underwater vehicles were described and solved using the theory of games and the vector quality index. The process of negotiations between the vehicles was modelled as the multiplayer cooperative game, which secured successful realisation of the task performed by the team of vehicles with respect to time, which represents the economic aspect of the task. The optimal solution was selected based on the vector quality index, which provided opportunities for minimisation of costs having the form of energy used by the entire team, and maximisation of profits in the form of time needed for completing the water region search task. The proposed method for dividing the action space in the water region search tasks performed by the team of underwater vehicles consists in assigning to each of cooperating underwater vehicles a task the realisation of which contributes to the realisation of the globally defined task. Finally, the results of water region search tasks performed by a team of cooperating underwater vehicles are presented and discussed taking into account possible vehicle failures happening during task realisation.

Key words: unmanned underwater vehicles; multi-agent systems; control; multiplayer cooperative games

INTRODUCTION

Nowadays, research activities concerning generally understood robotics are frequently oriented on the use of teams of cooperating robots performing tasks which cannot be performed, or will be performed less efficiently by a single robot. Such a situation can be observed in underwater robotics where concepts are developed for certain tasks to be performed by a team of underwater vehicles. These tasks most often include exploration and inspection activities, which in general can be done by a single robot but a team of robots can do them faster and more effectively. Another kind of tasks of this type are transport activities in which overall dimensions and the shape of the transported structure make the task to be only done by a team of cooperating vehicles.

A team of cooperating robots reveals numerous advantages, such as high resistance to failures, for instance, which makes it possible to perform the task even if one of robots beaks down. Moreover, in some cases the decomposition of the task to be performed by the team of robots allows us to use robots with simpler structure than that of a single robot performing the same task. However, the problem of controlling the team of cooperating robots is much more difficult than controlling a single vehicle. In case of a team of robots, additional issues

are to be discussed, including communication between the vehicles, coordination of actions, performing negotiations, and many others.

The computer sciences make more and more frequent use of multi-agent systems, especially to solve problems of distributed nature, or those requiring complicated calculations. The multi-agent system comprises a number of agents which communicate and cooperate with each other to perform a common task. The mechanism of the multi-agent system can be easily adopted to control the team of cooperating underwater vehicles in which each vehicle is treated as an individual agent.

Below presented is a concept of a multi-agent system which was used to perform a task of water region search by a team of cooperating underwater vehicles. The team is assumed to consist of homogeneous and cable-free underwater vehicles equipped with instruments for navigation, technical observation and communication used for data exchange between the vehicles. The underwater vehicles have docking stations situated at one point of the water region, where they can load their internal energy sources, transmit the collected data and receive commands to start work. The shape of the searched water region is defined by the vertexes of the polygon enclosing the region. The water region is divided by the superior system into areas, each of which is to be searched by a single

underwater vehicle. The information on the area to be searched and the corresponding passing trajectory is obtained by each vehicle from the docking station, together with the order to start work.

AGENT

The literature on the subject does not deliver any precise definition of an agent. Generally we can say that the agent is an element which is used for creating decentralised systems [2]. Another definition says that the agent is an object which can both observe the environment and act on it [15]. The most precise definition describes the agent as a system situated in a given environment which can make use of certain resources and be able to act autonomously in order to achieve assumed goals [4, 13, 14]. To make the underwater vehicle fulfil the above definition, it has to be equipped with sensors to record input signals coming from the environment, and effectors using which it can act on the environment. Additionally, it should have sort of internal awareness which will secure its autonomy manifesting itself as making decisions on actions to be performed to achieve the assumed goal. We can say that the agent can adapt its behaviour to a current situation. It should be noted, however, that the goal to be performed by one agent can differ from that assigned to another agent, and in case of common task realisation the request coming from the other agent can be realised only when it is in line with the interest of the asked agent.

To describe formally the action of the agent we introduce the following notations: $S = \{s_1, s_2, \dots\}$ represents possible environment states, and $A = \{a_1, a_2, \dots\}$ possible actions of the agent. In this situation the action can be meant as the function [13, 4]:

$$\text{action: } S^* \rightarrow A \quad (1)$$

where:

S^* – the selected sequence of environment states.

The environment can be defined as the function:

$$\text{environment: } S \times A \rightarrow S \quad (2)$$

The above notations mean that the undertaken action results from the environment state, while the environment modifies its state due to the action of the agent.

We should also define a function which allows the agent to read input signals. This action can be written as the function:

$$\text{perception: } S \rightarrow P \quad (3)$$

which maps the state of environment into perception P . Consequently, the action function takes the following form:

$$\text{action: } P^* \rightarrow A \quad (4)$$

where:

P^* – the perception sequence.

Assigning the property of autonomy to the agent consists in defining the function of actions which are to be initiated by the agent depending on input signals composing the perception. To do so, we should select a method of implementation of the decision function, at the same time selecting an appropriate type of agent. In case of underwater vehicles it seems a best solution to use the hierarchical layer architecture, the advantages of which include no need to define the decision making mechanism and simplicity of action. A popular sample of this type of architecture is the InterRRaP architecture (Fig. 1) [11, 12]. It consist of a series of layers, the lowest of which is responsible for reflex actions, the middle layer for planning, and the top layer for cooperation with other agents [4, 11, 12]. Each layer has its database which represents the state of environment attributed to this layer. The flow of control in this architecture is realised in two directions: first the control signal is transmitted from lower to higher layers, and then from higher to lower layers. If the lower layer, making use of its database, is not able to take a relevant action, it sends the signal to the higher layer. That means that the higher the layer, the more rarely it is activated.

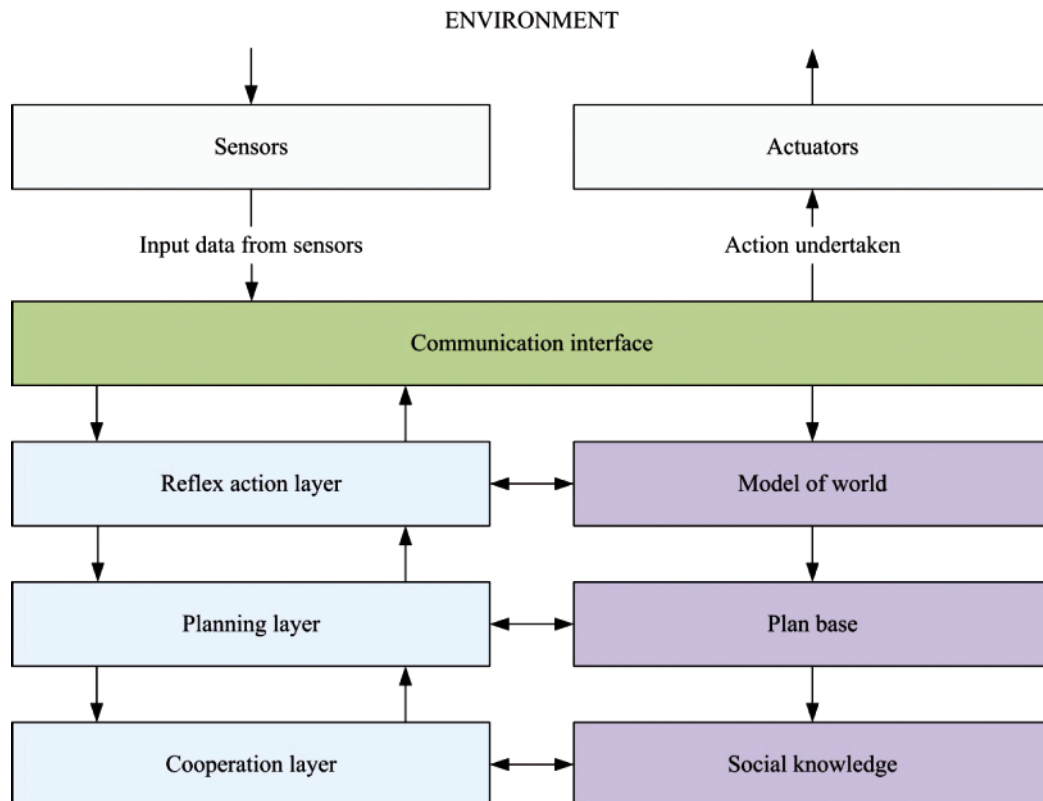


Fig. 1. Flow of control in InteRRaP type architecture [4]

According to the adopted assumptions, a single underwater vehicle is an agent whose task is to search the water region in cooperation with other vehicles. Therefore the lowest layer of the agent is responsible for avoiding obstacles [17]. The middle layer is responsible for precise motion of the underwater vehicle along the given trajectory [16], while the role of the highest layer is to cooperate with the remaining vehicles in the team.

MULTI-AGENT SYSTEM

Structure of the multi-agent system

A team of cooperating underwater vehicles in which each vehicle is an agent composes a multi-agent system. The agents in this system communicate with each other, at the same time preserving the autonomy of their operation and decision making, which is reflected in actions undertaken by particular agents. Such an interaction between the agents leads to the modification of knowledge and actions performed by individual agents based on the observation of the behaviour of other agents and information transmitted in the communication process. An individual agent is equipped with the strategy leading it to achieving the assumed goal. However, being part of the multi-agent system it has to put in practice the strategy of cooperation with other agents, especially when this strategy facilitates reaching the goal common for the entire team. Cooperation and competition between the agents in a multi-agent system is its key feature [9]. To make it possible, we should define the structure and formulate protocols of interaction to provide opportunities for describing message exchange scenarios and allow making decisions.

The multi-agent system can have a hierarchic structure, in which a decision about future actions is made by the team leader, or a flat structure, in which all agents are equal and decisions are made as a result of negotiations. The advantage of the hierarchical structure is high speed of decision making, as the time-consuming process of negotiations can be avoided here. Its disadvantage is relatively poor use of all team potential, as the team leader can make decisions based on the information on the environment and other agents which is insufficient to make the right decision. The problem also arises when the current leader breaks down and mechanisms of selection of a new leader are to be applied. In case of flat structure this problem does not exist and decisions are made collectively. Unfortunately, decision making in this structure is a very time consuming process.

Either of these two structures can be successfully used in the task of water region search realised by a team of autonomous underwater vehicles. However, since the water environment is very dangerous and unfriendly to technical equipment, we should assume that failures of vehicles can happen relatively often. Moreover, search tasks can be performed in relatively long times, which means no limits concerning the speed of decision making processes. That is why the flat structure seems more appropriate and better promises success in the realisation of tasks of the above type.

Data exchange

The essence of the multi-agent system is coherent behaviour of all agents composing the team. Difficulties in the realisation of this task result from the fact that multi-agent systems have no central control, and securing coherent action of particular agents requires data exchange via mutual communication. Therefore we should assume that each agent has ability to send, receive and analyse the data, and that there is a well-defined protocol of interaction, the same for all agents.

The interaction protocols are divided, in general, into coordination protocols and communication protocols. The coordination protocols are used for periodical exchange of information on current condition of particular agents, including redundancy avoiding, while the cooperation protocols are used for settling cooperation between particular agents, i.e. task decomposition and distribution. The action of both protocols requires a relevant mechanism of data exchange. An interesting solution in this context seems to be the interaction mechanism of Blackboard type, the idea of which consists in the existence of common memory, frequently bearing the name of a blackboard, in which agents can write and read data. This way each agent has access to the data recorded by other agents and can, at an arbitrary time, write and read data in the blackboard. The data stored in the blackboard are valid for certain time, or until they are updated by more current data. Since the adopted structure is flat without a defined leader which would be responsible for data storage, the common memory will be stored by each agent. In other words, each agent will have a copy of the information stored in the blackboard. In this case data modification in the blackboard will consist in transmitting new data by one agent to all remaining agents, after which the data will be updated in the blackboard.

Since the underwater vehicles perform their tasks in the water environment, the common transmission medium of all agents is water, and the transmitted messages will have the form of mechanical (sound) waves. In this context it seems reasonable to use a token ring mechanism, which was successfully used in computer networks. The action of this data exchange mechanism makes use of the exchange of authorisation, or a so-called token. The vehicles are numbered in accordance with the increased distance of the area to be searched by them from the docking place. The agents, one by one, receive a token which allows them to pass a message, and then pass the token over to the next vehicle. The last vehicle passes the token to the first one. The agent which wants to pass the message waits for a free token, and having received it changes it into the occupied token and passes the data block bearing the name of a frame.

Cooperative action

The cooperative action in multi-agent systems can be described as a multiplayer cooperative game. The cooperative game will be an ordered pair having the form [1]:

$$\Gamma = (N, v) \quad (5)$$

where:

$N = \{1, \dots, n, \dots, N\}$ – the set of player numbers

$v: 2^N \rightarrow \mathfrak{R}^1$ – the characteristic function of the game.

The characteristic function of the game assigns to each set $S \subset N$, where S represents all possible coalitions in the team of agents including those composed of single agents, a total maximal secured payment $v(S)$ which can be obtained by the members of coalition S irrespective of the action undertaken by the remaining players. It is additionally assumed that $v(\emptyset) = 0$ and $v(\cdot)$ is super-additive i.e.:

$$v(S) + v(T) \leq v(S \cup T); S, T \subset N; S \cap T = \emptyset \quad (6)$$

A solution to the multiplayer cooperative game can be presented as the solution to the multi-criteria optimisation of the following type:

$$(X, F, R) \quad (7)$$

where:

X – the nonempty set of feasible solutions,

$F: X \rightarrow \mathfrak{R}^N$ – the vector quality index, and R defines the relation of domination.

When analysing the cooperation between the agents performing the task of water region search, the set of feasible solutions is the set of all possible coalitions which can be formed between these agents. The criterion function assigns to each feasible solution $x \in X$ its numerical valuation, important for selecting the best solution. In search-type tasks we tend to minimise the time of task realisation, which is directly connected with the minimisation of the length of the path to be covered by each vehicle. Since the cooperation game is played when one of agents cannot do the assigned task and another agent, or coalition of agents, is to take it over, we will want the profit from the task done by this vehicle or coalition of vehicles to be the maximal, the cost borne by each vehicle to perform the supplementary work to be the minimal, and the coalition performing the supplementary work to be the largest. The above assumptions would allow the team of vehicles to do the water region search task at the shortest possible time. Consequently, the quality index can be defined as:

$$F(x) = \{Z, K, L\} \quad (8)$$

where:

- Z – the profit which can be obtained as a result of supplementary action undertaken by the coalition of agents,
- K – the cost borne by each agent composing the coalition formed to do the supplementary work,
- L – the number of coalition members.

Let W_D represent the cost which a given agent has to bear to reach the place from which the supplementary action begins. This cost can be identified with the length of the path between the last point of its own trajectory and the point from which the supplementary action begins. Additionally, let W_T represent the cost connected with covering the remaining part of the trajectory within the framework of the realisation of the supplementary task, which can be identified with the length of the trajectory to be covered in this supplementary action. In this case the cost K_{max} is the maximal cost borne by a single vehicle performing the supplementary task with the longest approach path, which can be written as:

$$K_{max} = W_T + \max_{i \in N} (W_{D,i}) \quad (9)$$

where:

- i – the agent number from within a set of all efficient agents.

When a coalition between a number of agents is formed, the task will be performed simultaneously by all coalition members. Therefore the cost borne by a single agent composing the coalition will be the sum of the cost borne for realisation of the remaining trajectory part and the cost of approach, taking into account the number of agents composing the coalition, which can be written as:

$$K = \frac{W_T + \sum_{i \in S} W_{D,i}}{L} \quad (10)$$

The profit Z obtained by the given coalition of agents will be defined as:

$$Z = K_{max} - K \quad (11)$$

which means that it is the difference between the maximal cost of realisation of the supplementary work by a single agent with the longest approach path and the cost to be borne by the agent as a coalition member.

A set of all values of the criterion function F which it takes over a set X creates the criteria space Y:

$$Y = \{y = F(x) \in \mathfrak{R}^N \mid x \in X\} \quad (12)$$

being the map of the set X in \mathfrak{R}^N .

To select a desired solution x from the set X we have to compare different solutions. This comparison is realised by comparing numerical values of particular estimations $F_n(x)$ attributed to the compared solutions. Therefore we can say that the decision whether solution x_1 is better than solution x_2 is made by comparing their numerical images $F(x_1)$ and $F(x_2)$. We should define the relation $R \subset Y \times Y$, i.e. the relation of domination which will make it possible to decide whether the estimation of the image $F(x_1) = y_1$ is better than that of $F(x_2) = y_2$, or not.

The relation R can be defined using the propositional function in the following way:

$$R_\varphi = \{(y_1, y_2) \in Y \times Y \mid \varphi(y_1, y_2) = 1\} \quad (13)$$

where the propositional function $\varphi: Y \times Y \rightarrow \{0,1\}$ has the form:

$$\varphi(y_1, y_2) \equiv y_1 \text{ is better than } y_2 \quad (14)$$

In the analysed case, for the quality index having the form of (3.16) the relation of domination can be defined in the following way:

$$\varphi(y_1, y_2) \equiv L_1 \geq L_2 \quad (15)$$

$$\varphi(y_1, y_2) \equiv Z_1 \geq Z_2 \quad \text{and} \quad (16)$$

$$Z_1 \geq |L_1| \max_{n \in S_1} Z(\{n\}) \wedge Z_2 \geq |L_2| \max_{n \in S_2} Z(\{n\})$$

$$\varphi(y_1, y_2) \equiv K_1 \leq K_2 \quad \text{and} \quad (17)$$

$$K_{1,i} - W_{1,D,i} \geq 2W_{1,D,i} \wedge K_{2,i} - W_{2,D,i} \geq 2W_{2,D,i}$$

Condition (15) says that the coalition performing the supplementary task is to be as large as possible. Condition (16) says that the profit to be obtained as a result of coalition formation is to be the maximal, and at least L times as big as the maximal profit of all coalition members, where L is the number of coalition members. Condition (17) says that each coalition member is to have an attributed search trajectory with the length larger or at least equal to two lengths of the approach path to the point at which the supplementary action starts.

DIVISION OF ACTION SPACE

When a team of cooperating underwater vehicles performs a task, a problem which is to be decided upon is how to divide the action space. The division of the action space consists in allocating an individual task to each of cooperating underwater vehicles in such a way that all individual tasks compose the globally defined task. In case of water region search task performed by a number of underwater vehicles, the division of the action space will consist in physical separation of water region areas to be searched by a single underwater vehicle. Searching all areas of the water region divided in the above way will be equivalent with the realisation of the search of the entire water region.

A solution to this problem consists in geometrical division of the water region treated as a polygon into smaller polygons, being separate areas for which probing lines and underwater vehicle passing trajectories are then determined [3, 7, 8, 10]. However, this solution has some disadvantages. For instance, in this solution the time needed for reaching the searched area by the underwater vehicle, a parameter of certain importance, cannot be estimated. Moreover, when determining probing lines and passing trajectories for each of the separated areas, it may happen at the border between the adjoining areas that some area parts are omitted, or are searched twice or more times. These disadvantages can be eliminated by introducing another method of action space division, which consists in determining first the probing lines and passing trajectories for the entire searched water region, and then dividing the trajectories into segments, each of which to be covered by a single underwater vehicle. Such a solution has certain advantages, the most important of which is elimination of time-consuming procedures of geometrical division of the water region and substituting it by a simple iterative algorithm of trajectory division into segments. Moreover, after combining together, the data recorded by all underwater vehicles performing the water region search task have the same form as those obtained, hypothetically, by a single underwater vehicle. The proposed solution also secures uniform distribution of work over all underwater vehicles and provides opportunities for covering the entire area of the water region by technical observation means without multiplying the observation. Figure 2 shows differences between dividing the action space on the geometrical basis and using the passing trajectory division.

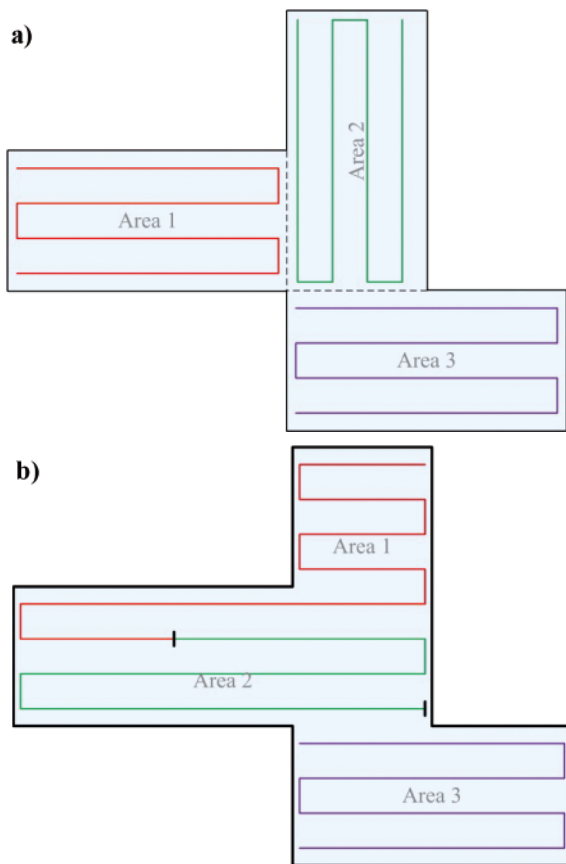


Fig. 2. Division of action space: a) geometrical division of water region, b) division of passing trajectory.

The basic idea of the proposed solution consists in dividing the full trajectory worked out for the entire searched water region into segment explored by particular underwater

vehicles. In order to meet the condition that all underwater vehicles taking part in the search are similarly loaded the trajectory is to be divided in such a way that each segment has approximately the same length, including the paths of vehicle approach to the starting point of search operation and return to the docking place.

The task consisting in trajectory division into segments can be defined in the following way: let $n \geq 2$ represent the number of segments into which the trajectory \overline{SK} is to be divided. We assume the existence of such points A_i belonging to the trajectory \overline{SK} that:

$$\left| \overline{SA_1} \right| + \sum_{i=1 \dots n-2} \left| \overline{A_i A_{i+1}} \right| + \left| \overline{A_{n-1} K} \right| = \left| \overline{SK} \right| \quad (18)$$

and that

$$\begin{aligned} \left| \overline{SA_1} \right| + d_0 &= \left| \overline{A_1 A_2} \right| + d_1 = \\ &= \dots = \left| \overline{A_i A_{i+1}} \right| + d_i = \dots = \left| \overline{A_{n-1} K} \right| + d_{n-1} \end{aligned} \quad (19)$$

where: d_i is the total length of the shortest path of approach to point A_i and return from point A_{i+1} , i.e.:

$$d_i = \left| \overline{SA_i} \right| + \left| \overline{A_{i+1} S} \right| \quad (20)$$

Condition (18) secures that the entire trajectory will be used when dividing the trajectory into segments, while condition (19) means that each trajectory segment, together with the approach and return paths, will have the same length.

RESULTS OF INVESTIGATIONS

In previous sections a solutions was proposed which allows controlling a team of underwater vehicles cooperating within the framework of the multi-agent system. The control algorithms making use of the multi-agent system and combined with the algorithm of control along a given trajectory 516 were implemented on the computer, which provided opportunities for performing their tests.

As a test sample, the task of Gdynia harbour search was performed by a team consisting of eight cooperating underwater vehicles. It was assumed in the test that the underwater vehicle 2 broke down after covering 3 947.6 [m] of the trajectory attributed to it. According to the adopted solution the remaining underwater vehicles started negotiations to settle which vehicle, or coalition of vehicles will complete the task started by vehicle 2. After negotiations, the vehicles presented costs of realisation of the supplementary task, see table 1.

As a result of the performed negotiations, profits from particular coalitions were calculated, and then coalitions securing highest profits were selected in groups of different numbers of coalition members (table 2). It was checked for each coalition whether the conditions (15) (16) and (17) are met. Based on that it was concluded that the most profitable solution will take place when the supplementary task is taken over by a coalition of agents consisting of vehicle 3 and vehicle 5. Since the coalition consists of two members the profit will be 2.96 times as high as in case of single vehicle coalition, while the cost of search will be 5.75 times as high, compared to the cost of approach of vehicle 3, and 3.76 times as high as for vehicle 5. In case of larger coalitions, condition (17) is not met for one or more vehicles. For coalitions composed of more than 3 vehicles condition (16) is not met either. Table 3 collects the numerical data describing the performed task, while Figure 3 shows the passing trajectories of each underwater vehicle against the electronic map of the searched water region.

Tab. 1. Presented costs of supplementary action to be undertaken after failure of vehicle 2

Vehicle number	1	3	4	5	6	7	8
Presented cost	1 100.6	526.4	1 042.9	769.2	1 404.1	1417.3	1942.7

Tab. 2. Data settled in the negotiation process after vehicle 2 break-down

Coalition	Profit	Cost borne by a single vehicle
{3}	1416.3	6336.9
{3, 5}	4200.15	3553.0
{3, 4, 5}	5036.9	2716.3
{1, 3, 4, 5}	5440.8	2312.4
{1, 3, 4, 5, 6}	5622.5	2130.74
{1, 3, 4, 5, 6, 7}	5741.4	2011.8
{1, 3, 4, 5, 6, 7, 8}	5751.2	2002.0

Tab. 3. Data of the performed task of Gdynia harbour search

Harbour area [m ²]:	1714708.2	Number of vehicles in the team [-]:	8
Shoreline length [m]:	15334.7	Vehicle 1:	path length [m]: 9 676.2
			realisation time [min]: 80.65
Water region depth [m]:	16.0	Vehicle 2:	path length [m]: 3 947.6
			realisation time [min]: 33.0
Distance from bottom when performing the task [m]:	13.0	Vehicle 3:	path length [m]: 12 640.8
			realisation time [min]: 105.4
Observation zone width [m]:	55.8	Vehicle 4:	path length [m]: 9 867.1
			realisation time [min]: 82.5
Distance between probing lines [m]:	54.4	Vehicle 5:	path length [m]: 13 044.1
			realisation time [min]: 108.7
Course of probing lines:	80°	Vehicle 6:	path length [m]: 9 437.1
			realisation time [min]: 78.7
Total path length [m]:	42494.4	Vehicle 7:	path length [m]: 9 647.7
			realisation time [min]: 80.4
Total time of task realisation by a single vehicle [min]:	354.12	Vehicle 8:	path length [m]: 9 879.3
			realisation time [min]: 82.5

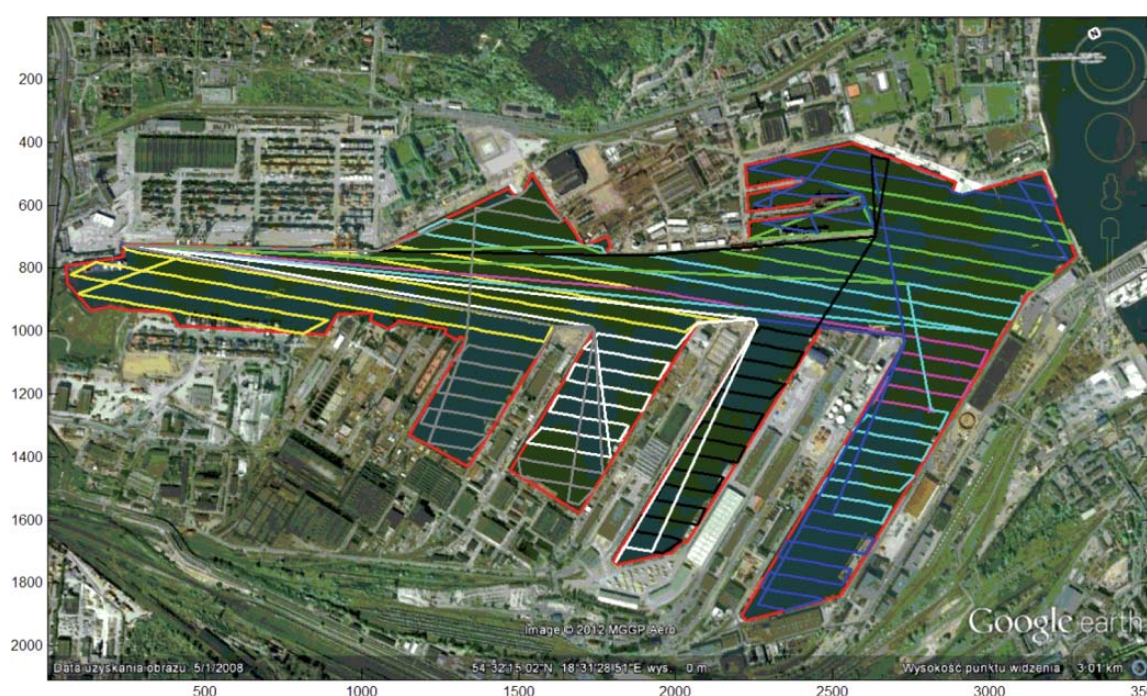


Fig. 3. Passing trajectories realised by each of underwater vehicles composing the team which performed the task of Gdynia harbour search

Based on the performed tests we can conclude that the use of many vehicles for searching a water region leads to considerable reduction of time needed for doing this task. It is noteworthy, however, that this time does not decrease proportionally to the number of the used vehicles, which results from the fact that the time of approach of each vehicle to the area of its operation is to be taken into account. Assuming no vehicle break-down, a single vehicle needs 129.2 [min] for covering the trajectory having the length of 15503.9 [m], while the cooperation of five underwater vehicles extends the trajectory by 7623.6 [m], which is the total approaching distance of the vehicles to the area of operation. However, at the same time the total searching time is 3.3 time shorter and is reduced to 39.4 [min]. Assuming that one vehicle breaks down during task realisation, a single vehicle needs 354.12 [min] for covering the trajectory having the length of 42494.4 [m], while the team of eight cooperating vehicles extends this distance nearly twice, to 78139.9 [m], but the time of task realisation is equal to 108.7 [min], i.e. 3.3 times faster than it would be done by a single underwater vehicle. Another advantage of coalition which should be mentioned here is that the search task for the entire water region can be successfully completed, which would not be possible in case of one vehicle performing the search and its subsequent failure during task realisation.

CONCLUSIONS

Controlling a team of autonomous underwater vehicles is a complicated issue, especially in case when the motion of vehicles is subject to limitations oriented on minimisation of the task realisation time. The problem becomes even more difficult when the vehicles have to cooperate to perform supplementary tasks after a failure of one or more vehicles taking part in the search action. Taking into account water as unfriendly environment and difficulties connected with precise realisation of the set trajectory, as well as with navigation and communication, we should conclude that the problem of controlling the team of underwater vehicles is extremely nontrivial. Its solution needs an untypical combined approach, which will link the knowledge from within the fields of automation, computer science, communication, and sociology. All these features can be found in multi-agent systems which are still in the phase of tests and definition of principles. Their basic idea secures cooperation of a team of robots acting to achieve a common goal which is the realisation of the formulated task.

The performed tests have revealed that controlling the team of underwater vehicles with the aid of a multi-agent system provides opportunities for efficient realisation of the task defined as searching a given water region. Adopting the above concept to the underwater search task resulted in doing the task in much shorter time than in case of a single vehicle performing the same task, simultaneously securing higher chances of success of the mission even when one or more underwater vehicles break down. The proposed solutions permit more efficient distribution of individual tasks, being parts of the global task, over individual vehicles composing the team. The proposed communication solutions make it possible to exchange efficiently the information between the agents, which secures fluent realisation of both coordination and cooperation actions. Moreover, defining the cooperative actions as the multiplayer cooperative game with vector criteria function allows us to use multi-criteria optimisation to solve problems of supplementary actions to be undertaken after failure of one or more agents. The adopted quality indices and the defined functions of domination secure the realisation of the

water region search task by a team of underwater vehicles in minimal time and at minimal costs. The proposed algorithms of agent's operation along with the defined actions of cooperation performed during the negotiations secure proper behaviour of individual agents and, consequently, of the entire team.

It is noteworthy that the combined use of a number of cooperating underwater vehicles in water region search tasks result in shortening the time needed for doing the task. However, the time reduction is not proportional to the increasing number of the used vehicles, which is connected with extra time expenses to be covered by each vehicle to reach the area of its action. Taking this into account when dividing the action space makes it possible to assign optimally partial tasks, while at the stage of cooperation actions it allows to choose the coalition of vehicles performing the supplementary action in such a way that both the time of operation of the entire team and cost of the supplementary operation are minimal. The adopted solutions make it possible to determine the minimal time needed for performing the search action by the team of underwater vehicles in the given water region, even after assuming the failure of one or more vehicles before the start of the search. Moreover the proposed solutions make it possible to determine the optimal number of underwater vehicles which will perform the action in the given water region, thus minimising both the time of search and the number of vehicles.

REFERENCES

1. Ameljańczyk A.: *Multi-criteria optimisation in control and management problems*, (in Polish), Zakład Narodowy im. Ossolińskich, 1984
2. Cetnarowicz K., Gruer P., Hilaire V., Koukam A.: *A Formal Specification of M-Agent Architecture*, Revised Paper from the Second International Workshop of Central and Eastern Europe on Multi-Agent Systems, Springer-Verlag, London UK, 2002, pp. 62-72
3. Choset H.: *Coverage for robotics – A survey of recent results*, Annals of Mathematics and Artificial Intelligence 31, Kluwer Academic Publishers, 2011, pp. 113-126
4. Ferber J.: *Multi-Agents Systems. An Introduction to Distributed Artificial Intelligence*, Addison Wesley, London 1999
5. Garus J., Żak B.: *Using of soft computing techniques to control of underwater robot*, 15th International Conference on Methods and Models in Automation and Robotics (MMAR), 2010, pp. 415 - 419
6. Gnatowski M.: *Application of multi-agent systems in cooperation of mobile robots* (in Polish), Ph.D. thesis, Institute of Fundamental Technological Research PASN, Warsaw 2005.
7. Hert S., Lemelsky V.: *Polygon Area Decomposition for Multiple-Robot Workspace Division*, International Journal of Computational Geometry and Application, vol. 8, no. 4, 1998, pp. 437-466
8. Hert S., Tiwari S., Lumelsky V.: *A Terrain-Covering Algorithm for an AUV*, Underwater Robots, Kluwer Academic Publisher, Boston, 1996, pp. 17-45
9. Łuszpaj A.: *JADE Java Agent Development Framework*, Internet page: <http://home.agh.edu.pl/~kozlak/SA/jade2/jade.htm>, access: 10.07.2012
10. Maza I., Ollero A.: *Multiple UAV cooperative searching operation using polygon area decomposition and efficient coverage algorithms*, Distributed Autonomous Robotic Systems 6, 2007, pp. 221-230
11. Muller J.P., Pischel M.: *The Agent Architecture InteRRaP. Concept and Application*, German Research Center for Artificial Intelligence, 1993
12. Muller J.P.: *The Design of Intelligent Agents. A Layered Approach*, Lecture Notes in Computer Science, Volume 1177/1996, 1996
13. Weiss G.: *Multiagent Systems. A Modern Approach to Distributed Artificial Intelligence*, The MIT Press, 1999

14. Wooldridge M.: Jennings N. R.: *Intelligent Agents. Theory and Practice*, The Knowledge Engineering Review 10 No 2, 1995, pp. 115-152
15. Zieliński C.: *Formal Approach to the Design of Control Software for Assistive Robots in Advanced Manufacturing Systems*, Seminar on Human-Robot Collaboration in Manufacturing, Singapore Institute of Manufacturing Technology, SIMTech 2005
16. Zak A.: *Trajectory-Tracking Control of Underwater Vehicles*, Solid State Phenomena Vol. 196 (2013), Trans Tech Publications Ltd. Switzerland, 2013, pp. 156-165
17. Zak B.: *The minimal-time control in collision situation on the sea*, Proceedings of the 6th WSEAS International Conference on Systems Theory & Scientific Computation, 2006, pp. 175-180

CONTACT WITH THE AUTHOR

Andrzej Zak, Ph.D.,
Polish Naval Academy
ul. Smidowicza 69,
81-103 Gdynia, POLAND
e-mail: a.zak@amw.gdynia.pl
mobile: +48 691 999 318

The influence of organic polymer on properties of mineral concentrates

Part II

Marzenna Popek, Ph.D.
Gdynia Maritime University, Poland

ABSTRACT



Transport of mineral concentrates is associated with high risk of liquefaction of the cargoes. This type of goods containing water may liquefy and shift dangerously across the cargo compartments. Therefore, it is rational to limit the moisture content of the cargoes which may liquefy. To prevent sliding and shifting of ore concentrates in storage biodegradable materials composed of starch are added to the mineral concentrates. The influence of adding starch materials to the mineral concentrates on its parameters determining ability for safe shipment was assessed on the basis of determination of the following parameters: permeability, cohesion and internal friction angle of concentrates.

Keywords: mineral concentrates; liquefaction; shifting; starch materials

INTRODUCTION

Bulk cargo shipping has been used for many years to reduce the cost of sea transport and the transport of bulk cargoes is a vital component of international trade. Such trade requires a sufficient volume of cargo suitable for bulk handling and hence justifies a tailored shipping operation. The five major dry bulk cargoes are: coal, mineral concentrates, grain, bauxite and rocky phosphate, and the trade in bulk increases each year [1].

Mineral concentrates and other similar fine – grained materials are transported by sea in a wet state. The process has become increasingly associated with high risk of liquefaction of the cargoes. The International Maritime Organization (IMO), recognising that some losses had occurred due to improper loading, issued codes of practice for such operations [2, 3, 4].

To each of mineral concentrates liable to liquefaction is assigned a Transportable Moisture Limit (TML) representing the maximum moisture content of such cargo to be considered safe for carriage in ships. The cargoes prone to liquefaction should never be carried without checking their moisture content. The International Maritime Solid Bulk Cargo Code (IMSBC Code) lays down that a certificate stating the relevant characteristics of the material to be loaded, including also its TML value, should be provided at the loading port. The Code provides information how the moisture content of mineral concentrates can be tested and assessed.

The liquefaction is caused by migration of moisture. The moisture migration occurs when vibration at sea progressively

makes the water contained in a cargo to migrate down to the bottom of a hold. The process might eventually lead to forming a free surface triggering dangerous violent shifting the cargo from side to side. The resulting much wetter bottom layer may therefore be prone to liquefaction and provoke instability of the entire cargo even though the average moisture content of the whole cargo remains lower than the TML [5, 6].

In general, finer material will liquefy (due to rise of water pressure in pores) more easily than coarser grained cargo because the water moves more easily through the larger pores between coarser particles. As a result, the pore pressure in coarse material dissipates more rapidly or does not build up at all. This is a generalization because many cargoes are not all fine or all coarse but usually consist of a mixture of particles of various size. They have a wide distribution of size of particles.

Natural and synthetic polymers (and their respective composites) are currently extensively used as biomaterials and in biodegradable applications because they are available in a wide variety of composition and their properties can be tailored to meet specific demands. Differences in the manufacturing process and in the composition of the raw material can significantly alter the functionality of the final product [7, 8].

In recent decades a major position has been taken by the materials made of synthetic polymers processed from crude oil. The cost of their production is low while their functional properties are very good and so is their resistance to environmental influences. Their durability regarded as a favourable feature, has become a serious ecological problem

[9]. As a result, attempts have been made to solve the problems by introducing biodegradability into polymers through slight modifications of their structure.

In the last few years it has been noticed an increasing interest in biodegradable polymers derived from annually renewable feedstock such as starch and starch-based materials [10, 11, 12]. Starch is a polymer which occurs widely in plants. In all plants starch is produced in the form of granules. In general, the linear polymer, amylose, makes up about 20% of the granule, and the branched polymer, amylopectin, the remainder. The starch molecule has two important functional group, the –OH group that is susceptible to substitution reaction and the C-O-C bond that is susceptible to chain breakage. The hydroxyl group of glucose has a nucleophilic character. By the reaction of its –OH group, modification of various properties can be obtained. Cross-linking or bridging the –OH groups changes the structure into a network thus increasing the viscosity and reducing water retention.

Chemical and physical properties of starch have been widely investigated because it is easy to convert it into a thermoplastic and then to use it in different applications. A favorable feature of such material is its ability to absorb large quantities of water from the material of high humidity.

In this work the results of the investigation on possible using the starch as an absorber (hydrophilic material), are presented.

EXPERIMENTAL PROCEDURE

Material

For the tests in question was used a sedimentary lead concentrate (sedimentary galena) composed mainly of PbS.

The main component of the concentrate is the mineral galena whose chemical formula is PbS (lead sulphide). The sedimentary galena is a product of gravimetric separation of large mineral particles. The lead content in the sedimentary galena amounts to about 80%. The water content in the sedimentary concentrate is equal to 1÷2%. The sedimentary galena is empirically judged as a material “which may liquefy if shipped above the TML”.

The following starch materials were tested (potato starch obtained from Potato Industry Company, Luboń, Poland):

- cross-linked starch - diamylaceous phosphate - “Lubostat”
- cross-linked starch - acetylic diamylaceous adipate - “AD”
- natural starch - a granulated product

The samples of starch materials were in a granular form. The experiments were conducted for samples of a concentrate without starch materials and of mixtures containing 99.5%, 99% and 98% of the concentrate and 0.5%, 1%, and 2% of starch materials, respectively. The used starch materials are classified as a product of a low environmental impact.

Methods

The influence of adding starch materials to the mineral concentrates on their parameters which determine ability for safe shipment by sea, was assessed on the basis of determination of the following parameters:

Permeability of concentrates

The permeability is the rate at which water under pressure can diffuse through the voids in the mineral concentrates. Such materials are permeable to water because the voids between the particles are inter-connected. The degree of permeability

is characterized by the permeability coefficient k , also referred to as hydraulic conductivity.

According to the classification of soils, based on their permeability coefficient, mineral concentrates are the materials with a low degree of permeability. The permeability of mineral concentrates depends primarily on the size and shape of grains, shape and arrangement of voids, void ratio, degree of saturation, and temperature.

Permeability is an important parameter which determines the ability to liquefy the solid bulk cargoes in conditions of maritime transport. Liquefaction occurs first at the bottom layer of cargo as a result of filtration of water from the upper layers of cargo and for this reason its permeability should be determined.

Measurement of cohesion and internal friction angle

The estimation of cohesion and internal friction angle was performed in a direct shear apparatus by carrying the shearing with the use of the lower and upper part of displacing box containing the tested concentrate. In the experiment the samples were compacted in a dry state. The moisture content corresponded to the TML value estimated by means of Proctor C/Fagerberg Test.

The cohesion does not occur in dry materials with pores entirely filled with air nor in moist materials having pores entirely filled with water. The cohesion increases with the increasing content of water and reaches its maximum values at a moisture approaching the TML, and then it goes down again. The internal friction angle reaches its minimum value when the moisture content is chosen close to TML [13].

The 0.5% and 2% content of starch material in mixture with sedimentary galena does not significantly changes grain size distribution. Starch absorbed water from the mixtures at the amount approximately proportional to the starch material content in the mineral concentrate. It can be noticed that modified starch shows a higher solubility than natural starch. In general, higher TML values were observed in the case of testing the sedimentary galena mixed with 2% of starch material [14].

In the experiments for estimation of the permeability, cohesion and internal friction angle, the samples were compacted. The consolidation conditions in the holds were simulated by applying the vertical loads equal to: 0 N, 98 N, 196 N, 294 N and 490 N, corresponding to the normal stresses of: 0 , $1.532 \cdot 10^4$ N/m², $3.0645 \cdot 10^4$ N/m², $4.589 \cdot 10^4$ N/m², $7.659 \cdot 10^4$ N/m², respectively. The test of samples without stresses corresponded to the stress conditions of cargo in the hold during its loading. The increasing values of normal stresses represented the changes in the bulk cargoes during their shipping by sea.

RESULTS AND DISCUSSION

The results of the permeability tests are presented in Tab. 1.

Based on the results of the tests, the effect of different content of the samples on their permeability was observed.

The maximum value of the permeability coefficient k was achieved for the mineral concentrate without any starch materials; it reached the value of $1.46 \cdot 10^{-2}$ m/s. The value indicates that the tested concentrate may be classified as prone to liquefaction because its permeability coefficient significantly exceeds the limiting value $k = 10^{-8}$ m/s [15].

Large spaces between particles, confirmed by the porosity ratio, mean that the sedimentary galena is the cargo of the highest permeability among the tested samples.

Tab.1. Results of permeability test

Sample type	Permeability coefficient [m/s]	
	Sedimentary lead concentrate + 1% of starch material	Sedimentary lead concentrate + 2% of starch material
Sedimentary lead concentrate	$1.46 \cdot 10^{-2}$	
Sedimentary lead concentrate + Lubostat	$1.8 \cdot 10^{-3}$	$5.82 \cdot 10^{-4}$
Sedimentary lead concentrate + AD	$2.34 \cdot 10^{-3}$	$1.12 \cdot 10^{-3}$
Sedimentary lead concentrate + granulated starch	$3.84 \cdot 10^{-3}$	$2.34 \cdot 10^{-3}$

The presence of starch materials in the concentrate material reduces, by absorption of water, their ability to filtration. The ability to absorption of water is related primarily to the composition of starch material and the percentage of starch in a mixture.

For all samples with starch material the decrease of permeability was found. If the content of starch material in the mineral concentrate increases the value of permeability coefficient decreases. The greatest decrease of the permeability coefficient was observed in the mixture containing 2% of Lubostat.

Measurement of cohesion and internal friction angle

The changes of cohesion in function of moisture content are presented in Fig. 1 through 3.

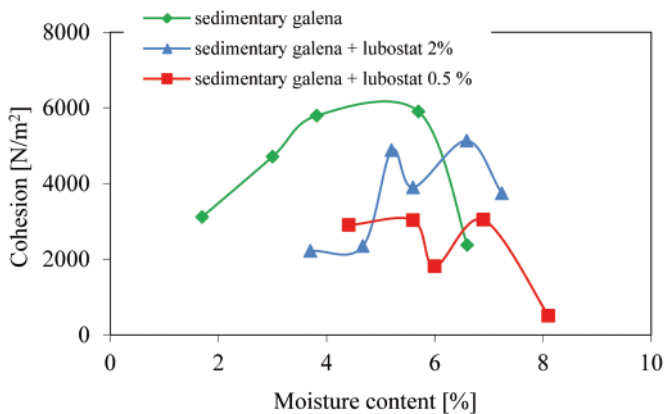


Fig. 1. The changes of cohesion in function of moisture content for sedimentary galena + Lubostat

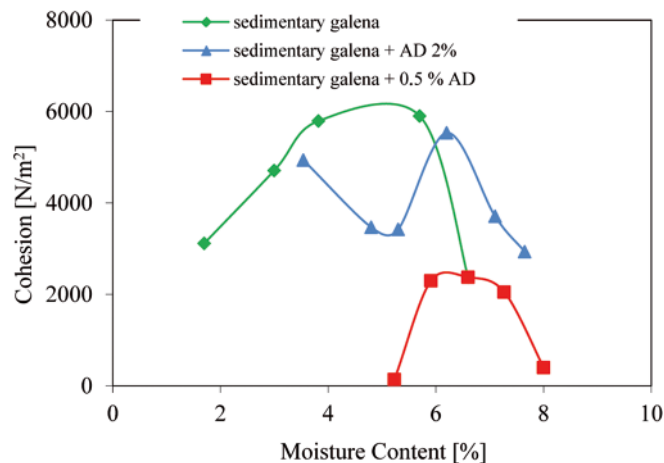


Fig. 2. The changes of cohesion in function of moisture content for sedimentary galena + AD

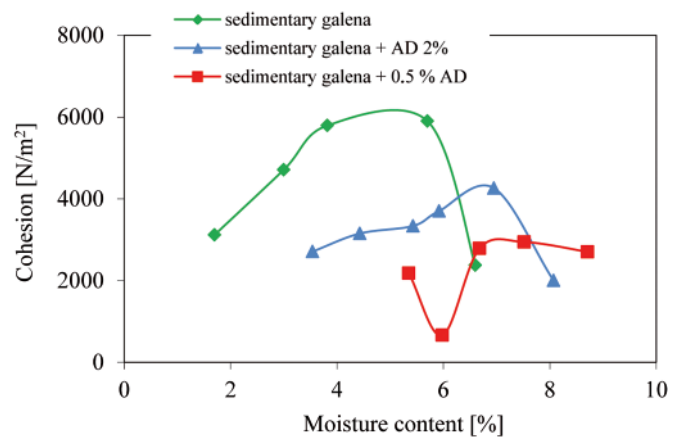


Fig. 3. The changes of cohesion in function of moisture content for sedimentary galena + granulated starch

The result indicates that the starch materials significantly change the cohesion. The presence of the starch materials in mineral concentrates tends to reduce cohesion. In all tested samples cohesion increases with the increasing of moisture content and reaches its maximum with the moisture approaching the TML, and then it goes down. The extreme values are not reached at the same moisture content for all mixtures. The maximum values of cohesion are affected by the type of mixture. The result confirms presence of correlations between TML values of mixtures and maximum values of cohesion. For mixtures containing 0.5% of starch material, the greatest decreasing of maximum cohesion was observed.

The changes of internal friction angle in function of moisture content are presented in Fig. 4 through 6.

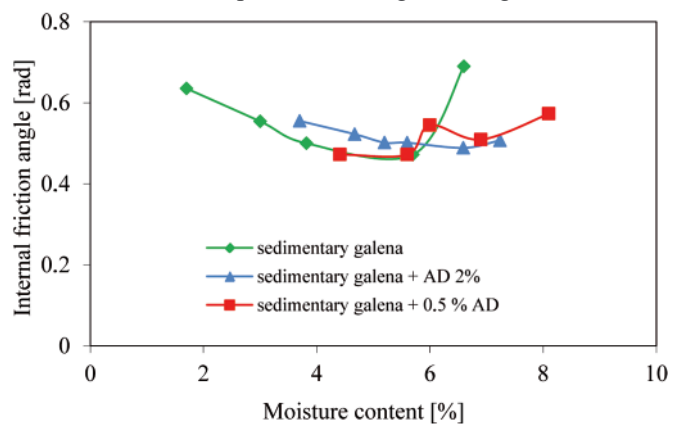


Fig.4. The internal friction angle in function of moisture content for sedimentary galena + Lubostat

For the sedimentary galena with starch material no significant changes in values of internal friction angle are observed. The presence of starch materials in the tested mineral

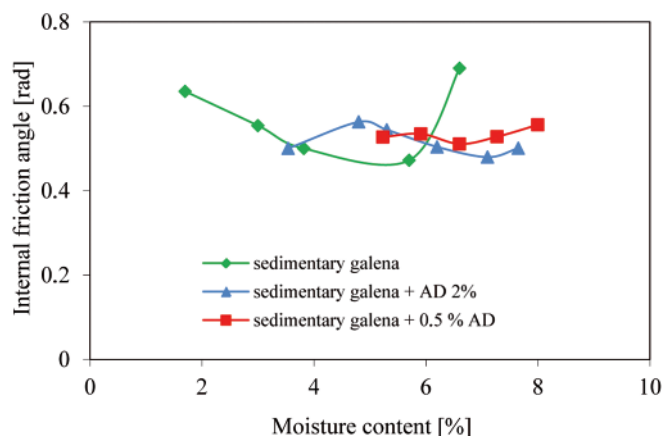


Fig. 5. The internal friction angle in function of moisture content for sedimentary galena + AD

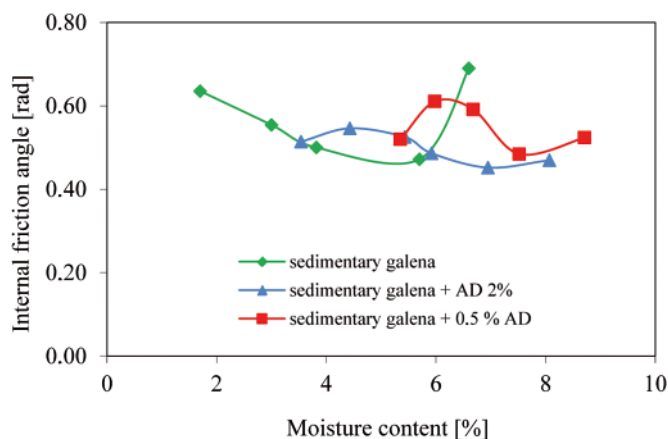


Fig. 6. The internal friction angle in function of moisture content for sedimentary galena + granulated starch

concentrate influences the minimum value of internal friction angle. In each case the values are higher than those for the sample without starch material. For mixtures containing 0.5% of starch material the greatest increase of minimum internal friction angle was observed. The minimum values are not reached at the same moisture content for all samples. Content of starch material in mixture contributes to increase of the moisture content at which the maximum value of internal friction angle is achieved. Increasing the internal friction angle reduces the proneness of mineral concentrate to shifting.

CONCLUSION

For all samples with starch material, a reduction of the degree of permeability was obtained. Starch materials absorbed water from the mixtures at the amount approximately proportional to the starch material content in mineral concentrates. The results of the tests indicate that the permeability influences significantly the properties of the concentrates, important from the point of view of sea transport safety.

Water absorption and swelling the particles results in a reduction of space between the particles and, as the migration of water is thus more difficult, the concentrate capability to filtrate water into the lower part of cargo where the liquefaction process usually starts, is also reduced.

In consequence, starch materials prevent mineral concentrates against drainage of water from pores between particles, and consequently, sliding and shifting such cargoes in storage.

The comparison of the cohesion, internal friction angle and TML values confirms that for the tested mixtures the correlation occurs between values of the quantities in question. Due to the presence of starch materials in the mixtures the risk of passing mineral concentrates into the liquid state is lower.

BIBLIOGRAPHY

1. Roberts S., Marlow P.: *Casualties in dry bulk shipping*. Maritime Policy, pp. 437÷450, 2004
2. International Maritime Organization: *International Convention for the Safe of Life at Sea – SOLAS 1974/1978*. London, 2001
3. International Maritime Organization: *Code of practice for the safe loading and unloading of bulk carriers, BLU Code*. London, 2004
4. International Maritime Organization: *International Maritime Solid Bulk Cargoes Code – IMSBC Code*. London, 2009
5. Sieder R., van den Beukel A.: *The liquefaction cycle and the role of drainage in liquefaction*. Granular Matter 6, pp.1÷9, 2004
6. Eckersley J.D.: *Coal cargo stability*. The AusIMM Proceedings, No.1, pp. 33÷42, 1997
7. Demirgoz D. et al.: *Chemical modification of starch based biodegradable polymeric blends: effects on water uptake, degradation behaviour and mechanical properties*. Polymer Degradation and Stability 70, pp. 161÷170, 2000
8. Ramaswamy M. & Bhattachary M.: *Properties of Injection Moulded Blends of Starch and Modified Biodegradable Polyesters*. European Polymer Journal 37, pp.515÷526, 2001
9. Figiel A., Zięba T., Leszczyński W.: *The effect of moisture content and composition on tensile properties of the synthetic polymer/starch composition*, Polimery 49, pp. 547÷550, 2004
10. Bastoli C., Belloti V., Baerel L.: *Eur. Pat. Appl. WO 90/EP 1286*, 1990
11. Bulatovic, S. M.: *Use of organic polymers in the flotation of polymetallic ores: A Review*, Minerals Engineering 12/4, pp. 341÷354, 1999
12. Tudoracchi N., Lipsa R.: *Comparative study on starch modification with lactic acid and polylactic acid*, Polimery 51, pp. 425÷430, 2006
13. Popek M.: *The evaluation of Ability to Liquefaction of Solid Bulk Cargoes*, The 3-rd Safety and Reliability International Conference, Warszawa, 2003
14. Popek M.: *Liquefaction of Water Saturated Mineral Concentrates in Mixtures with starch*, Zeszyty Naukowe UE, No. 211, Poznań, pp. 102÷112, 2011
15. Head K.: *Soil Technicians' Handbook*. Pentech Press Publishers, London, 1989.

CONTACT WITH THE AUTHOR

Marzenna Popek, Ph. D.
Department of Chemistry
and Industrial Commodity Science,
Gdynia Maritime University
Morska 83
81-225 Gdynia, POLAND
e-mail: marzenap@am.gdynia.pl



The Ship Handling Research and Training Centre at Ilawa is owned by the Foundation for Safety of Navigation and Environment Protection, which is a joint venture between the Gdynia Maritime University, the Gdansk University of Technology and the City of Ilawa.

Two main fields of activity of the Foundation are:

- Training on ship handling. Since 1980 more than 2500 ship masters and pilots from 35 countries were trained at Ilawa Centre. The Foundation for Safety of Navigation and Environment Protection, being non-profit organisation is reinvesting all spare funds in new facilities and each year to the existing facilities new models and new training areas were added. Existing training models each year are also modernised, that's why at present the Centre represents a modern facility perfectly capable to perform training on ship handling of shipmasters, pilots and tug masters.
- Research on ship's manoeuvrability. Many experimental and theoretical research programmes covering different problems of manoeuvrability (including human effect, harbour and waterway design) are successfully realised at the Centre.

The Foundation possesses ISO 9001 quality certificate.

Why training on ship handling?

The safe handling of ships depends on many factors - on ship's manoeuvring characteristics, human factor (operator experience and skill, his behaviour in stressed situation, etc.), actual environmental conditions, and degree of water area restriction.

Results of analysis of CRG (collisions, rammings and groundings) casualties show that in one third of all the human error is involved, and the same amount of CRG casualties is attributed to the poor controllability of ships. Training on ship handling is largely recommended by IMO as one of the most effective method for improving the safety at sea. The goal of the above training is to gain theoretical and practical knowledge on ship handling in a wide number of different situations met in practice at sea.

For further information please contact:

The Foundation for Safety of Navigation and Environment Protection

Head office:
36, Chrzanowskiego Street
80-278 GDAŃSK, POLAND
tel./fax: +48 (0) 58 341 59 19

Ship Handling Centre:
14-200 ILAWA-KAMIONKA, POLAND
tel./fax: +48 (0) 89 648 74 90
e-mail: office@ilawashiphandling.com.pl
e-mail: office@portilawa.com